Ab initio modeling of dense water ices at extreme conditions of pressure and temperature

Jean-Alexis Hernandez

Numéro National de Thèse : 2017LYSEN028

THESE de DOCTORAT DE L'UNIVERSITE DE LYON

opérée par
l'Ecole Normale Supérieure de Lyon

Ecole Doctorale N°34
Ecole Doctorale Matériaux de Lyon

Discipline de doctorat : Sciences de la Terre et de l'Univers
Spécialité de doctorat : Matériaux en conditions extrêmes

Soutenue publiquement le 05/07/2017, par :

Jean-Alexis HERNANDEZ

Ab initio modeling of dense water ices at extreme conditions of pressure and temperature

---

Modélisation *ab initio* des glaces d'eau en conditions extrêmes de pression et de température

---

Devant le jury composé de :

Wendy Panero	Professor	Ohio State University	Rapporteure
A. Marco Saitta	Professeur	Université Pierre et Marie Curie	Rapporteur
Alessandra Ravasio	Chargée de recherche	CNRS (CEA)	Examinatrice
Isabelle Daniel	Professeure	Université de Lyon (LGLTPE)	Examinatrice
Razvan Caracas	Directeur de recherche	CNRS (LGLTPE)	Directeur de thèse

Remerciements

Abstract

In icy planets, complex interactions are expected at the interface between the rocky core made of oxides and silicates and the icy mantle made of mixtures of water, methane, and ammonia. The hydration of the silicate layer produces salts ($MgSO_4$, NaCl, KCl) that could mix with the ice, and change considerably its properties. In this thesis, we used *ab initio* molecular dynamics to investigate the stability and the properties of the pure and NaCl-bearing water ices at the relevant thermodynamic conditions for planetary interiors of ocean exoplanets. In these conditions, the ice presents a body-centered cubic sub-lattice of oxygen atoms. The sub-lattice of hydrogen atoms undergoes several structural and dynamical transitions that affect considerably the ionic conductivity and the elastic properties of ice.

By analyzing the different bonding regimes we find the first ab initio evidence for a plastic phase of water ice at 600 K between 7 and 15 GPa. At higher pressure, we retrieve the well-know hydrogen bond symmetrization (ice VII – ice VII′ – ice X transition sequence). Increasing the temperature, we show that the ice VII domain closes around 750 K and 15 GPa. Above 1000 K, several transitions related to the symmetrization of the hydrogen bonds occur in presence of superionic conduction. At 1600 K, a first-order phase transition separates the superionic ice VII″ to the superionic ice VII′ at 52 GPa; at 70 GPa ice VII′ is no longer superionic; at 100 GPa, ice VII′ transforms in ice X. Above 1800 K, the complete transition sequence occurs in the superionic domain.

Next, we compute the Gibbs free energy of H_2O and NaCl-bearing ices along the 1600 K isotherm taking into account both vibrational and configurational entropy. We show that up to 5.88 wt% NaCl can be included in the ice structure. The inclusion of Na^+ and Cl^- ions strongly enhances the orientational disorder in the ice. From 2.5 wt% the superionic conduction is extended up to 300 GPa and the complete symmetrization of the hydrogen bonds is shifted towards high pressures.

Last, we provide a description of the $\langle 110 \rangle$ and $\langle 111 \rangle$ screw dislocation core structures in pure ice X at 80 GPa. This constitutes the basis towards the construction of rheological laws for body-centered cubic ices.

Résumé

Dans les planètes de glace, des interactions complexes sont attendues à l'interface entre le noyau rocheux, composé de silicates et d'oxydes, et le manteau de glace, composé d'un mélange eau – methane – ammoniac. L'hydratation des silicates produit des sels ($MgSO_4$, NaCl, KCl) qui, lorsqu'ils sont mélangés avec la glace, peuvent changer considérablement ses propriétés. Dans cette thèse, nous étudions la stabilité et les propriétés des glaces d'eau de haute pression et de haute température comportant ou non des inclusions de NaCl dans leur structure cristalline. Nous utilisons une approche théorique basée sur des dynamiques moléculaires *ab initio* ce qui nous permet de nous placer dans les conditions thermodynamiques propres aux intérieurs de ces exoplanètes océans. Dans ces conditions, les atomes d'oxygène forment un sous-réseau cubique volume-centré, et les différentes phases sont déterminées par la position et la dynamique des atomes d'hydrogène. En fonction des conditions thermodynamiques, le sous-réseau d'hydrogène subit de profondes transformations ce qui affecte considérablement la conductivité ionique et les propriétés élastiques de la glace.

En analysant la dynamique des liaisons entre hydrogènes et oxygènes, nous reportons la présence de la phase plastique de la glace entre 7 et 15 GPa à 600 K. À plus haute pression, nous retrouvons la séquence de transition caractéristique de la symétrisation des liaisons hydrogènes (glace VII – glace VII′ – glace X). Nous montrons que le domaine de stabilité de la glace VII se ferme à 750 K and 15 GPa. Au-dessus de 1000 K, plusieurs transitions de phases associées avec la symétrisation des liaisons hydrogènes découpent le domaine superionique. À 1600 K et 52 GPa, une transition de phase du premier ordre sépare la glace superionique VII″ de la glace superionique VII′ ; à 70 GPa, la diffusion protonique stoppe dans la glace VII′ ; à 100 GPa, la symetrisation des liaisons hydrogènes est complète ce qui définit la glace X. Au-dessus de 1800 K, cette séquence de transitions de phases se produit dans le domain superionique. Ensuite, nous calculons l'énergie libre de Gibbs de H_2O et des glaces salées le long de l'isotherme 1600 K. Dans ce calcul, nous prenons en compte l'entropie vibrationnelle ainsi que l'entropie configurationnelle. Nous montrons que jusqu'à 5.88 % en masse de NaCl peuvent être inclus dans la structure de la glace. L'inclusion des ions Na^+ et Cl^- stimule le désordre orientationel des molécules d'eau par rapport à la glace d'eau pure. À partir de 2.5 % en masse de NaCl, la conduction superionique s'étend à l'ensemble de la gamme de pression étudiée, c'est-à-dire jusqu'à 300 GPa, et la symétrisation des liaisons hydrogènes (glace X) se produit à plus haute pression.

Enfin, nous décrivons les structures de cœur des dislocations vis ayant des vecteurs de Burgers $\langle 110 \rangle$ et $\langle 111 \rangle$ dans la glace X à 80 GPa, ce qui constitue une étape préliminaire importante à la construction de lois rhéologiques pour les glaces cubiques de haute pression.

Contents

Chapter 1

Introduction

Contents

Early 2017, about 5900 planets have been detected out of the Solar System[1]. This diversity of extra-solar world has deeply challenged our conception of the planetary formation processes and invigorated the search for extraterrestrial life. During the last decade, the continuous observation of known planetary systems, the improvement of detection techniques, and both Kepler and CoRoT missions have permitted to find planets with diverse sizes and orbital periods (see Figure 1.a.). Nevertheless, the large interstellar distances still exclude a direct mapping of their surface composition, and estimations of their bulk composition and their internal structure rely on the measurements of their mass and radius.

The comparison of mass-radius measurements with mass-radius relations of different compositions revealed that many planets present a bulk density compatible with large amounts of water in their interiors[2]. Among the new discoveries a continuum of planets has been found in mass and radius between the Earth and the ice giants Neptune and Uranus.These potentially H_2O-rich exoplanets have been referred as ocean planets for the ones presenting liquid water on their surface and as mini-Neptunes for the bigger ones that are expected to be enriched in other volatiles (ammonia, methane,

[1] On January 26th, 3442 exoplanets detections have been confirmed and 2416 are Kepler telescope additional detections that require further measurements.

[2] Mass-radius relations are calculated for a model planet with a given composition along a given temperature profile considering a spherical symmetry and an isostatic equilibrium. It requires solving a system of coupled equations relating the gravity, the pressure and the density profiles along the planet radius. The density dependence on the pressure and on the temperature is described by the equation of state of the material considered.

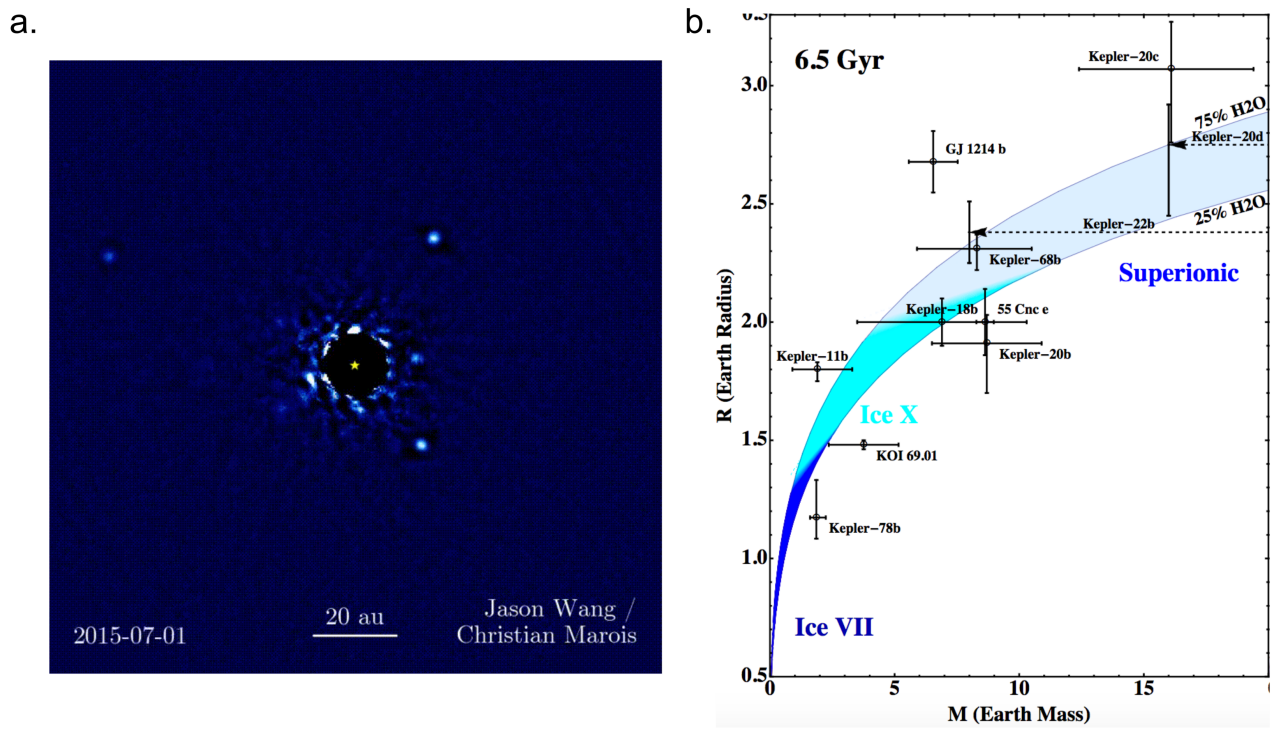

Figure 1.1: a. Direct imaging of the HR8799 system at the Keck observatory using adaptitive optics to compensate atmospheric turbulence and coronagraphy techniques to hide the star. The isolated little dots are four giant planets with orbital periods ranging from 40 years for the closest to more than 400 years for the farthest. b. Mass-radius relations as function of cooling age for H_2O-silicate planet with 25 % to 75 % H_2O in mass. The different colors correpond to the phase of water stable at the interface with the silicates. The black dots refers to mass-radius measurements of some exoplanets. From Zeng et al. (2014).

helium, hydrogen). They complete the gap between the dwarf planets and the ice giants that exists in the Solar System.

The succession of spatial missions (Voyager 1 and 2, Galileo, Cassini, Dawn, New Horizons) in the outer Solar System during the last decades provides valuable insights on the composition and on the dynamics of water-rich bodies. Spectroscopic measurements of their surface, and of the Enceladus' plumes, have revealed that the water is always mixed with other impurities such as salts, sulfates, volatiles or other ices. The presence of an interface between a rocky core and a H_2O-rich layer may result in the hydration of the silicates as well as the incorporation of hydration products in the ice structure.

The intimate relation between life as we know it and aqueous solutions emphasizes the importance of an accurate and realistic description of these bodies. Such objective requires exploring the states of water and water-based mixtures under the huge range of pressures and temperatures spanned by

the planerary interiors. So far, the phase diagram of water has shown a great complexity, and many interrogations subsist in the pressure range of the megabar with the prediction of some exotic states.

The purpose of this work is to investigate the phase diagram, the stability and the properties of pure and NaCl-bearing dense water ice between 4 and 300 GPa and up to 2000 K from atomistic modeling.

In this introductory chapter, we present the phase diagram of pure water and propose a state-of-the-art of the high-pressure and high-temperature phases related to the dissociation of the water molecules. Then, we focus on the binary mixture $NaCl - H_2O$ at the same thermodynamic conditions. The last section gives a detailed outline of this thesis.

1.1 H_2O phase diagram

In this section we discuss the main properties of the liquid and solid phases of H_2O and their relations to the exotic behaviors observed at high-pressure.

1.1.1 Molecular phases

H_2O is V-shaped polar molecule composed of two hydrogen atoms covalently bonded to an oxygen atom. The value of the $\widehat{HOH}$ angle depends on the environment of the molecule and varies between 104.5° and 109.5°. When non-isolated, the H_2O units tend to form hydrogen bonds ($O - H \cdots O$) due to the highly heterogeneous distribution of the electrons inside the H_2O molecule. The electron density is ten times higher around the oxygen than around hydrogen atoms inducing a polarization at the scale of the covalent $O - H$ bond and by symmetry at the scale of the H_2O molecule.

A hydrogen bond (HB) results from the interaction between the dipolar moment associated to a $O - H$ bond and the dipolar moment of a neighbouring H_2O molecule. This strong and directional bond results in the formation of HB networks in condensed phases, responsible for most of the "anomalous" properties of water (density maximum at 4°C in liquid water high latent heat of evaporation, negative Clapeyron slope bteween the liquid and the ice Ih, self-ionization, etc.) that are crucial for biological and climatic processes.

Due to the large inter-molecular distances, water has a high compressibility. Under increasing pressure, the volume reduction is accomodated by changing the packing of H_2O units. In the liquid and amorphous phases it increases the number of H_2O molecules in the first coordination shell around a

given molecule. In crystalline phases, the H_2O units rearrange to form a new periodic network. The exploration of the phase diagram of pure H_2O has revealed a large polymorphism with more than ten different equilibrium molecular ices, three metastable amorphous ices, more than two liquid states and a number of metastable crystals (see Figure 1.2).

As a consequence of the formation of hydrogen bonds, the arrangement of H_2O molecules in molecular ices respects some rules (Bernal and Fowler, 1933; Pauling, 1935). Known as the *ice rules* they stipulate that: i) each oxygen atom is covalently bonded to two hydrogen atoms; ii) each H_2O molecule is hydrogen bonded with the four H_2O molecules that surround it in a tetrahedral arrangement; iii) only one H atom lies between the O atoms occupying the summits of the tetrahedron (see Figure 1.3).

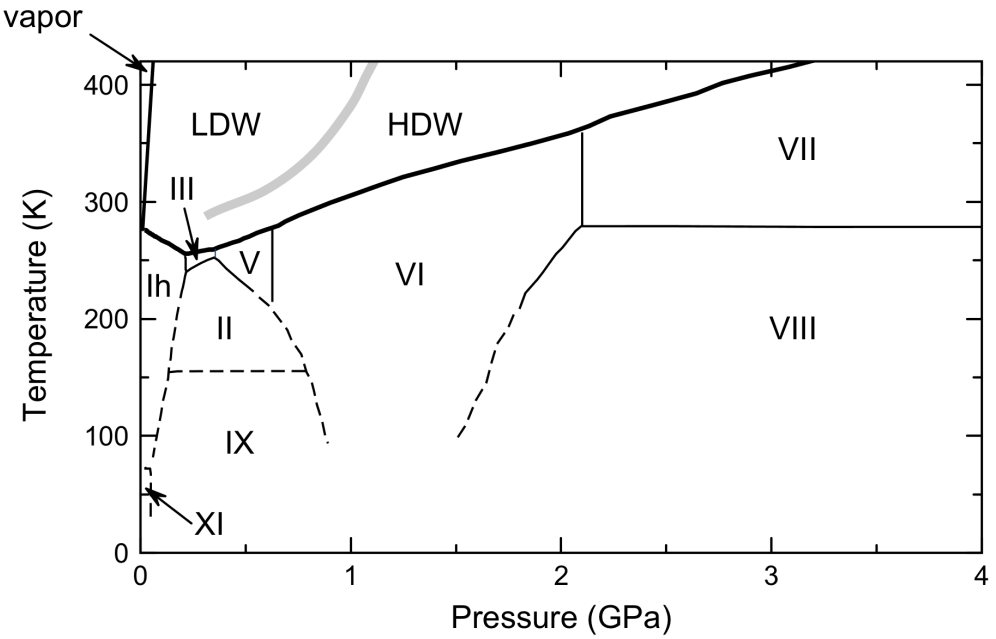

Figure 1.2: Phase diagram of molecular water up to 4 GPa. Neither metastable crystalline or amorphous phases are represented. Thick black lines correspond to solid-liquid and liquid-vapor curves. Thin lines represent the crystalline phase boundaries. The low-density (LDW) to high-density (HDW) water transition appears in grey.

Molecular ices differ by the periodical arrangement formed by the O atoms and/or by the orientation of the molecules related to the position of the H atoms. Such statement allows to distinguish ordered ices in which the periodicity is only present in the sub-lattice formed by the O atoms. In this case, the orientation of the water molecules is random while respecting the ice rules. Orientational disorder implies that all orientations satisfying the ice rules are possible. This gives rise to a configurational entropy S_p. Using a combinatorial approach, Pauling (1935) successfully estimated S_p to $Nk_B \ln(3/2)$ where k_B is the Boltzmann constant and N the number of molecules. This value corresponds to the

residual entropy observed experimentally (Giauque and Ashley, 1933). The deviation from the ice rules leads to the formation of Bjerrum and ionic defects (see Figure 1.3). Usually, both ordered

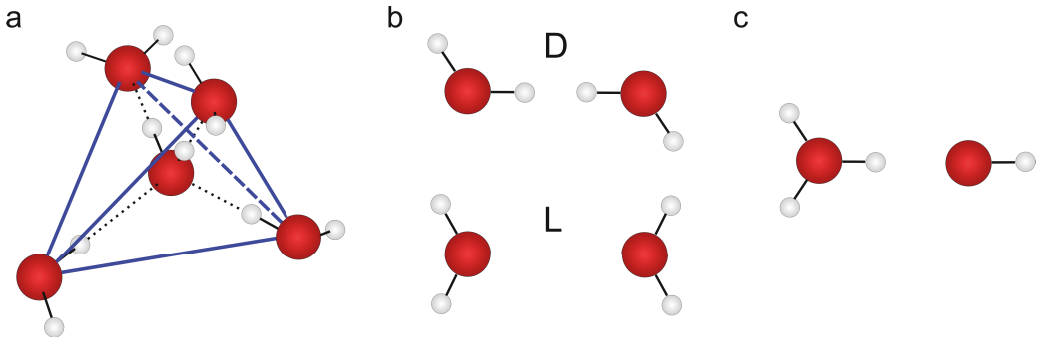

Figure 1.3: a. The water molecule lying at the center of the blue tetrahedron fully respects the ice rules. b. Bjerrum defects. D-type defects corresponds to the presence of 2 H atoms along the O–O separation. L-defects refer to the case where no H atom is found along the O–O separation. c. Ionic defects form by bimolecular self-ionization of the water molecule and results in a $H_3O^+ - OH^-$ pair. Red and white spheres respectively represent the O and H atoms.

and disordered phases exist for a given sub-lattice of O atoms. Fully ordered crystalline structures are observed at low temperature (XI, II, XV and VIII) whereas disordered phases always share a boundary with the liquid or fluid phase (Ih, III, V, VI and VII). Moreover, at least 4 metastable crystalline molecular ices (Ic, IV, IX and XIII) have been found to coexist with stable phases[3] for kinetic reasons.

Although all these phases are relevant for the study of the interior of icy satellites and small icy bodies, we do not describe them here except for ice VII and ice VIII. For more information on this fascinating part of the phase diagram we refer the reader to the following books Petrenko and Whitworth (1999) and Gudipati and Castillo-Rogez (2012), as well as Martin Chaplin's website which provides an up-to-date phase diagram of water Martin (2017).

Figure 1.4 shows the phase diagram of H_2O ice in the stability domain of the dense cubic ices. Ice VII, identified for the first time by Bridgman (1937), is a molecular H-disordered phase with a bcc sub-lattice of oxygen atoms (cf. Figure 1.4). It belongs to the space group $Pn3m$ and often seen as two interpenetrating ice Ic lattices. As shown in Figure 1.4, $O - H \cdots O$ bonds are oriented along the diagonals of the bcc sub-lattice.

Ice VIII is the corresponding low-temperature H-ordered structure (order-disorder transition at 278 K below 20 GPa). Its tetragonal O sub-lattice results from a slight distortion of the bcc arrangement

[3] According to Martin Chaplin's website `http://www1.lsbu.ac.uk/water/water_phase_diagram.html`, ice Ic has been observed in ice Ih stability field below 193.14 K, ice IV has been observed in ices III, V and VI stability fields, and ices IX and XIII have been found in ice II domain at low temperature.

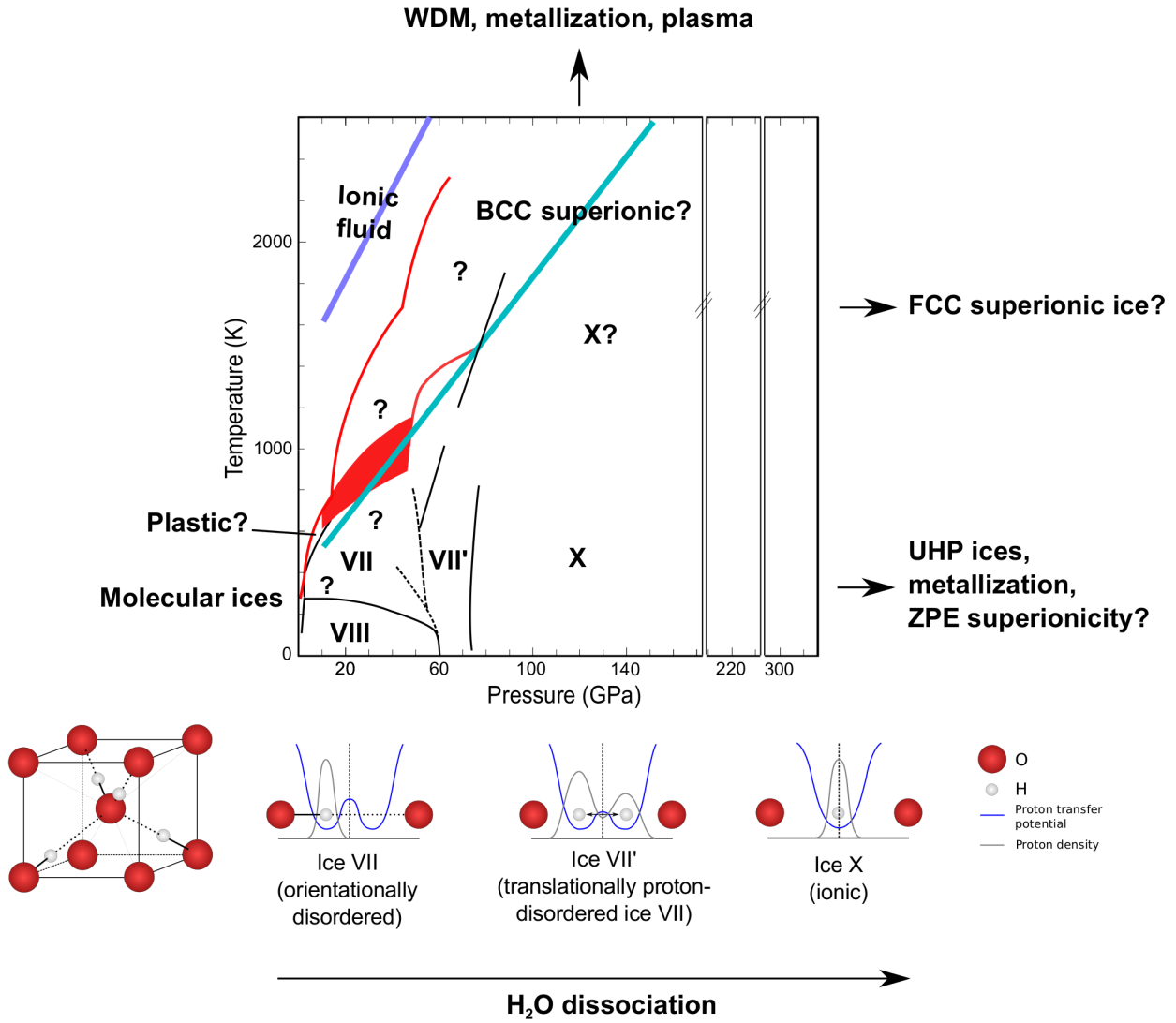

Figure 1.4: High-pressure phase diagram of H_2O in the thermodynamic conditions of cubic ices. Black lines indicate the phase boundaries found in the literature (see text for the low temperature part, see Goncharov and Crowhurst (2007) for temperatures greater than 500 K). Red lines correspond to the two groups of melting curves described in the literature (see text for the references). Thick pale blue and cyan lines refer to the isentropes of Neptune (Redmer et al., 2011) and of a five terrestrial mass H_2O-rich exoplanet (Sotin et al., 2007). A unit-cell of ice VII is represented on the left. The evolution of the proton transfer potential during th progressive dissociation of H_2O is illustrated. Anomalies and uncertain phase identifications are marked with question markers.

due to the H ordering (difference of 0.2 Å at 2.4 GPa between c and the two other unit-cell parameters). Ice VIII belongs to the space group $I4_1/amd$ and is antiferroelectric (Pruzan et al., 1992, 1993).

Theoretical studies predicted the existence of a second-order transition between the ice VII and a plastic phase at the vicinity of the melting line (Aragones and Vega, 2009; Takii et al., 2008; Himoto et al., 2014). In this phase the sub-lattice of O atoms is analogous to ice VII (body-centered cubic

arrangement) but the water molecules behave as free rotors. The transition from the ice VII to the plastic ice can be described as from a static orientational disorder to dynamic orientational disorder. The fluid-VII-plastic triple point is found at 352 K and 6 GPa (TIP4P/2005 model, Aragones and Vega (2009)), and a tricritical point between ice VII and the plastic body-centered cubic (bcc) ice is predicted at 13.3 GPa and 665 K. Such plastic state exists in solid ammonia over a broad thermodynamic domain with both hexagonal close packed and face-centered N sub-lattices (Cavazzoni et al., 1999; Ninet et al., 2012). However, it is worth mentioning that no experimental evidence of a plastic phase for H_2O exists. Up to date, only studies based on atomistic simulations with rigid H_2O classical models (TIP4P/2005, TIP5P, TIP5P/E, SPC/E) depict a plastic phase. It is currently investigated by high-pressure *in situ* neutron diffraction experiments.

1.1.2 Pressure-induced dissociation of water molecules

Increasing the pressure or the temperature in a molecular crystal or molecular fluid leads inevitably to the dissociation of the molecules and ultimately to the metallization. In the case of temperature-induced dissociation, the amplitude of the vibrations of the atoms becomes high enough to break the bonds and allow the atoms to diffuse. The case of pressure-induced dissociation is more complicated and highly depends on the topology of the crystal. The volume reduction cannot be accomodated by molecular reorientation anymore and affects the intra-molecular distances.

Kamb and Davis (1964) suggested that the dissociation of the water molecule should occur with the complete symmetrization of the hydrogen bonds when increasing the pressure in ice VII. Holzapfel (1972) modeled the phenomenon using a symmetric double Morse potential. He estimated that the double well potential should progressively symmetrize into a single potential around 50 GPa at 0 K in ice VII. Taking into account the zero-point energy of H and D atoms, Holzapfel (1972) also predicted that the symmetrization should occur at higher pressure in D_2O than in H_2O. Since then and up to the end of the 1990s, the stability domains of the ices VII and VIII had been highly debated. By this time, the development of high-pressure spectroscopy enabled the search for the symmetric ice X. X-ray diffraction measurements revealed that the ice VII bcc oxygen sub-lattice persists up to 210 GPa at room temperature (Goncharov et al., 1996). Conversely, the ice VIII was found to lose its antiferroelectric H-ordering and its tetragonal oxygen sub-lattice for a bcc one around 60 GPa at 100 K (Pruzan et al., 1993).

In situ Raman and infrared spectroscopies (Pruzan et al., 1993; Aoki et al., 1996; Goncharov et al., 1996; Wolanin et al., 1997; Goncharov et al., 1999; Song et al., 1999), and theoretical studies (Schweizer and Stillinger, 1984; Benoit et al., 1998, 1999, 2002) gave deeper insights. Under compression, the softening, the broadening and the disappearance of the OH stretching mode ν_1, combined with the H/D isotopic effect on the transition pressure indicate the transition towards a dynamically disordered state between 40 and 60 GPa. Path-integral and DFT-based molecular dynamics (Benoit et al., 1998, 1999, 2002; Bronstein et al., 2014) showed that it corresponds to a proton translational disordering along the $O-O$ axis due to the enhancement of the proton tunneling and to the reduction of the potential barrier at higher pressure. First, this results in a bimodal proton density along the $O-O$ bond associated with the underlying double well proton tranfer potential: this is ice VII$'$. The transition between ice VIII and ice VII$'$ is an order-disorder transition. At ambient temperature, both tunneling and thermal hopping participate to the translational disordering. Because the ice VII is affected by a static orientational disorder, the ice VII to ice VII$'$ transition is a static to dynamical translational disorder transition. Recently, the pressure range accessible to neutron diffraction experiments has considerably expanded, giving now access to the structure of the hydrogen sub-lattice in ice VII up to 50 GPa (Guthrie et al., 2013). Guthrie et al. (2013) reports a structural change in ice VII at 13 GPa implying a large H occupancy of the octahedral interstitial site of the bcc sub-lattice. Nevertheless, Iitaka et al. (2015) have shown that the interstitial model is incompatible with X-ray Raman spectroscopy measurements. Other anomalies have been reported around 10–15 GPa in both ice VII and ice VIII, and are discussed in Chapter 3.

Under further compression, the two wells progressively merge lowering the barrier up to the point that the proton density becomes unimodal even in presence of an underlying double well potential: this is the symmetric but dynamically disordered ice X$'$. Finally, in this model, ice X is obtained under further compression when a single proton tranfer potential remains at the center of the $O-O$ bond with its associated unimodal proton density. At this stage the dissociation is done, i.e. the integrity of the H_2O molecules is lost. In practice, ice X$'$ and ice X cannot be distinguished because they both present a unimodal proton density at the center of the $O-O$ bond. Therefore, we will not use the denomination ice X$'$ in this manuscript anymore.

Experimental evidence for ice X was clearly found from Raman and infrared spectroscopy with the disappearance of the vibrational modes associated with the H_2O molecules (bending and rotational modes) and the appearance of the deformational and translational modes associated to the cuprite

structure of ice X between 80 and 95 GPa (Aoki et al., 1996; Goncharov et al., 1996, 1999; Song et al., 1999).

Molecular dynamics and lattice dynamics predict that ice X exists up to at least 300 GPa (Benoit et al., 1996; Caracas, 2008). Phonon dispersion exhibits the development of an unstable phonon at the M-point of the reciprocal space (Caracas, 2008). This instability is reflected in the evolution of the elastic constants with C_{12} becoming greater than C_{11} (Journaux et al., 2013). At higher pressure, theoretical calculations predict post-ice X structures that are still subject to experimental verification. We refer the reader to the following studies for more details about these ultra-high-pressure ices: Benoit et al. (1996); Caracas (2008); Militzer and Wilson (2010); Ji et al. (2011); McMahon (2011); Pickard et al. (2013); Wilson et al. (2013); Hermann et al. (2013); Sun et al. (2015).

1.1.3 Temperature-induced dissociation of H_2O in fluid water

1.1.3.1 Melting curve of bcc ice

As shown by Figure 1.5, the high-pressure and high-temperature measurements of the melting curve of water show a relatively good agreement up to 15 GPa (Pistorius et al., 1963; Mishima and Endo, 1978; Fei et al., 1993; Datchi et al., 2000; Dubrovinskaia and Dubrovinsky, 2003; Frank et al., 2004; Lin et al., 2004; Schwager et al., 2004; Schwager and Boehler, 2008; Goncharov et al., 2005; Goncharov and Crowhurst, 2007; Goncharov et al., 2009; Ahart et al., 2014; Kimura et al., 2014). At this pressure, a major discrepancy appears between the experimental studies in which a kink towards higher temperatures is observed (Schwager et al., 2004; Schwager and Boehler, 2008; Klotz et al., 2010; Ahart et al., 2014), and others in which no discontinuity occurs (Dubrovinskaia and Dubrovinsky, 2003; Lin et al., 2004; Frank et al., 2004; Goncharov et al., 2005; Kimura et al., 2014). The melting temperature difference between the two groups becomes larger as the pressure increases and reaches ~1000 K at 50 GPa. However, both low and high temperature melting curves present a kink around 40 GPa where the Clapeyron slope increases brutally. The changes in the Clapeyron slope are related to triple points, indicating that a solid-solid phase transition should occur at the same conditions in the solid.

The high-temperature melting curve proposed by Schwager et al. (2004); Schwager and Boehler (2008) is obtained in a laser-heated diamond anvil cell (DAC) from a visual observation of the laser-speckle pattern from the reflection of the laser beam on the sample-absorber interface. This non-

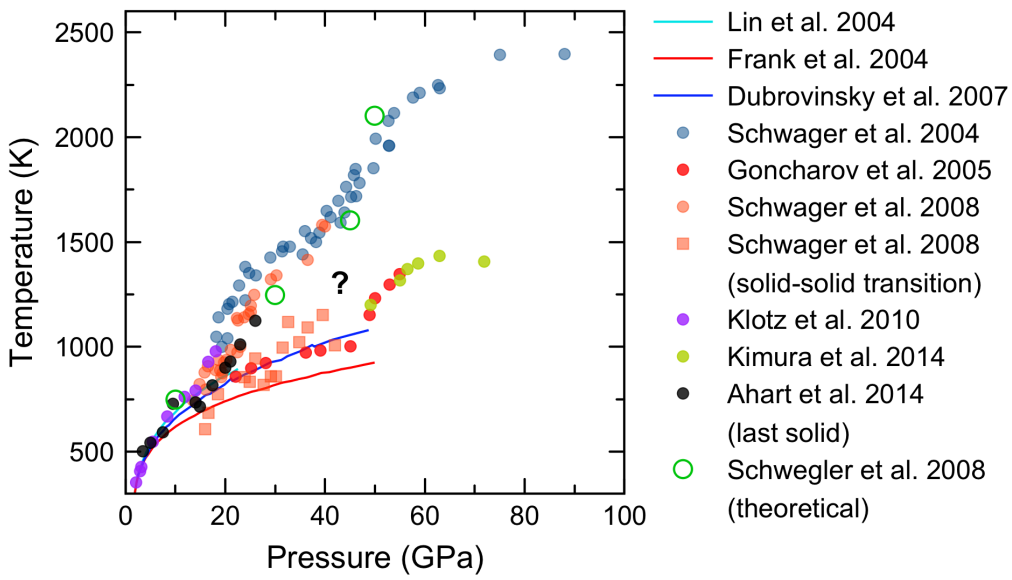

Figure 1.5: Measurements of the high-pressure melting curve of water. Above 15 GPa, a widening discrepancy separates two groups of measurements with a temperature difference reaching 1000 K and 50 GPa.

conventional method is not considered robust enough by other authors. But since then, three studies based on three different approaches support the result of Schwager et al. (2004); Schwager and Boehler (2008): i) *ab initio* two-phase simulations (Schwegler et al., 2008); ii) X-ray diffraction in an externally heated DAC (Klotz et al., 2010); iii) Brioullin spectroscopy in an externally heated DAC (Ahart et al., 2014). The low-temperature melting line has been measured both by disappearance of characteristic peaks in *in-situ* Raman or x-ray diffraction spectra in both externally heated and laser heated DAC, and monitoring of the laser power.Schwager and Boehler (2008) propose a solid-solid phase transition line coinciding with the low temperature melting curves for pressures ranging between 15 and 40 GPa. However, Ahart et al. (2014) do not observe this transition. We also mention that Dubrovinsky and Dubrovinskaia (2007) observe an amorphous ice at 30 GPa and 950 K that transforms reversibly to ice VII.

1.1.3.2 Speciation and dissociation in supercritical water

The vapor-liquid critical point of water is located at 647 K and 0.022 GPa. Consequently, in Figure 1.5 the fluid domain corresponding to temperatures greater than 647 K is supercritical. The low-pressure supercritical water properties have been largely studied because of its industrial applications such as geothermal heating and its implications in hydrothermal chemistry. However, the properties

of hot dense water are still debated (Schwegler et al., 2001; Dellago et al., 2002; Goldman et al., 2005; Goncharov et al., 2005; Mattsson and Desjarlais, 2006; Goncharov et al., 2009; French et al., 2010). The proximity of the H_2O units increases its reactivity and makes it highly corrosive. Hot dense water is of great interest in planetary science as the ice giants see their isentropes crossing this region.

Both the compressibility and the Grüneisen parameter reach a maximum at 12 GPa and 800 K (Walsh and Rice, 1957; Holmes et al., 1985). More extreme conditions lead to the breaking of the hydrogen bonds. Water retains its molecular integrity up to 10 GPa and 1300 K. At this point either a temperature or a pressure increase leads to a significant rise of the electrical conductivity (Chau et al., 2001). Such onset of electrical conduction is compatible with an increase in the concentration of an ionic charge carrier. The presence of the OH^- stretching signal and the absence of H_3O^+ signature in the Raman spectra (Lyzenga et al., 1982) supports that the intra-molecular ionization reaction $H_2O \rightarrow OH^- + H^+$ takes place.

Several theoretical studies based on *ab initio* molecular dynamics attempted to determine the dissociation mechanism and to identify the charge carriers to reproduce the electrical conductivity of the electronically insulating fluid. Nevertheless, the lack of definition of a bonding state in a dynamically ionized molecular fluid led to very different estimations of the speciation (Schwegler et al., 2001; Goncharov et al., 2005; Mattsson and Desjarlais, 2006; Goncharov et al., 2009; French et al., 2010). Various cutoff distance- and time-based criteria have been used during the last decade to define if two atoms are bonded (more details in Chapter 2). In these studies, the calculation of the electrical conductivity is mainly performed from the Nernst-Einstein equation and requires the attribution of a fixed charge to a given ionic species as well as the diffusion coefficients of O and H. By considering a mechanism-independent approach based on the polarization and the linear response theories, French et al. (2011) calculated the electrical conductivity in fluid water at 2000 K and 2 $g.cm^{-3}$. The reported conductivity of 30 $S.cm^{-1}$ is in agreement with experimental data, and validates the conductivity model based on O and H diffusion coefficients and on the fraction of bonded H (Mattsson and Desjarlais, 2006).

Finally, electronic conductivity rises at 4000 K to reach the level of the ionic contribution and dominates at higher temperature indicating the transition towards a metallic state (Mattsson and Desjarlais, 2006; French et al., 2010).

1.1.4 The superionic state

In water ice, the combination of pressure-induced and temperature-induced H_2O molecule dissociation results in a high proton diffusion while the oxygen sub-lattice remains unchanged: this is the superionic state. Its existence was first suggested by Ryzhkin (1985).

1.1.4.1 Generalities about superionic compounds

In a superionic conductor, one atomic species presents a high rate of diffusion whilst the other atomic species form a crystalline structure. This results in an electronically insulating solid with a liquid-like ionic conductivity (Boyce and Huberman, 1979). Such properties allow the use of superionic compounds as solid electrolytes in solid-state batteries. Although there is no simple way to determine if a material is superionic or not, an arbitrary minimum ionic conductivity of 0.01 $S.cm^{-1}$ is set (Keen, 2002). Three types of superionic conductors have been defined based on the development of the superionicity when increasing the temperature at constant pressure (Boyce and Huberman, 1979; Keen, 2002; Hull, 2004). In type I superionic conductors (e.g. α-AgI), the ionic conductivity increases abruptly due to a first-order structural transition. In type II superionic materials (e.g. β-PbF_2), the ionic conductivity increases gradually between the low temperature normal regime and the high-temperature superionic regime. In type III superionic conductors (e.g. Na β-Al_2O_3), thermally activated defects become increasingly mobile with the temperature, and no clear transition occurs (Keen, 2002). In most superionic compounds, the charge carriers are small cations such as Ag^+, Cu^+, Li^+ or H^+. In some cases, electronegative ions such as F^- (in the β-phase of PbF_2) or O^{-2} diffuse (Boyce and Huberman, 1979; Keen, 2002; Hull, 2004). In any case, the diffusive ions jump between crystallographic sites and do not flow in a solid lattice.

1.1.4.2 Superionic water

In 1999, Cavazzoni et al. (1999) predicted from molecular dynamics simulations that bcc ice tranforms into a superionic compound at high temperature before reaching the fluid. In this exotic state, highly mobile hydrogen atoms diffuse through the fixed bcc oxygen sub-lattice (see Figure 1.6). The resulting high ionic conductivity makes it a great candidate to explain the non-dipolar magnetic fields of Uranus and Neptune. The strong quadrupolar component measured by Voyager 2 may originate from the interaction between a conductive superionic ice mantle and a dipolar magnetic field produced

in the metallic core (Connerney et al., 1987, 1991; Redmer et al., 2011). Since then, the superionic water has been studied mainly from *ab initio* molecular dynamics simulations (Goldman et al., 2005; Goncharov et al., 2005; Schwegler et al., 2008; French et al., 2010, 2011, 2016; Wilson et al., 2013; Sun et al., 2015; Hernandez and Caracas, 2016) and shock experiments (Tahir et al., 2010; Knudson et al., 2012; Kimura et al., 2015), especially at temperatures and pressures characteristic of the warm dense matter[4]. Some static high-pressure and high-temperature diamond anvil cell experiments have also claimed the detection of a superionic ice (Goncharov et al., 2005; Goncharov and Crowhurst, 2007; Goncharov et al., 2009; Sugimura et al., 2012). Hereafter, we review some of the properties of this state.

Stability of the bcc superionic ice In their study, Cavazzoni et al. (1999) sample the phase diagram at four different pressures (30, 60, 150 and 300 GPa) and at temperatures ranging from 500 K to 7000 K in steps of 500 K. On the time scales involved in that study (1 to 3 ps of acquisition), they observe a transition solid – superionic solid at ∼2000 K with a jump of 0.4 eV/H_2O per water molecule along the isothermal internal energy curve indicating a first-order phase transition. Then, they validate the stability of the superionic phase by performing several tests: i) the bcc sub-lattice is still stable when removing a water molecule; ii) the cooling of a fluid phase in the superionic pressure-temperature domain results in a superionic amorphous phase that is found to melt at 500 K and 150 GPa, below the solid to superionic transition temperature; iii) a second internal energy jump of 0.8 eV/H_2O is found at the transition between the superionic state and the supercritical fluid.

Transport properties In the superionic phase, the H atom diffusion coefficients are as high as $6.10^{-8}m^2.s^{-1}$ at 150 GPa and 2500 K (Cavazzoni et al., 1999) and increase up to $\sim 2.10^{-7}m^2.s^{-1}$ at ∼1 TPa and 8000 K (French et al., 2010). By comparison the self-diffusion coefficient of H_2O in liquid water at ambient conditions is 2.5 10^{-9} $m^2.s^{-1}$ (Wang, 1965). The temperature dependence of the H diffusion shows that the development of the superionicity is associated with a continuous change of the diffusion regime, indicating that water is a type II superionic compound (Schwegler et al., 2008). While diffusing extremely rapidly, the motion of the H atoms remains highly correlated to the oxygen sub-lattice.

Electronic conduction increases around 4000 K and 3.5 $g.cm^{-3}$ (French et al., 2010). The closure of

[4]Warm dense matter designates the thermodynamic region in which matter is subject to both thermal and compressional ionization. It is of particular interest for the study of the interior of giant planets

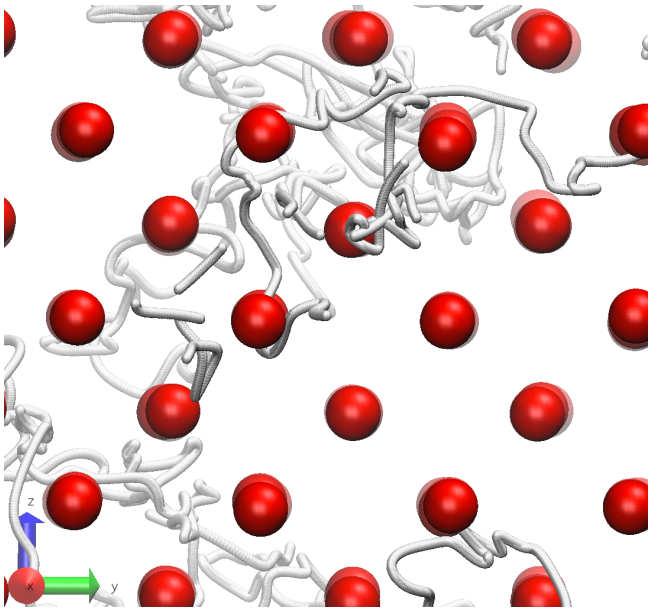

Figure 1.6: 10 ps-long trajectory of a single H atom (white spheres) in the superionic bcc ice at 4000 K and 200 GPa. Red spheres corresponds to oxygen atoms.

the electronic band gap reveals that at this temperature the superionic phase presents a boundary with a plasma state. Nevertheless, the estimation of the total electrical conductivity requires accounting for both the ionic and the electronic conductivities in the entire superionic domain. In the electronically insulating state, the dynamical screening of the H nucleus charge by the surrounding electron cloud prohibits a direct estimation of the electrical conductivity from the proton charge (French et al., 2011). While the proton jumps between two O atoms, the electrons implicated in the breaking bond between the donor O and the proton are "pulled back" to the donor O atom, and the electrons of the acceptor O atom are attracted by the incoming proton. This induces an electrical current in the opposite direction of the H motion (French et al., 2011). By treating explicitly these effects using the polarization and the linear response theories, French et al. (2011) have estimated the electrical conductivity of the superionic ice at 140 ± 15 S.cm^{-1} at 3000 K and 3 g.cm^{-3}.

The viscosity is an essential parameter to determine the internal evolution of a planet. However, it exists a single estimation of the shear viscosity of the superionic water to our knowledge (Redmer et al., 2011). From *ab initio* molecular dynamics, the author propose a shear viscosity of about 1 mPa.s at 4000 K and 3.5 g.cm^{-3}. This is less than the viscosity of the fluid at 3000 K and 2.5 g.cm^{-3}. Therefore, the authors conclude that the superionic water behaves as a fluid when sheared.

The viscosity is intrinsically related to the diffusivity (Stokes-Einstein relation) and to the type and the strength of the chemical bonds between the constituents of the material, including defects and

vacancies. Although the estimated shear viscosity is very low in the superionic water at 4000 K, it may change drastically in the low temperature domain at the transition with the non-diffusive ices. Therefore, a careful inspection of the bonding regime would give precious insights.

Bonding regimes The low temperature limit of the superionic domain as well as its relations with the ice VII, VII′ and X are poorly constrained. Ice X had often been considered as the low temperature precursor of the superionic phase (Cavazzoni et al., 1999; Wilson et al., 2013). This affirmation has been refuted by the measurements of high hydrogen diffusivity in the high-temperature ice VII (Katoh et al., 2002; Sugimura et al., 2012; Noguchi and Okuchi, 2016), and by theoretical and experimental observations of changes in the bonding regimes in superionic water below 2000 K (Goldman et al., 2005; Goncharov et al., 2005; Goncharov and Crowhurst, 2007) with a transition from a VII-like to a X-like proton structure occuring around 3 g.cm^{-3} at 2000 K. French et al. (2009) also report such transition between 4 and 5 g.cm^{-3} between 4000 K and 6000 K.

Stability of other oxygen sub-lattices Superionic conduction is predicted to occur in several oxygen sub-lattices. A transition from a bcc to a face-centered cubic arrangement should occur either around 100–200 GPa (French et al., 2016) or 300 GPa (Wilson et al., 2013) based on different estimations of the Gibbs free energy of these phases. Higher pressure phases are also predicted to be superionic but their effective stability relies on DFT calculations at 0 K (McMahon, 2011; Hermann et al., 2013; Sun et al., 2015). In some ultra-high-pressure ices the low diffusion barrier would be entirely overcome by the zero-point motion of the protons (Hermann et al., 2013).

1.2 Salty ices

From a chemistry point of view water is never pure in planetary environments. Planetary formation processes involve the interaction of water, rock and other volatiles over a broad range of thermodynamic conditions. In the following we present the occurences of water-rock interaction products discovered in the Solar System, and the effects of inclusion of salts in water ice under pressure.

1.2.1 Silicate hydration and relevance in planetary sciences

The complex chemistry associated to the hydrothermal environment might allow the formation of life on the Earth (Daniel et al., 2006). The hydration of the oceanic crust and of the underlying mantle

by the circulation of the hot water forms hydrated minerals (serpentine, brucite, clays) and enriches water in transition metal ions, salts and dissolved gases. The concentration of all these species leads to complexion reactions, clathrate formation, and surface adsorption processes all mediated by liquid water. Reciprocally, the incorporation of solute deeply affects the structure of water and its transport properties. For example, carbonated species tend to strengthen the hydrogen bond network due to the formation of highly organised solvation shells (Martinez et al., 2004; Bruneval et al., 2007) whereas halide salts tend to weaken it (Sun, 2012).

The presence of salt inclusions in ordinary chondrite breccias (Zolensky et al., 2000) and the aqueous leaching experiments of carbonaceous chondrites (Izawa et al., 2010) suggest that hydration reactions occured in the early Solar system. The heat produced from radioactive decay, impacts and self-compaction of planetary embryos might have maintained favorable conditions for the silicate core hydration to persist over geological time scales. During the last decade, unmanned missions have revealed the omnipresence of hydration products on planetary surfaces. Magnesium and sodium sulfates have been detected on the surfces of Ganymede and Europa by the spacecraft Galileo (McCord et al., 1998, 2001). Cassini spacecraft detected sodium chloride in the material ejected by Enceladus' geysers (Postberg et al., 2011). Mars reconnaissance Orbiter imaged periodical brine flows on Mars (Chevrier and Rivera-Valentin, 2012). Dawn mission discovered that Ceres high-albedo features are composed of sodium carbonate mixed with smaller amounts of magnesium-, ammonia- and chlorine-based phyllosilicates (De Sanctis et al., 2016). However, these planetary bodies differ by their thermal history, their differentiation degree and by the thermodynamic conditions spanned by their interior. Enceladus and Europa likely present an interface between a liquid water layer and a silicate-based core (Sohl et al., 2002; Iess et al., 2014). In these cases, Earth-like hydrothermal reactions would take place and liberate solutes in the pressurized liquid ocean that underlies the ice Ih shell. The depressurization of the ocean (from a tectonic event or an impact) would lead to the dispersion of the solutes at the surface of the body. Conversely, in larger icy satellites (Titan, Ganymede) and H_2O-rich super-Earths, the formation of high-pressure ice layers prevents a direct contact between the liquid water and the rocky material. However, hydration products may have formed during the accretion, and their transport depends on their solubility in the high-pressure ice and on the density of the mixture. Moreover, due to the extreme thermodynamic conditions, solid-state metamorphic reactions between the ice and the silicates should be considered too. Both scenarios require the knowledge of the behavior of the aqueous solution under the relevant thermodynamic conditions. Although many difference species are

involved, it is worth understanding a few major binary systems first: $NaCl - H_2O$, $MgSO_4 - H_2O$, $Na_2SO_4 - H_2O$, $H_2SO_4 - H_2O$, etc.

Chemical models of chondrite alteration in aqueous solution (Zolotov, 2012) and carbonaceous chondrite leaching (Fanale et al., 2001; Izawa et al., 2010) tend to show that the reaction enriches the fluid in sodium chloride. Hereafter, we focus on the behavior of electrolyte solutions with a presentation of their effects on the high-pressure phase diagram and properties of water.

1.2.2 Halide salt aqueous solutions and analogs at high-pressure

At ambient pressure, salty solutions produce eutectic phase diagrams with the formation of various hydrates with their own crystalline structures. During the crystallization, the solute ions are expelled through the hexagonal tunnels that characterize the ice Ih structure, prohibiting the formation of a solid-solution. Then, the solute crystallizes into hydrohalite $NaCl \cdot 2H_2O$. In high-pressure ices, the incorporation of electrolytes should be possible due to the more compact arrangement of H_2O units. The presence of NaCl in the high-pressure fluid considerably decreases the melting temperature of ices VI and VII, and induces a density inversion between the liquid and ice VI (Journaux et al., 2013). In particular, ice VII has been found to include substantial amounts of NaCl by direct crystallization of a $NaCl - H_2O$ solution when increasing the pressure (up to 2.48 mol% NaCl according to Frank et al. (2006)). By proceeding to a preliminary low temperature amorphization of the salty solution, Klotz et al. (2009) succeed in including large amounts of LiCl in the deuterated ice VII structure (up to $LiCl \cdot 7H_2O$). However, recent results show that the application of this procedure to $NaCl - H_2O$ induces a phase separation for concentrations higher than $NaCl \cdot 52H_2O$ (Ludl et al., 2017). Klotz et al. (2009, 2016) shows that the local environement of the ions in the high-density glassy state resembles to the one in the ice structure. Neutron diffraction and atomistic modeling of LiCl, LiBr and $MgCl_2$ solutions have revealed that Li^+ and Mg^{2+} occupy the octahedral voids (fcc sites) of the bcc sublattice while Cl^- and Br^- substitute a water molecule on the bcc sites. In the case of NaCl solutions, Bove et al. (2015) and Ludl et al. (2017) proposed that both Na^+ and Cl^- ions substitute a water molecule on a bcc site whereas Frank et al. (2006, 2013) supported the inclusion of both Na^+ and Cl^- in octahedral sites.

The inclusion of salts in the bcc structure breaks the hydrogen bond network, and thus affects the phase diagram as all the phases are determined by the behavior of the protons. In presence of LiCl, the transition to ice X occurs at higher pressure than in pure water (Bove et al., 2015). The pressure

difference reaches 50 GPa for $LiCl \cdot 7H_2O$. The author precise symmetrization does not occur in the vicinity of the impurities.

We do not know the effect of salt inclusions on the high-pressure melting curve, on the development of the superionicity and on the symmetrization of the hydrogen bonds. The stability of NaCl in superionic ice needs to be investigated at high-temperature, as it may be more favorable and more relevant for the planetary interiors. Finally, although the change in the bulk modulus has been evaluated by the measurement of the equation of state (Frank et al., 2006), the complete effect of NaCl on the elastic constant tensor of the bcc ice remains to be investigated.

1.3 Outline of the thesis

In Chapter 2, we present the theoretical framework used in our atomistic simulations. We briefly describe the resolution of the many-body system through the density functional theory, and the sampling of the phase space with the molecular dynamics simulations. We detail the calculations of the structural and transport properties accessible from the *ab initio* molecular dynamics simulations. Next, we focus on the calculations of the vibrational entropy and the quantum corrected thermodynamic properties with the two-phase thermodynamic memory-function model. Then, we present the calculations of the elastic constants in the framework of the linear elasticity. Last, we describe the configurational space sampling and the calculation of the Gibbs free energy when considering disordered solid solutions.

In Chapter 3, we focus on the properties of pure water in the low temperature domain of the superionic regime. These conditions correspond to important changes in the bonding dynamics and have not been sampled with a fine enough pressure–temperature grid. The investigation of a clear relation between the development of the superionicity and the high-pressure dissociation is the first objective. We also examine the existence of the plastic phase.

In Chapter 4, we investigate the binary $NaCl - H_2O$ system along the 1600 K isotherm. We determine the structural and dynamical properties of the NaCl-bearing water ice and evaluate its relative stability from free energy calculations at the relevant thermodynamic conditions.

In Chapter 5, we look at the plasticity of ice X by computing the stability and the properties of the relevant screw dislocation cores.

Chapter 2

Atomistic modeling of matter at planetary interior conditions

Contents

In this chapter we describe the underlying theory used in the simulations employed to model water ice at extreme conditions, and some advanced diagnostics that we used and developped during this thesis.

2.1 Introduction

Experimentally, the exploration of the phase diagram of a material is performed by monitoring macroscopic variables such as the temperature T, the pressure p, the volume V, the total energy E or

the number of moles of each constituent. When these variables are fixed, the system ultimately reaches an equilibrium. This defines a macrostate. An experimental diagnostic then reveals its properties. However, the extreme thermodynamic conditions, the cost of the experiment or the necessity to get theoretical insights may require modeling the system at the microscopic scale. The bulk material reduces to a blend of interacting particles, whose number N, positions $\{\mathbf{R}_I\}$ and momenta $\{\mathbf{P}_I\}$ at a given time t defines a microstate. The physical quantities of the macroscopic and microscopic systems differ of several orders of magnitude. Thus, the macroscopic equilibrium state associated to given macroscopic constrains, corresponds to a certain collection of microstates associated to a given statistical ensemble. In a statistical ensemble, the occurence of a microstate is defined by a probability distribution p_{dis}. Several statistical ensembles are used classically: the microcanonical NVE ensemble (N, V and E fixed); the canonical NVT ensemble (N, V and T fixed); the isokinetic ensemble NVE_K (N, V and kinetic energy E_K fixed); the grand canonical μVT ensemble (chemical potential μ, V and T fixed); the isothermal-isobaric NpT ensemble (N, p and T fixed); and the isobaric-isoenthalpic NpH ensemble (N, p and H fixed).

In a canonical ensemble, the probability distribution p_{dis} of all the microstates $\{\mathbf{R}_I, \mathbf{P}_I\}$ corresponding to a given macrostate follows the Boltzmann distribution (Allen and Tildesley, 1989; Kittel and Kroemer, 1998):

$$p_{dis}\left(\{\mathbf{R}_I, \mathbf{P}_I\}\right) = \frac{1}{Z} \exp\left(-\mathcal{H}\left(\{\mathbf{R}_I, \mathbf{P}_I\}\right)/k_B T\right) \tag{2.1}$$

where Z denotes the canonical partition function and $\mathcal{H}\left(\{\mathbf{R}_I, \mathbf{P}_I\}\right)$ is the Hamiltonian of the system. Z is the normalization constant of the probability distribution and is obtained by summing the probability distribution over all the states accessible to the system. Therefore a good description of the macrostates implies an effective sampling of all the microstates contributing to the probability distribution associated with the macrostate (phase space). The estimation of an observable $\langle \mathcal{O} \rangle$ of the macrostate is obtained by the ensemble averaging of its microscopic counterpart ($\mathcal{O}$) (see equation (2.2)).

$$\langle \mathcal{O} \rangle = \int_{\{\mathbf{R}_I, \mathbf{P}_I\}} p_{dis}\left(\{\mathbf{R}_I, \mathbf{P}_I\}\right) \mathcal{O}\left\{\mathbf{R}_I, \mathbf{P}_I\right\} \mathrm{d}\mathbf{R}_I \mathrm{d}\mathbf{P}_I \tag{2.2}$$

where $\int_{\{\mathbf{R}_I, \mathbf{P}_I\}}$ is the sum over all the configurations of the phase space written for a continuous spectrum of states. In the case that the spectrum of states is discrete the integral is replaced by a sum

(Allen and Tildesley, 1989).

Additionally, the ergodicity principle stipulates that the microscopic system adopt all the configurations belonging to the phase space if it remains long enough in the equilibrium imposed by the macroscopic constraints. This allows to convert the ensemble average in a time average:

$$\langle \mathcal{O} \rangle = \frac{1}{\tau} \lim_{\tau \to +\infty} \int_0^\tau \mathcal{O}(t) \mathrm{d}t \tag{2.3}$$

In this thesis, we estimate the average properties of H_2O, NaCl and individual configurations of NaCl·RH$_2$O by sampling the phase space using the Born-Oppheimer molecular dynamics. Moreover, we evaluate the average Gibbs free energy of the NaCl $\cdot$ 126H$_2$O by performing a Boltzman averaging over the reduced configurational space.

2.2 Born-Oppheimer molecular dynamics

In the previous section, we show that the calculation of macroscopic quantities can be performed by averaging the observables of a dynamical microscopic system over a time period long enough for the average to converge. Now, we focus on the resolution of the dynamical problem.

2.2.1 The Born-Oppenheimer approximation

The microscopic description of a system requires the description of the interaction between its fundamental units or particles. The choice of these units depends on the *a priori* knowledge of their interactions. In classical molecular dynamics, the atoms are represented by empirically fitted interaction potentials. Here, we know from experimental studies that H_2O dissociates in the targeted range of thermodynamic conditions. Therefore, we expect a complex bonding behavior between the different atoms, highly dependent on thermodynamic conditions. Additionally, we do not know how the addition of electrolytes will affect the system. Consequently, we need to describe the system at the fundamental level of the interactions between the electrons and the nuclei. This problem is extremely complex: because of their small mass the electrons are subject to quantum effects, impliying the resolution of the time-dependent Schrödinger equation for a large number of particles which is impractical. Heavier, the nuclei generally behave as classical particles. In 1927, Born and Oppenheimer (Born and Oppenheimer, 1927) propose that the large mass difference between the nuclei and the electrons lead to a decoupling of their dynamics. At the time-scale of the nuclei motion, the electronic cloud

instantaneously adopts the electronic ground-state corresponding to the nuclei positions. Considering the Born-Oppenheimer adiabatic assumption (Born and Oppenheimer, 1927), the electronic problem becomes time-independent and the dynamics of the nuclei is decoupled from the one of the electrons. The total hamiltonian of the system can be split into a electronic hamiltonian $\mathcal{H}_e$ that depends on the ensemble of the nuclei positions $\{\mathbf{R}_I\}$ at a given time, and into a nuclear part $\mathcal{H}_n$ that accounts for the electronic screening. The two parts of the total hamiltonian are separated in a kinetic and a potential energy terms. Their respective expressions for an isolated system are detailed in equations (2.4) and (2.5) (Parr and Yang, 1994; Car, 2006).

$$\mathcal{H}_e = \underbrace{\sum_{i=1}^{N_e} \frac{\mathbf{p}_i^2}{2m_e}}_{\text{kinetic energy } e^-} + \underbrace{\frac{1}{4\pi\varepsilon_0} \sum_{i=1}^{N_e} \sum_{I=1}^{N_n} \frac{-Z_I e^2}{|\mathbf{R}_I - \mathbf{r}_i|}}_{\text{Coulomb interactions } e^-/\text{nuclei}} + \underbrace{\frac{1}{4\pi\varepsilon_0} \frac{1}{2} \sum_{i \neq j} \frac{e^2}{|\mathbf{r}_i - \mathbf{r}_j|}}_{\text{Coulomb interactions } e^-/e^-} \tag{2.4}$$

$$\mathcal{H}_n = \underbrace{\sum_{I=1}^{N_n} \frac{\mathbf{P}_I^2}{2M_I}}_{\text{kinetic energy nuclei}} + \underbrace{\frac{1}{4\pi\varepsilon_0} \frac{1}{2} \sum_{I \neq J} \frac{Z_I Z_J e^2}{|\mathbf{R}_I - \mathbf{R}_J|}}_{\text{Coulomb interactions nuclei/nuclei}} + \underbrace{E_{e,0}\left(\{\mathbf{R}_I\}\right)}_{\text{electronic ground state energy surface}} \tag{2.5}$$

where N_e (N_n), $\mathbf{p}_i$ ($\mathbf{P}_I$), $\mathbf{r}_i$ ($\mathbf{R}_I$), m_e (M_I) respectively refer to the number, the momentum, the position and the mass of the electron i (nucleus I). e is the elementary charge, Z_I is the number of protons of the nucleus I and ε_0 is the void permitivity. Now, the two problems can be treated separately at each time step; the positions of the nuclei constitute an external parameter for the electronic problem, and the electronic ground state potential energy surface adds to the total potential energy surface of the nuclei before the integration of the equations of motions. Nevertheless, the determination of the ground state energy of the electrons $E_{e,0}\left(\{\mathbf{R}_I\}\right)$ is a many-body problem impossible to solve directly. The main complexity arises from the electron-electron interactions and the electron quantum properties due to their fermionic nature (exchange). Several formulations allow for tackling the problem using different approximations (Hartree-Fock methods for example). Hereafter, the resolution of the electronic problem is performed in the framework of the density functional theory (DFT).

2.2.2 Solving the electronic structure through the density functional theory

The idea behind the DFT is the modeling of an electronic system affected by an external potential with a fictious system of independent electrons described by its electronic density. It allows to reduce

the problem to a set of N_e independent equations and to deal with a known kinetic energy (Parr and Yang, 1994).

2.2.2.1 Hohenberg and Kohn theorem

In 1964, Hohenberg and Kohn (Hohenberg and Kohn, 1964) demonstrate that the external potential V acting on the electronic sub-system (i.e. interactions e^-/nuclei in equation (2.4)) is a unique functional of the electronic density $n(\mathbf{r})$. This implies that the total energy of the electronic sub-system is also a functional of the electronic density. Moreover, they state that a unique functional for the total electronic energy E_e can be expressed in terms of the electronic density (see equation (2.6)). If the electronic density verify the normalization condition $\int n(\mathbf{r})\mathrm{d}\mathbf{r} = N_e$, the minimization of this functional gives the ground state energy of the electronic sub-system.

$$E_e[n(\mathbf{r})] = \underbrace{\int V_e(\mathbf{r})n(\mathbf{r})\mathrm{d}\mathbf{r}}_{\text{external contribution}} + \underbrace{F_e[n(\mathbf{r})]}_{\substack{\text{electronic kinetic and} \\ \text{potential contributions}}} \tag{2.6}$$

However, the dependence of the electronic kinetic energy, correlations, and exchange in terms of the electronic density is still unknown.

2.2.2.2 Kohn and Sham formulation

In 1965, Kohn and Sham (Kohn and Sham, 1965) propose to split $F_e[n(\mathbf{r})]$ into three different terms:

$$F_e[n(\mathbf{r})] = \underbrace{\frac{1}{4\pi\varepsilon_0}\frac{1}{2}\iint \frac{n(\mathbf{r})n(\mathbf{r}')e^2}{|\mathbf{r}-\mathbf{r}'|}\mathrm{d}\mathbf{r}\mathrm{d}\mathbf{r}'}_{\text{Average Coulomb energy of the e}^-} + \underbrace{\mathcal{T}_0[n(\mathbf{r})]}_{\substack{\text{Kinetic energy of} \\ \text{a system of non-interacting } e^- \\ \text{of same density}}} + E_{xc}[n(\mathbf{r})] \tag{2.7}$$

The functional E_{xc} is the so-called *exchange-correlation functional* but it also includes the difference between the kinetic energy of the system of interacting electrons and the kinetic energy of the system of non-interacting electrons at the same density. The injection of equation (2.7) in equation (2.6) and the application of a variation principle leads to the introduction of N_e independent orbitals (the Kohn-Sham orbitals) that satifies the electronic density in each point. The following set of equations is known as the Kohn-Sham equations:

$$\begin{cases} \left(\dfrac{-\hbar}{2m_e}\nabla^2 + V_{\text{eff}}(\mathbf{r})\right)\phi_i(\mathbf{r}) = \varepsilon_i\phi_i(\mathbf{r}) & (2.8) \\ V_{\text{eff}}(\mathbf{r}) = V_e(\mathbf{r}) + \dfrac{1}{4\pi\varepsilon_0}\dfrac{e^2}{2}\displaystyle\int \frac{n(\mathbf{r}')}{|\mathbf{r}-\mathbf{r}'|}\mathrm{d}\mathbf{r}' + V_{xc}(\mathbf{r}) & (2.9) \\ n(\mathbf{r}) = \displaystyle\sum_i^{N_e} |\phi_i(\mathbf{r})|^2 & (2.10) \end{cases}$$

where $V_{xc}(\mathbf{r}) = \dfrac{\delta E_{xc}[n(\mathbf{r})]}{\delta n(\mathbf{r})}$ is the exchange-correlation potential. ϕ_i and ε_i respectively denote a given Kohn-Sham orbital and its energy. The Kohn-Sham equations are solved self-consistently. First, the orbitals are computed from a guess electronic density that fixes the effective potential V_{eff}. The new density is calculated, and then the new orbitals. The procedure continues up to the convergence of the electronic density. The ground state energy of the complete electronic system is obtained by the intermediary of $\mathcal{T}_0$ that relates equation (2.6) with the Kohn-Sham equations. Indeed, the kinetic energy of the system of N_e independent electrons is the sum of the kinetic energies of the independent electrons. Consequently, the ground-state energy is expressed as:

$$E_{e,0} = \sum_{i=1}^{N_e}\varepsilon_i - \frac{1}{4\pi\varepsilon_0}\frac{e^2}{2}\int \frac{n(\mathbf{r}')}{|\mathbf{r}-\mathbf{r}'|}\mathrm{d}\mathbf{r}' \tag{2.11}$$

However, the problem of the choice of the exchange-correlation term subsists. We present the generalized grandient approximation functional that we use in this thesis.

2.2.2.3 Exchange-correlation functionals

The exchange-correlation energy arises from two phenomena: i) first, the fermionic nature of the electrons requires that two electrons of the same spin must occupy distinct orthogonal orbitals, this reduces the electronic density as it removes the repulsion energy and forms an exchange hole; ii) two electrons with different spins are allowed to occupy the same orbital but repulse together because of their negative charge, this also reduces the electronic density and forms a correlation hole. Combined together, these two interactions forms the exchange-correlation holes in the electronic density. The full consideration of this effect requires to account for the Coulombian interactions between the electron with the exchange-correlation holes.

The simplest approximation consists in considering the exchange-correlation as locally dependent of the electronic density. This is reasonable as the long-range effects (at least for the gas of independent electrons) are already accounted in the terms of kinetic energy $\mathcal{T}_0$ and of the average electrostatic interactions. The local density approximation (LDA) uses only the local electronic density to evaluate the exchange and correlation contributions to the energy. A part of the exchange-correlation functional $E_{xc}^{LDA}[n(\mathbf{r})]$ contains the exact formulation of the exchange and correlation for a homogeneous electron gas while the other part needs to be parameterized. The exchange-correlation potential v_{xc} is then obtained by derivation of $E_{xc}^{LDA}[n(\mathbf{r})]$ and the Kohn-Sham equations can be solved. It appears that the energies obtained within the LDA approximation are in good agreement with experimental values, especially for systems in which the electronic density varies smoothly.

Nevertheless, for systems presenting short range variations of the electronic density the LDA is not sufficient. A better accuracy is achieved by the generalized-gradient approximation (GGA). In the GGA, the exchange-correlation functional is based both on the local electronic density and on its gradient. Because of the short range variations of the electronic density in molecules, we mainly use this functional with the (non-emprical) Perdew-Burke-Ernzerhof (PBE) parameterization (Perdew et al., 1996).

It is worth mentionnning that numerous exchange and correlation functionals have been developed to increase the accuracy of the calculation of the XC energy in specific cases. These functionals are mixes of LDA, GGA and Hartree-Fock formalism, and account better for non-local correlations. More recent developments have included London-dispersion forces (i.e. van der Waals interactions). These functionals are generally a mixture of a PBE-style GGA exchange, a LDA correlation and a non-local correlation functionals (Dion et al., 2004; Klimeš et al., 2011). In particular, we validate some of our GGA-based calculations with the optB86-vdW exchange-correlation functional (Klimeš et al., 2011).

2.2.2.4 Finite-temperature DFT

When the thermal energy of the system is comparable to the electronic energies, it can lead to the thermal excitation of the electrons. The inclusion of the temperature effect in the DFT has been done by Mermin (1965). The excited electronic states are described in the grand canonical ensemble and distributed according to a Thomas-Fermi distribution. Mermin (1965) have shown that the gran potential (the relevant potential for the grand canonical ensemble) is a functional of the electronic density. The new functional now contains a free energy of exchange-correlation as well as a term of

electronic entropy. It changes the Kohn-Sham equations such that the occupancy of the Kohn-Sham orbitals, i, is related to their energy and the electronic temperature through the Fermi occupation numbers f^i_{occ}. The total electronic entropy of the system S_{el} is expressed as a function of the Fermi occupation numbers (equation (2.12)).

$$S_{el} = -k_B \sum_i f^i_{\text{occ}} \ln f^i_{\text{occ}} + \left(1 - f^i_{\text{occ}}\right) \ln \left(1 - f^i_{\text{occ}}\right) \tag{2.12}$$

In this thesis we use the finite temperature DFT. This choice is motivated by the high-temperatures of interest and the lack of a priori knowledge of the electronic behavior of some of the systems investigated.

2.2.2.5 Basis set of wavefunctions

Although the DFT simplifies considerably the many-body problem, the Kohn-Sham equations cannot be solved for the number of particles characteristic of a macroscopic system. To limit the number of particles, the resolution is performed at the microscopic scale in a periodic supercell.

According to the Bloch theorem (Bloch, 1928), in a periodic system the electronic wavefunction differs from a plane wave only by a proper periodic modulation of wave-vector $\mathbf{k}$. This implies that the wavefunction may be expressed as the product of two plane-waves: a first one $u^{\mathbf{k}}_i(\mathbf{r})$ that has the same periodicity as the primitive volume, and a second one $\exp(i\mathbf{k}\cdot\mathbf{r})$ with its own period corresponding to a $\mathbf{k}$-point of the reciprocal space associated to the primitive cell. The wavefunction associated to the modulation of wave-vector $\mathbf{k}$ is:

$$\psi^{\mathbf{k}}_i(\mathbf{r}) = u^{\mathbf{k}}_i(\mathbf{r}) \exp(i\mathbf{k}\cdot\mathbf{r}) \tag{2.13}$$

The expansion of $u^{\mathbf{k}}_i(\mathbf{r})$ in a Fourier series leads to the following expression for $\psi^{\mathbf{k}}_i(\mathbf{r})$:

$$\psi^{\mathbf{k}}_i(\mathbf{r}) = \sum_{\mathbf{G}} c^{\mathbf{k}}_{i,\mathbf{G}} \exp(i\mathbf{G}\cdot\mathbf{r}) \exp(i\mathbf{k}\cdot\mathbf{r}) = \sum_{\mathbf{G}} c^{\mathbf{k}}_{i,\mathbf{G}} \exp(i(\mathbf{G}+\mathbf{k})\cdot\mathbf{r}) \tag{2.14}$$

where $\mathbf{G}$ are vectors of the reciprocal lattice associated to the primitive cell that impose the plane-wave to respect the primitive cell periodicity. $c^{\mathbf{k}}_{i,\mathbf{G}}$ are the Fourier coefficients of the plane-waves of wave-vectors $\mathbf{G}$. Moreover, the choice of the $\mathbf{k}$-points can be limited to the first Brillouin zone. This leads to:

$$\psi^{\mathbf{k}}_i(\mathbf{r}) = \sum_{\mathbf{G}} c_{i,\mathbf{k}+\mathbf{G}} \exp(i(\mathbf{G}+\mathbf{k})\cdot\mathbf{r}) \tag{2.15}$$

The expansion of the orbitals in a plane-wave basis leads to the reexpression of the Kohn-Sham equations in the reciprocal space. In the reciprocal space, their resolution corresponds to the diagonalisation of a hamiltonian matrix whose size in not infinite and depends on the truncation at the cutoff kinetic energy of the plane-wave basis set. The diagonalization is performed iteratively with respect to the plane wave coefficients. The truncation occurs at a value $\mathbf{G_{cut}}$ indirectly choosen in term of cutoff kinetic energy minored by the highest kinetic energy accessible to the electron, the one of the free electron: $E_{cut} \geq \frac{\hbar}{2m_e}|\mathbf{k}+\mathbf{G}|^2$.

Ideally, the electronic eigenstates should be evaluated for all $\mathbf{k}$-points of the first Brillouin zone. However, a single point sampling at the high-symmetry Γ-point was found to be sufficient and practical due to our large supercells.

Moreover, for disordered systems (e.g. liquids), the periodicity do not exist in the macroscopic system. Therefore, the supercell must be large enough to converge the properties of the macroscopic system, and several configurations have to be averaged.

2.2.2.6 Projected augmented-wave representation of the pseudo-nuclei

Close to the nuclei, the external Coulomb potential becomes infinitely deep, resulting in a strong increase of the oscillation frequency of the electronic wavefunctions. Consequently, a large number of plane-waves with very high-frequency is required. Numerically, this corresponds to a very high value for the plane-wave kinetic energy cutoff, and rapidly the computation becomes too time consuming.
A solution to this problem is to solve the Kohn-Sham equations only for the valence electrons, and to consider together the core electrons and the nucleus as an pseudo-nucleus or ionic center. This is the frozen-core approximation. Inside the pseudo-nuclei, the effective potential that applies to the electrons V_{eff} is changed into a *pseudopotential* $\tilde{V}_{\text{eff}}$ such that the valence electron wavefunctions are considerably smoother. Outside the pseudo-nuclei, $\tilde{V}_{\text{eff}}$ mimics exactly V_{eff}. This allows to keep a reasonable value for the cutoff kinetic energy of the plane-wave basis set.

Different formalisms have been developed to reproduce such features (norm-conserving pseudopotentials, ultrasoft pseudopotential). We used the projector-augmented wave method (PAW, Blöchl (1994); Kresse and Furthmüller (1996a)). In this formalism, a linear transformation is defined to relate the all-electron wavefunction solutions of the Kohn-Sham equations to smoother pseudowavefunctions. This goes through a decomposition of the all-electron wavefunctions into a linear combination of an on-site (i.e. inside the pseudo-nuclei) contribution and the soft part outside the pseudo-nuclei. The

resolution of the Kohn-Sham equations for the pseudized system gives the smooth pseudowavefunctions expanded in a plane-wave basis set. The on-site contribution of the pseudowavefunction is then removed and replaced by the local on-site all-electron contribution (see Figure 2.1).

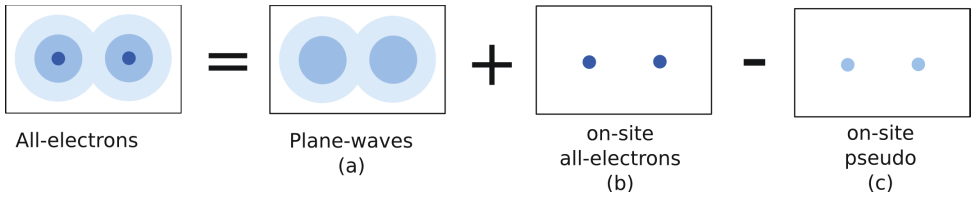

Figure 2.1: Schematic representation of the PAW linear transformation.

The on-site all-electron wavefunction is calculated for a given radius of the pseudo-nuclei, or in other word for a given number of core electrons. Thus, if the density or the temperature conditions are not expected to affect the core electrons, and if the distance between the pseudo-nuclei is large enough to avoid that they overlap, then the PAW potentials are valid for a given atom species whatever its environment. The defined transformation allows to calculate the local observables (electronic density, kinetic, average coulombian interaction energy = Hartree energy, exchange-correlation). The calculated pseudopotential transfer very well from a system to another. The ground state energy of the electronic configuration $E_{e,0}\left(\{\mathbf{R}_I\}\right)$ is then calculated from the transformed electronic density and included in the potential acting on the nuclei.

2.2.3 Dynamics of the nuclei

2.2.3.1 Equations of motion of the nuclei

The DFT gives us the electronic ground state energy, $E_{e,0}\left(\{\mathbf{R}_I\}\right)$ in equation (2.5). From the expression of the hamiltonian $\mathcal{H}_n$ we write the equations of motions for the nuclei I (or more exactly the pseuso-nuclei I) that account for the electronic screening in an isolated system in which the total energy is conserved (NVE ensemble):

$$\begin{cases} \dfrac{\mathrm{d}\mathbf{R}_I}{\mathrm{d}t} = \dfrac{\mathbf{P}_I}{M_I} & (2.16) \\ \dfrac{\mathrm{d}\mathbf{P}_I}{\mathrm{d}t} = -\nabla_{\mathbf{R}_I}\mathcal{H}_n\left(\{\mathbf{R}_I,\mathbf{P}_I\}\right) = -\dfrac{1}{4\pi\varepsilon_0}\displaystyle\sum_{I\neq J}\frac{Z_I Z_J e^2}{|\mathbf{R}_I-\mathbf{R}_J|^2} - \nabla_{\mathbf{R}_I}\left(E_{e,0}\left(\{\mathbf{R}_I\}\right)\right) & (2.17) \end{cases}$$

where $\nabla_{\mathbf{R}_I}$ refers to the gradient with respect to the positions $\mathbf{R}_I$, and $\nabla_{\mathbf{R}_I}\left(\dfrac{\mathbf{P}_I^2}{2M_I}\right) = 0$.
$-\nabla_{\mathbf{R}_I}\mathcal{H}_n\left(\{\mathbf{R}_I,\mathbf{P}_I\}\right)$ represents the forces that apply to the pseudo-nuclei I. For N pseudo-nuclei, this

system is $2 \times 3N = 6N$-dimensional and impossible to solve analytically. The forces associated to the electronic ground-state potential are calculated from the Hellmann-Feyman theorem (Feynman, 1939) and are exact subject to the completeness of the plane-wave basis set.

The equation of motions are numerically integrated after their discretization and their expansion in Taylor series. Different algorithms have been developed to perform the numerical integration. We used the Verlet algorithm (Verlet, 1967) that calculates the forward position $\mathbf{R}_I(t+\Delta t)$ from a Taylor expansion of forward and backward position up the third order.

2.2.3.2 Extensions to the canonical ensemble

Some modifications of the equations of motion are required to obtain pseudo-nucleus trajectories that sample the phase spaces associated with other statistical ensembles. To impose the temperature of the system at a given volume, we adopt two different approaches. First, we fix the total kinetic energy to a value corresponding to the desired temperature T_0. At each time step of the molecular dynamics, the instantaneous temperature $T(t)$ is given by:

$$T(t) = \frac{1}{N_f k_B} \sum_{I=1}^{N_n} \frac{\mathbf{P}_I^2}{M_I} \tag{2.18}$$

where N_f is the number of degrees of freedom. Then, the velocities of the atoms $\mathbf{v}(t)$ are rescaled as follows:

$$\mathbf{v}_{\text{rescaled}}(t) = \mathbf{v}(t)\sqrt{\frac{T_0}{T(t)}} \tag{2.19}$$

In the thermodynamic limit, the isokinetic ensemble reaches the canonical ensemble.

The Nose-Hoover thermostat (Nose, 1984; Hoover, 1985) includes the effect of the temperature by extending the sub-system of pseudo-nuclei to a fictional heat bath of mass Q and temperature T_0. The evolution of the temperature is controled by the action of a friction coefficient P_s that acts on the momemtum of the pseudo-nuclei. The dynamics of the extended system is decribed by the following equations of motion:

$$\begin{cases} \dfrac{\mathrm{d}\mathbf{R}_I}{\mathrm{d}t} = \dfrac{\mathbf{P}_I}{M_I} & (2.20) \\ \dfrac{\mathrm{d}\mathbf{P}_I}{\mathrm{d}t} = -\dfrac{1}{4\pi\varepsilon_0}\dfrac{1}{2}\displaystyle\sum_{I\neq J}\frac{Z_I Z_J e^2}{|\mathbf{R}_I-\mathbf{R}_J|^2} - \nabla_{\mathbf{R}_I}\left(E_{e,0}\left(\{\mathbf{R}_I\}\right)\right) - P_s\mathbf{P}_I & (2.21) \\ \dfrac{\mathrm{d}P_s}{\mathrm{d}t} = \dfrac{1}{Q}\left(\displaystyle\sum_{I=1}^{N_n}\frac{\mathbf{P}_I^2}{2M_I} - \frac{N_f+1}{2}k_B T_0\right) & (2.22) \end{cases}$$

The mass of the fictious heat bath Q controls the dynamics of the friction coefficient, and thus the frequency of the temperature oscillations around the desired value T_0.

The majority of our simulations were performed in the isokinetic ensemble with a rescaling of the atom velocities at each time step. Although considered as crude and not applicable to the calculation of the dynamical properties, we find no differences with the results obtained with a Nose-Hoover thermostat. Indeed, after thermalization, the rescaling factor $\sqrt{T_0/T(t)}$ is always extremely close to one indicating that the velocities are poorly affected.

2.2.3.3 Extensions to the isobaric-isothermal ensemble

Experiments are generally performed at fixed pressure and temperature. In order to facilitate the comparison of the experimental and theoretical diagnostics, the equation of motion of the nuclei have been adapted to the sampling of the NpT ensemble. Following the idea of the Nose-Hoover thermostat, Andersen (Andersen, 1980) proposes to impose a constant pressure, i.e. a constant isotropic stress, by introducing the volume as a new dynamical variable. Then, Parrinello and Rahman (Parrinello and Rahman, 1980, 1981) propose to extent the system by introducing the three cell parameters as dynamical variables, leading to a constant stress ensemble in which the shape and the volume of the cell are allowed to change. The dynamics of the cell shape variations is controled by a fictious mass that has to be choosen as in the case of the Nose-Hoover thermostat.

The combination of the Rahman-Parrinello barostat with a thermostat makes possible isobaric-isothermal molecular dynamics. The shape cell adaptation to the stress field also permits to obtain the supercell parameters for the pressure–temperature conditions targeted so as to perform a NVT or NVE sampling. In this thesis, the temperature has been monitored with a Langevin thermostat when using Rahman-Parrinello molecular dynamics.

The Langevin thermostat is a stochastic method (Allen and Tildesley, 1989). It modifies directly the equation of motion by appling a random force $\mathbf{f}_f$ associated with a friction coefficient γ_f to all the N_f degrees of freedom of the system. The norm of $\mathbf{f}_f$ is defined by a Gaussian white noise of standard deviation $\sigma_f = \sqrt{2m_f\gamma_f k_B T/\Delta T}$ where m_f is the mass associated to the degree of freedom. Thus, in the case of the Rahman-Parrinello molecular dynamics, we need to choose $3N_n + 3$ friction coefficients respectively for the nuclei and lattice degrees of freedom. In pratice, we fix one friction coefficient per atomic species and another one for the three lattice degrees of freedom.

2.2.3.4 Nuclear quantum effects

At this point, the trajectories of the nuclei can be computed in diverse statistical ensembles assuming the nuclei behave classically. The validity of such assumption needs to be considered in the case of hydrogenated systems. Hydrogen atoms (or protons as the two terms are employed equally in this thesis) are extremely light, and are subject to nuclear quantum effects (NQEs) at low temperature and/or high density. In particular, as mentionned in Chapter 1, quantum tunneling causes the low temperature dissociation of the H_2O molecules in ice VII′. In the terapascal pressure range, the ultra-high-pressure forms of H_2O are expected to be superionic even at 0 K due to the high zero-point energy of the H atoms.

Several theoretical tools are available to account for the NQEs such as path-integral molecular dynamics (Marx and Parrinello, 1996) or the addition of a semiclassical thermostat to the classical system (Bronstein et al., 2014). In this work, we choose to model the dynamics of the H nuclei considering them as classical particles. However, we account for their quantum nature when calculating the energetics of the system. The application of these quantum corrections is developed in the section 2.5 of this Chapter. We expect the NQEs to not affect significantly the dynamics of the protons at the temperatures and pressures of interest here. From a 1D model, Morrone et al. 2009 (Morrone et al., 2009) show that the momemtum distribution of the H in ice VII′ tends to the classical limit above 300 K.

2.2.4 The code VASP and general parameterization of the simulations

We perform the DFT and Born-Oppenheimer molecular dynamics simulations with the Vienna Ab initio Simulation Package (VASP v4.6 and v5.2, Kresse and Furthmüller (1996a,b)). To model

the atoms, we use the PAW potentials (Blöchl, 1994; Kresse and Joubert, 1999) with the following electronic configurations: O:[He] $2s^2 2p^4$, H:$1s^2$, Na:[Ne] $3s^1$ and Na:[He] $2s^2 2p^6 3s^1$, and Cl:[He] $2s^2 2p^5$. The exchange-correlation term is calculated in the Perdew-Burke-Ernzerhof general gradient approximation (Perdew et al., 1996). For the *ab initio* molecular dynamics simulations we use a kinetic cutoff energy of 550 eV that ensures internal energy converged within 5 meV per atoms, and 1.5 GPa precision in pressure. We calculated electronic wave functions at the Γ-point of the Monkhorst k-point grid (Monkhorst and Pack, 1976).

Appendix A presents a battery of tests realized during the parameterization of the simulations that validates our default setup.

The simulations are carried out on the Occigen machine at the CINES supercomputing facility (Montpellier, France) and on the Curie machine at the CEA TGCC facility (Bruyères-le-Châtel, France) using computational Grant No. eDARIx2015106368. In average, for a system composed of 128 water molecules, a 10 ps-long molecular dynamics run with 128 water molecules lasts ∼30h with 196 cpus on Occigen and ∼50h with 192 cpus on Curie.

2.3 Structural properties

2.3.1 Estimation of the thermodynamic variables

At a given moment t of the molecular dynamics, we calculate the internal energy of the supercell $U_{MD}(t)$ as the sum of the kinetic and potential energies (respectively $E_k(t)$ and $E_p(t)$). We compute the temperature from the kinetic energy (see equation (2.23)), and the pressure p_{MD} from both the stress tensor $\sigma(t)$ and the thermal contribution of an ideal gas (see equation (2.24)). In the case of a NpT simulation, we obtain the volume of the supercell from the determinant of the matrix composed by the lattice vectors.

$$T(t) = \frac{2E_k(t)}{N_f k_B} \tag{2.23}$$

$$p_{MD}(t) = p_{\text{th}}(t) + p_{\text{ext}}(t) = \frac{Nk_BT}{V} + \frac{1}{3}\text{tr}(\sigma(t)) \tag{2.24}$$

where $\text{tr}(\sigma(t))$ denotes the trace of the stress tensor at the time t. p_{th} and p_{ext} refer to the thermal and the external pressures. In the assumption of the ergocity of the system, the macroscopic properties are obtained from the time averages of the corresponding microscopic properties (equation (2.3)). Figure

2.2 gives an example of the typical internal energy and pressure fluctuations in a system in statistical equilibrium.

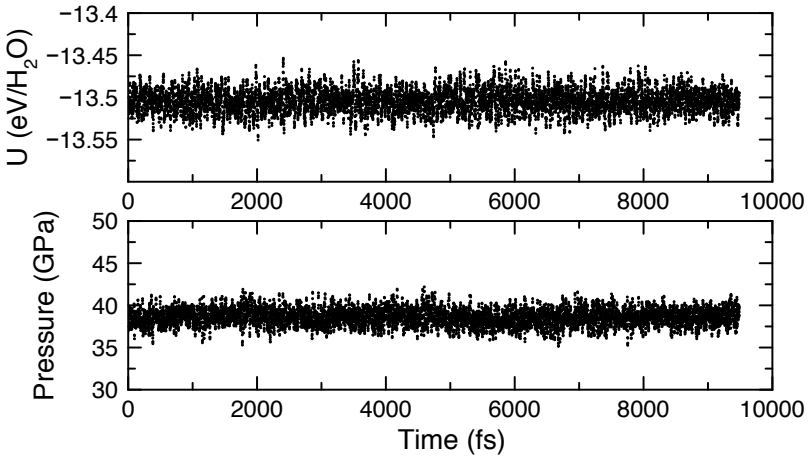

Figure 2.2: Internal energy (U_{MD}) and pressure (p_{MD}) fluctuations in a molecular dynamics in statistic equilibrium.

2.3.2 Radial distribution functions and coordination numbers

The radial distribution function (RDF or $g_{\alpha\beta}(r)$) gives the probability of finding an atom β at a distance r of an atom α relative to the probability of finding β at the same distance (and same density) in a random distribution. It gives insights on the distance between atoms but does not provide directional information. Numerically, it consists in counting the number of atoms of a species β per volume unit in a shell of width δr and inner radius r around an atom of a species α (α and β can be identical). Replicating this procedure around each atom α at each time produce a configurational average if the system is ergodically sampled. We computed the RDF using the following discretized form (Allen and Tildesley, 1989):

$$g_{\alpha,\beta}(r) = \left\langle \frac{V}{N_\beta N_\alpha} \sum_{i=1}^{N_\alpha} \frac{N_{i,\beta}(r)}{\frac{4}{3}\pi\left((r+\delta r)^3 - r^3\right)} \right\rangle \tag{2.25}$$

where $N_{i,\beta}(r)$, V, N_α and N_β respectively refer to the number of atoms β in the shell of inner radius r, the volume of the supercell, the number of atoms α, and the number of atoms β in the supercell. $\langle\ \rangle$ denotes the ensemble average. The term V/N_β corresponds to the average number of atoms β in the supercell, *i.e.* the random distribution normalization term. In pratice, the calculation of the RDF only makes sense in the minimal image convention, *i.e.* up to r equal to half the length of the shortest axis

of the supercell. Beyond this distance the periodicity of the system includes non-realistic additional long-range ordering. In the case of a fluid or an amorphous phase, the RDF may show short-range ordering but it will tend to 1 at large r which means that the distribution particles β around particles α is random.

The integration of the RDF over the distance r to the considered atom species α gives the cummulative number of atoms β as a function of r. This is the coordination function (see equation (2.26)).

$$\mathcal{N}_{\alpha\beta}(r) = \frac{4\pi}{V}\int_0^r r^2 g_{\alpha\beta}(r)\mathrm{d}r \tag{2.26}$$

The coordination numbers associated with coordination shells are obtained from the values of $\mathcal{N}_{\alpha\beta}(r)$ at inflexion points.

2.4 Transport properties

2.4.1 Green-Kubo formalism and autocorrelation functions

In statistical mechanics, the linear response theory stipulates that a small perturbation of a given field induces a linear variation of its conjugated flux. The field and the flux form a linear constitutive equation whose proportionality is given by the associated transport coefficient. Green and Kubo (Green, 1954; Kubo, 1957) show that for a system in thermodynamic equilibrium in which the applied field is null, the transport coefficient is directly related to the time-integral of the autocorrelation of the appropriate flux (equation (2.27)).

$$A = \frac{V}{k_B T}\int_0^{+\infty} \langle \mathbf{F}(t)\cdot\mathbf{F}(0)\rangle \,\mathrm{d}t \tag{2.27}$$

where $\mathbf{F}$ and A are respectively the considered flux and its associated transport coefficient. The time autocorrelation $\langle \mathbf{F}(t)\cdot\mathbf{F}(0)\rangle$ and is given by:

$$\langle \mathbf{F}(t)\cdot\mathbf{F}(0)\rangle = \lim_{\tau\to+\infty}\frac{1}{\tau}\int_0^{+\infty} \mathbf{F}(t-t_0)\cdot\mathbf{F}(t_0)\mathrm{d}t_0 \tag{2.28}$$

If the system is in statistical equilibrium the autocorrelation is invariant under time translation. We use this last property to average the autocorrelation over different time-windows.

2.4.2 Diffusion coefficients

In order to determine if the equilibrium system is solid, fluid (molecular or ionic) or superionic, we calculate the diffusion coefficients D_α of each atomic species α. Although D_α can be obtained by the time integral of the velocity autocorrelation, for numerical reasons we opt for the Einstein formulation that uses the mean square displacements (MSD, equation (2.30)).

$$\mathrm{MSD}_\alpha(\tau) = \frac{1}{N_\alpha}\sum_{i=1}^{N_\alpha}\langle|\mathbf{r}_i^\alpha(\tau+t_0)-\mathbf{r}_i^\alpha(t_0)|^2\rangle_{t_0} \tag{2.29}$$

$$\mathrm{MSD}_\alpha(\tau) = \frac{1}{N_\alpha}\sum_{i=1}^{N_\alpha}\frac{1}{t_{0,max}}\sum_{t_0=0}^{t_{0,max}}|\mathbf{r}_i^\alpha(\tau+t_0)-\mathbf{r}_i^\alpha(t_0)|^2 \tag{2.30}$$

In this expression, $\langle\ \rangle_{t_0}$ denotes an average over the time origins t_0. The maximal value for t_0, $t_{0,max}$ is equal to half the length of the thermalized trajectory. τ does not represent the time but the time window between the positions. Therefore, the maximal value for τ is also half the length of the thermalized trajectory.

In the infinite time limit, the diffusion coefficient is proportional to the slope of the linear regime of the MSD. Equation (2.31) gives the relation in the three-dimensional case.

$$D_\alpha = \lim_{\tau\to+\infty}\frac{\mathrm{MSD}_\alpha(\tau)}{6\tau} \tag{2.31}$$

In pratice, we calculate the successive values of $D_\alpha(\tau) = \frac{1}{6}\frac{\mathrm{dMSD}_\alpha(\tau)}{\mathrm{d}\tau}$ and we acquire statistics about D_α between in the interval $[\tau_{max}/2;\tau_{max}]$. Figure 2.3 illustrates the MSD and D_α statistics in the different states of H_2O. In the fluid state, D_α is positive and we distinguish four cases: i) in the molecular fluid all the atoms diffuse similarly; ii) in the ionic fluid all the atom diffuse but with different D_α; iii) in the solid state, $D_\alpha = 0$ for all species as we model a perfect crystal without vacancy: iv) in a superionic compound, at least one type of atom does not diffuse while another has $D_\alpha > 0$.

2.4.3 Electrical conductivity

In superionic H_2O the ions are dynamically screened by the electrons; this prohibits the calculation of the electrical conductivity from the Nernst-Einstein relation that would only involve the diffusion coefficient of H and its nuclear charge $+e$ (French et al., 2011). According to the linear response theory, the electrical conductivity σ_e is related to the electrical current $\mathbf{J}(t)$ by the following Green-

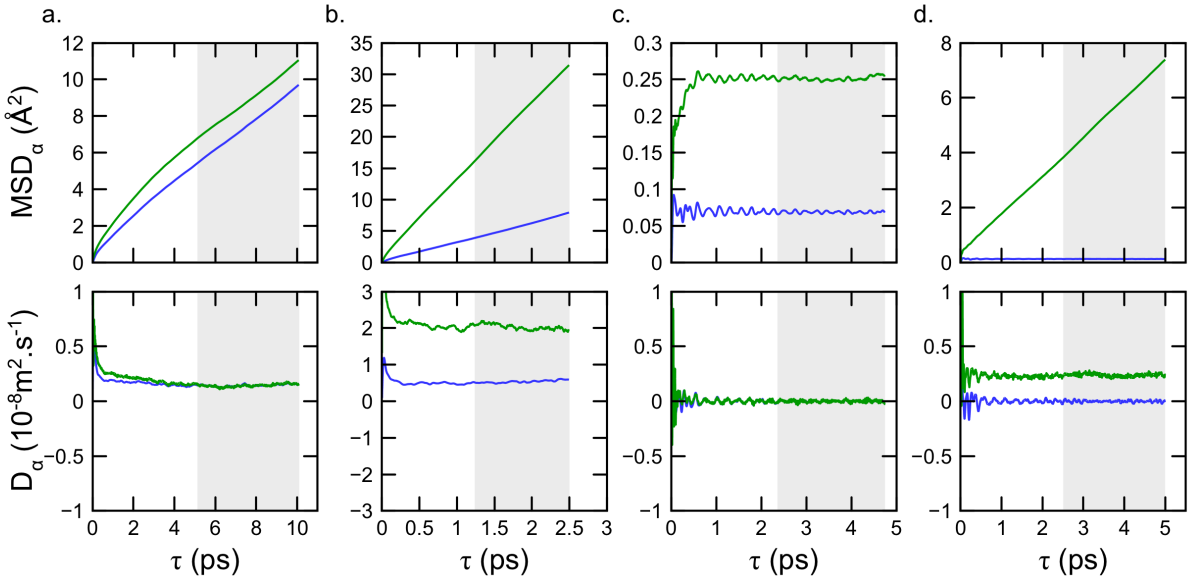

Figure 2.3: Mean square displacements (up) of oxygen (blue) and hydrogen atoms (green) and its derivative times 1/6 (down). Grey areas correspond to the intervals in which D_α are averaged. (a) Molecular fluid: $D_H = D_O > 0$. (b) Ionic fluid: $D_H > D_O > 0$. (c) Non-diffusive solid: $D_H = D_O = 0$. (d) Superionic solid: $D_H > 0$ and $D_O = 0$.

Kubo relation:

$$\sigma_e = \frac{1}{3Vk_BT}\int_0^{+\infty} \langle \mathbf{J}(t)\cdot\mathbf{J}(0)\rangle \,\mathrm{d}t \tag{2.32}$$

As long as the system is electronically insulating (which is the case in this thesis except for two tests on liquid Na and of H_2O at 4000 K), we can assume that only screened nuclear charges ensure the charge transport. Therefore, the total electrical current at a time t depends on the proportion of the electronic cloud transported by the ions, which is given by the Born effective charge tensor $\overline{\mathbf{Z}}(t)$ (French et al., 2011):

$$\mathbf{J}(t) = e\sum_{i=1}^{N} \overline{\mathbf{Z}}_i(t)\cdot\mathbf{v}_i(t) \tag{2.33}$$

where N is the number of particles in the system and $\mathbf{v}_i$ the velocity vector of a particle i. The estimation of the Born tensor is a time-consuming process as it involves the calculation of the response of the electronic polarization to the ion displacements. In practice, French et al. (2011) have shown that for superionic water, the replacement of the Born effective charge tensor by the average charges of the O and H ions ($Z_O = -2$ and $Z_H = +1$) in equation (2.33) leads to the same electrical conductivity (see Table 2.1). We use this last approximation in this work.

Table 2.1: From French et al. (2011). Comparison of electrical conductivities calculated at 3000 K and 3.0 g.cm^{-3} from: (i) current-current autocorrelation functions with time-dependent Born effective charges (σ_e), with constant charges of +1 for H atoms and −2 for O atoms ($\sigma_{+1,-2}$); (ii) Nernst-Einstein equation (σ'); (iii) current-current autocorrelation with time-dependent Bader charges (σ_B).

σ_e	$\sigma_{+1,-2}$	σ'	σ_B
140 ± 15	140 ± 15	91 ± 3	55 ± 5

2.4.4 Vibrational density of states

Most of the experimental diagnostics in diamond anvil cells are performed with Raman and infrared spectroscopy, and both information are contained in the total vibrational density of states (VDoS) that is easily computable from molecular dynamics trajectories. It represents the distribution of the density of normal modes as a function of the vibrational frequency.

Let us denote $\mathcal{S}_\alpha(\nu)$ the vibrational spectrum of N_α equivalent particles of a given species α with mass m_α. $\mathcal{S}_\alpha(\nu)$ is obtained by integration of the real part of the Fourier transform of the particle velocities ($\mathbf{v}_\alpha$) autocorrelation:

$$\mathcal{S}_\alpha(\nu) = \frac{4m_\alpha}{3k_BT} \int_0^{+\infty} \langle \mathbf{v}_\alpha(t) \cdot \mathbf{v}_\alpha(0) \rangle \cos(2\pi\nu t)\, \mathrm{d}t \tag{2.34}$$

where $\langle \mathbf{v}_\alpha(t) \cdot \mathbf{v}_\alpha(0) \rangle$ denotes the autocorrelation of the velocity vectors, averaged over the ensemble of the particles α. The normalization condition is choosen such that:

$$\int_0^{+\infty} \mathcal{S}_\alpha(\nu) \mathrm{d}\nu = 1 \tag{2.35}$$

The total vibrational density of states $\mathcal{S}(\nu)$ is given by a weighted sum over the vibrational spectra of each sub-systems:

$$\mathcal{S}(\nu) = 3 \sum_\alpha^{N_{sp}} N_\alpha \mathcal{S}_\alpha(\nu) \tag{2.36}$$

where N_{sp} is the number different species that compose the system. The integral of $\mathcal{S}(\nu)$ over the frequencies corresponds to the number of degrees of freedom of the system.

2.5 Quantum corrections of the thermodynamic quantities and estimation of the vibrational entropy

In this section, we present the formalism adopted to calculate the vibrational entropies and to correct the internal energies for the nuclear quantum effects of H_2O and NaCl·RH$_2$O systems at finite temperature from the vibrational density of states. The derivation of the equations is done in the canonical ensemble and is largely inspired by the work of Berens et al. (1983), Lin et al. (2003), Lai et al. (2012), Desjarlais (2013), French and Redmer (2015); French et al. (2016).

2.5.1 Introduction and objectives

Lin et al. (2003) propose to separate the velocity spectrum into a gas-like and a solid-like component; this is the two-phase thermodynamic model (2PT). First developed for monoatomic fluids, the gas-like part of the velocity spectrum is calculated by fitting a hard-sphere (HS) gas model based on the diffusivity of the system (zero-frequency component of the spectrum). The thermodynamic properties of the system are calculated by integration of properly weighted gas-like and solid-like parts.

Recently, the 2PT model has been extended to mixtures (Lai et al., 2012) and the gas-like part has been modified to account for memory effects (2PT-MF model, Desjarlais (2013)). These extensions permit to evaluate the free energies of more complicated systems such as superionic water (French et al., 2016; Meyer et al., 2016), and molecular mixtures (Lai et al., 2012).

Hereafter we present the 2PT-MF model as used in our free energy calculations. Our objective is to obtain the vibrational entropy and to correct the internal energy and the pressure from nuclear quantum effects. We discuss the assumptions on which the model is based and the assumptions that we have made in this thesis in our estimation of the vibrational entropy in mixed systems.

2.5.2 Relations between the thermodynamic variables and the vibrational spectrum in the canonical ensemble

In the canonical ensemble, the thermodynamic variables are expressed as functions of the canonical partition function Z. For the internal energy U, the nuclear entropy S and the heat capacity C_v we

have:

$$U\left(T,\rho\right) = k_B T^2 \frac{\partial \ln Z}{\partial T} \tag{2.37}$$

$$S\left(T,\rho\right) = k_B \ln Z + k_B T \frac{\partial \ln Z}{\partial T} \tag{2.38}$$

$$C_v\left(T,\rho\right) = 2k_B T \frac{\partial \ln Z}{\partial T} + k_B T^2 \frac{\partial^2 \ln Z}{\partial T^2} \tag{2.39}$$

Previously, we mentioned that the vibrational density of states $\mathcal{S}(\nu)$ represents the distribution of the normal modes of the system. The thermodynamic variables can thus be expressed as a continuous sum of the partition functions $z\left(\nu\right)$ associated to these normal modes.

$$\ln Z = \int_0^{+\infty} \mathcal{S}\left(\nu\right) \ln z\left(\nu\right) \mathrm{d}\nu \tag{2.40}$$

The internal energy, the vibrational entropy and the heat capacity thus write:

$$U\left(T,\rho\right) = k_B T^2 \frac{\partial}{\partial T} \left(\int_0^{+\infty} \mathcal{S}(\nu) \ln z\left(\nu,T,\rho\right) \mathrm{d}\nu \right) \tag{2.41}$$

$$S\left(T,\rho\right) = k_B \int_0^{+\infty} \mathcal{S}(\nu) \ln z\left(\nu,T,\rho\right) \mathrm{d}\nu + k_B T \frac{\partial}{\partial T} \left(\int_0^{+\infty} \mathcal{S}(\nu) \ln z\left(\nu,T,\rho\right) \mathrm{d}\nu \right) \tag{2.42}$$

$$C_v\left(T,\rho\right) = 2k_B T \int_0^{+\infty} \mathcal{S}(\nu) \ln z\left(\nu,T,\rho\right) \mathrm{d}\nu + k_B T^2 \frac{\partial^2}{\partial T^2} \left(\int_0^{+\infty} \mathcal{S}(\nu) \ln z\left(\nu,T,\rho\right) \mathrm{d}\nu \right) \tag{2.43}$$

As implicitly suggested by the notation $\mathcal{S}(\nu)$, we consider that the vibrational spectra of the sub- and/or total systems do not change rapidly as a function of pressure. Such assumption allows to simplify the above expressions to avoid the temperature derivatives of $\mathcal{S}(\nu, T, \rho)$.

2.5.3 The 2PT-MF model

First, we separate the system into the different atom species α, and use the definition of $\mathcal{S}_\alpha(\nu)$ given in equation (2.34).

Then, for each species α, we partition the vibrational spectrum into a gas-like ($f_\alpha \mathcal{S}_\alpha^g$) and a solid-like ($(1-f_\alpha)\mathcal{S}_\alpha^s$) component such that $\mathcal{S}_\alpha(\nu) = f_\alpha \mathcal{S}_\alpha^g(\nu) + (1-f_\alpha)\mathcal{S}_\alpha^s(\nu)$, where f_α represents the gas fraction.

The gas-like component is diffusive and presents $3f_\alpha N_\alpha$ degrees of freedom. The solid-like component does not diffuse ($\mathcal{S}_\alpha^s(0) = 0$) and is associated with the remaining degrees of freedom, i.e.

$3N_\alpha - 3f_\alpha N_\alpha = 3N_\alpha(1-f_\alpha)$. The total partition function of the system is thus the product of the partition function associated to the solid part with the partition function associated to the gas part. Such product leads to the sum of the corresponding logarithm, and using equation (2.40) we express the total partition function as:

$$\ln Z = 3\sum_{\alpha=1}^{N_{sp}} N_\alpha \left[\int_0^{+\infty} f_\alpha \mathcal{S}_\alpha^g(\nu) z_\alpha^g(\nu,T)\mathrm{d}\nu + \int_0^{+\infty}(1-f_\alpha)\mathcal{S}_\alpha^s(\nu) z_\alpha^s(\nu,T)\mathrm{d}\nu\right] \tag{2.44}$$

Inserting equation (2.44) into equations (2.38) to (2.39), and considering the vibrational spectra only dependent on ν ultimatively leads to the following expression for a given thermodynamic property A:

$$A = 3\sum_{\alpha=1}^{N_{sp}} N_\alpha \left[\int_0^{+\infty} f_\alpha \mathcal{S}_\alpha^g(\nu) W_{\alpha,A}^g(\nu,T)\mathrm{d}\nu + \int_0^{+\infty}(1-f_\alpha)\mathcal{S}_\alpha^s(\nu) W_{\alpha,A}^s(\nu,T)\mathrm{d}\nu\right] \tag{2.45}$$

where $W_{\alpha,A}^g(\nu,T)$ and $W_{\alpha,A}^s(\nu,T)$ are the appropriate weighting functions of the gas and solid components that correspond to the property A. The associated specific thermodynamic property $a = A/m$ with $m = \sum_{\alpha=1}^{N_{sp}} m_\alpha N_\alpha$ the mass of the system. In the following, we treat separately the solid- and the gas-like spectra.

2.5.3.1 Diffusive component from a hard-sphere model

We describe the diffusive behavior of the species α by a gas of hard spheres (HS) whose properties are well known. A HS gas is composed of equivalent rigid spheres of diameter σ_α^{HS} which interact only by elastic collisions. It is described entirely by the number of HS, their diameter, their mass, the volume, and the temperature. Therefore, the relations between the diffusive component of the sub-system of particle α and the HS gas is the following:

- N_α is the number of particles in the HS gas = the total number of particles α
- V_α corresponds to the total volume of the HS gas, and is related to the partial molar volume $\overline{V}_\alpha$ of the real system as $\overline{V}_\alpha = V_\alpha/N_\alpha$
- m_α is the mass of a HS = the mass of a particle α
- σ_α^{HS} is the diameter of a HS

The objective is to calculate the gas fraction f_α (also called *fluidicity factor*) that partitions the vibrational spectrum based on a given form for the gas-like component.

The gas fraction f_α is defined as proportional to the diffusivity $D_\alpha(T, N_\alpha, V_\alpha, m_\alpha)$ of the particles α:

$$f_\alpha = \frac{D_\alpha(T, N_\alpha, V_\alpha, m_\alpha)}{D^{HS}_{\alpha,0}(T, N_\alpha, V_\alpha, m_\alpha)} \tag{2.46}$$

where $D^{HS}_{\alpha,0}(T, N_\alpha, V_\alpha, m_\alpha)$ is the zero-pressure HS gas diffusion coefficient. Lin et al. (2003) have made this choice so that $f_\alpha = 0$ in a non-diffusive system ($D_\alpha(T, \rho) = 0$), and $f_\alpha = 1$ when $D_\alpha(T, \rho)$ reaches $D^{HS}_{\alpha,0}(T, \rho; \sigma^{HS}_\alpha)$.

According to Chapman and Enskog (Enskog, 1911; Chapman and Cowling, 1939; Brush, 2013), $D^{HS}_{\alpha,0}(T, N_\alpha, V_\alpha, m_\alpha)$ is related to the diameter of the HS and to their mass as follows:

$$D^{HS}_{\alpha,0}(T, N_\alpha, V_\alpha, m_\alpha) = \frac{3}{8}\sqrt{\frac{k_B T}{\pi m_\alpha}}\frac{V_\alpha}{N_\alpha \sigma^{HS^2}_\alpha} \tag{2.47}$$

Now, in order to have f_α we need to estimate the HS diameter. Lin et al. (2003) impose the diffusivity of the gas-like component ($D_\alpha(T, N_\alpha, V_\alpha, m_\alpha)/f_\alpha$) to correspond to equal the diffusivity predicted for the HS gas at a volume V_α/f_α and a temperature T (equation (2.48)).

$$D^{HS}_\alpha(T, N_\alpha, V_\alpha/f_\alpha, m_\alpha) = D_\alpha(T, N_\alpha, V_\alpha, m_\alpha)/f_\alpha \tag{2.48}$$

Moreover, using the Carnahan-Starling equation of states (Carnahan and Starling, 1969) of the HS gas one can relate the diffusion coefficient of the compressed HS gas $D^{HS}_\alpha(T, N_\alpha, V_\alpha/f_\alpha, m_\alpha)$ to its zero-pressure value at the same particle density $D^{HS}_{\alpha,0}(T, N_\alpha, V_\alpha/f_\alpha, m_\alpha)$:

$$D^{HS}_\alpha(T, N_\alpha, V_\alpha/f_\alpha, m_\alpha) = D^{HS}_{\alpha,0}(T, N_\alpha, V_\alpha, m_\alpha)\frac{4y_\alpha f_\alpha}{z(y_\alpha f_\alpha) - 1} \tag{2.49}$$

where z is the compressibility of the HS that depends on the packing fraction y_α as follows:

$$\begin{cases} z(y_\alpha f_\alpha) = \dfrac{1 + y_\alpha f_\alpha + (y_\alpha f_\alpha)^2 - (y_\alpha f_\alpha)^3}{(1 - y_\alpha f_\alpha)^3} & (2.50) \\ y_\alpha = \dfrac{\pi}{6}\dfrac{N_\alpha}{V_\alpha}\sigma^{HS^3}_\alpha & (2.51) \end{cases}$$

At this point, we can see that f_α and σ^{HS}_α will have to be solved simultaneously. Indeed, by fixing f_α and inserting equations (2.47) and (2.48) in equation (2.49) permits to solve it for σ^{HS}_α, but f_α depends on σ^{HS}_α. Following the work of Lin et al. (2003) and Desjarlais (2013), it is useful to

define a new variable Δ_α that represents a normalized diffusivity and is related to the gas fraction and the packing fraction as $\Delta_\alpha = y_\alpha^{-2/3} f_\alpha$. Using equations (2.46) and (2.47) and remembering that the diffusion coefficient $D_\alpha(T, N_\alpha, V_\alpha, m_\alpha)$ is obtained from $\mathcal{S}_\alpha(0)$, Δ_α can be expressed as:

$$\Delta_\alpha = \frac{2}{3}\mathcal{S}_\alpha(0)\sqrt{\frac{\pi k_B T}{m_\alpha}}\left(\frac{6}{\pi}\right)^{2/3}\overline{V}_\alpha^{-1/3} \tag{2.52}$$

Δ_α only depends on the system parameters and $\mathcal{S}_\alpha(0)$. Now, let be $\gamma_\alpha = y_\alpha f_\alpha$ the packing fraction of the gas-like component. It can be shown that γ_α and Δ_α are related by equation (2.53) which is solved numerically for γ_α.

$$\gamma_\alpha^{2/5}\Delta_\alpha^{3/5} = \frac{2(1-\gamma_\alpha^3)}{2-\gamma_\alpha} \tag{2.53}$$

As $f_\alpha = \gamma_\alpha^{2/5}\Delta_\alpha^{3/5}$, we finally obtain the fraction of gas-like component f_α.

Now, we need to choose a form for the gas-like spectrum $\mathcal{S}_\alpha^g(\nu)$. A first choice is to use the HS gas spectrum. The HS gas velocity autocorrelation decays exponentially which results in a Lorentzian form for the spectrum. While this choice leads to a good estimation of the thermodynamic properties, Desjarlais (2013) shows from calculations on liquid sodium that at high frequencies the tail of the Lorentzian spectrum decays slower than the total vibrational spectrum. This results in a systematic error on the estimation of the thermodynamic properties. Desjarlais (2013) improves the form of the gas-like component by including "memory effects" described below. It has been adapted to multi-component systems by French et al. (2016). We use this model in this thesis in order to account for correlation in the diffusive motion of the hydrogen atoms.

In the itinerant oscillator model (Sears, 1965; Singwi and Sjölander, 1968), a set of stochastic equations describes the correlated motion of a diffusive atom in a media. The velocity autocorrelation Φ_α^g (of the gas-like component here) is associated to a memory function (MF) representation:

$$\frac{\mathrm{d}\Phi_\alpha^g(t)}{\mathrm{d}t} = -\int_0^t K_\alpha^g(\tau)\Phi_\alpha^g(t-\tau)\mathrm{d}\tau \tag{2.54}$$

where $K_\alpha^g(\tau)$ is a memory function kernel. The vibrational spectrum is related to $K_\alpha^g(\tau)$ by:

$$\mathcal{S}_\alpha^g(\nu) = \frac{1}{2}\left(\frac{1}{\widehat{K}_\alpha^g(i2\pi\nu) + i2\pi\nu} + \frac{1}{\widehat{K}_\alpha^g(-i2\pi\nu) - i2\pi\nu}\right) \tag{2.55}$$

where $\widehat{\ }$ denotes the Laplace transform of the quantity. Desjarlais (2013) chooses a Gaussian kernel to reproduce the high frequency decay of $\mathcal{S}_\alpha(\nu)$. Therefore, two coefficients describe $\mathcal{S}^g_\alpha(\nu)$, and the Laplace transform of the gaussian kernel writes:

$$\widehat{K}^g_\alpha(x) = A^g_\alpha \sqrt{\frac{\pi}{4B^g_\alpha}} \exp\left(\frac{x^2}{4B^g_\alpha}\right) \operatorname{erfc}\left(\frac{x}{2\sqrt{B^g_\alpha}}\right) \tag{2.56}$$

In $\nu = 0$, $\mathcal{S}^g_\alpha(0)$ provides a first relation between A_g and B_g:

$$\mathcal{S}^g_\alpha(0) = \frac{1}{\widehat{K}^g_\alpha(0)} = \frac{1}{A^g_\alpha}\sqrt{\frac{4B^g_\alpha}{\pi}} = \frac{\mathcal{S}_\alpha(0)}{f_\alpha} \tag{2.57}$$

Moreover, $\mathcal{S}^g_\alpha(0)$ has to be equal to $\mathcal{S}_\alpha(0)/f_\alpha$, which brings another constraint between A^g_α and B^g_α:

$$A^g_\alpha = \frac{4B^g_\alpha}{2 + \sqrt{\pi\left(1 + \dfrac{B^g_\alpha \mathcal{S}^2_\alpha(0)}{4\gamma_\alpha^{4/5}\Delta_\alpha^{6/5}}\right)}} \tag{2.58}$$

B^g_α controls the strength of the high-frequency decay and is formally determined by the determination of relations between A^g_α, B^g_α and the even moments of $\mathcal{S}_\alpha(\nu)$ (Desjarlais, 2013).

Finally, the gas fraction f_α is obtained from A^g_α, B^g_α and $\mathcal{S}_\alpha(0)$:

$$f_\alpha = \frac{A^g_\alpha \mathcal{S}_\alpha(0)}{8}\sqrt{\frac{\pi}{B^g_\alpha}} \tag{2.59}$$

In pratice, we choose B_g so that $f_\alpha \mathcal{S}^g_\alpha(\nu)$ matches the high-frequency tail of $\mathcal{S}_\alpha(\nu)$.

It is worth mentioning that Meyer et al. (2014, 2016) also improve the 2PT-MF model by adding even more correlations. They build an expression for the velocity autocorrelation directly based on the friction parameters of the itinerant harmonic oscillator model. They obtain simultaneously the gas-like and solid-like components by fitting the velocity autocorrelation function of the system. We test the approach proposed by Meyer et al. (2016) but we find that the vibrational spectrum resulting from the fit of the velocity autocorrelation function is too different from the data.

2.5.3.2 Estimation of the partial molar volumes

The partial molar volume $\overline{V}_\alpha$ of a species α is defined as the change of volume in the system due to the addition or substraction of an atom of α at constant pressure and temperature:

$$\overline{V}_\alpha = N \left(\frac{\partial V}{\partial N_\alpha} \right)_{T,p,N_{\beta \neq \alpha}} \tag{2.60}$$

In the case of a simple monoatomic fluid, it corresponds to the molar volume $\overline{V} = V/N$ with V the total volume of the system and $N = N_\alpha$ the total number of particles. Nevertheless, for a multi-component mixture $\overline{V}_\alpha$ needs to be evaluated. By definition, the partial molar volume represents the change of volume due to the addition or the subtraction of one or several α atoms in the system at constant pressure and constant number of other species β. Two rigourous methods provide an estimation for $\overline{V}_\alpha$. The first one is based on the Kirkwood-Buff theory (Kirkwood and Buff, 1951) and on the radial distribution functions between components α and β. The second implies to perform several molecular dynamics runs to calculate the change of volume due to the variation of N_α.

Partial volume from Kirkwood-Buff theory According to Kirkwood and Buff (Kirkwood and Buff, 1951; Lai et al., 2012), $\overline{V}_\alpha$ is related to the radial distribution functions $g_{ij}(r)$ as described hereafter. Let be G_{ij} the Kirkwood-Buff integral (KBI):

$$G_{ij} = \int_0^{+\infty} (g_{ij}(r) - 1)\, 4\pi r^2 \mathrm{d}r \tag{2.61}$$

If we define B_{ij} as:

$$B_{ij} = \frac{N_i N_j}{V^2} G_{ij} + \frac{N_i}{V} \delta_{ij} \tag{2.62}$$

with δ_{ij} being the Kronecker delta function. Then the partial molar volume of the component α writes:

$$\overline{V}_\alpha = \frac{\sum_i \frac{N_i}{V} B^{i\alpha}}{\sum_{i,j} \frac{N_i N_j}{V} B^{ij}} \tag{2.63}$$

where B^{ij} is the cofactor of the element B_{ij} in the determinant of $\mathbf{B}$, the matrix corresponding to the elements B_{ij}. Therefore, the main point is the convergence of the KBI. G_{ij} converges very slowly as function of r, requiring large supercells. We attempt this method on fluid systems but we did not reach the convergence for the KBI.

Partial volume from additional molecular dynamics simulations $\overline{V}_\alpha$ can be calculated from NpT calculations but it requires to adjust carefully the pressure between calculations which have a different number of atoms. In order to use NVT simulations, we can apply the following transformation:

$$\overline{V}_\alpha = \left(\frac{\partial V}{\partial N_\alpha}\right)_{T,p,N_{\beta\neq\alpha}} = -\left(\frac{\partial V}{\partial p}\right)_{T,N_\beta,N_\alpha}\left(\frac{\partial p}{\partial N_\alpha}\right)_{T,p,N_{\beta\neq\alpha}} \tag{2.64}$$

Morevover, the isothermal bulk modulus is defined as:

$$K_T = -V\left(\frac{\partial p}{\partial V}\right)_{T,N_\beta,N_\alpha} \tag{2.65}$$

Thus,

$$\overline{V}_\alpha = \frac{V}{K_T}\left(\frac{\partial p}{\partial N_\alpha}\right)_{T,p,N_{\beta\neq\alpha}} \tag{2.66}$$

And for small variations of N_α:

$$\overline{V}_\alpha = \frac{V}{K_T}\left(\frac{\Delta p}{\Delta N_\alpha}\right)_{T,p,N_{\beta\neq\alpha}} \tag{2.67}$$

Because the partial volumes are only needed for the diffusive species, i.e. the hydrogen atoms, we only have to calculate Δp when changing the number of H in the system. We performed a simulation removing 2 H and another one adding 2 H. We check our approximation in the ice VII″ regime at 2000 K. At this conditions our pressure – volume relation are in a prefect agreement with the EOS of French et al. 2016 that we used to calculate K_T.

Assumptions In order to avoid additional molecular dynamics simulations, several assumptions are possible. First, we can crudely consider that the effective partial volume of a given species is equal to its molar volume. Secondly, we can assume that all atomic species are hard spheres and then relate the radius of the HS to the effective partial volume. This approach is not valid any more as soon as the atomic radii are too different from each other like it is the case for H and O. Here, we decided to use the Bader volume as partial effective volumes. Bader volumes are calculated from the electronic charge density in the simulation cell. Bader volume boundaries are defined by the minimum values of charge density around a given atoms. Averaging these volumes for each atomic species gives us an estimation of the effective partial volume. Because we have a large supercell, we calculate the Bader volumes from the charge density of one snapshot of the MD trajectory at a given density and temperature. To

verify this assumption we first explore the influence of the partial volume of the diffusive species on the results of the vibrational entropy. Then, we calculated the partial volumes of O and H for H_2O at 2000 K and a density of 2.762 g.cm^{-3} (82 GPa). The comparison between the two estimations is discussed in Â§2.5.3.5.

2.5.3.3 Estimation of the thermodynamic properties

To complete the 2PT-MF model, we calculate the vibrational entropy and the heat capacity of the total system by applying the appropriate weighting functions to the different vibrational spectra $\mathcal{S}_\alpha(\nu)$. From the partition function of the HS gas, we derive the weighting functions for the HS gas (Lin et al., 2003; Lai et al., 2012) needed in equation (2.45) as:

$$W_{U,\alpha}^{HS}(\nu) = k_B T \tag{2.68}$$

$$\begin{cases} W_{S,\alpha}^{HS}(\nu) = \dfrac{k_B}{3}\left[\dfrac{S^{IG}}{k_B} + \ln\left(\dfrac{1+\gamma_\alpha+\gamma_\alpha^2-\gamma_\alpha^3}{(1-\gamma_\alpha)^3}\right) + \dfrac{3\gamma_\alpha^2-4\gamma_\alpha}{(1-\gamma_\alpha)^2}\right] & (2.69) \\ \dfrac{S^{IG}}{k_B} = \dfrac{5}{2} - \ln\left[\left(\dfrac{h^2}{2\pi m_\alpha k_B T}\right)^{3/2}\dfrac{f_\alpha}{\overline{V}_\alpha}\right] & (2.70) \end{cases}$$

$$W_{C_v,\alpha}^{HS}(\nu) = k_B \tag{2.71}$$

where $W_{U,\alpha}^{HS}(\nu)$, $W_{S,\alpha}^{HS}(\nu)$ and $W_{C_v,\alpha}^{HS}(\nu)$ are respectively the weighting functions for the vibrational entropy and the heat capacity of the gas-like component.

The non-diffusive part is modeled from a sum of quantum harmonic oscillators whose individual partition functions $z_{\alpha,i}^{QHO}(\nu,T)$ are:

$$z_{\alpha,i}^{QHO}(\nu,T) = \frac{\exp\left(\dfrac{h\nu/k_BT}{2}\right)}{1-\exp\left(-h\nu/k_BT\right)} \tag{2.72}$$

which leads to the following weighting functions for the solid-like component:

$$W_{U,\alpha}^{QHO}(\nu) = k_B T\left[\frac{h\nu/k_BT}{2} + \frac{h\nu/k_BT}{\exp\left(h\nu/k_BT\right)-1}\right] \tag{2.73}$$

$$W_{S,\alpha}^{QHO}(\nu) = k_B\left[\frac{h\nu/k_BT}{\exp\left(h\nu/k_BT\right)-1} - \ln\left(1-\exp(-h\nu/k_BT)\right)\right] \tag{2.74}$$

$$W_{C_v,\alpha}^{QHO}(\nu) = k_B \left[\frac{\exp\left(h\nu/k_BT\right)\left(h\nu/k_BT\right)^2}{\left(1-\exp\left(h\nu/k_BT\right)\right)^2} \right] \tag{2.75}$$

It should be noted that $W_{S,\alpha}^{QHO}(\nu)$ and $W_{C_v,\alpha}^{QHO}(\nu)$ respectively diverge toward $+\infty$ and $-\infty$ at the zero-frequency. Considering a typical Debye solid, $\mathcal{S}_\alpha^s(\nu)$ is expected to decrease as ν^3 when approaching zero. Because power functions approach zero faster than exponential functions it can be shown that the value of the integrand is zero when assuming a Debye solid.

Finally, using equation (2.45) with the appropriate weighting functions we calculate the vibrational entropy and heat capacity of the multi-component system.

2.5.3.4 Quantum correction for the internal energy

The classical component (i.e. all except NQEs) of the internal energy $U_{MD}(T,\rho)$ is already calculated during the *ab initio* molecular dynamics simulation. Consequently, we need to correct it only from nuclear quantum effects. Because the quantum correction $U_{qc}(T,\rho)$ is based on the quantum harmonic oscillator, the correction only applies on the solid-like part $\mathcal{S}_\alpha^s(\nu)$. The total internal energy of the system $U_{tot}(T,\rho)$ writes:

$$U_{tot}(T,\rho) = U_{MD}(T,\rho) + U_{qc}(T,\rho) \tag{2.76}$$

Because it has been obtained classically, $U_{MD}(T,\rho)$ is equivalent to the internal energy given by a 2PT-MF model whose solid component is represented as a sum of classical harmonic oscillators (CHO). So,

$$U_{MD}(T,\rho) = 3\sum_{\alpha=1}^{N_{sp}} N_\alpha \int_0^{+\infty} \left[f_\alpha \mathcal{S}_\alpha^g(\nu) W_{U,\alpha}^{HS}(\nu) + (1-f_\alpha)\mathcal{S}_\alpha^s(\nu) W_{U,\alpha}^{CHO}(\nu) \right] \mathrm{d}\nu \tag{2.77}$$

where $W_{U,\alpha}^{CHO}(\nu) = k_BT$.

The total energy $U_{tot}(T,\rho)$ is equivalent to the internal energy given by a 2PT-MF model whose solid component is represented as a sum of quantum harmonic oscillators (QHO).

$$U_{tot}(T,\rho) = 3\sum_{\alpha=1}^{N_{sp}} N_\alpha \int_0^{+\infty} \left[f_\alpha \mathcal{S}_\alpha^g(\nu) W_{U,\alpha}^{HS}(\nu) + (1-f_\alpha)\mathcal{S}_\alpha^s(\nu) W_{U,\alpha}^{QHO}(\nu) \right] \mathrm{d}\nu \tag{2.78}$$

Therefore, the $U_{qc}(T,\rho)$ corresponds to the energy difference between the two models, which reduces

to:

$$\begin{cases} U_{qc}(T,\rho) = 3\sum_{\alpha=1}^{N_{sp}} N_\alpha \int_0^{+\infty} (1-f_\alpha)\mathcal{S}_\alpha^s(\nu)\left[W_{U,\alpha}^{QHO}(\nu) - W_{U,\alpha}^{CHO}(\nu)\right] \mathrm{d}\nu & (2.79) \\ W_{U,\alpha}^{QHO}(\nu) - W_{U,\alpha}^{CHO}(\nu) = k_B T\left[\frac{h\nu/(k_BT)}{2} + \frac{h\nu/(k_BT)}{\exp\left(h\nu/(k_BT)\right)-1} - 1\right] & (2.80) \end{cases}$$

2.5.3.5 Validation of the implementation

Monoatomic system: liquid Na. We investigate the vibrational entropy of liquid sodium at 723 K and 0 GPa as it is done by Desjarlais (2013). We perform a first-principles molecular dynamics in a cubic supercell containing 128 Na atoms at 723 K in the isokinetic ensemble. We choose the volume of the supercell according to an experimental equation of states (Vargaftik et al., 1978). We acquire 72 ps of data (36000 steps) after the thermalization with an average total pressure of -0.19 ± 0.73 GPa. After application of the 2PT-MF model and addition of the electronic entropy, we obtain a gas fraction $f_{Na} = 0.388$ and a vibrational entropy of 10.094 k_b/atom which is exactly the value tabulated in Hultgren et al. (1973) and calculated by Desjarlais (2013) with the 2PT-MF (see Figure 2.4).

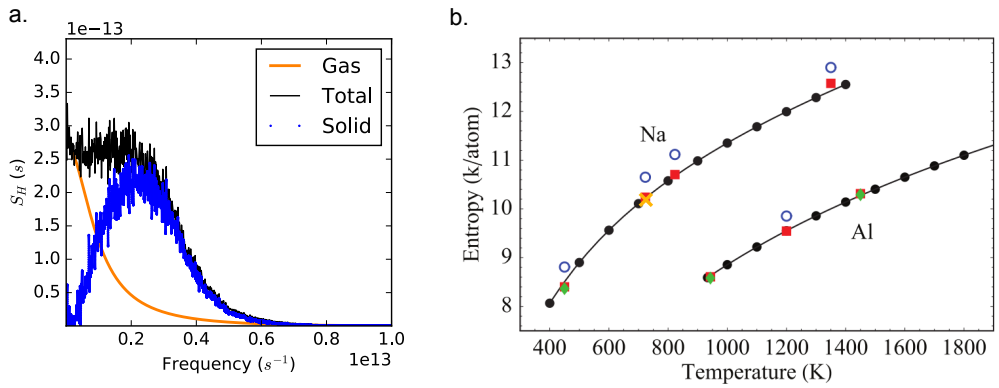

Figure 2.4: a. Decoupling of the different part of the partial VDOS from a 2PT-MF model applied to liquid sodium at 723 K and 0 GPa. The black line corresponds to the partial VDoS $\mathcal{S}_H(\nu)$ obtained from the H velocity autocorrelation, the orange line represents $\mathcal{S}_H^g(\nu)$ and the blue line is the solid partial VDoS $\mathcal{S}_H^s(\nu)$ obtained by subtracting $\mathcal{S}_H^g(\nu)$ from $\mathcal{S}_H(\nu)$. b. Entropy for liquid sodium. Black line and dots corresponds to data obtained by Hultgren et al. (1973), open circles and red squares respectively refer to calculations based on the 2PT model and on the 2PT-MF model. Blue cross corresponds to the results of the 2PT-MF from our calculation. This figure is modified from Desjarlais (2013).

Therefore, it validates our implementation of the 2PT-MF model for atomic compositions.

Superionic water ice. Superionic H_2O can be decoupled into a sub-system constituted by the H atoms and another one constituted by the O atoms. We treat the O atom sub-lattice as fully solid (i.e.

$f_O = 0$) and the H atom sub-system as a sum of a gas-like and a solid-like component. For hydrogen, the partial molar volume $\overline{V}_H$ is assumed to be equal to the Bader volume.

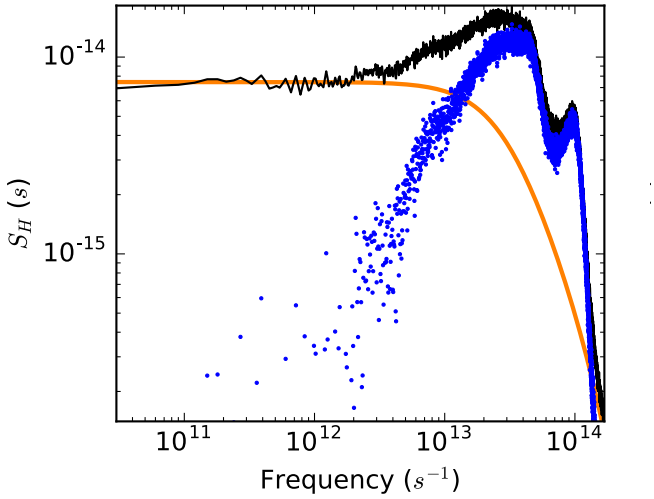

Figure 2.5: Decoupling of the different part of the partial VDOS from a 2PT-MF model applied to water ice at 2000 K and 82 GPa. The black line corresponds to the partial VDoS $\mathcal{S}_H(\nu)$ obtained from the H velocity autocorrelation, the orange line represents $\mathcal{S}_H^g(\nu)$ and the blue line is the solid partial VDoS $\mathcal{S}_H^s(\nu)$ obtained by subtracting $\mathcal{S}_H^g(\nu)$ from $\mathcal{S}_H(\nu)$.

Figure 2.5 shows the results of the decoupling of the HS gas and harmonic oscillator parts of the H vibrational spectrum at 1600 K and 2.36 g.cm^{-3} (47 GPa). In comparison to the liquid Na spectrum, the gas component extends up to high frequencies. This is not surprising considering the mass difference between Na and H. It also comes from our fitting procedure that imposes B_H^g to match the high-frequency tail of the total H spectrum, which is at much higher frequency that the one of liquid Na.

Figure 2.6 is the evolution of the Bader volumes of O and H as functions of the thermodynamic conditions:

Now we look at the influence of the hydrogen partial molar volume on the determination of the vibrational entropy. To validate our assumption we test step-by-step the dependence of the calculation of the vibrational entropy as a function of $n_\alpha^{\text{eff}} = 1/\overline{V}_\alpha$ the number of effective particles α for a given vibrational spectrum at given density and temperature conditions (Figure 2.7). First, the normalized diffusivity presents a positive dependence with respect to n_α^{eff} (see equation (2.52)). The hard-sphere packing fraction γ_α decreases significantly as function of increasing n_α^{eff} especially in the range $]0, 2]$ where it is halved. The quasi-totality of the effective partial volumes calculated from the Bader volumes

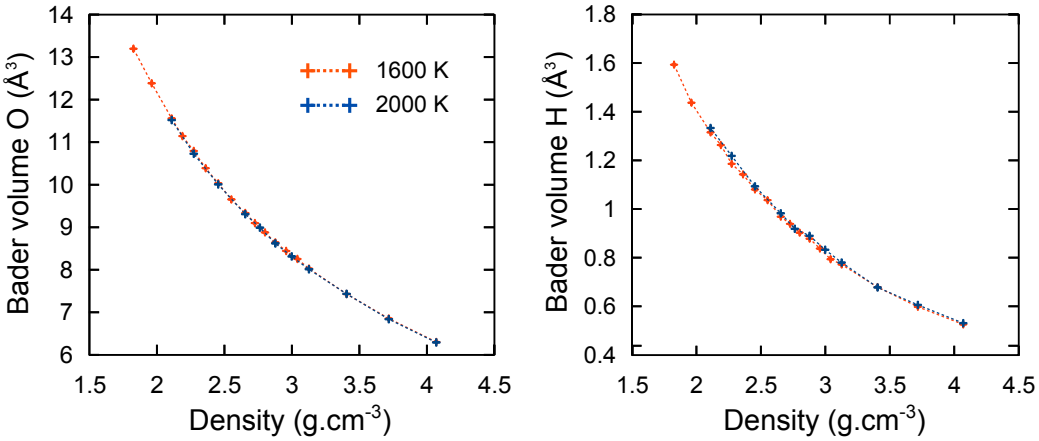

Figure 2.6: Bader volumes of O and H as functions of the thermodynamic conditions in bcc H_2O ice.

are in this range of n_α^{eff} values.

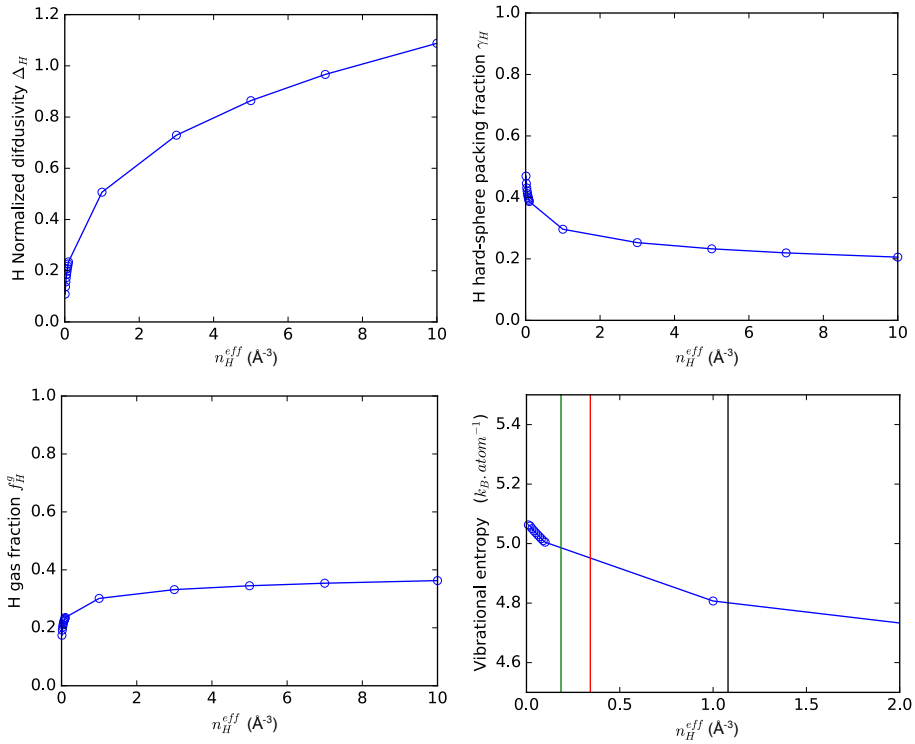

Figure 2.7: Dependence of given parameters of the 2PT-MF model on the number effective H atoms n_H^{eff}. a. Normalized diffusivity Δ_H. b. H hard sphere gas packing fraction γ_H. c. Gas fraction f_H. d. Vibrational entropy. The green and black lines respectively represent the values of n_H^{eff} obtained from the molar volume of H and the Bader volume; the red line corresponds to the calculated value of n_H^{eff} (cf. 2.5.3.2)

The gas fraction f_H increases of 0.1 between $n_\alpha^{\text{eff}} = 0.01$ and $n_\alpha^{\text{eff}} = 10$. Finally,in this range of n_α^{eff} the vibrational entropy decreases from 5 to 4.5 k_B.atom^{-1}. Such dependence indicates that a bad estimation of n_α^{eff} could lead to an error of $\sim$0.1 k_B/atom on the vibrational entropy and thus on the

calculation of the Gibbs free energy when H is diffusive.

Convergence of the thermodynamic properties The length of the MD trajectory is a crucial parameter to ensure that the velocity autocorrelation and thus the thermodynamic properties are converged. For the vibrational entropy the convergence is respectively achieved in 7 ps and 10 ps for the superionic water and the liquid sodium. We explain the slowest convergence in liquid Na by the

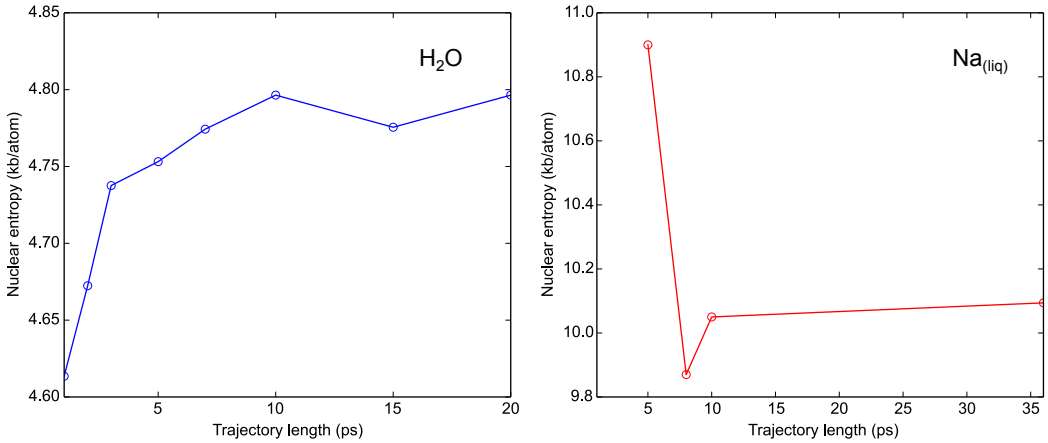

Figure 2.8: Convergence of the calculation of the vibrational entropy as a function of the length of the MD trajectory for H_2O at 2000 K and 82 GPa.

lower frequencies involved in the VDoS due to the higher mass of the sodium in comparison to the O and H. In average, we achieve the normalization condition on $\mathcal{S}_\alpha$ within $2-3$ % for the spectra associated with H and O. In the case of the NaCl·RH$_2$O systems, the error on $\mathcal{S}_{\mathrm{Na}}$ and $\mathcal{S}_{\mathrm{Cl}}$ depends on the number of Na and Cl ions in the supercell. In NaCl $\cdot$ 126H$_2$O the errors on $\mathcal{S}_{\mathrm{Na}}$ and $\mathcal{S}_{\mathrm{Cl}}$ can reach 10 %.

2.6 Elasticity

In this section, we present our determination of the elastic constants at the relevant thermodynamic conditions.

In the assumption of small deformations, the stress and strain tensors are linearly related by the fourth order elastic constants tensor (Nye, 1985). In the Voigt notation, the indices I and J are defined such that for a given symmetric tensor $\mathbf{T}$:

$$\mathbf{T} = \begin{pmatrix} T_{11} & T_{12} & T_{13} \\ . & T_{22} & T_{23} \\ . & . & T_{33} \end{pmatrix} = \begin{pmatrix} T_1 & T_6 & T_5 \\ . & T_2 & T_4 \\ . & . & T_3 \end{pmatrix} \tag{2.81}$$

The linear relation of elasticity then writes:

$$\sigma_I = C_{IJ}\varepsilon_J \tag{2.82}$$

where σ_I, ε_J and C_{IJ} are respectively the stress, strain and elastic constant tensors. In a cubic system, C_{IJ} has only three independent coefficients:

$$C_{IJ} = \begin{pmatrix} C_{11} & C_{12} & C_{12} & 0 & 0 & 0 \\ C_{12} & C_{11} & C_{12} & 0 & 0 & 0 \\ C_{12} & C_{12} & C_{11} & 0 & 0 & 0 \\ 0 & 0 & 0 & C_{44} & 0 & 0 \\ 0 & 0 & 0 & 0 & C_{44} & 0 \\ 0 & 0 & 0 & 0 & 0 & C_{44} \end{pmatrix} \tag{2.83}$$

The stress–strain relation thus becomes:

$$\begin{cases} \sigma_1 = C_{11}\varepsilon_1 + C_{12}(\varepsilon_2 + \varepsilon_3) \\ \sigma_2 = C_{11}\varepsilon_2 + C_{12}(\varepsilon_1 + \varepsilon_3) \\ \sigma_3 = C_{11}\varepsilon_3 + C_{12}(\varepsilon_1 + \varepsilon_2) \\ \sigma_4 = C_{44}\varepsilon_4 \\ \sigma_5 = C_{44}\varepsilon_5 \\ \sigma_6 = C_{44}\varepsilon_6 \end{cases} \tag{2.84}$$

We obtain the elastic constants applying a monoclinic strain (ε) to the cubic lattice:

$$\varepsilon = \begin{pmatrix} e & 0 & 0 \\ 0 & 0 & e/2 \\ 0 & e/2 & 0 \end{pmatrix} \tag{2.85}$$

The strained lattice A' is thus obtained from the unstrained lattice A from $A' = (\mathbf{1} + \varepsilon) \cdot A$ where $\mathbf{1}$

is the identity matrix. For each constant volume – temperature conditions, we apply two strains of $e = 0.01$ and $e = -0.01$ in addition to the unstrained simulation. We obtain the elastic constants by fitting the corresponding stress – strain relations. Typical stress variations are shown in Figure 2.9. We check the mechanical stability of the structures according the Born criterion (Born, 1940; Mouhat and Coudert, 2014) for cubic crystals: $C_{11} - C_{12} > 0$, $C_{11} + 2C_{12} > 0$ and $C_{44} > 0$.

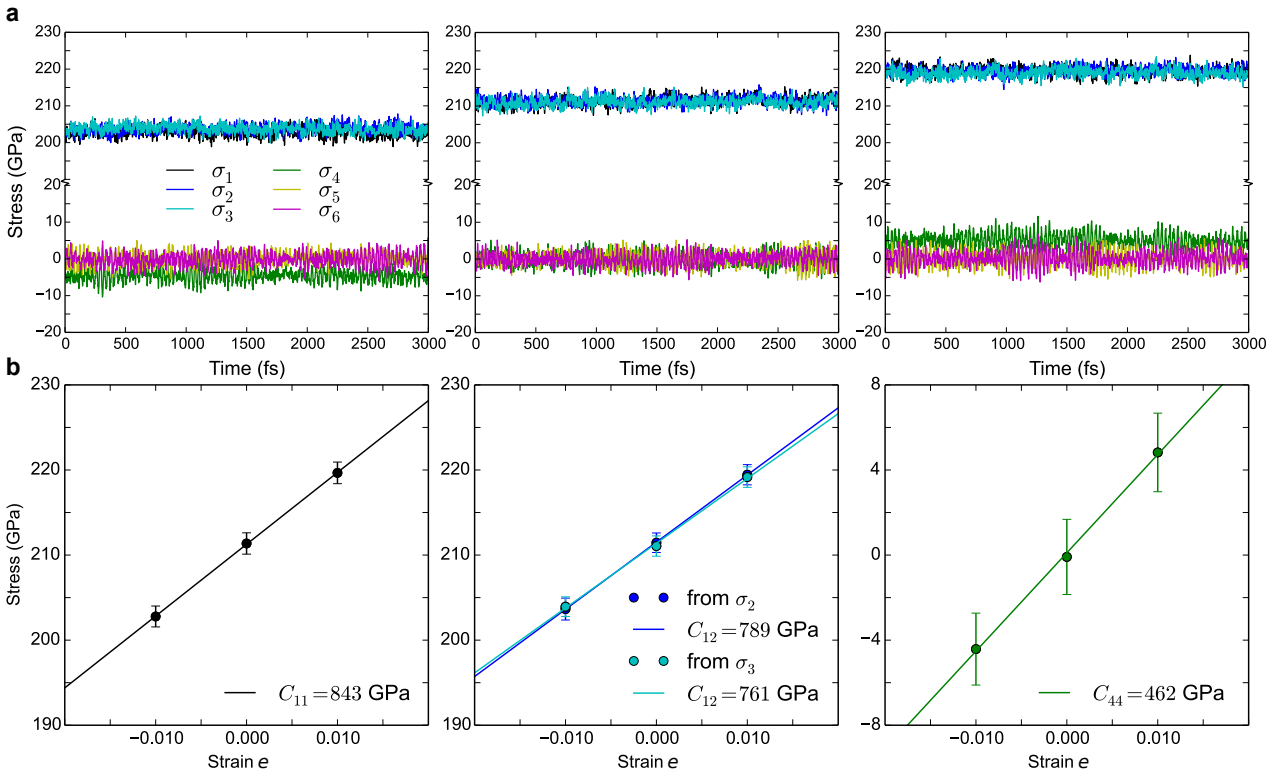

Figure 2.9: (a) Evolution of the stress components during the acquisition phase for the strained lattices with $e = -0.01$ and $e = 0.01$ (respectively the left and right panels) and for the unstrained lattice (center). (b) Stress – strain relations obtained from data presented in (a) (circles). Lines represent linear fits whose slopes correspond to the elastic constants.

Figure 2.9 shows that we estimate twice C_{12} (cf. equation (2.84)). The final value corresponds to the average of the two estimations. In practice, we prepare the strained supercells from the last configuration of the unstrained molecular dynamics equilibrated at the corresponding thermodynamic conditions.

2.7 Thermodynamics of binary solid solutions

In this section we present our approach to investigate the possible inclusion of some amounts of salt in the bcc ice structure at high-temperature. As mentioned in the introduction of this thesis, this

question is relevant for planetary science and extra-terrestrial life as the incorporation of electrolytes in the ice structure should modify the planet interior dynamics and should permit the transport of electrolytes from the core to a surface or underlying ocean.

The estimation of the thermodynamic stability of the binary system requires the calculation of the Gibbs free energy of mixing $\Delta g_{mix}(w)$ at a given concentration for given pressure and temperature conditions. One obtains $\Delta g_{mix}(w,p,T)$ from the Gibbs free energies of the pure phases ($g_{\mathrm{H_2O}}(p,T)$, $g_{\mathrm{NaCl}}(p,T)$) and the configurational averaged Gibbs free energy of the mixture ($g_{sol}(w,p,T)$) as shown by equation (2.86).

$$\Delta g_{mix}(w,p,T) = g_{sol}(w,p,T) - (w g_{\mathrm{NaCl}}(p,T) + (1-w) g_{\mathrm{H_2O}}(p,T)) \tag{2.86}$$

$g_{sol}(x,p,T)$ includes a configurational entropy $s_{conf}(w,p,T)$ which depends on the number of configurations accessible to the system.

In solid solutions, the configurations that present the major contribution are generally separated by high energy barriers although their own energies can be very close or similar. Consequently they cannot be sampled by standard molecular dynamics.

Let K be the total number of these low energy configurations accessible in a given supercell. A given configuration k is a local minimum of the global energy landscape and presents itself smaller scales energy variations due to its accessible states e_{kl}. According to Allan et al. (2001); Todorov et al. (2004), if we ignore the high-energy states that induce large changes in the internal and external lattice strains, we can write a given thermodynamic property A and the Gibbs free energy G of the total system in the NpT ensemble as:

$$A = \frac{\sum_{k=1}^{K} A_k \exp\left(-G_k/(k_B T)\right)}{\sum_{k=1}^{K} \exp\left(-G_k/(k_B T)\right)} \tag{2.87}$$

$$G = -k_B T \ln K - k_B T \ln \left(\frac{1}{K} \sum_{k=1}^{K} \exp\left(-G_k/(k_B T)\right) \right) \tag{2.88}$$

where H_k and G_k are respectively the enthalpy and the Gibbs free energy of the configuration k. Equation (2.88) has been written such that the first term corresponds to $-TS^{id}_{conf}$ with S^{id}_{conf} the ideal configurational entropy of the mixture associated to the supercell. Because the total number of configurations K increases extremely rapidly as a function of the supercell size, it is impractical to

calculate the Gibbs free energy of each configurations k. Allan et al. (2001); Todorov et al. (2004) proposed to randomly sample the configurational space until reaching the desired convergence for A. Defining K' as the number of sampled configurations, A and G thus write:

$$\langle A \rangle_c = \frac{\sum_{k=1}^{K'} A_k \exp\left(-G_k/(k_B T)\right)}{\sum_{k=1}^{K'} \exp\left(-G_k/(k_B T)\right)} \tag{2.89}$$

$$G = -k_B T \ln K - k_B T \ln \left(\frac{1}{K'} \sum_{k=1}^{K'} \exp\left(-G_k/(k_B T)\right) \right) \tag{2.90}$$

where $\langle\ \rangle_c$ is the average over the configurational space. The ideal contribution to the free Gibbs energy remains unchanged and the entropy of the mixture is finally given by:

$$S = \frac{\langle H \rangle_c - G}{T} = \langle S_{vib} \rangle_c + S_{conf} \tag{2.91}$$

The converge of the properties depends of course on the size of the supercell and on the number of possible configurations. Allan et al. (2001); Todorov et al. (2004) show that for a 50/50 binary mixture a good convergence of the properties is achieved for $K' \sim 100$. Although manageable for purely static or lattice dynamics approaches, this number is still too large for us as we need long MD trajectory to estimate the vibrational entropy, the quantum correction for the internal energy, and thus the free energies of our highly anharmonic systems.

More recently, Grau-Crespo et al. (2007) proposed to sample only the reduced configurational space, i.e. the K_{red} configurations independent by symmetry operations. The independent configurations k are weighted based on their degeneracy Ω_k such that:

$$K = \sum_{k=1}^{K_{red}} \Omega_k \tag{2.92}$$

Once again, the number of independent configurations increases very rapidly with the solute concentration and the size of the supercell. However, if K_{red} allows for the calculation of the Gibbs free

energy for all the reduced configurations, the estimation of the reduced weights $\tilde{P}_k$ is done as follows:

$$\tilde{P}_k = \frac{\exp\left(-\dfrac{G_k - k_B T \ln \Omega_k}{k_B T}\right)}{\sum_{k=1}^{M} \exp\left(-\dfrac{G_k - k_B T \ln \Omega_k}{k_B T}\right)} \tag{2.93}$$

And the configurationally averaged properties:

$$H = \sum_{k=1}^{K_{red}} \tilde{P}_k H_k \tag{2.94}$$

$$V = \sum_{k=1}^{K_{red}} \tilde{P}_k V_k \tag{2.95}$$

$$S^{vib} = \sum_{k=1}^{K_{red}} \tilde{P}_k S_k^{vib} \tag{2.96}$$

$$\tag{2.97}$$

The configurational free energy G_{red} contains the ideal contribution and writes:

$$G_{red} = -k_B T \ln K - k_B T \ln \left(\frac{1}{K} \sum_{k=1}^{K_{red}} \exp\left(-\left(G_k - k_B T \ln \Omega_k\right)/(k_B T)\right) \right) \tag{2.98}$$

Then, the configurational entropy is obtained from H and G:

$$S = \frac{H - G_{red}}{T} \tag{2.99}$$

Chapter 3

Bonding regimes and superionic conduction in cubic water ice

Contents

3.1 Introduction

The determination of the phase diagram of the pure components is the first step toward the study of the $NaCl-H_2O$ mixture. While the phase diagram of NaCl is well known in the thermodynamic conditions of interest for this study, the phase diagram of water requires some investigations. The relations between the development of the superionicity and the dynamics of the hydrogen bond are still unclear especially at high temperature.

This chapter presents the properties and the phase diagram of the high-pressure pure water ices as found from our simulations.

We employ a $4\times4\times4$ supercell containing 128 H_2O molecules, initially arranged either in an ice VII or an ice X structure. The molecular dynamics simulations are performed in the isokinetic ensemble with a time step of 1 fs.

The published results from this chapter are presented as a stand-alone article at the end of this chapter.

3.2 Diffusion and electrical conductivity

Our starting point is the determination of the low temperature extent of the superionic regime. This goes through the calculation of the diffusion coefficients and of the total conductivity at moderate thermodynamic conditions at which limited experimental data are avalaible.

We calculate the diffusion coefficients of the oxygen (D_O) and hydrogen (D_H) atoms from their mean square displacements (details in Chapter 2). We distinguish the fluid phase (D_O and $D_H > 0$), the superionic regime ($D_O = 0$ and $D_H > 0$), and the nondiffusive regime ($D_O = 0$ and $D_H = 0$). Only the results corresponding to a fixed bcc sublattice of oxygen atoms ($D_O = 0$) are presented hereafter. Figure 3.1.a. shows the evolution of the hydrogen diffusion coefficient as a function of the oxygen-oxygen (OO) distance (the corresponding densities and pressures are given in Appendix B). In measurements, electrical conductivities greater than 1 $S.cm^{-1}$ are typically considered to characterize the superionic phases (Boyce and Huberman, 1979). Here we consider that finite and positive D_H indicates the superionic regime. Figure 3.1.b. shows that all the positive values of D_H yield conductivity greater than the threshold. The superionic regime expands to higher pressures as the temperature increases. Along all isotherms, the superionic regime is characterized by a transition from high values of D_H (e.g. 3.6×10^{-8} $m^2.s^{-1}$ at 2000 K), corresponding to low compression, to small values of D_H (less than 1.0×10^{-8} $m^2.s^{-1}$), corresponding to higher compression. We note that this transition is sharper at lower temperatures. The values of D_H are coherent with the ones found by French et al. (2010) in the fluid phase and with the ones of Goldman et al. (2005) in the superionic regime at 2000 K in their simulations starting from a solid initial configuration. At higher pressure (i.e. a smaller OO distance), H atoms diffusion stops altogether, marking the normal, nondiffusive regime. As expected, the limit between the superionic regime and the nondiffusive one moves upwards in pressure with increasing temperature.

Superionic conduction still exists at 1000 K between 20 GPa and 30 GPa and disappears completely

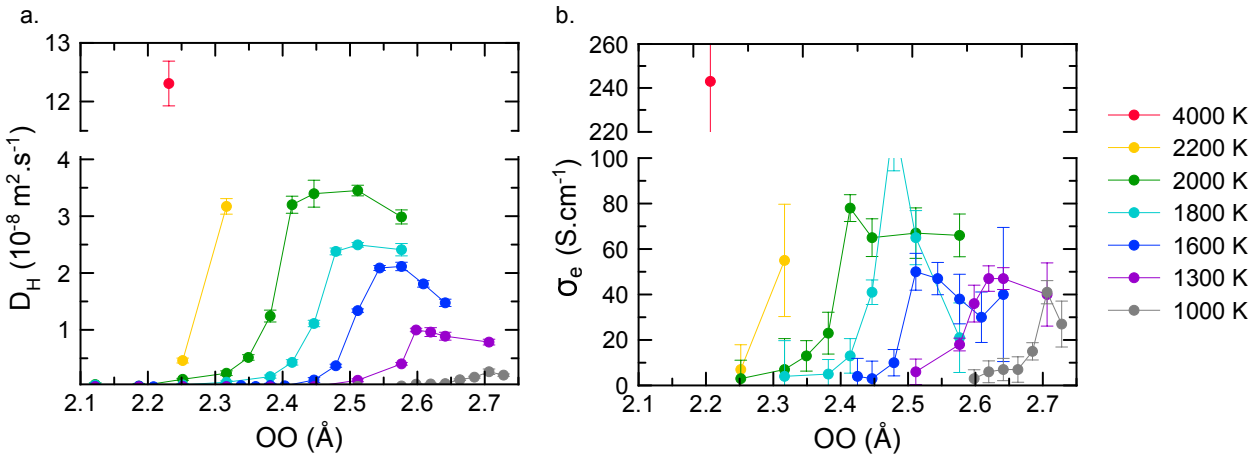

Figure 3.1: a. Diffusion coefficients of the hydrogen atoms (D_H) in solid ice ($D_O = 0$) as function of the OO distance. Superionic diffusion regime corresponds to positive D_H. The transition pressure to the superionic regime increases with increasing temperature. b. Corresponding electrical conductivities calculated from the current-current autocorrelations.

at 800 K.

The electrical conductivity obeys the same trend as the proton diffusion coefficients. At 2000 K, the transition between the two superionic regimes produces a change of 40 S.cm^{-1} in the electrical conductivity, and the maximum values reach 70-80 S.cm^{-1}. This magnitude agrees with the theoretical value of 140 ± 15 S.cm^{-1} at 3000 K and 3 g.cm^{-3} i.e. OO $\sim$ 2.34 Å (French et al., 2011), and the experimental value of 1 S.cm^{-1} obtained at 1000 K and 60 GPa (Sugimura et al., 2012).

3.3 Structure

Here we focus on the transition between the different bcc ices. This requires to determine accurately the positions of the protons in a high temperature environment. The visual inspection of the atomic trajectories allows first to exclude the simulations in which the oxygen sub-lattice has melted. It also gives a qualitative diagnostic of the localization degree of the atoms. Figure 3.2 shows that the protons are mainly localized along the $\langle 111 \rangle$ directions, and that the occupation of the octahedral sites becomes non-negligeable in the diffusion regime characterized by the highest proton diffusion.

3.3.1 Hydrogen bond symmetrization

We are looking for the phase transition between ice VII′ and ice X. We remind that ice VII′ is a characterized by a dynamical disorder caused by the translation of the protons from an acceptor to a

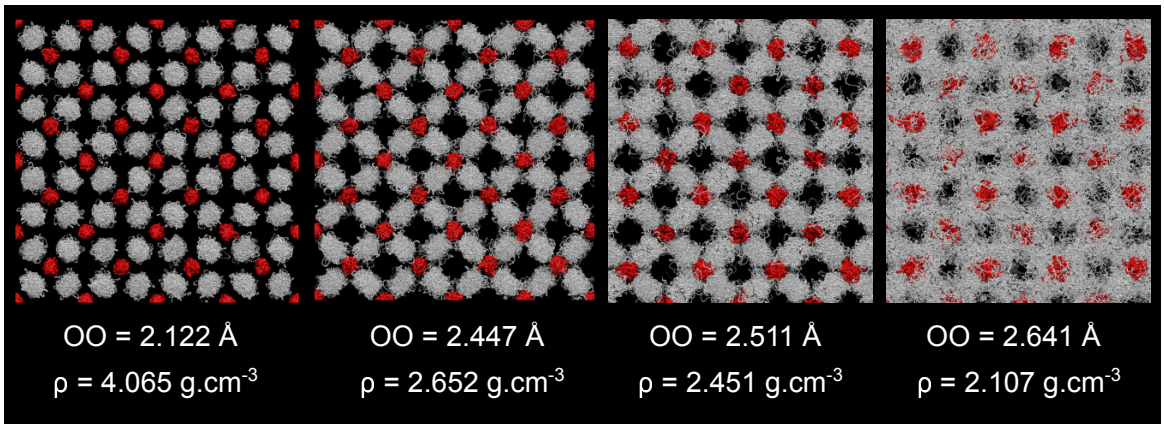

Figure 3.2: Behavior of the H (grey dots) and O (red dots) atoms along the 1300 K isotherm. a. Representation of the atomic trajectories in a supercell representing the simulation box during a 2.5-ps long run at different levels of compression.

donor O atom. This results in a bimodal distribution of the proton density along the O-O axis. Under compression the $O-H\cdots O$ bond becomes symmetric with a single maximum for the proton density at the middle of the OO distance, this is ice X. Hereafter, we present the different approaches we use to examine the symmetrization of the $O-H\cdots O$ bond.

3.3.1.1 Projection of the trajectories in one $O-H\cdots O$ triplet

First, we project the atom trajectories in one $O-H\cdots O$ triplet. Figure 3.3.a shows the projections obtained along the 1600 K. At this temperature the proton translation is always activated. At $\rho = 4.065$ g.cm^{-3} the proton density clearly presents a unique maximum halfway between the two oxygen atoms. Conversely, at $\rho = 2.549$ g.cm^{-3} the proton density distribution is clearly bimodal (ice VII$'$). In the two intermediate cases, the protons have a "cigar-like" shape (Benoit and Marx, 2005) and it is not possible to determine visually the number of maxima of the proton density without a quantitative analysis.

3.3.1.2 Radial distribution functions

Then, we compute the radial distribution functions $g_{OH}(r)$ and $g_{HH}(r)$ to describe the hydrogen bond symmetrization in more detail (Figure 3.4). At 300 K and low density, the lengths of the $O-H$ and $O\cdots H$ bonds are clearly identified by the positions of the first and second maxima of $g_{OH}(r)$. In $g_{HH}(r)$, the position of the first peak corresponds to the distance between the two H atoms of the water molecule; the position of the second peak is the distance between a given H atom and the H

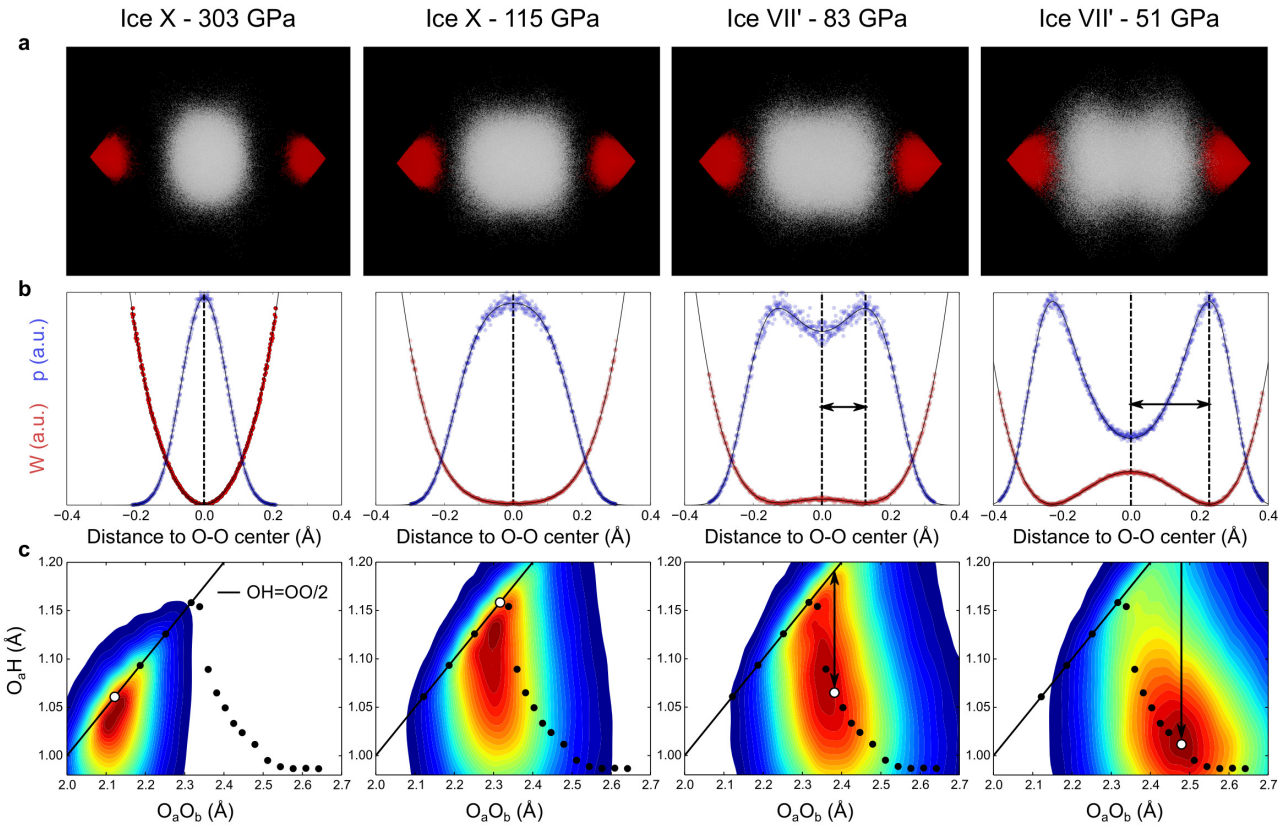

Figure 3.3: Pressure-induced symmetrization of the $O-H\cdots O$ bond at 1600 K. a. Projections of all nuclei positions along one $O-H\cdots O$ bond. Red and white dots correspond respectively to oxygen nuclei and hydrogen nuclei. b. Red: potential as function of the distance to the O–O center. Blue: corresponding proton density distribution. c. Colored areas represent the distribution $O_aH = f(O_aO_b)$ obtained from all the $O_a-H\cdots O_b$ bond of a simulation. Dark red indicates highest point densities. Black line corresponds to ice X. Dots allow to compare the three-body analysis with the two-body analysis results shown in b. and are placed as follow: x-coordinate is the average OO distance; y-coordinate is obtained by reporting the distance between one of the maxima of the proton density and the center of the O–O bond in b. This last distance is illustrated by the double-sided arrows in b. and reported in c. Black dots represent all the data obtained along the 1600 K isotherm.

atom of the neighbouring water molecule that forms the hydrogen bond. At high temperature (see right panel of Figure 3.4), the thermal agitation broadens the peaks and it becomes much harder to distinguish the different peaks. The onset of diffusion leads to very unstructured $g_{HH}(r)$.

Under compression, the first two peaks of both $g_{OH}(r)$ and $g_{HH}(r)$ merge together. This indicates the transition towards the symmetric state. However, the position of the maximum of this peak does not give the $O-H$ distance anymore. Although two H atoms account both for the first and the second coordination shell, the second shell has a larger volume than the first one resulting in a smaller density and thus a smaller intensity for the second peak. Therefore, when the two peaks merge the maximum of the sum of the two peaks is not half the OO distance. Such considerations have not

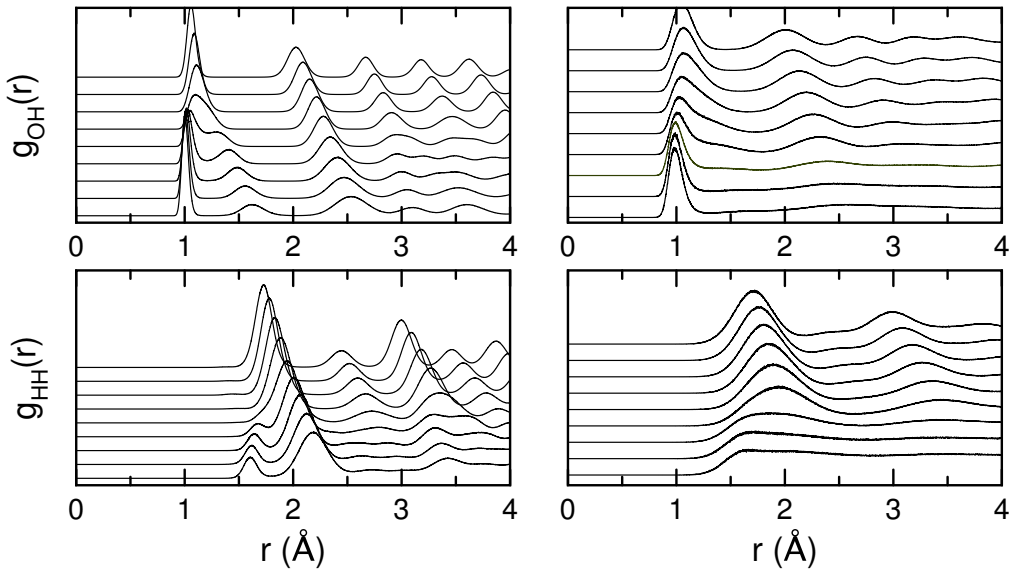

Figure 3.4: Radial distribution functions as function of compression. Left: T = 300 K. Right: T = 1600 K.

been taken into account by several theoretical studies in which the transition towards ice X is inferred based on the radial distribution function. This could explain why Goldman et al. (2005) find that the symmetrization is not complete at 115 GPa and 2000 K. Here, we use the radial distribution function $g_{OH}(r)$ to build a potential of mean force for the OH pair that we employ to model the proton distribution in an $O-H\cdots O$ bond.

3.3.1.3 Construction of a double well potential with the potential of mean force

From the OH pair distribution function ($g_{OH}(r)$) we extract the potential of mean force (see equation (3.1)) which is a spherically averaged 1D interaction pair potential between an oxygen atom and a hydrogen atom (Kirkwood, 1935).

$$W_{\alpha\beta}(r) = -k_B T \ln\left(g_{\alpha\beta}(r)\right) \tag{3.1}$$

Considering this approximation, the interaction potential $W(\delta)$ (with δ is the distance to the O–O center) of each H atom corresponds to the sum of the OH mean force potentials around each neighbouring O. $W(\delta)$ has two minima in the ice VII′ and only one in the ice X. The corresponding H distribution along the $O-H\cdots O$ bond ($p_H(\delta)$) is given by the equation (3.2).

$$p_H(\delta) = \exp\left(\frac{-W(\delta)}{k_B T}\right) \tag{3.2}$$

The potential $W(\delta)$ and the corresponding distributions of H are shown in Figure 3.3.b. In this model, the proton distribution is always symmetric with respect to $\delta = 0$. Therefore, ice VII and ice VII′ cannot be differenciated. However, we find that at $T > 800$ K the H translational disorder is activated at all pressures (see details in 3.3.3). Finally, in this approach the dynamics of the O-O bond is not considered here.

3.3.1.4 Description of O–H$\cdots$O from three-body interactions

In order to validate the 1D model based on the potential of mean force, we use a three-body analysis to evaluate the exact distribution of H atoms in the $O - H \cdots O$ bond. Such methods is more straightfoward but requires long trajectories and/or large supercells. At low temperature, several studies have been able to monitor the position of the H atoms along O-O axis based on the analysis of the atom trajectories (Benoit et al., 1998, 1999, 2002; Benoit and Marx, 2005; Bronstein et al., 2014). Initially, each H is associated to its two closest oxygen neighbors, and the analysis of the distance between each atom constitutive of the same initial triplet is followed along the trajectory. Such approach is optimal as long as no diffusion occurs in the system. In this study, the presence of H diffusion requires that we choose an instantaneous geometrical definition to define a $O - H \cdots O$ bonds. At each time step of the simulation, we identify the $O - H \cdots O$ triplets by first associating each H to its closest oxygen (O_a); the second oxygen (O_b) is the one minimizing the length of $O_aH + O_bH$. The distance O_aH is then compared to the O_aO_b distance. If the bond is completely symmetrized, the distribution presents a maximum along the line $O_aH = O_aO_b/2$. Such method allows to perform a structural analysis of the $O - H \cdots O$ triplets even when H atoms diffuse during the simulation.

Figure 3.3.c. shows that the two previously described approaches give similar results about the symmetrization of the $O - H \cdots O$ bonds. Consequently, for clarity reasons only the approach using the mean force potential is presented hereafter.

3.3.1.5 Results

As shown in Figure 3.5, the relation between OH and OO is described by three different regimes. For large OO distances, the OH distance remains almost constant under compression: this is ice VII″. This regime is not present at 300 K. As the OO distance decreases, the OH distance starts to increase: this is ice VII′. In this range the $O-H\cdots O$ bond is symmetrizing; i.e., the H continuously changes position approaching the fully symmetric state, halfway between the two O atoms. A fully symmetric $O-H-O$ bond is reached for OO distances between 2.31 and 2.35 Å: this is ice X. The beginning of the $O-H\cdots O$ symmetrization, namely, the transition between ice VII′ and ice VII″, corresponds to the abrupt decrease of the hydrogen diffusion, marked by dotted lines in Figure 3.1. The comparison of the degree of symmetrization of the $O-H\cdots O$ bond with the diffusion rate of the H atoms indicates that the transition between ice VII′ and ice X occurs in the superionic regime at 1800 K and above.

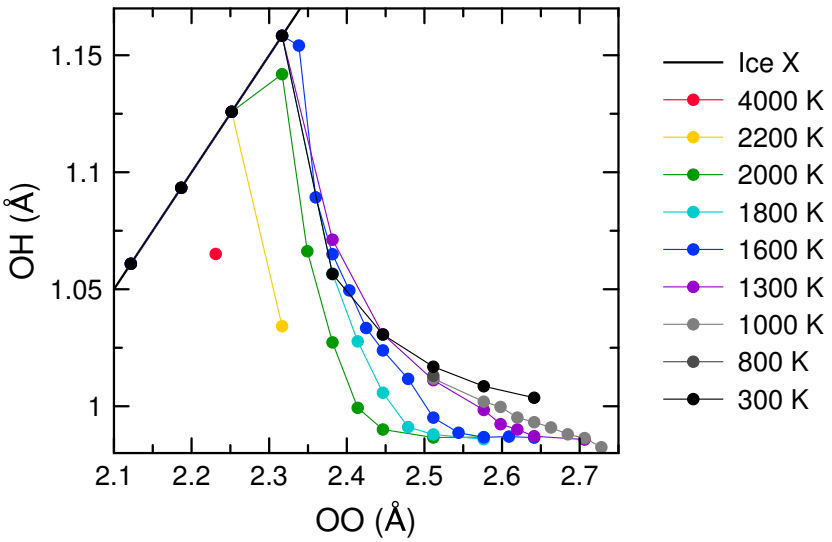

Figure 3.5: Variation of the position of H in the $O-H\cdots O$ bond under compression. Black line represents $OH = OO/2$, corresponding to ice X.

3.3.2 H delocalization out of the hydrogen bonds

We estimate the onset of delocalization of the protons out of the $O-H\cdots O$ bonds by calculating the distribution of the $O-H$ bond orientations. Stereographic projections of these distributions are presented in Figure 3.6. Maxima of the distributions correspond to the ⟨111⟩ directions along which $O-H\cdots O$ are arranged. The extreme distributions, for ice X and for the fluid, are not surprising:

they show respectively totally localized and totally delocalized H atoms. The various VII-like phases have distinct signatures. A delocalization is visible going from ice VII′ to superionic ice VII′ and finally to superionic ice VII″. In particular the latter shows a non-null probability of random orientation of the $O-H$ bonds due to the delocalization of the protons in the interstitial space.

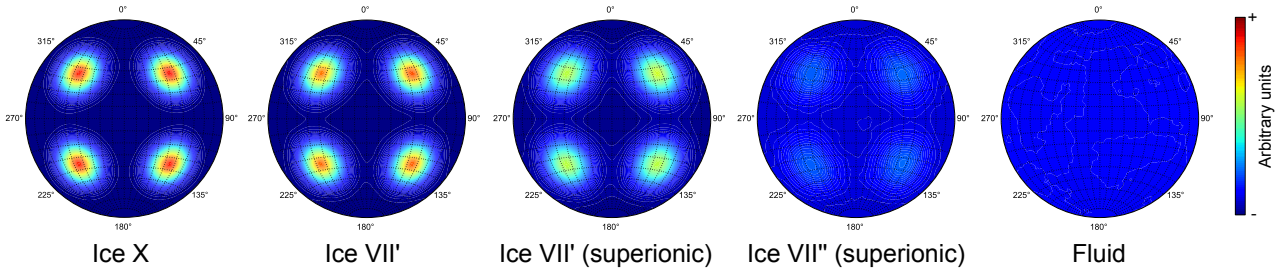

Figure 3.6: Stereographic representations of the spatial distribution of $O-H$ bond orientations along the 1600 K isotherm. Color scale is the same for the whole figure.

Close to the melting line at 600 K, in the domain of the predicted plastic ice, we obtain a distribution close to the one associated in ice VII′ in Figure 3.6. This indicates that the water molecules are not free rotors around the bcc positions. Thus, even if the molecules rotate, between two rotations the $O-H$ bond remains oriented towards the $\langle 111 \rangle$ directions. A details analysis of the bonding dynamics as described in 3.3.1.4 will allow to prove that the H_2O molecules efffectively rotate.

3.3.3 Bonding dynamics of the $O-H\cdots O$ bonds

Numerically, an ID number is attributed to all the atoms. This ID remains the same during the whole simulation. At a given time step and for a given H atom, we find the two closest O neighbors and store their ID number in a list. The first element of the list corresponds to the ID of the closest O and the second to the ID of the second closest O atom.

Looking at the time evolution of this 2-element list for a given H atom allows to characterize the bonding dynamics by defining two achievable "jumps" for the H. We define a translation as a change of closest O atom inside a given $O-H\cdots O$ for a given H atom. A change of $O-H\cdots O$ triplet for the H while keeping the same closest O is considered as a rotation of $O-H$. The simultaneous change of both first and second O neighbors does not occur. In the time sequence of the first and second O neighbors list, a translation appears as a permutation of the two ID numbers, and a rotation as a change of second element only. These identifications allow us to calculate the lifetime of the $O-H\cdots O$ bonds (oriented), of the $O-H-O$ triplets (unaffected by translations) and the lifetime of the $O-H$ bond.

Moreover, we also calculate the rates of translations and rotations, and their relative proportions.

Now, the identification of the remaining phases is possible. Ice VII is charactrized by the absence of both translations and rotations. Ice VII′ does present translations but no rotations. Plastic ice (Takii et al., 2008; Aragones and Vega, 2009), if it exists, should present only rotations. Superionic ices present both translations and rotations.

Following the time evolution of the defined $O-H-O$ triplets, we compute the rates of rotations and translations as well as the average lifetimes of the $O-H\cdots O$ bonds (oriented), of the $O-H-O$ triplets (unoriented), and of the $O-H$ bonds (see Appendix B for the lifetimes). Figure 3.7 shows that the different phases have distinct bonding regimes. Ice VII do not present any translation or rotation, and the lifetime of the different bonds is infinite in our simulations (see 300 K isotherm). Ice VII′ and ice X cannot be distinguished from this analysis. When not superionic, they are both affected by translations without rotations as the proton remains located within the half-diagonal of the bcc sub-lattice. Under compression the lifetimes of the covalent $O-H$ bonds and of the oriented hydrogen bonds decrease sharply down to ∼25 fs. At 600 K and low density, we identify the plastic ice: the analysis reveals that the rate of rotations is high (∼10 rotations per picosecond) while there is no translation. This is the mark of a dynamic orientational disorder. Moreover, we previously show that at these conditions the H atoms are not particularly delocalized out of the $O-H\cdots O$ triplets. Consequently, in plastic ice the water molecules do not rotate freely but only between positions verifying that the $O-H$ bonds are oriented along the $\langle 111\rangle$. Between two successive rotations the plastic ice behaves as ice VII. Above 1000 K the development of the superionicity is associated with the presence of both rotations and translations. Their relative proportion determines the efficiency of the diffusion and thus the superionic regime. In superionic ice VII′ and superionic ice X, the rate of translation is higher than the rate of rotations. The evolution of the rotation and translation rates is anticorrelated under compression. The superionic ice VII″ can be conceived as a plastic ice in which translations are permitted: the rotation rate remains constant under compression and is always higher than the translation rate. The proton diffusion coefficient tends to reach its maximum when the coupling between the rotations and the translations is the strongest, i.e. when the number of rotations is close to its maximum and when the number of translations starts to increase because of compression. In superionic ice VII″ the lifetime of the $O-H-O$ triplets and $O-H\cdots O$ bonds is extremely short (between 20 and 30 fs at all temperatures) but the lifetime of the covalent $O-H$ reaches its maximum

(∼100 fs for $T \geq$1300 K and up to 500 fs at 1000 K).

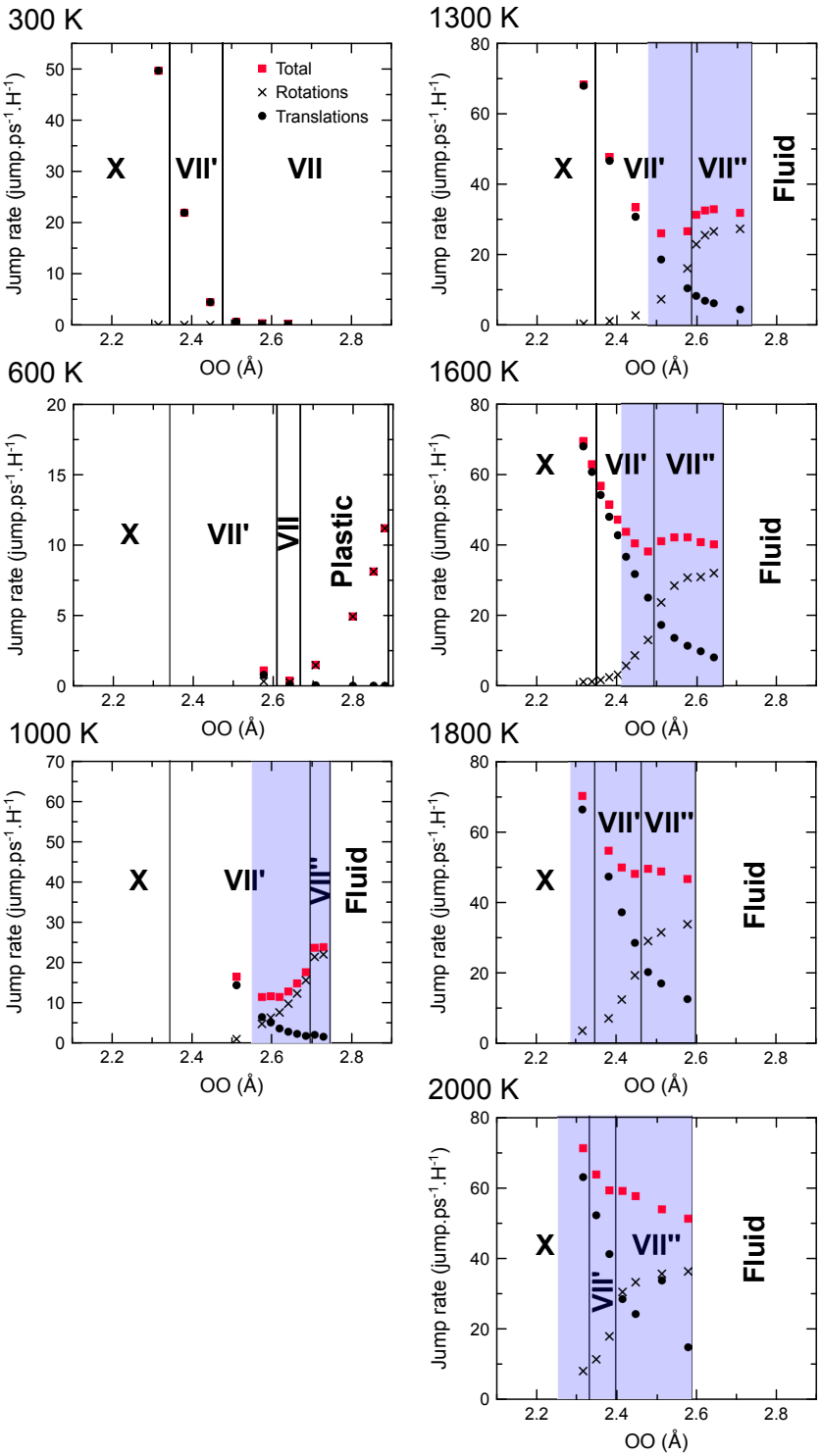

Figure 3.7: Evolution of the number of total jumps (red squares), rotations (black crosses) and translations (black dots) per hydrogen atom and per picosecond along several isotherms. The blue areas indicates the regions in which the ice is superionic, i.e. where D_H is statistically positive.

3.4 Speciation

3.4.1 From the atom trajectories

In the previous section we identify the different phases from the characterization of the bonding regimes based on our definition of a $O-H\cdots O$ bond. Here, we look at the speciation. Because of the short lifetimes of the $O-H\cdots O$ bonds at high temperature, we expect to describe transient exotic molecular species. In the literature, speciation has been studied (mainly in fluid water) from the trajectory of the nuclei, and several criteria have been proposed to define a bonding state. Schwegler et al. (2001) associate each H atom to its closest O neighbor. Consequently it defines instantaneous species and H^+ cannot be accounted for. Goldman et al. (2005) and Goncharov et al. (2005) use a cutoff radius around each oxygen and count the number of hydrogen atoms within this sphere. The cutoff radius is defined by the first maximum of the OH potential of mean force ($W_{OH}(r)$) and thus depends on the density. Applying this analysis along the 2000 K isotherm reveals that the fluid and the superionic ice VII″ are mainly composed of short-lived H_2O molecules (80 mol%), plus clusters containing up to six O atoms (from 10 to 30 mol%), as well as a small fraction of OH^- and H_3O^+ (∼5 mol%). Above 2.6 g.cm^{-3}, all these species tend to disappear in favor of larger species they denote as polymers (Goldman et al., 2005). Mattsson and Desjarlais (2006) and Goncharov et al. (2009) add a minimum lifetime of the molecular species in addition to the distance criterion. Mattsson and Desjarlais (2006) shows that the choice of the time and distance parameters is somehow arbitrary and highly influence the resulting speciation. Lastly, French et al. (2009) associate each H atoms to its closest O atom neigbor and add a bonding time criterion of 21 fs which represents the longest period of vibration of the water molecule.

We find that the last definition is the most efficient to discriminate the different phases we determined previously. Figure 3.8 shows the molar fractions of the corresponding molecular and atomic species along several isotherms.

The system only presents three major species: H_2O, O^{2-} and H^+. Each isotherm follows the same trend: at large OO distances, the molar fraction of H_2O is high, then it exponentially decreases down to zero while the fraction of O^{2-} and H^+ respectively increase up to 0.33 mol% and 0.66 mol% in ice X. Thus, from this approach, ice X is an ionic solid. The temperature affects the proportion of H_2O, O^{2-} and H^+ in the VII-like phases (ice VII and superionic ice VII″). In ice VII, the molar fraction of H_2O is one, indicating that the integrity of the water molecules is preserved. At 1000 K and above, the

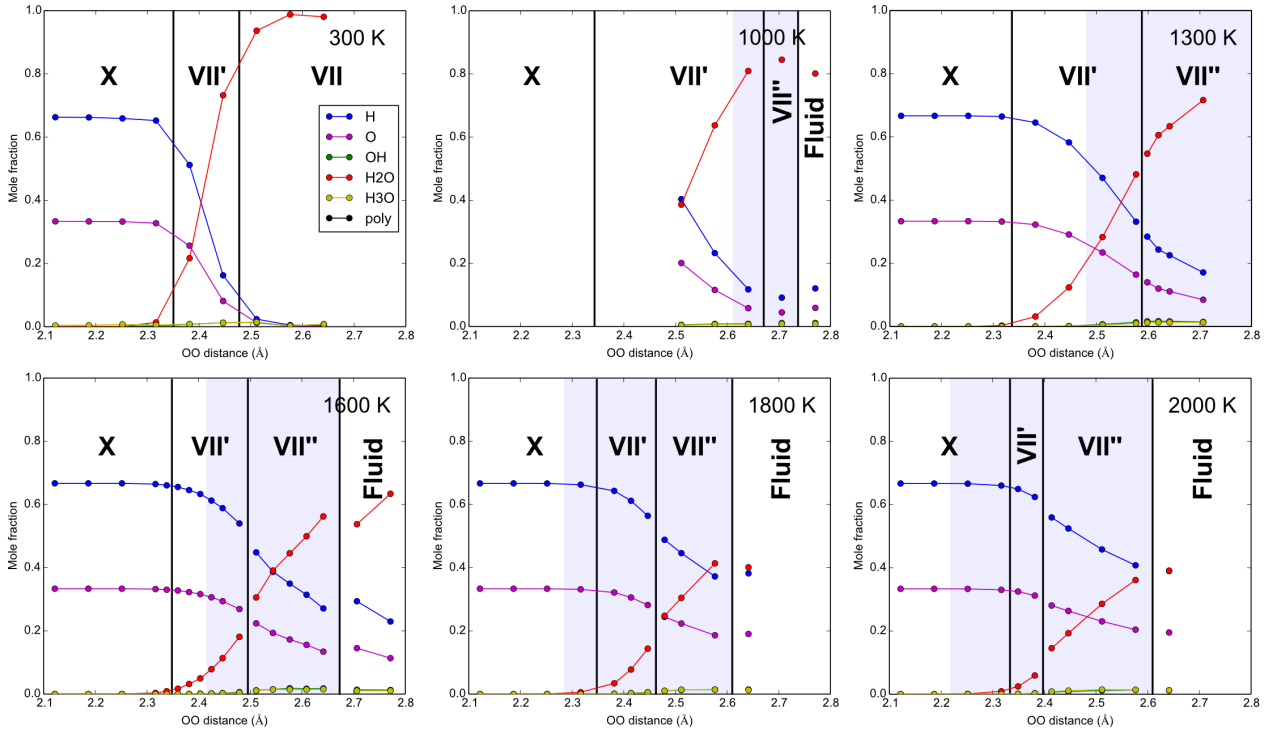

Figure 3.8: Molar fractions of the atomic and molecular species found in our simulations based on analysis of the atom trajectories and bond lifetime as defined in French et al. (2009). Discontinuities correspond to the first-order phase transitions (VII″–VII′ or fluid–VII″).

molar fraction of O^{2-} and H^+ increases with the temperature. This is coherent with the development of the superionicity and the presence of both translational and rotational events. Therefore, in ice VII″, the molar fraction of H_2O decreases linearly. At higher density when the first-order transition towards superionic ice VII′ is reached, the decrease becomes exponential.

3.4.2 From the charge density

In our *ab initio* calculations we compute the electronic structure at each time step of the molecular dynamics under the Born-Oppheimer approximation. We take advantage of it to evaluate the speciation along given molecular dynamics trajectories, by counting the number of nuclei in an isosurface of given charge density. In order to deal with a reasonable amount of data, we perform statistics over 30 configurations randomly sampled along a given MD trajectory. Consequently, this approach considers only instantaneous species but gives access to much bigger molecular species.

The first step consists in searching the volumes enclosed by the isosurfaces of a given charge density in a 3D grid (see Figure 3.9). We proceed as follows. All the points of the grid presenting a charge

density smaller that the threshold see their charge density set to zero. An iterative procedure attributes the index of the neighboring point with the highest charge density to each point presenting a non-null charge density. This procedure ends when all the points of a given volume present the same value. We take into account the periodicity. The positions of the nuclei are discretized in the charge density grid and compared to the positions of the volumes. The type and the number of nuclei within a given volume define the molecular species.

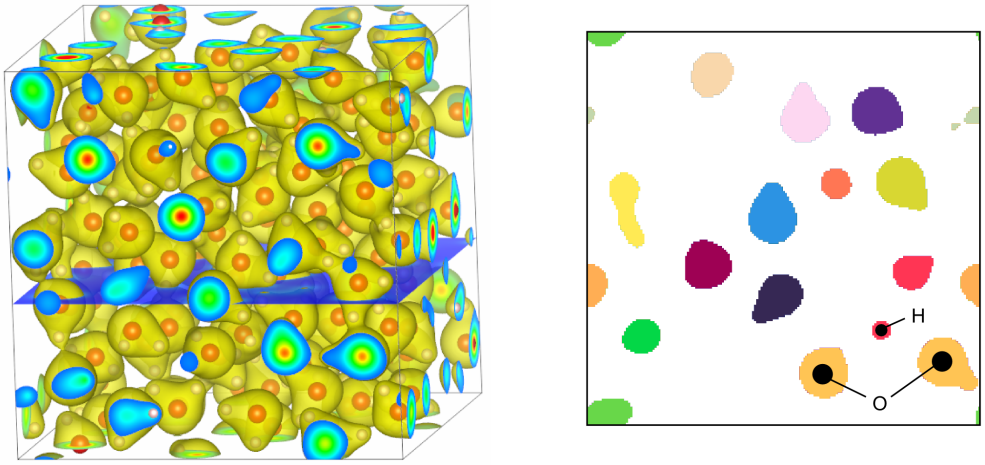

Figure 3.9: Left: Isosurfaces of a given charge density in the 3D grid corresponding to a fluid (yellow envelopes). Red and white spheres respectively represent the O and H atoms. Right: Slice of the 3D grid after the iterative procedure. Each color corresponds to a given volume enclosed in an isosurface. Black dots denote the positions of the nuclei within the slice.

Figure 3.10 presents the results of the application of this analysis to the 2000 K isotherm for different threshold values.

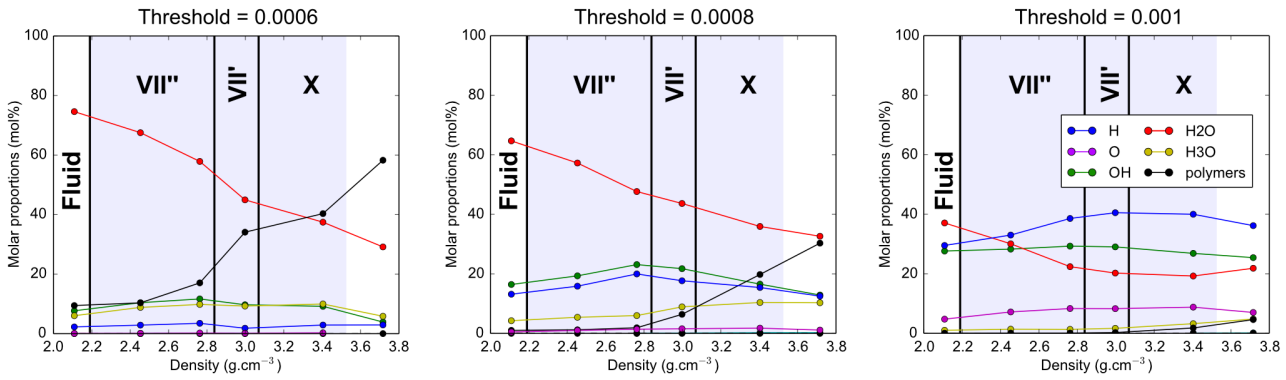

Figure 3.10: Mole fraction of the molecular or atomic species found from the electronic density analysis for different isodensity surfaces (thresholds) along the 2000 K. Here, polymers are defined as all the molecular species that contain two atoms or more.

The smaller is the threshold the larger are the volumes enclosed by the isodensity surfaces. Thus, the nature and the proportions of the molecular species highly depend on the chosen threshold, especially for the "polymers", which are defined as all the species composed of two O atoms or more. We find that a threshold of 0.0006 of the maximal charge density gives results in better agreement with the analysis of the atom trajectories. In this case, H_2O is the dominant species (the polymers represent several molecular species). The molar proportion of OH^- and H_3O^+ remains around 10 mol% at all densities. Atomic species are poorly represented (under 5 mol%). Separating the polymers into a first category with the molecular species containing between two and six oxygen atoms and another category with the bigger species reveals that between 2.6 and 3.6 g.cm^{-3} the first category represents the majority of the large molecular species. All other isotherms corresponding to a temperature higher or equal to 1000 K present the same behavior. This analysis notably reveals the covalent nature of the bonds in ice X. Ice X is often perceived as an ionic ice as it results from the dissociation of the H_2O molecules, but the electron localization function (Becke and Edgecombe, 1990) shows that it is a covalent crystal. Although ice X is insulating, the covalency together with the high-level of symmetry make it a good candidate for a high-temperature superconductor when doped. Recently, it has been predicted that nitrogen-doped ice X becomes superconducting at 60 K and 150 GPa (Flores-Livas et al., 2016).

3.5 Elasticity

The existence of a VII″ phase and the transition between ice VII′ and ice VII″ are obvious when computing the pressure variation of the elastic properties. Figure 3.11 shows the elastic constants at several temperatures as a function of pressure. In ices X and VII′, all elastic constants decrease with decreasing pressure (increasing OO distance). The slopes are different for each constant, and they are not affected by the development of the superionic regime. C_{12} approaches C_{11} consistently with the development of elastic instabilities observed at 0 K (Caracas, 2008; Journaux et al., 2014). The transition between the VII″ phase and ice VII′ appears very clearly in the diagram: there is a dip in the pressure variation of the C_{11} and C_{12} elastic constants, exactly at the transition pressure, at all temperatures. The dip shows a clear change in the elastic behavior of H_2O ice during the transition from the VII″ phase into ice VII′. Similar behavior is observed in other elastic phase transitions, like stishovite and hollandite (Carpenter et al., 2000; Ballaran et al., 2009). In the transformations of H_2O ice, because the oxygen sublattice is not affected, the elastic transition must be only induced

by a change of the localization degree of the H atoms in the superionic regime. As the OO distance increases, the H becomes more and more delocalized; they are less confined to a linear $O-H\cdots O$ triplet. They can move more freely around the O atoms while still preserving the weak $H\cdots O$ bonds that hold the structure together. This is the mark of the superionic ice VII″ phase.

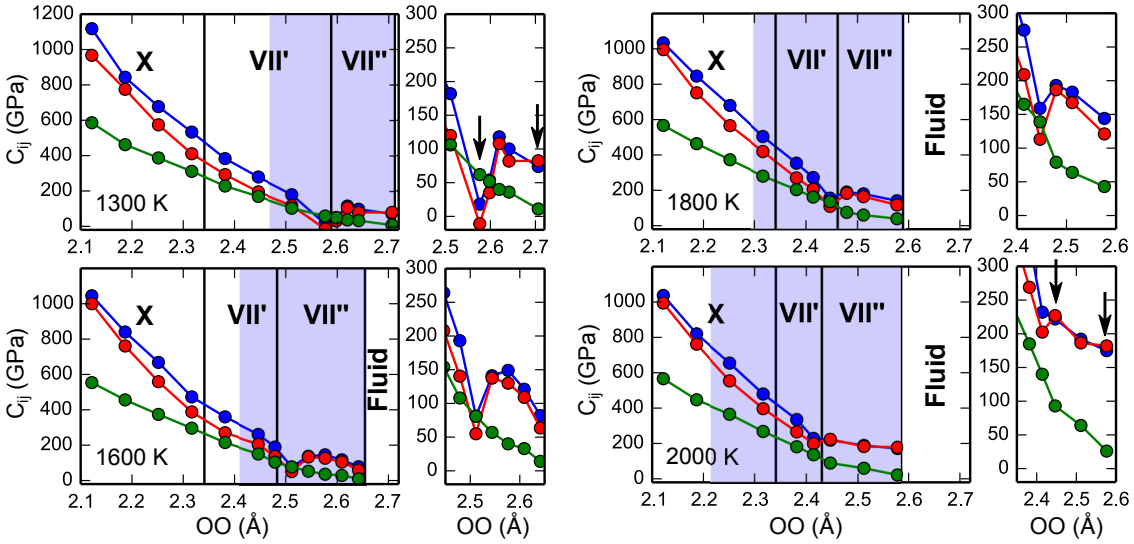

Figure 3.11: Elastic constants calculated along the 1300 K, 1600 K, 1800 K and 2000 K isotherms. C_{11}, C_{12}, and C_{44} are, respectively, represented in blue, red, and green. In the left panels, the stability fields of the different phases are separated with the black vertical lines, and the pale blue area corresponds to the superionic regime. Right panels are zooms of the transition region between the VII″ phase and ice VII′. Black arrows show the conditions in which the Born criterion is not respected.

Figure 3.12 shows the elastic moduli and the elastic wave velocities as a function of compression (see equations (3.3) to (3.6)). We compute the bulk modulus κ_v and the shear modulus μ_v according to the Voigt expression.

$$\kappa_v = \frac{C_{11} + 2C_{12}}{3} \tag{3.3}$$

$$\mu_v = \frac{C_{11} - C_{12} + 3C_{44}}{5} \tag{3.4}$$

$$v_P = \sqrt{\frac{\kappa_v + \frac{4}{3}\mu_v}{\rho}} \tag{3.5}$$

$$v_S = \sqrt{\frac{\mu_v}{\rho}} \tag{3.6}$$

As expected from the elastic constants, the transition between the ice VII″ and the ice VII′ is respectively marked by a dip and a plateau in the P- and S-wave velocities. Then, at higher pressure

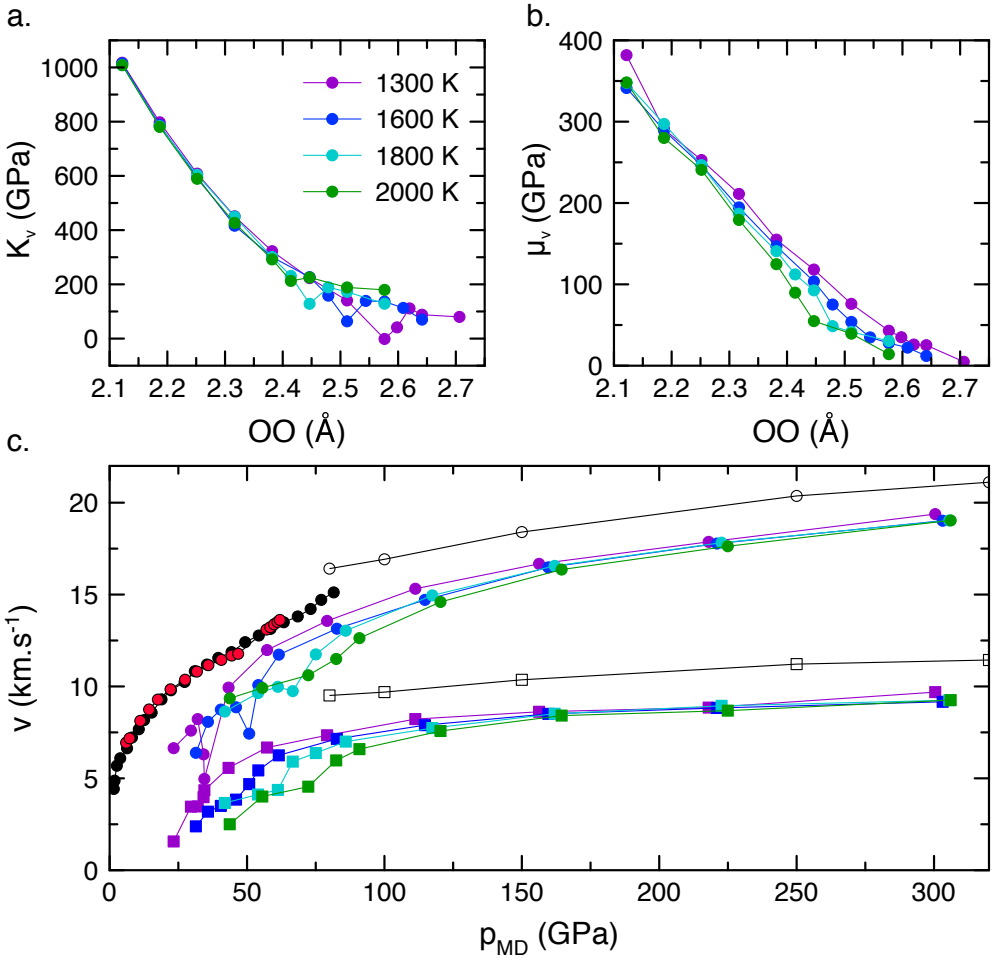

Figure 3.12: a. Bulk modulus. b. Shear modulus. c. Elastic wave velocities as function of the pressure. Dots and squares respectively correspond to the P and S wave velocities. The color code is the same as in a. and b. for our results. We compare the computed high-temperature v_P and v_S with DFT calculations at 0 K (Journaux et al., 2014), and experimental Brioullin spectroscopy measurement of v_P at 300 K from Asahara et al. (2010) (red dots) and Ahart et al. (2011) (black dots).

the velocities align progressively with the trend predicted in ice X at 0 K (Journaux et al., 2014). The temperature decreases the propagation velocities of the elastic waves. Experimental measurements at 300 K (Asahara et al., 2010; Ahart et al., 2011) agree very well with the the theoretical estimations based on calculations at 0 K and 1300 K.

3.6 Vibrational density of states

3.6.1 Vibrational spectra at 300 K: mode assignment

Here we present the total vibrational density of states obtained at 300 K between 20 and 300 GPa. At ambient temperature anharmonicity is relatively low, the vibrational modes appear clearly and do not overlap too much. For this reason, we use the vibrational spectra computed at 300 K to identify the different vibrational based on the phonon dispersions in ice X calculated by Caracas (2008) and based on the experimental work of Song et al. (1999)).

In the range $0-800$ cm^{-1}, the translational modes present a clear signal at all pressures. The lowest frequency mode tends to shift to low frequencies as the pressure increases corresponding to the development of the instability of the triply degenerate T_{1u} LO mode at the high-symmetry point M of the ice X structure prior to the transition to the predicted orthorhombic *Pbcm* phase (Caracas, 2008). In the middle frequency range ($800-2500$ cm^{-1}), the rotational modes (ν_R and $\nu_{R'}$) appear as two broad peaks in the ice VII stability field. Their frequencies increase under compression and reach constant values in ice X as they account for the distortional mode ν_D. The bending mode ν_2 presents a constant frequency at all pressures. It merges with the rotational mode $\nu_{R'}$ in ice X. At high frequency (> 2500 cm^{-1}), we observe the softening of the stretching modes ν_1 and ν_3 up to a minimum at the ice X transition, as well as the frequency increase of the mix modes $\nu_2+\nu_R$ and $2\nu_{R'}$. In ice X we retrieve the A_{2u} and T_{1u} TO modes as predicted by Caracas (2008).

3.6.2 Comparison with the high-temperature vibrational densities of states

As shown by Figure 3.14, at high temperature the thermal agitation results in broadening of the frequency range sampled by a given mode.

At high temperature, ice X and ice VII′ present the same behavior as at 300 K. The position of the minimum in the stretching mode frequency agrees with the pressure transition found from our $O-H\cdots O$ bonding analysis (cf. 3.3.1.5). In the VII″ and the plastic phase, the frequency of the stretching modes does not change under compression. This is in agreement with the delocalization of the $O-H$ bonds out of the O–O axis, and with the high compressibility (small bulk modulus) of these phases. In the plastic phase at 600 K, the rotational modes move down to low frequencies and tend to overlap the translational modes. In the superionic phases, the zero-frequency component of the vibrational spectra becomes non-null due to the H diffusion. The partial VDoS (at 1600 K and

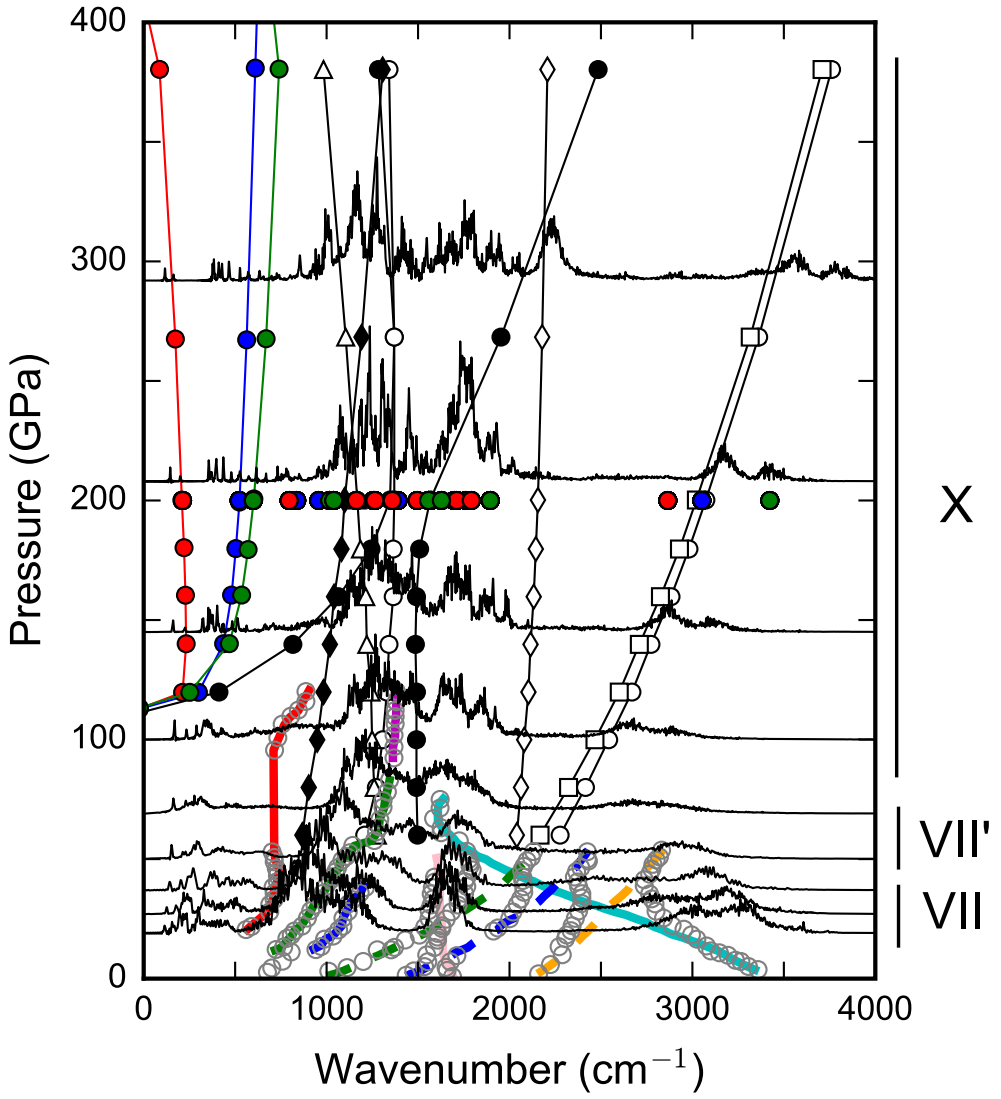

Figure 3.13: Computed vibrational densities of states at 300 K between 20 and 300 GPa (thick black lines). Thin black lines with markers correspond to normal modes frequencies calculated in ice X by Caracas (2008) in Γ: T_{1u} LO (black dots), T_{1u} TO (white dots), A_{2u} (white squares), E_u (white diamonds), T_{2g} (black diamonds), T_{2u} (white triangles). Thin colored lines with markers refer to T_{1u} LO modes frequencies calculated in ice X by Caracas (2008) in X (blue dots), M (red dots) and R (green dots). Colored dots at 200 GPa correspond to all the normal modes frequencies calculated in X (blue), M (red) and R (green). Colored thick continuous lines are normal modes frequencies from Song et al. (1999) based on IR measurements (gray circles): $\nu_{1,3}$ stretching modes (cyan), ν_2 bending mode (pink), $\nu_{R'}$ (blue) and ν_R (green) rotational modes, ν_T translational mode (red), and ν_D distortional mode (magenta). Finally, colored thick dashed lines are mode mixing frequencies from Song et al. (1999): $\nu_2 + \nu_R$ (orange), $2\nu_R$ (green), and $2\nu_{R'}$ (blue).

2000 K in Figure 3.14) show that only the H vibrational spectra present a non-null intensity at $\nu = 0$. However, it affects the total density of states, especially for the superionic ice VII″ whose translational modes are hidden by the H atom low frequency component. Consequently, the vibrational spectra of

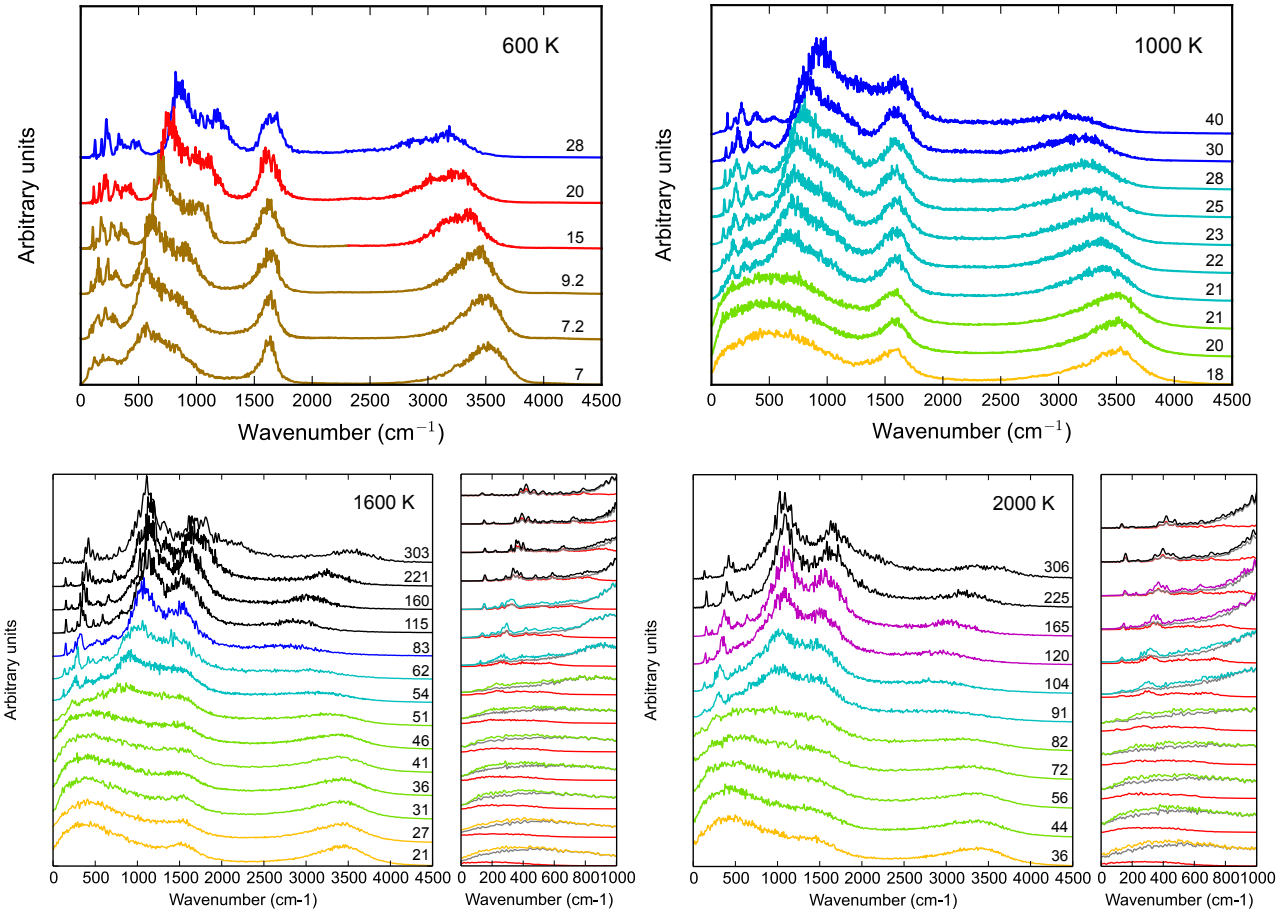

Figure 3.14: Vibrational spectra at 600 K, 1000 K, 1600 K and 2000 K. Corresponding pressures (p_{MD}) are indicated in gigapascals for each spectrum. Each color represents a phase: orange = fluid, brown = plastic, green = superionic ice VII″, cyan = superionic ice VII′, blue = ice VII′, magenta = superionic ice X, black = ice X. Right panels are zooms of the low frequency part of the 1600 K and 2000 K spectra. From the oxygen (red curves) and the hydrogen (grey curves) component of the vibrational spectra, they shows that the non-zero intensity at the zero frequency is only due to H in superionic regime and is due to both O and H in the fluid phase.

the superionic ice VII″ is very similar to the one of the fluid. Such feature may have been interpretated as a melting signature in experimental measurement based on vibrational spectroscopy.

3.7 Thermodynamics

We finish the analysis of the H_2O ice by presenting the thermodynamics of the phases described previously.

3.7.1 Internal energy

As described in Chapter 2, we apply a quantum correction u_{qc} to the specific internal energy obtained from the molecular dynamics simulations u_{MD} in order to account for nuclear quantum effects. This correction is based on the decomposition of the vibrational density of states of the total system into its sub-components that are the atom species and their diffusive and solid components. Figure 3.15.a. presents the magnitude of the internal energy correction along several isotherms.

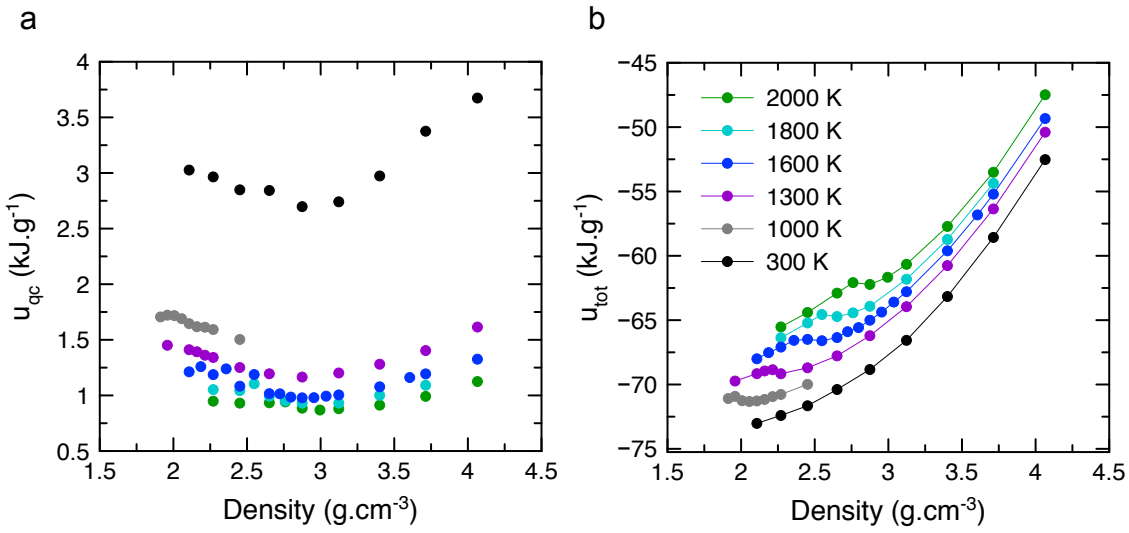

Figure 3.15: a. Quantum correction for the internal energy obtained from the 2PT-MF model. b. Quantum corrected internal energy u_{tot} under compression. The color code is the same for all the figure. Only data for the solid phases are presented here ($D_O = 0$).

As expected, the quantum correction increases at high density and decreases at high temperature. It presents a minimum between 2.75 g.cm^{-3} and 3 g.cm^{-3}. At 300 K and 4 g.cm^{-3}, u_{qc} accounts for 6 % of the total internal energy. This falls at 3.5 % at 3 g.cm^{-3}. At 2000 K and 4 g.cm^{-3}, it represents 2.3 %, and it reduces to 1.4 % at 3 g.cm^{-3}. Our results are in perfect agreement with the corrections found by French and Redmer (2015) and French et al. (2016).

Figure 3.15.b. gives the total internal energy along each isotherm. The transition between the superionic ice VII″ and the superionic ice VII′ is clearly associated with a sharp discontinuity above 1000 K. This is the mark of a first-order transition. We identify another discontinuity at lower density associated with the melting of the oxygen sub-lattice.

3.7.2 Entropy and free energy

The estimation of the Gibbs free energy is essential to investigate the stability of the NaCl·RH$_2$O system. The first step is the calculation of the entropy with the 2PT-MF model. Below 4000 K the ice is electronically insulating, and the total entropy of the system is the vibrational entropy. Figure 3.16 shows the comparison between our calculated entropies and the analytical expressions. These expressions are derived from the thermodynamical potential constructed for the ices VII and X (French and Redmer, 2015), and for the *superionic ice* (French et al., 2016) that we denoted as ice VII″ (Hernandez and Caracas, 2016). In their study, French et al. (2016) do not distinguish the different superionic regimes as they focus on much higher temperatures and densities (respectively up to 10000 K and 14 g.cm^{-3}).

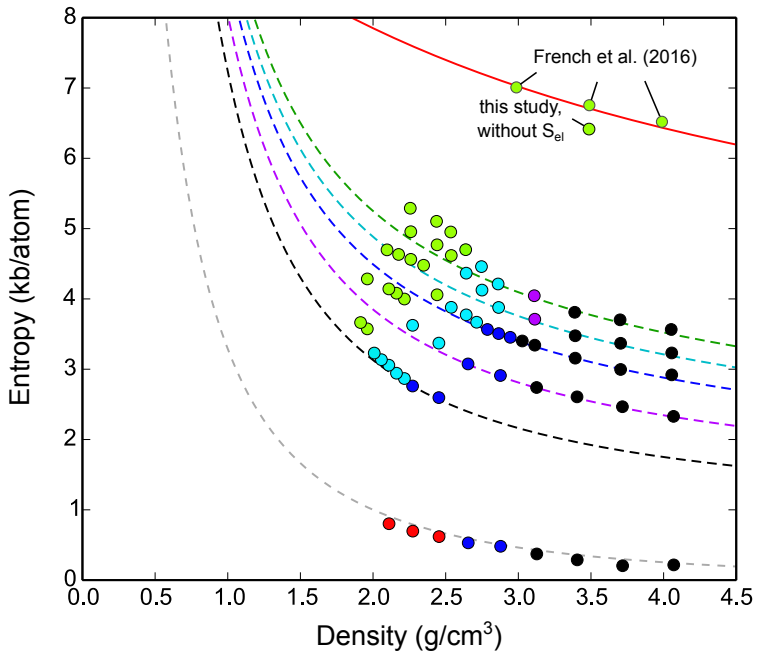

Figure 3.16: Entropy of ice under compression and heating. Dots represents our calculated entropies from the 2PT-MF model. They are colored according to the different phases: green = superionic ice VII″; cyan = superionic ice VII′; blue = ice VII′; magenta = superionic ice X; black = ice X; red = ice VII. The curves corresponds to the thermodynamical models derived for the ices VII/X (dashed lines, French and Redmer (2015)) and for the *superionic ice* (continuous lines, French et al. (2016)). Each color represents an isotherm: gray = 300 K; black = 1000 K; magenta = 1300 K; blue = 1600 K; cyan = 1800 K; green = 2000 K; red = 4000 K.

The entropy decreases under compression and increases with the temperature. At 300 K, the entropy varies continuously although we add the configurational component in ice VII to account for the static orientational disorder. At 1000 K and 1300 K, the entropy presents a sharp dis-

continuity at the first-order transition between the superionic ice VII′ and the VII″ phase. At higher temperature the transition is smoothened. The agreement between the two analytical expressions and the ices VII/X and VII″ is excellent. Nevertheless, we note that the superionic ice VII′ (cyan dots on Figure 3.16) seems to have its own regime as for each isotherm it lies between the two fits.

The Helmholtz free energy is obtained straightfowardly from the internal energy and the entropy (shown in Figure 3.15.b and Figure 3.17). The Gibbs free energy requires an estimation of the pressure. Although we take into account the external isotropic pressure and the thermal pressure in p_{MD}, the quantum correction for the NQEs associated with u_{qc} is missing. This is inconsistent with the other variables. Therefore, we choose to not use p_{MD} to compute the Gibbs free energy. Instead, we fit separately the Helmholtz free energy on the two sides of the discontinuity marking the first-order transition, at each isotherm. Then, we obtain the specific Gibbs free energy as function of the density from:

$$g(\rho, T) = f(\rho, T) + \rho \left(\frac{\partial f(\rho, T)}{\partial \rho} \right)_T \tag{3.7}$$

Finally, the Gibbs free energy is numerically expressed as a function of the pressure which is calculated from:

$$p(\rho, T) = \rho^2 \left(\frac{\partial f(\rho, T)}{\partial \rho} \right)_T \tag{3.8}$$

Figure 3.17 shows the free energies obtained from our simulations and compares them with the thermodynamical potentials recently constructed by French and Redmer (2015); French et al. (2016) for the ices VII/VII′/X and for the superionic ice VII″. The agreement is very good. Here, we do not pretend to construct such consistent thermodynamical potential which an extremely challenging task. We fit the high-pressure part of the Helmholtz free energy for each isotherm individually with a Vinet equation of state (Vinet et al., 1986). This allows us to obtain a continuous expression that we use to calculate the pressure and the Gibbs free energy, shown in Figure 3.17.b. For the ice VII″ we are limited by the small range of densities and the smaller number of data points. Thus, we fit only the Helmholtz free energy for the 1300 K, 1600 K and 2000 K isotherms.

Finally, we have the Gibbs free energy as a function of the pressure at 300 K, 1300 K, 1600 K, 1800 K and 2000 K for the ices VII, VII′ (both superionic and normal) and X (both superionic and normal). Concerning the VII″ phase, we express the Gibbs free energy for the 1300 K, 1600 K and 2000 K

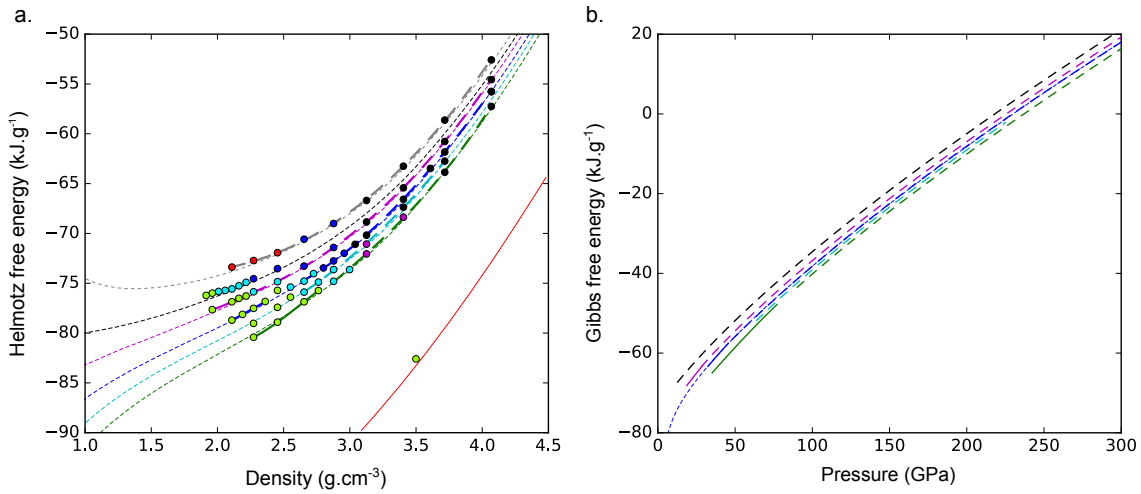

Figure 3.17: a. Helmholtz free energy as function of density. Dots represent our data points and are colored with respect to the phase with the same color code as in Figure 3.16. Thin dashed and continuous curves are the thermodynamical potentials respectively from French and Redmer (2015) for the ices VII/VII′/X and from French et al. (2016) for the *superionic ice* (VII″ phase in Hernandez and Caracas (2016)). Thick dashed and continuous lines represent our fits for the high-pressure side of the discontinuity and for the superionic ice VII″. The lines are colored according to the temperature as in Figure 3.16. b. Gibbs free energy as a function of the pressure. The same legend as a. applies. Only the 1600 K of the Gibbs free energy of the ices VII/VII′/X from French and Redmer (2015) appears (blue thin line) in order to not overwrite the figure.

isotherms. The thermodynamic treatment presented above represents the fundamental basis for the investigation of any binary system involving bcc water ice at high temperature. The changes and discontinuities in free energy correspond perfectly well to the changes and discontinuities observed in the bonding regimes, diffusion, and elasticity analysis showns in the begining of this chapter. In the next chapter, we investigate the $NaCl - H_2O$ binary at 1600 K as this is the temperature for which we have the most complete set of parameters.

3.8 Phase diagram and conclusion

In this chapter, we have investigated the phase diagram of pure water in the high temperature stability domain of bcc ices where the different phases are solely determined by the behavior of the protons (Figure 3.18). Here we show by coupling different analysis that multiple bonding regimes develop depending on the temperature and on the compression. We look at the structure and the dynamics of the $O - H - O$ triplets. We define two types of dynamical events for the triplets: a rotation is a change of $O - H \cdots O$ bonds for a given $O - H$ bond; a translation is a change of closest

oxygen for the proton inside a $O - H \cdots O$ triplet.

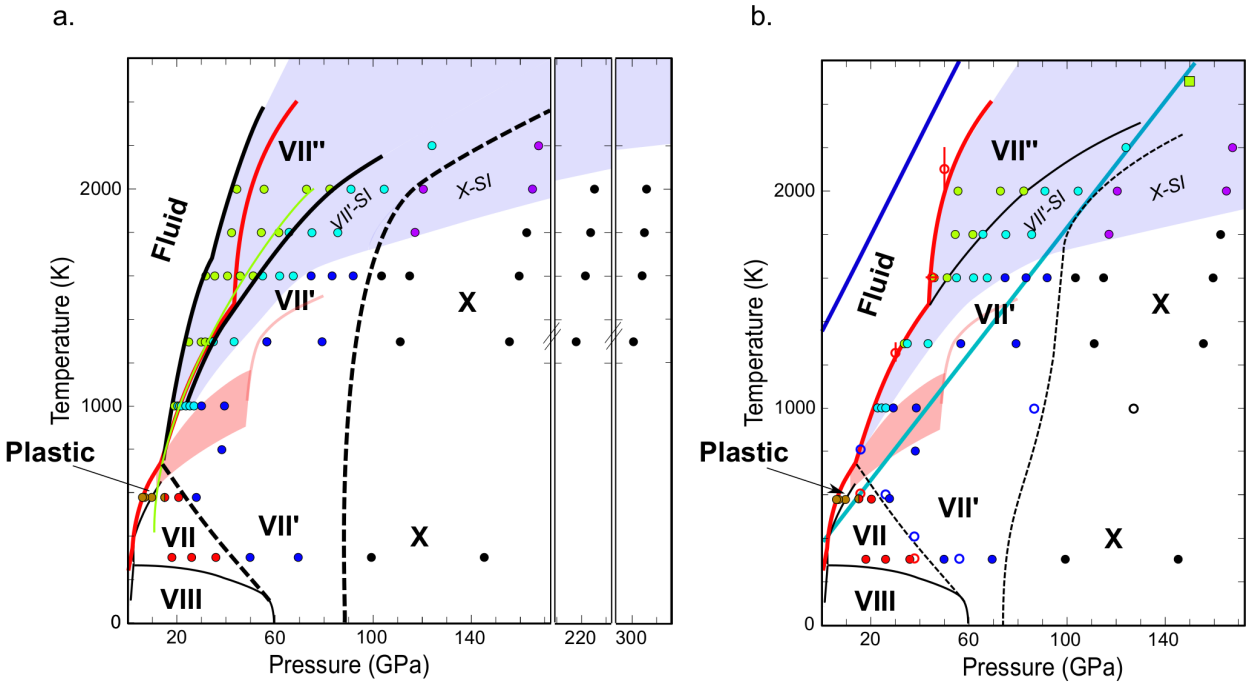

Figure 3.18: a. Phase diagram of bcc ices as obtained from our simulations. Dots correspond to the data points of this study and are colored according to the different phases or regimes. Continuous lines correspond to first-order phase transitions, and dashed line to second (or higher) order phase transitions. The pale blue area represents the superionic domain. Red lines refers to the high-temperature and low-temperature melting curves described in Chapter 1. b. Phase diagram of bcc ices when including results from other studies to accentuate the phase boundaries (open circles from French and Redmer (2015), green square from Cavazzoni et al. (1999)). Because of overheating effects (see text) we remove the data point that are on the low-pressure side of the high-temperature melting curve. The blue and cyan lines respectively represent the isentropes of Neptune (Redmer et al., 2011) and of a five terrestrial mass H_2O-rich exoplanet (Sotin et al., 2007).

At 300 K, we retrieve the ice VII – ice VII′ – ice X transition sequence. Below 40 GPa, ice VII does not present any translations or any rotations. Between 40 GPa and 100 GPa, ice VII′ is identified by a continuous increase of the translation rate. At higher pressure in ice X the $O - H - O$ bond is symmetrized, and the electron localization function shows a strongly covalent behavior of the whole crystal. At 600 K close to the melting line we find a dynamical orientational disorder with a high rate of rotations without any translation. This is the mark of the plastic ice predicted from classical molecular dynamics studies (Takii et al., 2008; Aragones and Vega, 2009; Himoto et al., 2011, 2014). The water molecules are intact and rotate around the oxygen atom so that the hydrogen atoms are oriented along the half-diagonals of the bcc oxygen sub-lattice. Under compression, the rate of rotation decreases down to zero while the rate of translations remains null. This indicates a transition

between the plastic ice and the ice VII. At 600 K, the extent of the ice VII stability domain is largely reduced, and at 25 GPa ice VII′ is reached as the proton translation is activated. The ice VII domain closes around 750 K corresponding to a kink in the melting curve measured by several experiments (Schwager et al., 2004; Schwager and Boehler, 2008; Klotz et al., 2010; Ahart et al., 2014). Above this temperature, the translation of the proton is always activated. Consequently if the thermodynamic conditions also allow for the rotations then the protons diffuse, and the ice becomes superionic (blue areas on Figure 3.18). We limit the stability domain of the solid phase with the theoretical and experimental high-temperature melting curves of Schwegler et al. (2008); Ahart et al. (2014) as it is known that our one phase simulations overheat the solid. Between 800 K and ∼1500 K we find a superionic regime close to the melting line that presents a moderately high rate of rotations and whose protons remain highly localized within the hydrogen bonds between two consecutive rotations. The hydrogen bonds are symmetrizing, the proton diffusion and the rotation rate continuously decrease under compression, and the thermodynamic variables are continuous to those of the ice VII′. Therefore, we consider this regime as a superionic ice VII′. At 1500 K, a second kink in the melting line is associated with the opening of the stability domain of the superionic ice VII″. This phase presents a first-order phase transition with the superionic ice VII′ that remarkably affects the elastic properties. The rate of rotation plateaus at a very high value (30-40 rotations per picosecond per H atom) whereas the rate of translation is always lower but increases under compression. The rotational energy is so high that the protons are largely delocalized out of the ⟨111⟩ directions. Such combination of rotations and translations produces the highest diffusion coefficients. An analysis of the speciation in ice VII″ reveals that it is mainly composed of short-lived H_2O molecules which is in agreement with previous studies (Goldman et al., 2005; Goncharov et al., 2005; Goncharov and Crowhurst, 2007; Goncharov et al., 2009). Finally, at 1800 K and above, the complete symmetrization of the $O-H-O$ bonds occurs in presence of superionic diffusion.

The strong change of bonding regime associated with the VII″ to superionic VII′ transition is analogous to the plastic ice to ice VII transition: it corresponds to a stronger localization of the proton within the hydrogen bond along the ⟨111⟩ directions. The extrapolation of the high-pressure boundary of the ice VII″ at lower temperature corresponds to the melting line between the two kinks. At still lower temperature, it goes through the tricritical point between the plastic ice and the ice VII. Its extrapolation down to 300-400 K corresponds to pressures of 10-14 GPa where anomalies have been observed for two decades in a variety of experiments measuring diffusion,

electrical conductivity, vibrational properties etc. From Raman spectroscopy Pruzan et al. (2003) observes a minimum of the width of the ν_1 vibrational mode and a softening of ice VIII translational modes. X-ray and neutron diffraction experiments (Somayazulu et al., 2008; Nelmes et al., 1998) both reveal a plateau in the c/a ratio at the same pressure in ice VIII. Additionally, electrical conductivity and proton diffusion reach a maximum around 10 GPa in ice VII (Okada et al., 2014; Noguchi and Okuchi, 2016). Based on the yield of the X-ray-induced photo-dissociation of H_2O, Fukui et al. (2016) propose that a change of charge transport mechanism occurs at 14 GPa with transition from H_2O rotations to double-well hoping of the protons. We propose that all these phenomena are related to a stronger localization in the hydrogen bonds that locks the rotational dynamics.

In the framework of all our findings presented in this chapter, it is remarkable that all the order-disorder types are achieved in bcc ice: static orientational (ice VII), dynamic orientational (plastic ice), dynamic translational (ice VII′), mainly dynamic orientational and to a lesser extent dynamic translational (superionic ice VII″), mainly dynamic translational and to a lesser extent dynamic orientational (superionic ices VII′ and X), no disorder and $O-H\cdots O$ not symmetrized (ice VIII), and no disorder and $O-H-O$ bond symmetrized (ice X).

3.9 Article: Superionic–superionic phase transitions in body-centered cubic H_2O ice

PRL 117, 135503 (2016) PHYSICAL REVIEW LETTERS week ending 23 SEPTEMBER 2016

Superionic-Superionic Phase Transitions in Body-Centered Cubic H_2O Ice

Jean-Alexis Hernandez* and Razvan Caracas†
Laboratoire de Géologie de Lyon, UMR CNRS 5276 (CNRS, ENS, Université Lyon1), École Normale Supérieure de Lyon, 69364 Lyon Cedex 07, France

(Received 1 May 2016; revised manuscript received 23 June 2016; published 21 September 2016)

From first-principles molecular dynamics, we investigate the relation between the superionic proton conduction and the behavior of the O—H···O bond (ice VII′ to ice X transition) in body-centered-cubic (bcc) H_2O ice between 1300 and 2000 K and up to 300 GPa. We bring evidence that there are three distinct phases in the superionic bcc stability field. A first superionic phase characterized by extremely fast diffusion of highly delocalized protons (denoted VII″ hereinafter) is stable at low pressures. A first-order transition separates this phase from a superionic VII′, characterized by a finite degree of localization of protons along the nonsymmetric O—H···O bonds. The transition is identified in structural, energetic, and elastic analysis. Upon further compression a second-order phase transition leads to the superionic ice X with symmetric O—H—O bonds.

DOI: 10.1103/PhysRevLett.117.135503

The thermodynamic conditions spanned by the planetary environments hosting H_2O ices are so diverse that almost all stable structures from the phase diagram have a chance to exist somewhere. These phases exhibit remarkable diversity up to about 3 GPa with various ordered and disordered molecular structures. Above this pressure the phase diagram is essentially dominated by structures that are built on a body-centered cubic (bcc) sublattice formed by oxygen atoms. At room temperature, under compression, these ices present continuous transition from a molecular crystal (ice VII) to an ionic crystal (ice X) [1–13].

In ice VII, water molecules preserve their identity and are arranged in a semirandom fashion obeying the Bernal-Fowler-Pauling ice rules [14,15], resulting in O—H···O bonds along the half-diagonals of the bcc sublattice. These bonds are characterized by an underlying double-well proton transfer potential. Increasing pressure and/or temperature activates the translation of the proton between the two potential wells, eventually resulting in a distinct H translationally disordered regime called ice VII′. This phenomenon was first predicted by Holzapfel [10] and then confirmed experimentally and computationally [1,3,4,8,11,12,16,17]. The potential barrier is crossed by proton tunneling and thermal fluctuations, which tend to decrease the transition pressure [3,17,18]. Morrone *et al.* [19] have shown that above 1000 K the proton tunneling becomes negligible in comparison to the thermal fluctuations, allowing us to model the transition classically. At higher pressure, ice VII′ transforms progressively in a symmetric ionic state, called ice X, which is stable up to about 400 GPa [20].

This transition sequence—orientational disorder (ice VII) to dynamical disorder (ice VII′) to ionic ice (ice X)—was studied at ambient temperature, but few studies mention it at high temperature [21,22]. With increasing temperatures, the mobility of the protons is enhanced such that H_2O ice reaches a superionic state [23] while the sublattice of oxygen atoms remains fixed. At several thousand kelvin and over several megabars superionic a bcc–face-centered cubic (fcc) transition affects the oxygen sublattice [24–26]. At 0 K and higher pressure, multiple ground-state structures are predicted to be stable [27–29]. Sun *et al.* [25] have recently shown that some of these structures become superionic at high temperature (the $P2_1/c$-SI phase).

Proton diffusion has been quantified in superionic H_2O with a bcc oxygen sublattice, and different bonding regimes have been noticed at 2000 K, suggesting a behavior close to the ice VII to ice X transition [22,30]. However, no clear relation between proton diffusion and these bonding regimes has been shown.

Here, we show from multiple analysis that several distinct phases populate the superionic regime of the bcc arrangement of the oxygen atoms. For this we study the superionic regime and its transition to the nondiffusive regime up to 300 GPa pressure range in the 1300–2200 K temperature range using first-principles molecular dynamics as implemented in the VASP package [31–34]. We employ the projector augmented-wave method approach [35] with the generalized-gradient approximation in the Perdew-Burke-Ernzerhof formalism [36] for the exchange correlation. We checked and confirmed that the correction for van der Waals interactions does not influence the physical properties of ice at the pressures encountered in our simulations. We model ice in a $4 \times 4 \times 4$ supercell containing 128 water molecules. At every volume-temperature point we generate the starting ice VII configuration independently to remove any possible memory effect. We allow 1–2 ps for thermalization and at least

2–8 ps for data production (more details in S1.A of the Supplemental Material [37]). All simulations are performed in an isokinetic *NVT* ensemble; i.e., the velocities of all the atoms are rescaled at each time step to match the desired temperature.

First, we calculate the diffusion coefficients (D_i) of the oxygen and hydrogen atoms from their mean square displacement (details in S1.B [37]). We distinguish the fluid phase (D_O and $D_H > 0$), the superionic regime ($D_O = 0$ and $D_H > 0$), and the nondiffusive regime ($D_O = 0$ and $D_H = 0$). Only the results corresponding to a fixed bcc sublattice of oxygen atoms ($D_O = 0$) are presented here. Figure 1(a) shows the evolution of hydrogen diffusion coefficient as a function of the shortest

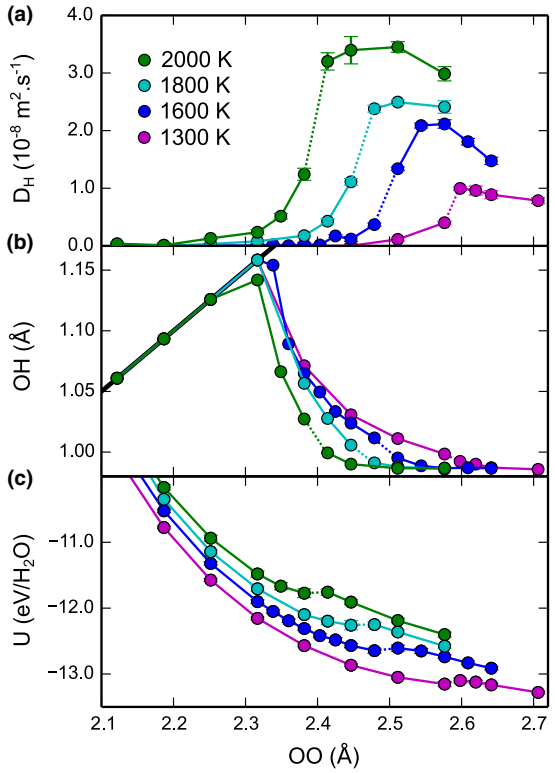

FIG. 1. (a) Diffusion coefficients of the hydrogen atoms (D_H) in solid ice ($D_O = 0$) as function of the OO distance. Superionic diffusion regime corresponds to positive D_H. The transition pressure to the superionic regime increases with increasing temperature. (b) Variation of the position of H in the O—H···O bond under compression. Black line represents OH = OO/2, corresponding to ice X. (c) Internal energy (U) under compression. The lattice parameter a is related to the OO distance as $a = \mathrm{OO} \times 2/\sqrt{3}$. The abrupt decrease in D_H in the superionic regime corresponds to the jump in the internal energy and to the beginning of the O—H···O bond symmetrization. This marks the phase transition between the superionic ice VII″ and the superionic ice VII′.

oxygen-oxygen (OO) distance (the corresponding densities and pressures are given in Table S1 [37]). In measurements, electrical conductivities larger than 1 $\mathrm{S \cdot cm^{-1}}$ are typically considered to characterize the superionic phases [50]. Here we consider that finite and positive D_H indicates the superionic regime. All our values yield conductivity larger than the threshold. The superionic regime expands to higher pressures as the temperature increases. Along all isotherms, the superionic regime is characterized by a transition from high values of D_H (3.6×10^{-8} $\mathrm{m^2\,s^{-1}}$ at 2000 K), corresponding to the low compression, to small values of D_H (less than 1.0×10^{-8} $\mathrm{m^2\,s^{-1}}$), corresponding to higher compression. We note that this transition is sharper at lower temperatures. The values of D_H are coherent with the ones found by French *et al.* [51] in the fluid phase and with the ones of Goldman *et al.* [22] in the superionic regime at 2000 K in their simulations starting from a solid initial configuration. At higher pressure (i.e., a smaller OO distance), H atoms diffusion stops altogether, marking the normal, nondiffusive regime. As expected, the limit between the superionic regime and the nondiffusive one moves upwards in pressure with increasing temperature.

Next we look at the relative position of the H atom in the O—H···O triplet, using the pair distribution functions and a three-body analysis (details in S2.A [37]). As shown in Fig. 1(b), there are several cases. For large OO distances, the OH distance remains almost constant under compression: this is ice VII″. As the OO distance decreases, the OH distance starts to increase: this is ice VII′. In this range the O—H···O bond is symmetrizing; i.e., the H continuously changes position approaching the fully symmetric state, halfway between the two O atoms. A fully symmetric O—H—O bond is reached for OO distances between 2.31 and 2.35 Å: this is ice X. The beginning of the O—H···O symmetrization, namely, the transition between ice VII′ and ice VII″, corresponds to the abrupt decrease of the hydrogen diffusion, marked by dotted lines in Fig. 1(a). The comparison of the degree of symmetrization of the O—H···O bond with the diffusion rate of the H atoms indicates that the transition between ice VII′ and ice X occurs in the superionic regime at 1800 K and above.

We perform one further step in our analysis and look at the individual trajectory of each H atom during the entire simulation time to identify specifically the translational and the rotational component of the H diffusion. This analysis shows that in the temperature range of our simulations H translations in between the two neighboring O atoms are always present. The superionic phases are associated and, thus, can be identified by the presence of both rotations of H around the O atoms and translations along the O—H···O triplets. Moreover, the transition to the superionic ice VII′ is associated with a brutal increase of the translation rate and a strong decrease of the rotation rate. The actual ratio of translations vs rotations is characteristic to each phase of

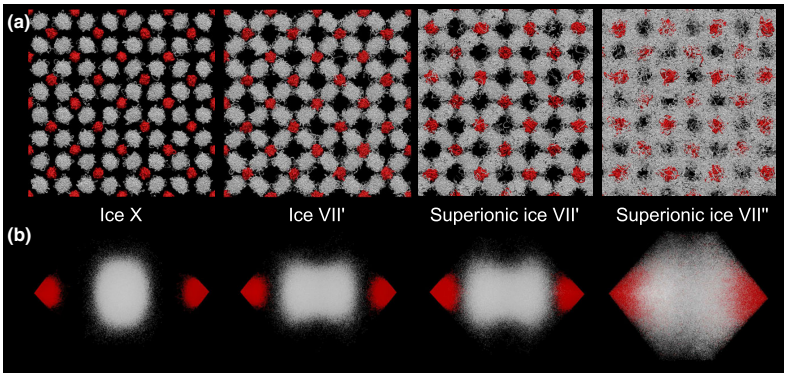

FIG. 2. Behavior of the H and O atoms along the 1300 K isotherm. (a) Representation of the atomic trajectories in one supercell representing the simulation box during a 2.5-ps long run in ice X ($P = 300$ GPa), in ice VII′ (57.3 GPa), in superionic ice VII′ (34.5 GPa), and in ice VII″ (34.2 GPa) just after the transition. (b) Projection of the above trajectories along one O—H $\cdots$ O bond. In ice X the H-atom distribution is unimodal and presents a maximum at the center of the O—H $\cdots$ O bond, whereas in ice VII′ the distribution is bimodal. In ice VII″, the delocalization of the H atoms is too large to clearly distinguish the O—H $\cdots$ O bond.

ice (S2.B [37]). Ice VII″ is, as expected, characterized by the highest rate of rotations and a linear increase of translation rate as a function of pressure. Superionic ice VII′ and superionic ice X still present a non-null rotation rate, whereas nondiffusive ice VII′ and X are only affected by translation jumps.

These structural observations are supported by a jump in the internal energy [Fig. 1(c)] associated with the beginning of the O—H $\cdots$ O symmetrization and with the start of the abrupt decrease in protonic diffusion. The jump is sharp at 1300 K and it smooths out at higher temperatures. This jump is a mark of a first-order phase transition, which takes place between a superionic phase with largely delocalized hydrogen atoms (found at lower pressures, hereinafter called ice VII″) and a superionic phase with H atoms in the O—H $\cdots$ O triplets (the superionic regime of ice VII′).

Figure 2(a) shows qualitative analysis of the H delocalization by comparing nuclei trajectories at 1300 K in the ice X, the superionic ice VII′, and the superionic VII″ phases. In the superionic ice VII′, H atoms remain along $\langle 111 \rangle$ directions (i.e., O—H $\cdots$ O bonds) between the diffusive jumps, whereas the H atoms are delocalized all around a given O atoms in the VII″ phase. In the former case the interstitial space is quasiunoccupied by H, but in the latter there is a non-null population of H traversing it. Another way of looking at the H delocalization, via the O—H bond orientation, shows a progressive delocalization of the H atoms over decompression from the ices X and VII′ to the superionic ice VII′ to the superionic ice VII″ (S2.C [37]). Figure 2(b) represents the projection along one O—H $\cdots$ O bond of all atomic positions sampled during a given simulation. It shows the symmetrization of H distribution when compressing ice VII′ up to ice X, and also the inadequacy of a double-well potential model for the VII″ phase—this is because of the too-broad distribution of the O—H bond orientations away from the O—H $\cdots$ O line, due to the higher degree of delocalization. The different pattern of H delocalization between ices VII′ and VII″ supports the distinction of two phases, as observed by the bonding and energetic analysis.

Based on the structural, diffusion, and energetic analysis we propose modifications to the phase diagram as shown in Fig. 3. It displays the proposed stability fields of the four different phases (fluid, VII″, VII′, and X) and the extent of the superionicity in the solids. A first-order phase transition separates the superionic phase VII″ from the superionic ice VII′. The stability of the VII″ phase is artificially extended at low pressures towards the fluid phase; this comes from classical overheating effects observed in molecular-dynamics simulations [52]. However the VII″ phase has its own distinct thermodynamic stability field between the melting curve [30,53], shown with the red line in Fig. 3, and the stability field of ice VII′. As such, it should be observed experimentally at low pressures and high temperatures before reaching the melting line. Vibrational spectroscopy, like Raman and/or infrared, could be used to trace these transitions from the change of slope in pressure of the stretching modes of the O—H bonds. This is visible in the analysis of the vibrational density of states (VDOS); for example, the softening of the OH-stretching during the transition between ice VII' and ice X (see S3.A [37]). Moreover, the finite component of the VDOS at zero frequency is related to the diffusion coefficients, present only for the superionic phases. We find that the transition to ice X is quasi-temperature-independent in the nonsuperionic regime; it takes place around 100 GPa, the same transition pressure as obtained at low temperature when the H atoms are treated classically [4,18]. In the superionic regime the transition pressure increases with increasing temperature.

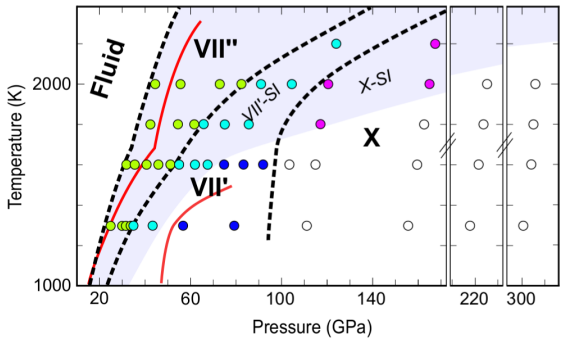

FIG. 3. Proposed phase diagram obtained from our structural, diffusion, and energetic analysis. Circles indicate the thermodynamic conditions sampled in this study. The colors of the circles correspond to the various phases and/or regimes identified in the phase diagram: light green, ice VII″; cyan, ice VII′ in the superionic regime; blue, ice VII′ in the nondiffusive regime; magenta, ice X in the superionic regime; and white, ice X in the nondiffusive regime. Black dotted lines correspond to the phase transitions lines. The fluid–ice VII″ and ice VII″–ice VII′ transitions are first order. The pale blue background area shows the thermodynamic conditions in which we found the superionic regime. The upper red line is the melting curve observed by Schwager *et al.* [53], as confirmed by calculations [30]; the lower red line is the melting curve as obtained by spectroscopic measurements [6,54,55].

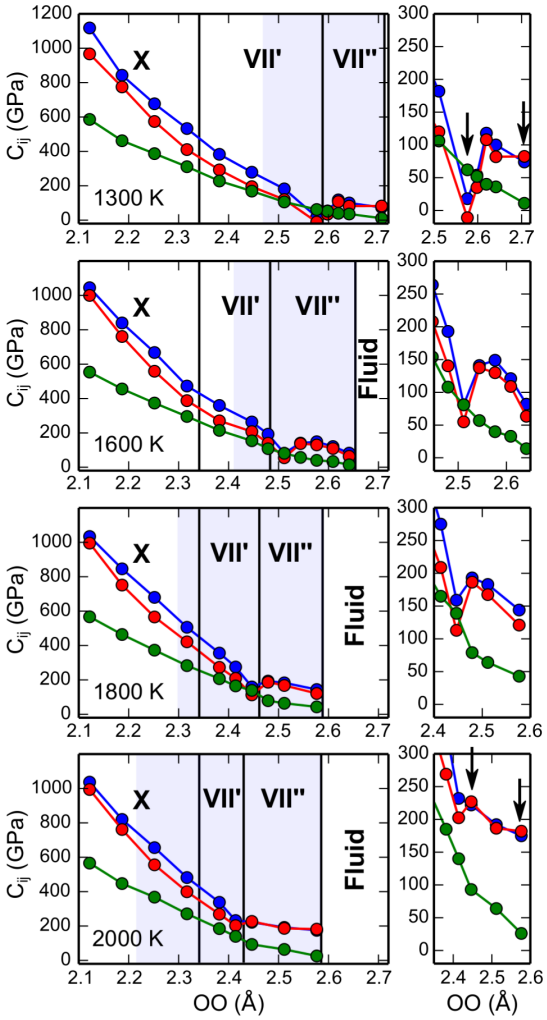

FIG. 4. Elastic constants calculated along different isotherms. C_{11}, C_{12}, and C_{44} are, respectively, represented in blue, red, and green. In the left panels, the stability fields of the different phases are separated with the black vertical lines, and the pale blue area corresponds to the superionic regime. Right panels are zooms of the transition region between the VII″ phase and ice VII′. Black arrows show the conditions in which the Born criterion is not respected.

The existence of a VII″ phase and the transition between ice VII′ and ice VII″ are obvious when computing the pressure variation of the elastic properties. Figure 4 shows the elastic constants at several temperatures as a function of pressure. In ices X and VII′, all elastic constants decrease with decreasing pressure (increasing OO distance). The slopes are different for each constant, and they are not affected by the development of the superionic regime. C_{12} approaches C_{11} consistently with the development of elastic instabilities observed at 0 K [20,56]. The transition between the VII″ phase and ice VII′ appears very clearly in the diagram: there is a dip in the pressure variation of the C_{11} and C_{12} elastic constants, exactly at the transition pressure, at all temperatures. The dip shows a clear change in the elastic behavior of H_2O ice during the transition from the VII″ phase into ice VII′. Similar behavior is observed in other elastic phase transitions, like stishovite and hollandite [57,58]. In the transformations of H_2O ice, because the oxygen sublattice is not affected, the elastic transition must be only induced by a change of the localization degree of the H atoms in the superionic regime. As the OO distance increases, the H becomes more and more delocalized; they are less confined to a linear O—H···O triplet. They can move more freely around the O atoms while still preserving the weak H···O bonds that hold the structure together. This is the mark of the proposed ice VII″ phase.

Therefore, we propose an addition to the phase diagram of H_2O ice at low pressures and high temperatures. We show that between the melting line and the superionic ice VII′ there is another superionic phase with distinct physical properties. This new phase, denoted here as ice VII″, is characterized by a large delocalization of the H atoms around the O atoms, which are no longer confined along the O—H···O triplet in between the diffusion jumps. This results in a higher rate of protonic diffusion and a constant OH distance under compression. The transition between ice VII′ and ice VII″ is marked by a change in the H diffusion rate, by a change in the relation between OH and OO

distances, by a jump in energy, and by a dip in the pressure variation of the elastic constants. This transition could be investigated experimentally by either conductivity or Brillouin measurements. Finally, at high pressures we show that ice VII′ and ice X can host H superionic diffusion. Thus the complete symmetrization of the O—H ⋯ O bond can occur in the superionic regime if the temperature is high enough.

The simulations were carried out on the Occigen machine at the CINES supercomputing facility (Montpellier, France) and on the Curie machine at the CEA TGCC facility (Bruyères-le-Châtel, France) using computational Grant No. eDARIx2015106368.

*jeanalexis.hernandez@ens-lyon.fr
†razvan.caracas@ens-lyon.fr

[1] K. Aoki, H. Yamawaki, M. Sakashita, and H. Fujihisa, Phys. Rev. B **54**, 15673 (1996).
[2] M. Benoit, M. Bernasconi, P. Focher, and M. Parrinello, Phys. Rev. Lett. **76**, 2934 (1996).
[3] M. Benoit, D. Marx, and M. Parrinello, Nature (London) **392**, 258 (1998).
[4] M. Benoit, A. H. Romero, and D. Marx, Phys. Rev. Lett. **89**, 145501 (2002).
[5] M. Bernasconi, P. L. Silvestrelli, and M. Parrinello, Phys. Rev. Lett. **81**, 1235 (1998).
[6] A. F. Goncharov, V. V. Struzhkin, M. S. Somayazulu, R. J. Hemley, and H.-K. Mao, Science **273**, 218 (1996).
[7] A. F. Goncharov, V. V. Struzhkin, H.-K. Mao, and R. J. Hemley, Phys. Rev. Lett. **83**, 1998 (1999).
[8] R. J. Hemley, A. P. Jephcoat, H.-K. Mao, C. S. Zha, L. W. Finger, and D. E. Cox, Nature (London) **330**, 737 (1987).
[9] R. J. Hemley and P. Dera, Rev. Mineral. Geochem. **41**, 335 (2000).
[10] W. B. Holzapfel, J. Chem. Phys. **56**, 712 (1972).
[11] P. Pruzan, J. C. Chervin, E. Wolanin, B. Canny, M. Gauthier, and M. Hanfland, J. Raman Spectrosc. **34**, 591 (2003).
[12] M. Song, Phys. Rev. B **60**, 12644 (1999).
[13] K. S. Schweizer and F. H. Stillinger, J. Chem. Phys. **80**, 1230 (1984).
[14] J. D. Bernal and R. H. Fowler, J. Chem. Phys. **1**, 515 (1933).
[15] L. Pauling, J. Am. Chem. Soc. **57**, 2680 (1935).
[16] R. J. Nelmes, J. S. Loveday, W. G. Marshall, G. Hamel, J. M. Besson, and S. Klotz, Phys. Rev. Lett. **81**, 2719 (1998).
[17] M. Benoit, D. Marx, and M. Parrinello, Comput. Mater. Sci. **10**, 88 (1998).
[18] Y. Bronstein, P. Depondt, F. Finocchi, and A. M. Saitta, Phys. Rev. B **89**, 214101 (2014).
[19] J. A. Morrone, L. Lin, and R. Car, J. Chem. Phys. **130**, 204511 (2009).
[20] R. Caracas, Phys. Rev. Lett. **101**, 085502 (2008).
[21] M. French and R. Redmer, Phys. Rev. B **91**, 014308 (2015).
[22] N. Goldman, L. E. Fried, I.-F. W. Kuo, and C. J. Mundy, Phys. Rev. Lett. **94**, 217801 (2005).
[23] C. Cavazzoni, Science **283**, 44 (1999).
[24] H. F. Wilson, M. L. Wong, and B. Militzer, Phys. Rev. Lett. **110**, 151102 (2013).
[25] J. Sun, B. K. Clark, S. Torquato, and R. Car, Nat. Commun. **6**, 8156 (2015).
[26] M. French, M. P. Desjarlais, and R. Redmer, Phys. Rev. E **93**, 022140 (2016).
[27] J. M. McMahon, Phys. Rev. B **84**, 220104 (2011).
[28] M. Ji, K. Umemoto, C.-Z. Wang, K.-M. Ho, and R. M. Wentzcovitch, Phys. Rev. B **84**, 220105 (2011).
[29] C. J. Pickard and M. Martinez-Canales, Phys. Rev. Lett. **110**, 245701 (2013).
[30] E. Schwegler, M. Sharma, F. Gygi, and G. Galli, Proc. Natl. Acad. Sci. U. S. A. **105**, 14779 (2008).
[31] G. Kresse and J. Hafner, Phys. Rev. B **47**, 558 (1993).
[32] G. Kresse and J. Hafner, Phys. Rev. B **49**, 14251 (1994).
[33] G. Kresse and J. Furthmiiller, Comput. Mater. Sci. **6**, 15 (1996).
[34] G. Kresse and J. Furthmüller, Phys. Rev. B **54**, 11169 (1996).
[35] P. E. Blöchl, Phys. Rev. B **50**, 17953 (1994).
[36] J. P. Perdew, K. Burke, and M. Ernzerhof, Phys. Rev. Lett. **77**, 3865 (1996).
[37] See Supplemental Material at http://link.aps.org/supplemental/10.1103/PhysRevLett.117.135503, which includes Refs. [38–49], for detailed information about first-principles simulations and post-processing of the molecular dynamics trajectories, additional supporting results and tests.
[38] P. Hohenberg and W. Kohn, Phys. Rev. **136**, B864 (1964).
[39] W. Kohn and L. J. Sham, Phys. Rev. **140**, A1133 (1965).
[40] G. Kresse and D. Joubert, Phys. Rev. B **59**, 1758 (1999).
[41] S. Nose, J. Chem. Phys. **81**, 511 (1984).
[42] W. G. Hoover, Phys. Rev. A **31**, 1695 (1985).
[43] M. Parrinello and A. Rahman, Phys. Rev. Lett. **45**, 1196 (1980).
[44] M. Parrinello and A. Rahman, J. Appl. Phys. **52**, 7182 (1981).
[45] J. F. Nye, *Physical Properties of Crystals: Their Representation by Tensors and Matrices* (Oxford University Press, New York, 1985).
[46] M. Born, Math. Proc. Cambridge Philos. Soc. **36**, 160 (1940).
[47] F. Mouhat and F. X. Coudert, Phys. Rev. B **90**, 224104 (2014).
[48] J. G. Kirkwood, J. Chem. Phys. **3**, 300 (1935).
[49] J. Klimeš, D. R. Bowler, and A. Michaelides, Phys. Rev. B **83**, 195131 (2011).
[50] J. Boyce and B. Huberman, Phys. Rep. **51**, 189 (1979).
[51] M. French, T. R. Mattsson, and R. Redmer, Phys. Rev. B **82**, 174108 (2010).
[52] A. B. Belonoshko, Am. Mineral. **86**, 193 (2001).
[53] B. Schwager, L. Chudinovskikh, A. Gavriliuk, and R. Boehler, J. Phys. Condens. Matter **16**, S1177 (2004).
[54] T. Kimura, Y. Kuwayama, and T. Yagi, J. Chem. Phys. **140**, 074501 (2014).
[55] J.-F. Lin, Geophys. Res. Lett. **32**, L11306 (2005).
[56] B. Journaux, R. Caracas, P. Carrez, K. Gouriet, P. Cordier, and I. Daniel, Phys. Earth Planet. Inter. **236**, 10 (2014).
[57] M. A. Carpenter, R. J. Hemley, and H.-K. Mao, J. Geophys. Res. **105**, 807 (2000).
[58] T. Boffa Ballaran, J. Liu, L. S. Dubrovinsky, R. Caracas, and W. Crichton, Phys. Rev. B **80**, 214104 (2009).

Chapter 4

Properties and stability of NaCl-bearing ice at high-temperature

Contents

4.1 Introduction

In H_2O-rich planets, the delivery of electrolytes to an ocean would bring essential nutrients to support life. If the silicate core is isolated from the liquid water layer, the transportation of the silicate core hydration products in the planetary interior depends on their solubility in the high-pressure ices.

The inclusion of NaCl in the bcc ice structure (mainly ice VII) have been suggested by several experimental studies (Frank et al., 2006; Journaux et al., 2013; Ludl et al., 2017). Nevertheless, the authors have proposed three different mechanisms for the inclusion of the Na^+ and Cl^- ions. Frank et al. (2006) inferred that both Na^+ and Cl^- ions occupy octahedral face-centered sites. Based on their results on LiCl-bearing ice, the IMPMC group (Klotz et al., 2009; Bove et al., 2015; Klotz et al., 2016) first proposed that Cl^- susbtitutes a water molecule and Na^+ remains in an octahedral site. Then, they suggested that both Na^+ and Cl^- replace H_2O molecules on bcc sites. The similar "sizes" of Na^+, Cl^- and H_2O support the last mechanism. To validate the substitutional inclusion, we compress two

$NaCl{\cdot}RH_2O$ solutions with $R = \{126, 30\}$ at ∼70 GPa, previously equilibrated in the fluid domain at 1600 K and 30 GPa. The two solution crystallize into a bcc ice during the 10 ps-long NVT-MD simulations (Figure 4.1). Both Na^+ and Cl^- occupy bcc sites.

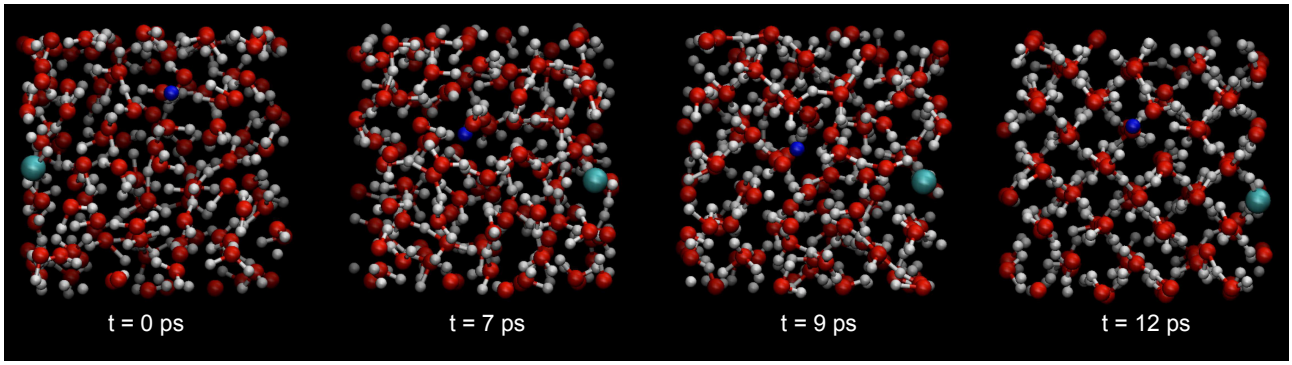

Figure 4.1: Crystallization of a $NaCl \cdot 126H_2O$ solution during a NVT-MD at ∼70 GPa. Red, white, blue and cyan spheres respectively represent O, H, Na and Cl.

Additionally, zero-temperature calculations of the mixing enthalpies of NaCl-bearing ices at 4 and 5 GPa, shows that NaCl-bearing ice ($NaCl \cdot 11.5H_2O$) could be stable at ∼300 K (Ludl et al., 2017). Experimental evidence of the inclusion of the sodium and chlorine ions have been reported by the same team at ambient temperature and around 10 GPa for a more dilute solution ($NaCl \cdot 52H_2O$).

Hereafter, we investigate the structural and dynamical properties, and the thermodynamics of the NaCl-bearing bcc water ice along the 1600 K isotherm at pressures relevant for the planetary interiors.

4.2 Sampling of the configurational space

First, we determine the total number of configurations K and the number of symmetry-independent configurations K_{red} for a given concentration of NaCl in a given supercell. We do not take into account the positions of the H atoms as they are dynamically disordered at high-temperature. Thus, K depends only on the number of bcc sites N_{bcc} and the numbers of atoms occupying these sites N_{Na}, N_{Cl}, N_{O}:

$$K = \frac{N_{\mathrm{bcc}}!}{N_{\mathrm{Na}}!N_{\mathrm{Cl}}!N_{\mathrm{O}}!} \tag{4.1}$$

We use the code Supercell (Okhotnikov et al., 2016) to compute the number of symmetry-independent configurations and their degeneracy. Table 4.1 contains the combinatorics of the substitutive incorporation of NaCl in bcc water ice.

It shows that the total number of configurations is large and grows extremely fast with the in-

Table 4.1: Combinatorics of the partial occupancies of the $(NaCl)_y - (2H_2O)_{1-y}$ solution ($NaCl{\cdot}RH_2O$) obtained from the Supercell program (Okhotnikov et al., 2016).

Supercell	Mole fraction x	Mass fraction w	y	R	Number of NaCl in the supercell	K	K_{red}
$4\times4\times4$	0.007874	0.025121	0.015625	126	1	16256	13
$4\times4\times4$	0.015873	0.049762	0.03125	62	2	64008000	12470
$3\times3\times3$	0.018868	0.058770	0.03704	52	1	2862	7
$4\times4\times4$	0.032258	0.097658	0.0625	30	4	$\sim 10^{14}$	-
$3\times3\times3$	0.03846	0.114945	0.074	25	2	1897506	1077
$3\times3\times2$	0.02857	0.087171	0.056	34	1	1260	8
$3\times2\times2$	0.043478	0.128604	0.084	22	1	552	7
$4\times4\times4$	0.06667	0.188257	0.125	14	8	$\sim 1.210^{24}$	-
$3\times3\times2$	0.05882	0.168694	0.112	16	2	353430	868
$2\times2\times2$	0.06667	0.188257	0.125	14	1	240	4
$4\times4\times4$	0.142857	0.351129	0.250	6	16	$\sim 8.910^{38}$	-
$3\times3\times3$	0.148936	0.362325	0.260	5.714	7	$\sim 1.110^{16}$	-
$2\times2\times2$	0.142857	0.351129	0.250	6	2	10920	50
$2\times2\times1$	0.142857	0.351129	0.250	6	1	56	3

creasing NaCl concentration. Of course, it is not practical to perform a molecular dynamics for all the configurations at a given pressure – concentration – temperature condition. Moreover the evaluation of the stability of the NaCl-bearing ices demands good configurational statistics whereas the transport properties depend less on the different configurations.

It appears that a complete sampling of the reduced configurational space is achievable for some combinations of supercell sizes and concentrations. $NaCl \cdot 126H_2O$ has only 13 independent configurations and the $4 \times 4 \times 4$ supercell provides a good convergence of the energies, a good sampling during the MD, and good autocorrelations due to the large number of atoms. At higher concentration, $NaCl \cdot 52H_2O$ presents only 7 independent configurations in a $3 \times 3 \times 3$ supercell. Consequently, we choose to fully sample the reduced configurational space of $NaCl \cdot 126H_2O$ and $NaCl \cdot 52H_2O$ at 100 GPa and 1600 K. These conditions are motivated by the accuracy of the equation of state we derive for H_2O, and the absence of quantum correction for the pressure: we find that $p_{MD}(100\text{ GPa}, 1600\text{ K}) \sim p(100\text{ GPa}, 1600\text{ K})$ in H_2O. These calculations and the resulting Gibbs free energies of mixing are presented in section 4.4.3.

In order to explore the concentration – volume space and to get insights on the dynamical properties of the $NaCl{\cdot}RH_2O$ ices, we sample the 1600 K isotherm at pressures ranging from ∼30 GPa to ∼300 GPa at different concentrations ($R = 126, 62, 30, 14, 6$). For each concentration – volume condition, we sample up to 4 random configurations plus a low-energy configuration. At a given concentration, we

determine this last configuration by calculating the internal energies of 100-200 random configurations generated from an equilibrated ice VII at a density of 2.453 g.cm^{-3}. The low-energy configuration is the one with the smallest internal energy after the electronic relaxation. Thus, as we do not apply this procedure at other densities and we do not take into account the effect of the temperature, this is not necessarily the most stable configuration. In the following section we compare the properties of the different systems to the ones of the pure water ice at the same volumes. The thermodynamics and the stability of the NaCl-bearing ices as obtained from the random sampling are presented in section 4.4.2.

4.3 Structural analysis and modification of H_2O phase diagram

At a given concentration – volume condition, the different configurations present similar transport and structural properties (obviously the distances between Na^+ and Cl^- differ). Consequently, the results presented in this section are averaged over the sampled configurations.

4.3.1 Bcc sub-lattice distortion

The analysis of the radial pair distribution functions reveals that the substitutions of water molecules by Na^+ and Cl^- ions distort the bcc sub-lattice (Figure 4.2). This distortion is not visible in the $g_{OO}(r)$ as the positions of the first two maxima, respectively the length of the half-diagonal of the bcc unit-cell and the length of the unit-cell parameter, remain the same in H_2O and in $NaCl{\cdot}RH_2O$ (Figure 4.2.a). The broadening of the peaks with the increasing NaCl concentration indicates that the oxygen atoms have larger displacements around their equilibrium bcc positions. The distortion becomes evident when looking at the oxygen-sodium and oxygen-chloride radial distribution functions at the same volume (Figures 4.2.b and c.). The shortest ONa distance (i.e. the half-diagonal of the bcc unit-cell) is ∼10 % shorter than the OO distance due to the stronger attraction between the negatively charged oxygen ion and the positively charged sodium ion. Conversely O and Cl repulse each other which results in longer O-Cl bonds. Again, for a given volume the NaCl concentration broadens the peaks but does not affect the lengths of the O-Na and O-Cl bonds. As a consequence of the distortion the first two peaks of $g_{ONa}(r)$ are clearly separated whereas they are merged in $g_{OCl}(r)$ indicating that the OCl is almost equal to the unit-cell parameter.

Figure 4.2.d shows the evolution of $g_{OO}(r)$, $g_{ONa}(r)$, $g_{OCl}(r)$ under compression in the

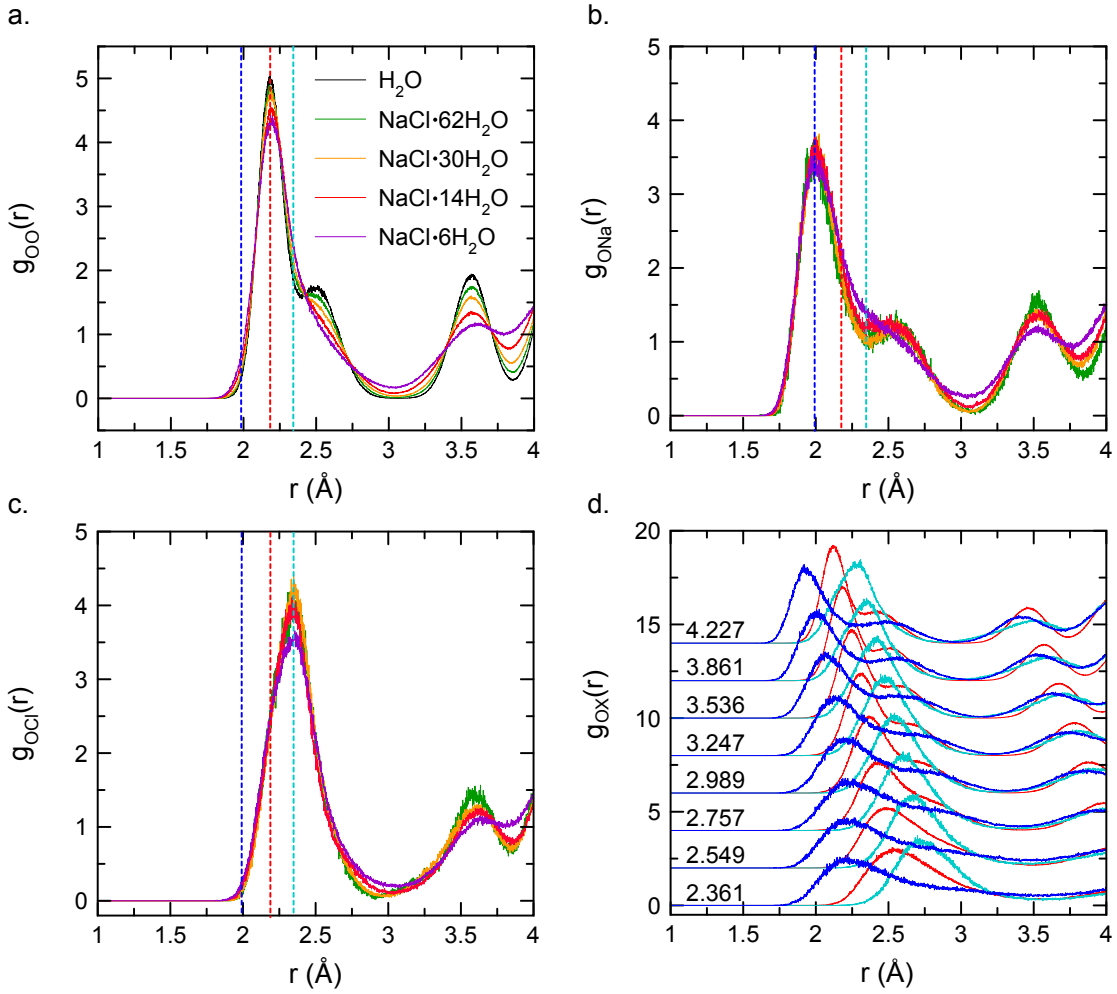

Figure 4.2: Distortion of the bcc sub-lattice. a. Oxygen-oxygen radial distribution functions at the same volume (a = 2.525 Å) for pure and NaCl-bearing ices. The positions of first two peaks that appear at $r < 3$ Å correspond respectively to the length of the half-diagonal and the length of the edge of the bcc sub-lattice unit-cell. b. and c. Oxygen-sodium and oxygen-chloride radial distribution functions. The dotted lines represent the average positions of the first maximum of $g_{OO}(r)$ (red), $g_{ONa}(r)$ (blue), $g_{OCl}(r)$ (cyan). d. $g_{OO}(r)$ (red), $g_{ONa}(r)$ (blue), $g_{OCl}(r)$ (cyan) of the $NaCl \cdot 30H_2O$ system at different densities (indicated in g.cm^{-3}).

$NaCl \cdot 30H_2O$ system. As the NaCl concentration does not influence the positions of the maxima it is representative of all the NaCl-bearing ices. At low compression (i.e. low density on Figure 4.2.d), the ONa and the OCl distances respectively differ from the OO distance by -14 % and by +6 %. The difference decreases to -9.5 % and +8 % at the highest density.

Finally the inclusion of NaCl results in melting of the bcc sub-lattice at a higher pressure than in pure H_2O (cf. pressure – composition diagram in section 4.3.4). Although in a binary mixture the melting is incongruent, in our one phase simulations we cannot form a fluid–solid equilibrium spontaneously. Therefore, we do not go further in interpretating the influence of NaCl on the melting

line of the ice.

4.3.2 Structure and dynamics of the H sub-lattice

Next we investigate the structure and the dynamics of the hydrogen sub-lattice as it determines the different regimes and phases in bcc ice.

4.3.2.1 Relations between H, Na^+ and Cl^-

The atom trajectories and the radial distribution functions $g_{NaH}(r)$, $g_{ClH}(r)$ and $g_{OH}(r)$ show the breaking of the hydrogen bond network in NaCl-bearing ices. From the proton trajectories we compute the proton density in the supercells. Figure 4.3.a shows isosurfaces of given proton density in $NaCl \cdot 14H_2O$ at ∼120 GPa.

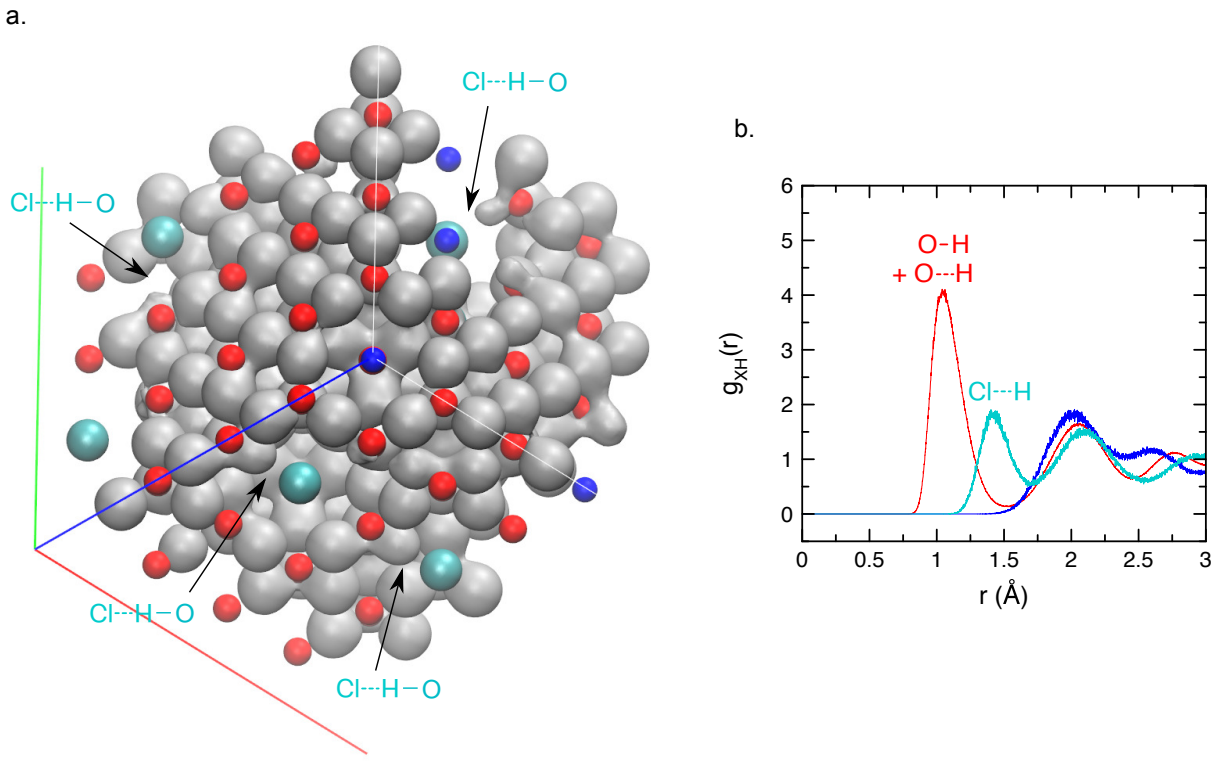

Figure 4.3: a. H density isosurface (gray) in $NaCl - 14H_2O$ and 120 GPa. Oxygen atoms (red spheres) and sodium (blue spheres) and chloride (cyan spheres) ions occupy the perfect bcc sites. No proton surrounds the sodium ions and $O - H \cdots Cl$ bonds are formed but the proton remains covalently bonded to the oxygen atoms. The crystal is oriented along a $\langle 111 \rangle$ direction. b. $g_{XH}(r)$ radial distribution functions where X refer to Na (blue), Cl (cyan), and O (red).

It clearly appears that the hydrogen bond network is broken due to the inability of the sodium ions to form any bonds with the protons. The chlorine ions do not form covalent bonds with the

protons but are involved in hydrogen bonds together with an oxygen atom. The average length of the $Cl\cdots H$ bond is longer than the average $O\cdots H$ bond length at the same density (see Figure 4.3.b). Moreover, the $O-H$ bond length is considerably reduced in the $O-H\cdots Cl$ bonds. Under compression it progressively decreases from 0.97 Å to 0.94 Å.

Therefore, in presence of NaCl, the connectivity of the hydrogen bond network is reduced and the protons are forced to occupy a smaller volume. Given a similar volume and amount of kinetic energy, this should either result in a faster dynamics or in a higher occupation of the interstitial space for the protons in NaCl-bearing ice in comparison to pure H_2O ice.

4.3.2.2 Hydrogen bond symmetrization

In the following we characterize the hydrogen bond network formed only by the $O-H\cdots O$ bonds. As in Chapter 3, we examine the hydrogen bond symmetrization in NaCl-bearing ices. In comparison to pure H_2O the inclusion of NaCl reduces the extent of the low compression regime with constant OH distances because of melting occurs at higher pressure (Figure 4.4). Then, in the symmetrizing regime (i.e. ice VII′), it decreases the OH distance for a given OO distance. At higher compression, the ice VII′ – ice X transition is reached at the same OO distance ($\sim$ 2.33 Å) up to $R = 14$. $NaCl\cdot 6H_2O$ transforms to ice X at higher compression. In terms of pressure, the complete symmetrization is progressively shifted towards higher pressures with the increasing NaCl concentration (see pressure – composition diagram for the corresponding values). At low temperature this effect is attributed to the reduction of the NQEs due to long-range electric fields induced by the salt ions (Bronstein et al., 2016). However, here we do not include the NQEs in the dynamics of the protons. Thus, we interpretate the transition pressure increase as a consequence to the onset of orientational disorder induced by the lattice distortions.

4.3.2.3 H delocalization out of the hydrogen bonds

Figure 4.5 shows that the incorporation of NaCl produces an onset of orientational disorder in the bcc ices. The spatial distribution of the $O-H$ bond orientations (Figure 4.5.a) still presents maxima along the $\langle 111\rangle$ directions but is much broader than in pure H_2O ice. Additionally small local maxima appear along the $\langle 100\rangle$ directions. They correspond to a proton diffusion through the octahedral sites. Looking at the trajectories we observe that such events occur during the transfer of a proton between two oxygen atoms located close to a sodium ion. Moreover, the quantification of the spread of the

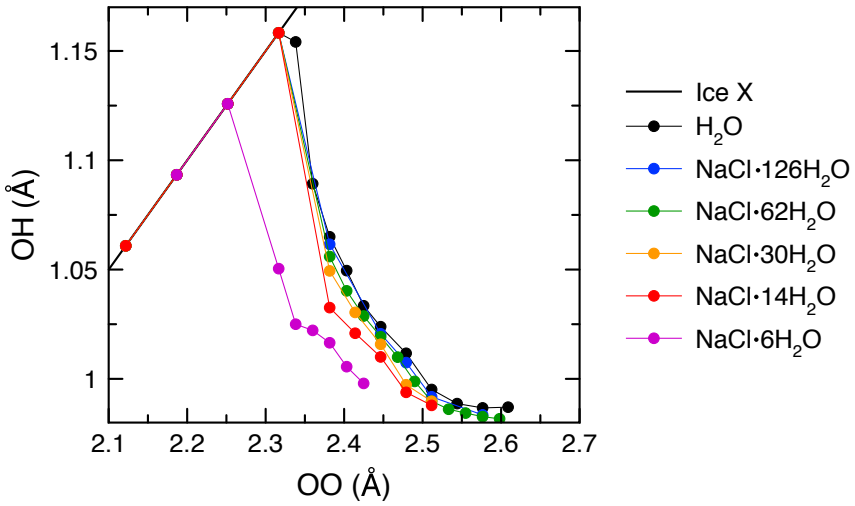

Figure 4.4: Hydrogen bond symmetrization in the NaCl-bearing bcc water ices. Except in $NaCl \cdot 6H_2O$ the complete symmetrization occurs for the same OO distance, i.e. same volume. However, the transition pressure increases with the NaCl concentration. In ice VII′ at a given volume the OH distance is smaller with the NaCl concentration due to the onset of orientational disorder.

distribution of the $O-H$ bond orientations out of the $\langle 111 \rangle$ directions (Figure 4.5.b) reveals that the orientational disorder increases progressively with the NaCl concentration at all volumes.

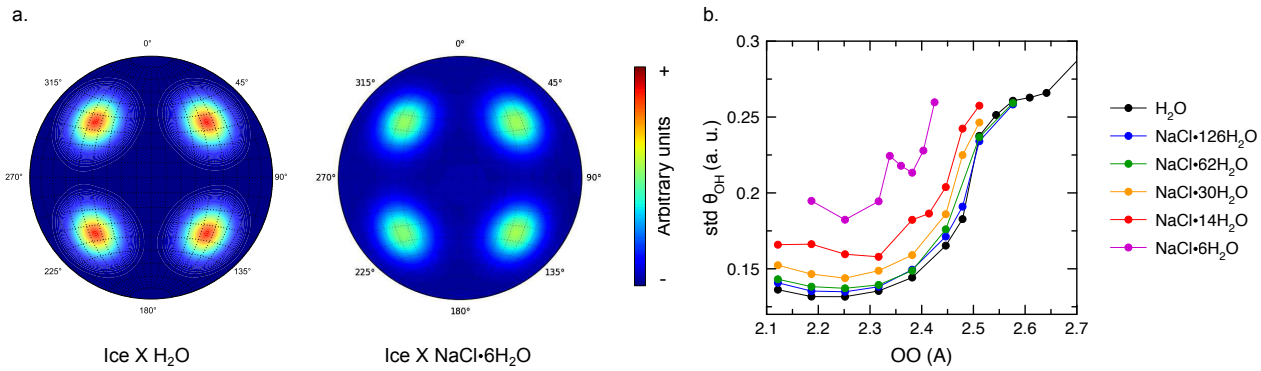

Figure 4.5: Orientational disorder induced from the inclusion of NaCl. a. Stereographic representation fo the spatial distribution of $O-H$ bonds orientations in pure and NaCl-bearing ice X at 1600 K and OO∼2.19 Å. The color scale is the same for the two projections. b. Standard deviation of the $O-H$ orientation, i.e. quantitative estimation of the dispersion of the $O-H$ orientation around the $\langle 111 \rangle$ directions.

We note that an onset of disordering in $NaCl \cdot 6H_2O$ and $NaCl \cdot 14H_2O$ is associated with a plateauing of the OH distance during the symmetrization of the $O-H \cdots O$ bonds (Figure 4.4). As in pure water ice, the general trend remains the same: at large volumes the orientational disorder is large and under compression first decreases abruptly and then more smoothly. The increase of disorder at the

highest pressures may indicate the development of instabilities in the NaCl-bearing ice X.

4.3.2.4 Bonding dynamics of the $O-H\cdots O$ bonds

Lastly, we analyze the bonding dynamics as described in Chapter 3 by distinguishing the changes of $O-H\cdots O$ bonds (rotations) and the changes of closest O atom for the proton within a $O-H\cdots O$ bond (translations). The addition of NaCl increases the rate of rotations and decreases the rate of translations at fixed volume. This result agrees with the previous analysis that supports the onset of orientational disorder in NaCl-bearing ice. Consequently the lifetime of the $O-H-O$ triplets is shorter than in H_2O but the lifetime of the covalent $O-H$ bonds is longer. The transition between the rotation- and the translation-dominated regimes (superionic ice VII″ to superionic ice VII′ transition) is progressively shifted at higher compression with the concentration of NaCl. Finally, for $R \leq 62$ the rate of rotation never reach zero at high compression, and the ice remains superionic at all pressures at 1600 K.

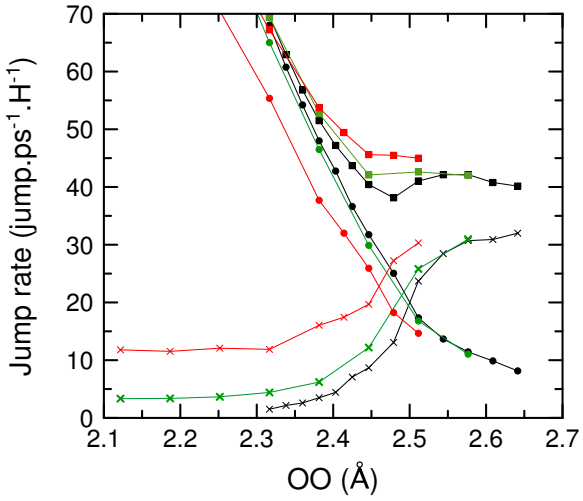

Figure 4.6: Influence of the NaCl concentration on the hydrogen bond dynamics. The color correspond to the different systems (black: H_2O; green: $NaCl \cdot 62H_2O$; red: $NaCl \cdot 14H_2O$). The squares, crosses and solid circles respectively represent the total jumps rate, the rate of rotations and the rate of translations.

4.3.3 Diffusion and electrical conductivity

The changes in bonding regime decribed previously are reflected in the proton diffusion and in the electrical conductivity (Figure 4.7).

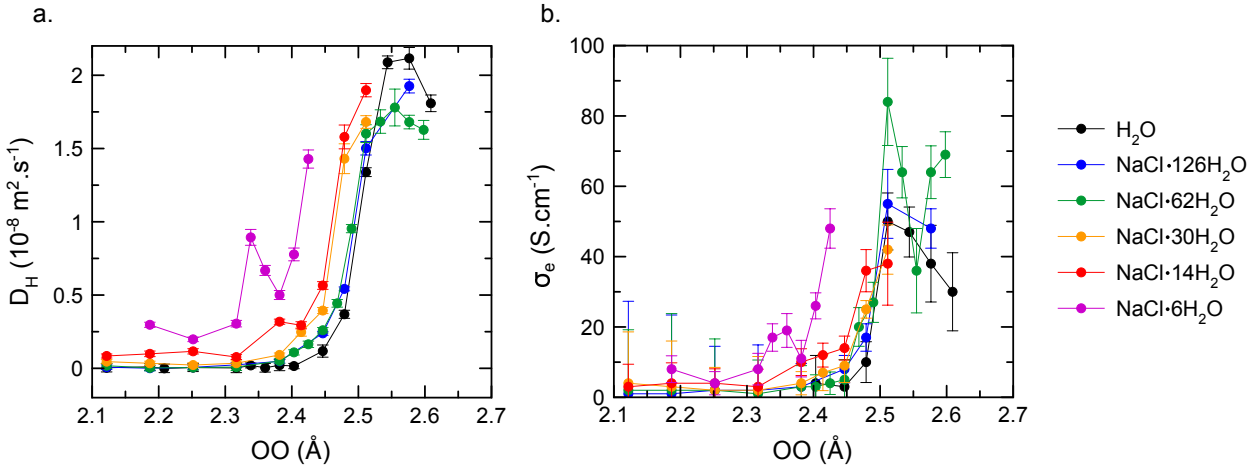

Figure 4.7: a. H diffusion coefficients as function of the OO distance of the half-diagonal of the bcc sublattice (i.e. as function of the supercell volume). b. Electrical conductivity. All the data points correspond to systems with a preserved bcc sublattice.

For a given NaCl concentration, the general trend is the same as for H_2O: the highest diffusion coefficients and conductivities are reached close to the melting and drop abruptly under compression. However, for $R = \{30, 14, 6\}$ the ice remains superionic at all pressures. In these systems, the plateauing of the OH distance (well-marked in NaCl $\cdot$ 6H_2O) during the hydrogen bond symmetrization associated with a bump of the H delocalization out of the O $-$ H $\cdots$ O bonds, increase the H diffusivity and the electrical conductivity at respectively OO = 2.42 Å, 2.37 Å, and 2.33 Å in NaCl $\cdot$ 30H_2O, NaCl $\cdot$ 14H_2O and NaCl $\cdot$ 6H_2O. Its amplitude increases with the concentration of NaCl. From OO $\leq$ 2.5 Å, at a given volume the proton diffusion increases with the concentration of NaCl.

4.3.4 Pressure – composition diagram of NaCl-doped bcc water ice

Figure 4.8 presents a pressure – composition diagram of the NaCl-bearing ice at 1600 K as found in our simulations. It summarizes the influence of the NaCl doping on the boundaries between the different regimes described in pure H_2O ice. We emphasize that this is not a phase diagram as we do not include yet information on the stability of the inclusion of NaCl in the ice.

As we cannot estimate the pressure range of the H_2O ice + fluid domain, we do not discuss the melting in the binary system. As anticipated by Bove et al. (2015), $\sim$2 mol% NaCl extents the superionic domain to the entire pressure range. The first-order phase transition between the superionic ice VII$''$ and the superionic ice VII$'$ is shifted at higher pressure with the addition of NaCl. Between H_2O and NaCl $\cdot$ 30H_2O the pressure difference reaches 10 GPa, but plateaus at higher

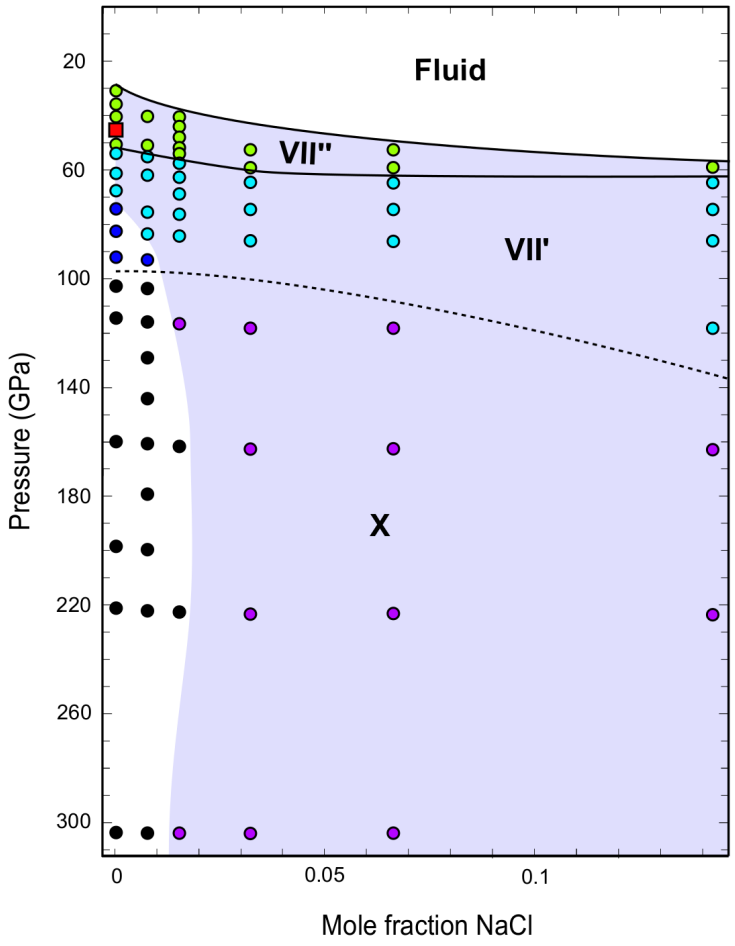

Figure 4.8: Pressure – composition diagram of NaCl-bearing bcc H_2O as found in our one phase simulations. The pressure is the classical pressure p_{MD}. It differs from the quantum corrected pressure by a maximum of 2 % at high compression. The dots represents the conditions that have been sampled, and they are colored according to the different phases and regimes described previously and in Chapter 3. The pale blue area corresponds to the superionic domain. Continuous and dotted lines respectively refer to the first- and higher-order phase transitions. The red square indicates the position of the melting line of H_2O at 1600 K (see Figure 3.18).

concentration. Moreover the transition towards the ice X is also shifted at high-pressure by about 40 GPa for $NaCl \cdot 6H_2O$ compared to the pure ice. Recently, this phenomenon has been observed in both $NaCl \cdot 53H_2O$ and several LiCl solutions at 300 K with a similar increase of the transition pressures of $\sim$ 30 GPa in $NaCl \cdot 52H_2O$, and up to $\sim$50 GPa in $LiCl \cdot 7H_2O$ (Bove et al., 2015; Bronstein et al., 2016). The authors mention that no symmetrization occurs near the ion impurity. We interpretate this as a consequence of the inclusion of Li^+ ions in octahedral sites: in NaCl-bearing ice X, we show that indeed no symmetrization occurs in the $O - H \cdots Cl$ bonds, but all $O - H - O$ bonds are symmetrized.

4.4 Stability of NaCl-bearing bcc H_2O ice

In this section, we perform free energy calculations based on the 2PT-MF model (cf. 2.5) that we use to calculate the thermodynamics of the mixing.

4.4.1 Thermodynamics of NaCl

First, we present the thermodynamics of NaCl which crystallizes in the CsCl (B2) structure at $p > 20 - 30$ GPa and 1600 K (Nishiyama et al., 2003).

We sample the 1600 K isotherm at 15 different volumes corresponding to pressures ranging from 35 GPa to 250 GPa. We perform the molecular dynamics in $4 \times 4 \times 4$ supercells (64 NaCl formula units) in the isokinetic ensemble. The time step is set at 1 fs and we use a cutoff of 550 eV for the kinetic energy of the plane-wave basis. Statistics are acquired during ∼9 ps after the thermalization.

As done previously for H_2O, we estimate the Helmholtz free energy at each volume from the calculation of the vibrational entropy and the quantum correction of the internal energy (see Appendix C for the evolution of u_{qc} under compression). Then, we fit the volume (density) dependence of the Helmholtz free energy with a Vinet equation of state (cf. dashed blue line in Figure 4.9.a). We obtain the corresponding volume – pressure relation by derivation of the free energy (cf. dashed blue line in Figure 4.9.b). The comparison of the computed pressures with experimental data (Nishiyama et al., 2003) at 1000 K and 2000 K shows a disagreement: at all volumes the calculated pressures are too high. This overestimation of the pressure at a given volume is a well-known effect of the GGA exchange-correlation functional. Consequently, we reduce all the unit-cell volumes by 0.3 $Å^3$/unit-cell so that our volume – pressure relation matches the experimental data over the broadest pressure range (cf. continuous blue lines in Figures 4.9.a and b.). The resulting equation of state is in good agreement with Ono et al. (2008) who also correct their volume – pressure relation based on other experimental data (Ono et al., 2006).

Finally, we apply the GGA correction to the Helmholtz – volume relation (blue dots in Figure 4.9.a) and fit a Vinet equation of state to the corrected data points (continuous blue lines). The specific Gibbs free energy of NaCl as function of the pressure is from both $f(\rho)$ and $p(\rho)$.

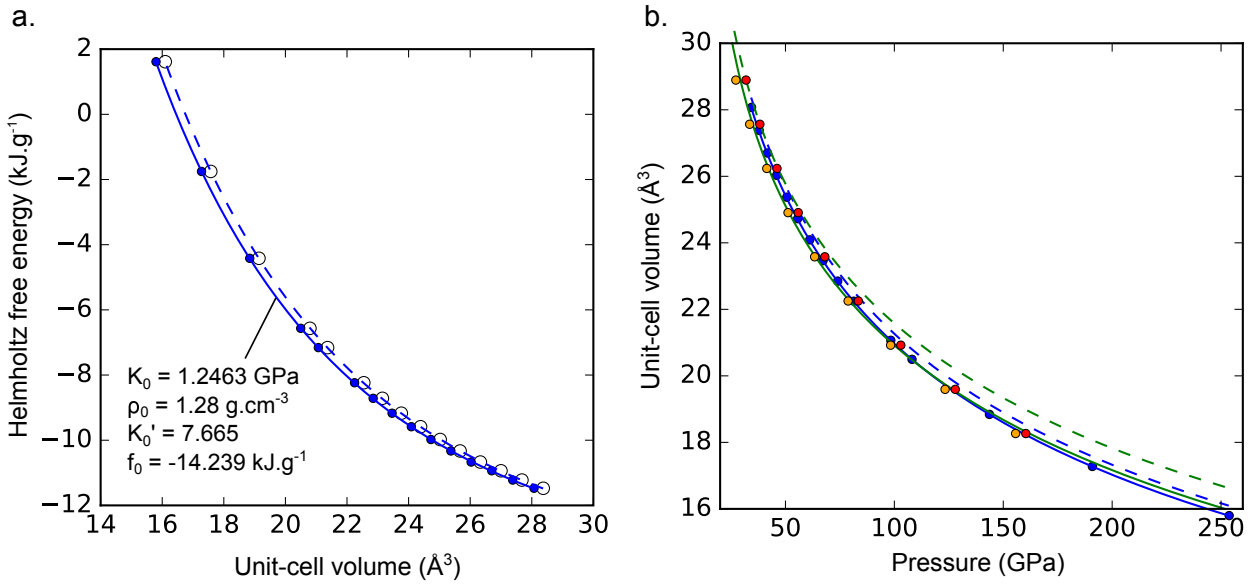

Figure 4.9: Equation of state of NaCl B2 phase at 1600 K. a. Specific Helmholtz free energy as function of the B2 unit-cell volume. The open circles correspond to the free energy computed from our simulations and the dashed blue line is the fit of a Vinet equation of state to these data. The blue dots and the blue continuous line respectively represent our data corrected from the GGA volume overestimation and the associated Vinet EOS fit. b. Volume – pressure relations in B2 NaCl. The orange and red dots correspond to experimental data obtained at 1000 K and 2000 K (Nishiyama et al., 2003). The dashed blue line represents the pressures given by the derivation of the non-GGA-corrected fit of the Helmholtz free energy. The volume difference between this curve and the experimental data is due to the overestimation of the volumes by the GGA. To obtain the continuous blue line we reduce all the volumes by $\Delta V_{\mathrm{GGA}} = 0.3$ Å^3/unit-cell. The blue dots refer to the non-quantum-corrected pressures p_{MD} obtained from our simulations whose corresponding volumes have been corrected by ΔV_{GGA}. GGA-corrected and non-corrected theoretical equations of state from Ono et al. (2008) are respectively represented by green continuous and dashed lines.

4.4.2 Random sampling along the 1600 K isotherm

For each NaCl·RH$_2$O system, we calculate the Helmholtz free energy ($F_k(R,\rho,T)$) of all the configurations computed at each volume along the isotherm. Then, we calculate the configurational average of the specific Helmholtz free energy ($f_{sol}(R,\rho,T)$) as presented in Chapter 2 for the Gibbs free energy:

$$F_{sol}(R,\rho,T) = -k_B \ln(Z_{tot}) = -k_B T \ln\left(\sum_{k=1}^{K} \exp\left(\frac{-F_k}{k_B T}\right)\right) \tag{4.2}$$

$$F_{sol}(R,\rho,T) = -k_B \ln K - k_B T \ln\left(\frac{1}{K'}\sum_{k=1}^{K'} \exp\left(\frac{-F_k(R,\rho,T)}{k_B T}\right)\right) \tag{4.3}$$

$$f_{sol}(R,\rho,T) = \frac{F_{sol}(R,\rho,T)}{\sum_\alpha m_\alpha N_\alpha} \tag{4.4}$$

where Z_{tot} is the partition function of the completely disordered system.

Because of the first-order transition between the superionic ice VII″ and the superionic ice VII′, we need two different equations of state along a given isotherm. However, due to the reduction of the superionic ice VII″ domain with the NaCl concentration, we do not have enough data to fit $f_{sol}(R, \rho, T)$ for the VII″ phase. Consequently, we fit a Vinet equation of state to $f_{sol}(R, \rho, T)$ for each concentration of NaCl on the high-pressure side of the transition only. The values of $f_{sol}(R, \rho, T)$ used for the fit and the fit parameters for each system are given in Appendix C. Again, the configurationally averaged Gibbs free energy $g_{sol}(p, T)$ is obtained from $f_{sol}(R, \rho, T)$.

Additionally, we correct the densities (volumes) for the overstimation of the volumes by the GGA. In bcc H_2O ice, no correction is needed as French and Redmer (2015) have shown that the GGA-PBE functional is in good agreement with experimental pressures up to 3 g.cm^{-3}. Consequently, we consider a linear dependence of the GGA correction for the volumes of NaCl·RH$_2$O with the NaCl concentration, between 0 and 0.3 Å^3/unit-cell (correction applied to NaCl).

Figures 4.10.a.b.c shows the specific internal energies, vibrational entropies and Helmholtz free energies of all configurations of all NaCl·RH$_2$O systems ($f_k(R, \rho, T)$). At a given volume, the internal energy increases with the concentration of NaCl whereas the vibrational entropy decreases. The first-order phase transition clearly appears as a jump in all variables between OO = 2.45 Å and OO = 2.55 Å depending on the NaCl concentration. As in pure water ice, the ice VII″ presents a larger entropy compatible with its large orientational disorder. In the Hemlholtz free energy, the discontinuity is still present but with a reduced amplitude. At any NaCl concentration and any volume, the maximum difference of Helmholtz free energy between two configurations is less than 0.2 kJ.g^{-1}. The Boltzmann averaged configurational energy is extremely close to the value corresponding to the configuration with the lowest energy, i.e. the configurations obtained from DFT at 0 K (cf. 4.2).

The configurationally averaged specific Gibbs free energies ($g_{sol}(R, p, T)$) are represented as functions of pressure in Figure 4.10.d.

Finally, we calculate the Gibbs free energy of mixing $\Delta g_{mix}(R, p, T)$ by comparison of $g_{sol}(R, p, T)$ with the Gibbs free energy of the mechanical mixture (Figure 4.11).

We find that NaCl · 126H$_2$O presents a negative Gibbs free energy of mixing (~ -0.7 kJ.g^{-1}) between 80 GPa and 200 GPa. NaCl · 62H$_2$O is on the edge of stability in the same pressure range and is likely stable below 80 GPa. At higher concentrations, NaCl·RH$_2$O becomes unstable. The volume correction does not influence these results.

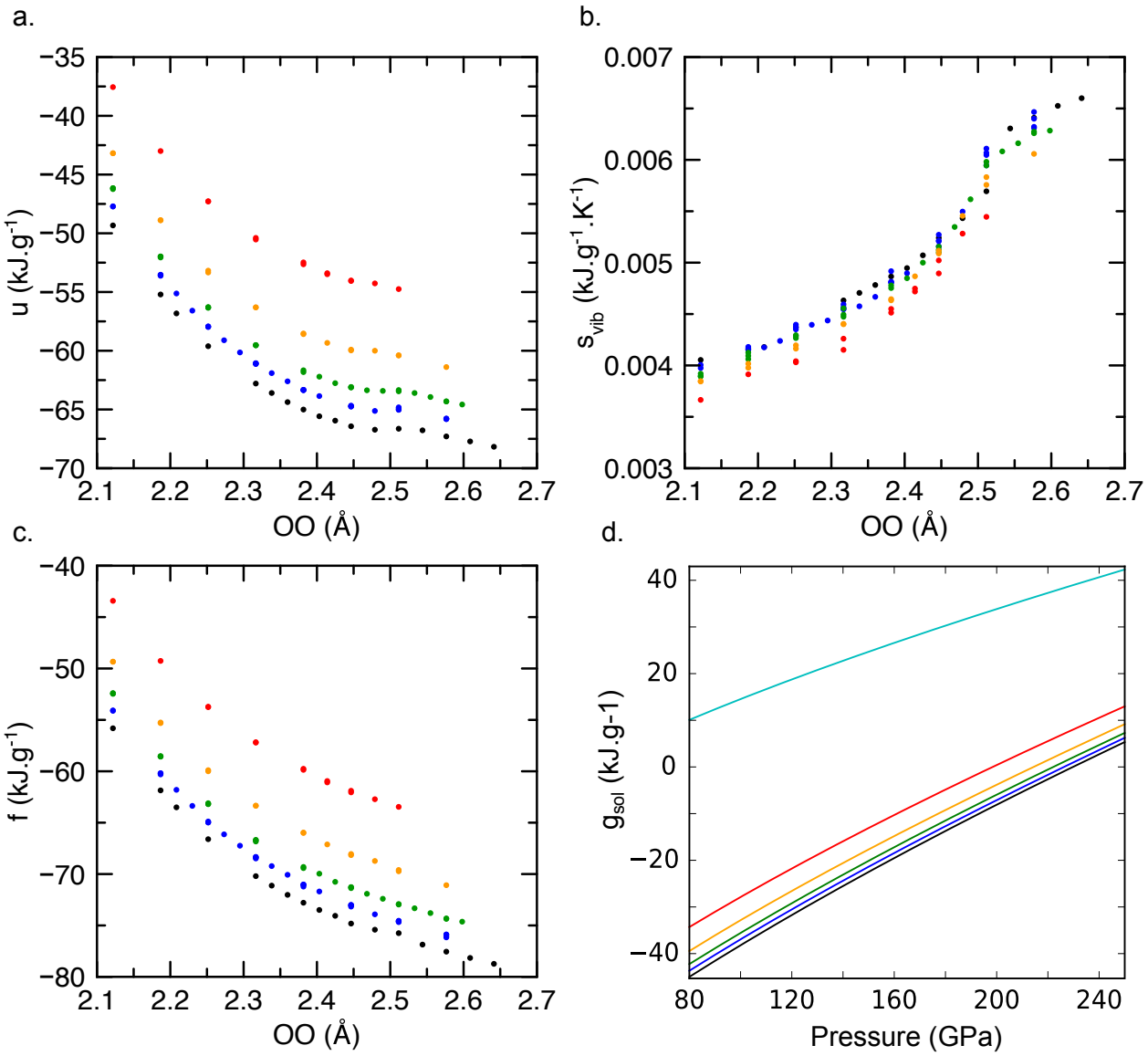

Figure 4.10: Thermodynamic variables of NaCl·RH$_2$O systems at 1600 K: black, $R = 0$; blue, $R = 126$; green, $R = 62$; orange, $R = 30$; red, $R = 14$; cyan, NaCl. a. Quantum corrected internal energies under compression. b. Vibrational entropies. c. Helmholtz free energies. d. Configurationally averaged Gibbs free energies ($g_{sol}(R, p, 1600\ K)$).

4.4.3 Complete sampling of the reduced configurational space

To compute exactly the Gibbs free energy, first, we equilibrate all the NaCl·126H$_2$O and NaCl·52H$_2$O configurations at 100 GPa and 1600 K using NpT Rahman-Parrinello molecular dynamics (Parrinello and Rahman, 1980, 1981). From the statistical equilibrium we obtain the average supercell volume corresponding to each configuration. Then, we perform the acquisition runs in the NVT ensemble at 1600 K using the average supercells. We find that 11- to 12-ps long trajectories

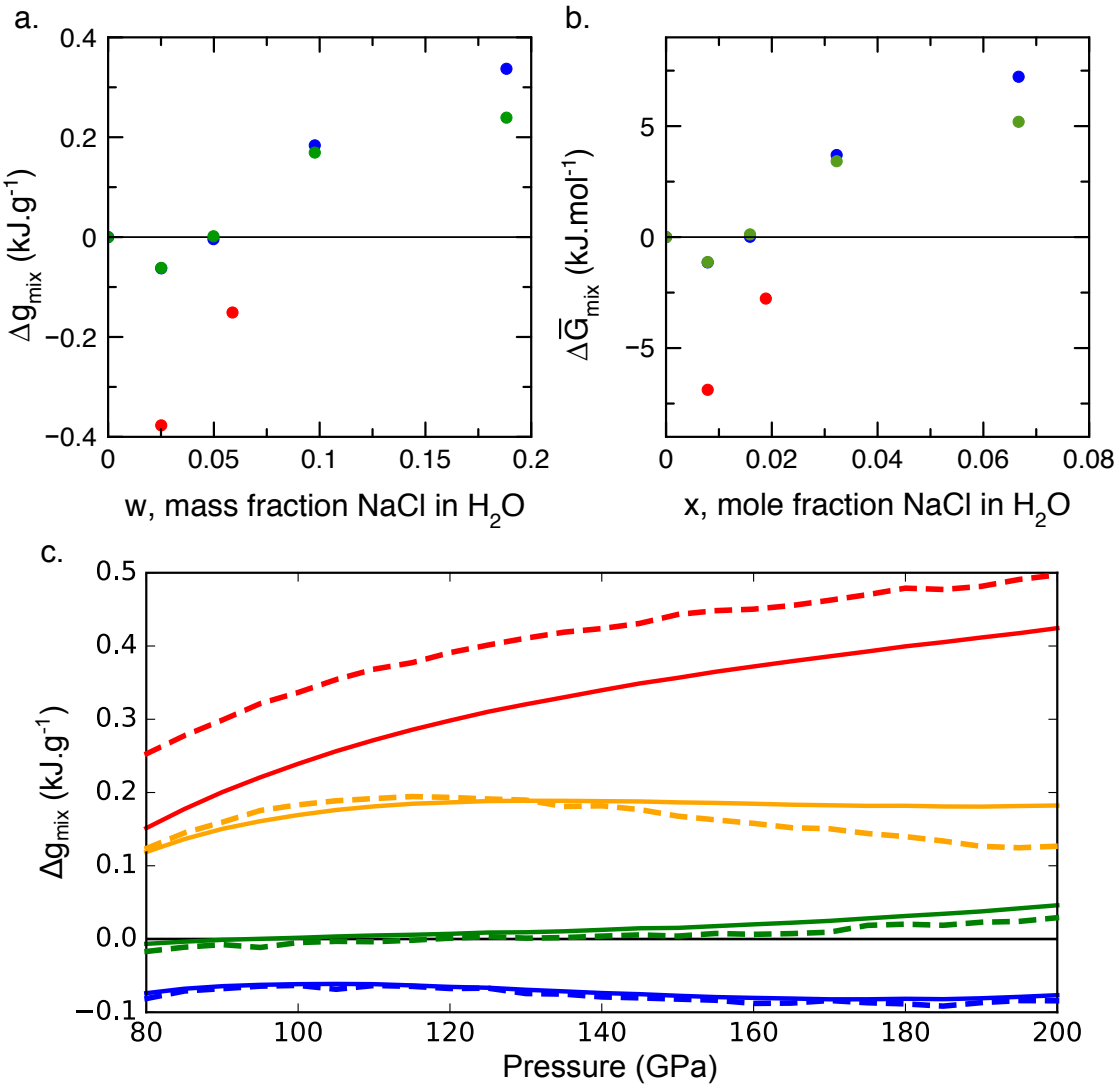

Figure 4.11: Gibbs free energy of mixing of NaCl-bearing bcc water ices at 1600 K between 80 GPa and 200 GPa. a. and b. respectively present the Gibbs free energy of mixing expressed in kJ.g^{-1} as a function of the mass fraction and the Gibbs free energy of mixing expressed in kJ.mol^{-1} as a function of the molar fraction at 100 GPa. The green (GGA corrected) and blue (non-corrected) dots correspond to the results obtained from the random sampling along the 1600 K. The red dots refer to the sampling of the reduced configurational space at 100 GPa. c. Evolution of the Gibbs free energy of mixing as a function of the pressure for each concentration of NaCl: blue, $R = 126$; green, $R = 62$; orange, $R = 30$; red, $R = 14$. Continuous and dahsed lines denote GGA corrected and non-corrected energies.

for $NaCl \cdot 126H_2O$, and 20- to 25-ps long trajectories for $NaCl \cdot 52H_2O$ ensure the convergence of the thermodynamic properties. The pressure of all the configurations is 99(0.5) GPa. We perform two additional NVT simulations for pure H_2O and NaCl at volumes corresponding to $p_{MD} = 99$ GPa. Here, we do not correct for the GGA overstimation of the volumes. We also consider that p_{MD} corresponds

to the total pressure (cf. section 4.2). The Gibbs free energy G_k of a given configuration k is thus given by:

$$G_k = U_{MD,k} + U_{qc,k} + p_{MD,k}V_k - TS_{vib,k} \tag{4.5}$$

where the upper case letters refer to the thermodynamic properties of the whole supercell. At a given concentration of NaCl, the reduced weights associated with each configuration and the Gibbs free energy of the solution (G_{sol}) are obtained from the total number of configurations, the degeneracy of each configuration and the Gibbs free energy of each configuration (cf. section 2.7).

At this point, we estimate the configurationally thermodynamic properties of $NaCl \cdot 126H_2O$ and $NaCl \cdot 52H_2O$. We find that they both have a larger volume (respectively +0.4% and +0.9%) than pure H_2O (Figure 4.12). This volume change is associated with the local distortion of the bcc sub-lattice described in section 4.3.1. However, the NaCl-bearing ices remain denser than the pure H_2O ice.

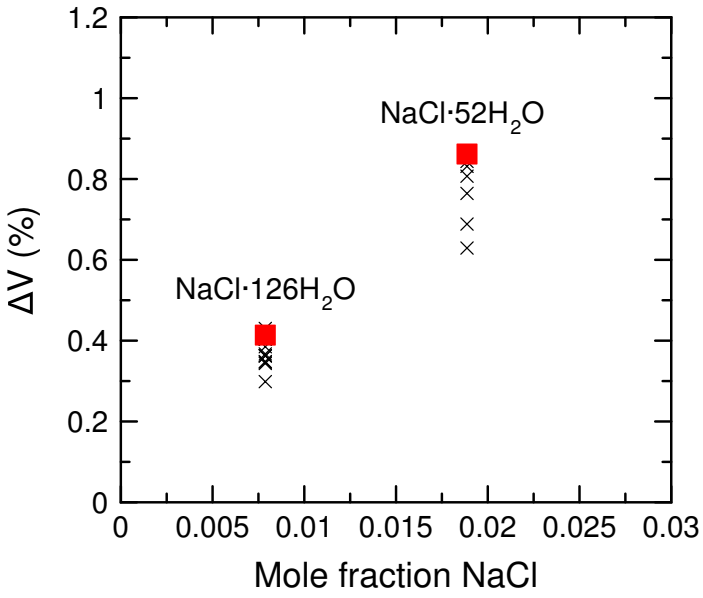

Figure 4.12: Volume difference between NaCl-bearing and pure H_2O ice. The crosses refer to the independent configurations and the red squares correspond to the configurational averages.

Additionally, in $NaCl \cdot 126H_2O$ ($NaCl \cdot 52H_2O$) the configurational entropy is 2.632 10^{-5} kJ.g^{-1}.K^{-1} (2.310 10^{-5} kJ.g^{-1}.K^{-1}). This value is reasonable as it remains smaller than 3.47 10^{-5} kJ.g^{-1}.K^{-1} (6.65 10^{-5} kJ.g^{-1}.K^{-1}), the ideal configurational entropy. Finally, we compute the specific Gibbs free energy of mixing according to equation (2.86). The red dots on

the figures 4.11.a and 4.11.b show the obtained Gibbs free energies of mixing for $NaCl \cdot 126H_2O$ and $NaCl \cdot 52H_2O$ systems. We find that both systems are thermodynamically stable. Due to the completeness of the reduced configurational space sampling, the free energies of mixing are smaller than the ones calculated from a non-converged random sampling. Consequently, the incorporation of 5.88 wt% NaCl (3.85 mol% NaCl) in the ice is still favorable.

4.5 Conclusion

In this chapter, we show that bcc water ice may include up to 5.88 wt% NaCl at 1600 K. The substitution of water molecules by Na^+ and Cl^- ions distorts the bcc sub-lattice, and results in a volume increase of $\sim 1\%$ for 5.88 wt% NaCl at 100 GPa in comparison to pure H_2O ice. The absence of $O-H\cdots Na$ and $Cl-H$ bonds breaks the hydrogen bond network which enhances the orientational disorder. Consequently, the superionic domain is largely extended towards high-pressures, and the transition between the superionic ice VII$''$ and the superionic ice VII$'$ is shifted at higher pressure with the NaCl concentration. The transition towards ice X is also found at higher pressures than in pure H_2O. Figure 4.13 presents the phase diagram of the binary $NaCl-H_2O$. We place an upper limit to the solubility of NaCl in bcc water ice, as the calculation of the true solubility requires the free energy of the phase that forms at higher NaCl concentration.

The inclusion of NaCl in bcc ices has strong implications for large H_2O-rich exoplanets. Let us consider the isentrope of a five terrestrial mass exoplanet with 50 wt% H_2O (Sotin et al., 2007). At 1600 K, the pressure reaches 80 GPa. At these conditions ice may incorporate up to 5.88 wt% (3.85 mol%) NaCl. But as soon as the salt concentration in ice reaches 2.5 wt% (0.7 mol%) the protonic conductivity enhances. Ice becomes electrically conducting. This has tremendous consequences for the behavior of the ice mantle and the entire functioning of these planets. In terms of magnetic field of the planet, the convective mass flow inside the solid ice layer is not enough to generate by itself a magnetic field. Instead, the magnetic field can be generated in the deep layers of the planets, in the convective liquid metallic core. In this case the superconducting ice layer will act on the contrary, as a screening layer (Christensen, 2006). This will attenuate or even render invisible at the surface the small-scale fluctuations of the magnetic field. The actual screening efficiency depends primarily on the thickness the ice layer via the magnetic conductance. In terms of density relations, the NaCl-bearing ice is more dense than the pure water ice. If the source of the salt, be it sodium chloride or another similar one, lies

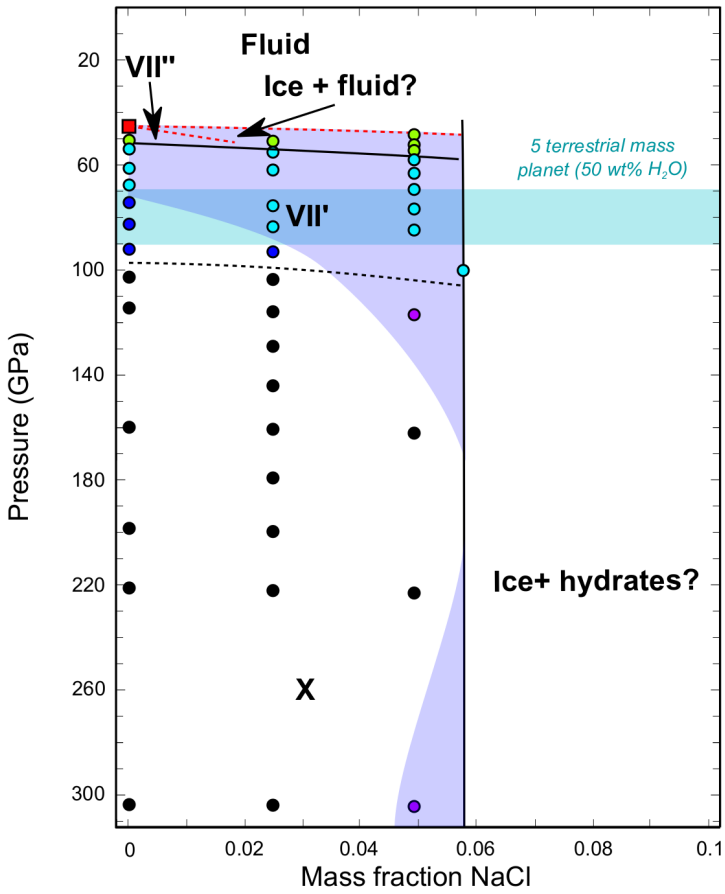

Figure 4.13: Pressure – composition phase diagram of NaCl-bearing bcc H_2O. The pressure is the classical pressure p_{MD}. The solid circles indicate the concentrations and pressures sampled in this study that present a negative Gibbs free energy. They are colored according to the different phases or regimes. The pale blue area corresponds to the superionic domain. The cyan area represents the pressure (±10 GPa) corresponding to a temperature of 1600 K in a five terrestrial mass exoplanet with 50 wt% H_2O (Sotin et al., 2007).

at the bottom of the ice mantle, at the contact with the deep silicate layer, the composition gradient would favor stratification and reduce convective flow. The description of the thermal convection relies on the thermal diffusion and on the viscosity and is prevented by the absence of rheological laws for the bcc ices. The investigation of the plasticity in ice X is the object of the next chapter.

Chapter 5

Atomistic modeling of screw dislocations in ice X

Contents

5.1 Introduction

In this chapter, we investigate the rheology of ice X at 0 K and 80 GPa. This work is done in collaboration with Pr. Philippe Carrez and Pr. Patrick Cordier from the University of Lille, France. As described in the previous chapters, ice X presents a bcc sub-lattice of oxygen atoms with the H atoms orderly and alternatively occupying four of the eight half-diagonals (Figure 5.1). It has space group $Pn\bar{3}m$ with the O and H atoms respectively located at the Wyckoff positions $2a(0,0,0)$ and $4b\left(\frac{1}{4},\frac{1}{4},\frac{1}{4}\right)$. The high-temperature ice X is predicted to exist in the icy mantles of large H_2O-rich super-Earths (Fu et al., 2009). Nevertheless the absence of rheological laws for the bcc water ices strongly limits the modelling of the internal dynamics of these bodies. The current geophysical models use the rheological laws of the ice VI, i.e. the highest-pressure ice whose rheology is accessible experimentally. Such extrapolation is likely to fail, as the ices VII and X do not present the same oxygen sub-lattice as the ice VI. This would result in an uncorrect description of the convection regimes in the icy mantles of large water-rich planets, and thus an unrealistic thermal history.

Although experimental investigation of the bcc ice rheology is extremely challenging, recent numerical developments gave insights about the dislocation creep mechanism in ice X (Journaux et al., 2014). The authors determined the easiest dislocation slip systems using a Peierls-Nabarro model

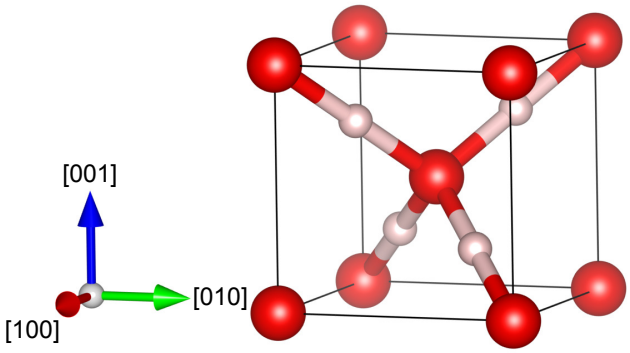

Figure 5.1: Ice X unit-cell. Red and white spheres respectively correspond to the O and H atoms.

(Peierls, 1940; Nabarro, 1947), and evaluated the shear distribution from the *ab initio* computation of the Generalized Stacking Fault (GSF) potential and its gradient (Vitek, 1968). They predicted a rheological transition in the mid-mantle of large icy exoplanets: $\langle 110 \rangle \{110\}$ is the easiest glide system below 250 GPa and $\langle 100 \rangle \{110\}$ becomes the easiest one at higher pressures. For both slip systems, screw dislocations require the highest critical stresses to activate the glide.

Additionally, bcc materials are known to present many active slip systems. At low temperature, the plasticity of bcc metals is controlled by the motion of $\langle 111 \rangle$ dislocations (Vitek, 1974). The $\langle 111 \rangle$ dislocations present a symmetric and compact nonplanar core (Ismail-Beigi and Arias, 2000; Wang et al., 2001; Li et al., 2004). Due to the inherent assumption of the Peierls-Nabarro model, the localization of the $\langle 111 \rangle$ dislocation cores cannot be apprehended from GSF calculations.

Therefore, based on the results of Journaux et al. (2014) and on the plasticity of bcc metals, we take one step further and numerically investigate the core energy and the structure of two types of screw dislocations with Burgers vectors $\mathbf{b_{110}} = a \langle 110 \rangle$ and $\mathbf{b_{111}} = a \langle 111 \rangle$ in ice X at 80 GPa at 0 K.

5.2 Atomistic modeling of the dislocations

A dislocation is a long-range anisotropic displacement field controlled by its core structure. The magnitude of the displacement decays in $1/r$, where r represents the distance to the dislocation core. This long decay makes the direct insertion of an isolated dislocation in a supercell computational prohibitive. Besides, the atomic displacement at the edge of the supercell would form an unrealistic void between two periodic images. This problem can be overcome by fixing the atomic positions at the edges of the supercell. However, in the frozen part the long-range elastic field is not the one produced

by the dislocation. Here, we avoid the problems related to fixed boundaries by inserting a dislocation quadrupole in the supercell (see Figure 5.2). This creates a mechanically stable periodic elastic field while no constrain is imposed on the atomic positions. Each dislocation type presents a stable position that minimizes its energy. The tested positions are constrained by the mechanical stability of the quadrupole. The dislocation quadrupole is expected to be stable only if the dislocation core is located in the energetically favourable site. Such approach requires large supercells so that the dislocations do not interact with each other. Moreover, the use of classical atomic potentials to relax the supercell is prohibited by the change in local electronic environment close to the dislocation core. Therefore, we employ the DFT in supercells, the largest containing 6732 atoms, which today represents an upper limit for this level of theory. All the ionic relaxations are performed at constant volume corresponding to 80 GPa in ideal ice X. To model the atoms we use the same PAW potentials for O and H as described in Chapter 2. We compute the electronic density with a cutoff energy of 875 eV for the plane-wave basis considered only at the Γ-point of the Monkhorst k-point grid (Monkhorst and Pack, 1976). We do not take into account nuclear quantum effects which are minimal at this pressure (Benoit et al., 1999; French and Redmer, 2015).

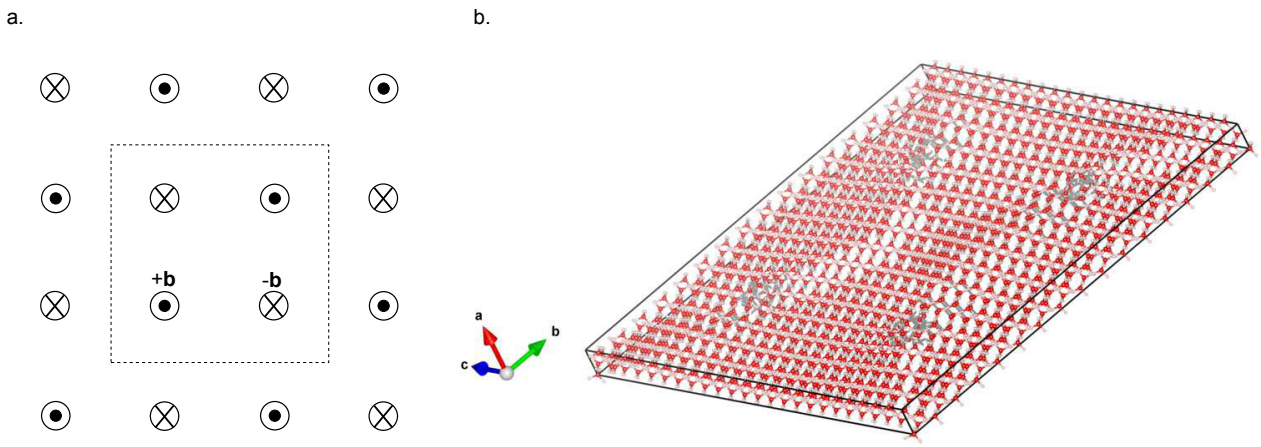

Figure 5.2: a. Quadrupolar lattice of screw dislocations. The black dots and crosses indicate the polarity of the Bugers vectors that are oriented perpendicular to the plane of the figure. The dashed line delimitates the zone in which we perform the calculations. b. Ice X supercell containing a quadrupole of screw dislocations with Burgers vectors $+\mathbf{b_{111}}$ and $-\mathbf{b_{111}}$. Red and white spheres respectively represent the O and H atoms. Thick gray line correspond to the hydrogen bonds.

To study the ⟨110⟩ dislocations we prepare a supercell with has the following lattice parameters: $\mathbf{u_1} = a\,[110] = \sqrt{2}a\,[100]$; $\mathbf{u_2} = a\,[\bar{1}10] = \sqrt{2}a\,[100]$ and $\mathbf{u_3} = a\,[001] = a\,[100]$. For the ⟨111⟩ dislocations: $\mathbf{v_1} = a\,[111] = \sqrt{3}a\,[100]$, $\mathbf{v_2} = a\,[\bar{1}10] = \sqrt{2}a\,[100]$, and $\mathbf{v_3} = a\,[\bar{1}\bar{1}2] = \sqrt{6}a\,[100]$ (Figure

5.3). In both cases, we obtain the supercell by replicating the basic block along the y and z directions. The dislocations are included such that the Burgers vectors are oriented along the x axis. We prepare the initial atomic configurations of the dislocations using the software *Atomsk* (Hirel, 2015). For the $\langle 110 \rangle$ dislocations we test several core positions labelled A, B and C (Figure 5.3.a), and evaluate their stability by computing atomic differential displacement maps (Vitek et al., 1970). In bcc materials, the screw dislocations with a Burgers vector oriented along $\langle 111 \rangle$ are known to have a stable configuration denoted "easy" and a metastable one denoted "hard" (Vitek et al., 1970; Ismail-Beigi and Arias, 2000). Their respective locations considering a given Burgers vector is given in Figure 5.3. In pratice, reversing $\mathbf{b_{111}}$ in a given easy or hard site changes the configurations.

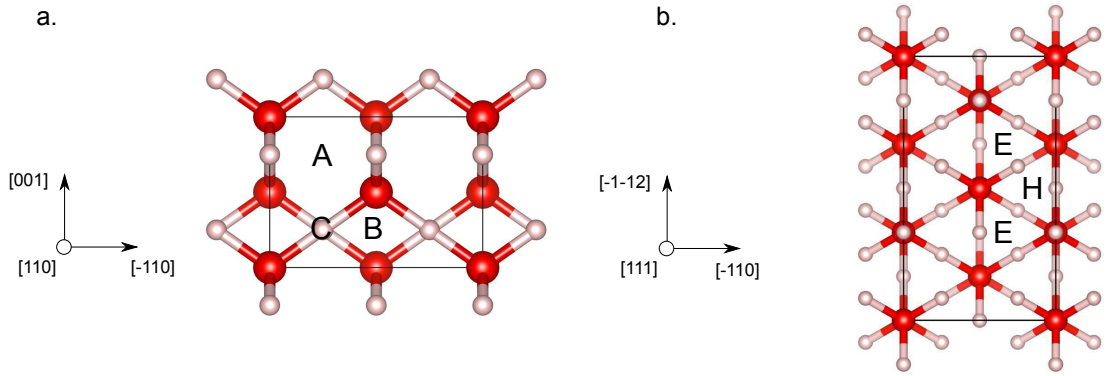

Figure 5.3: a. Basic block of the supercell in which are introduced the $\langle 110 \rangle$ dislocations. A, B and C indicate the possible locations of the dislocation core. b. Basic block of the supercell used to study the $\langle 111 \rangle$ dislocations. E and H indicates the respective locations of the easy and hard dislocation core considering the same orientation for $\mathbf{b_{111}}$.

In our periodic cells, the energy of a straight dislocation line with a Burgers vector $\mathbf{b}$ is the sum of the dislocation core energy ($E(r_c)$) and the elastic energy of the supercell:

$$E_d = E_d(r_c) + \mathcal{K}\left[\ln\left(\frac{d_1}{2}\right) + \Lambda\left(\frac{d_1}{d_2}\right)\right] \tag{5.1}$$

The core dislocation radius r_c represents a cutoff radius inside which the continuum description fails. $\mathcal{K}$ is an elastic modulus computed from the elastic constants based on the anistropic elasticity theory (Head, 1964). Here, we use the elastic constants calculated by Journaux et al. (2014) in ice X. The function $\Lambda(x)$ contains all the dislocation pair-interactions and depends only on the aspect ratio of the supercell d_1/d_2 where d_1 and d_2 correspond to the distances between two dislocations of opposite Burgers vector in respectively the y and z directions (Clouet, 2011). We compute the elastic energy

of the supercells with the code Babel[1]. We obtain the energy of the dislocation E from the DFT calculations by subtracting the energy of the perfect crystal from the energy of the supercell that contains the dislocation normalized by the number of dislocations in the supercell. The subtraction of the elastic energy from the total energy of the dislocation gives the energy of dislocation core $E(r_c)$.

5.3 Results and discussion

5.3.1 Dislocations with Burgers vector $a\langle 110\rangle$

We determine the more stable position for the dislocation with Burgers vector $a\langle 110\rangle$ by minimizing the energy of three $|\mathbf{u_1}| \times 12|\mathbf{u_2}| \times 16|\mathbf{u_3}|$ supercells (2304 atoms) that contain the dislocation quadrupoles corresponding to the core position in A, B, and C. The quadrupole remains stable during the ionic relaxation only if the dislocations cores are located on the site C. In order to check the stability of the dislocation core for finite-size effects, we perform the same calculation for one smaller and two larger supercells: $|\mathbf{u_1}| \times 8|\mathbf{u_2}| \times 12|\mathbf{u_3}|$ (1152 atoms), $|\mathbf{u_1}| \times 16|\mathbf{u_2}| \times 20|\mathbf{u_3}|$ (3840 atoms) and $|\mathbf{u_1}| \times 16|\mathbf{u_2}| \times 24|\mathbf{u_3}|$ (4608 atoms). Figure 5.4 shows the evolution of the total energy of the dislocation E as a function of the elastic energy of the dislocation for the four supercells.

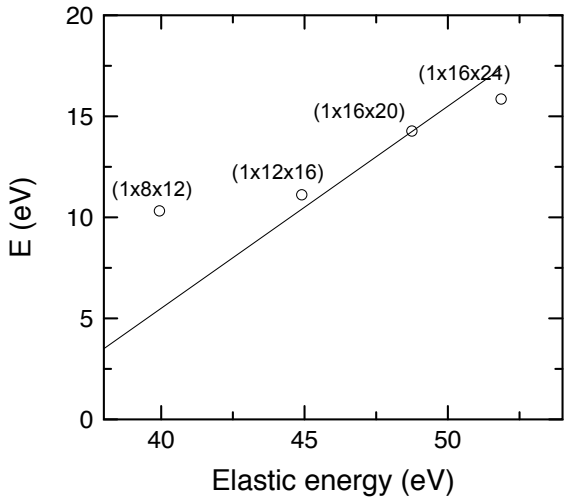

Figure 5.4: Evolution of the total energy of the dislocation with Burgers vector $a\langle 110\rangle$ as a function of the elastic energy of the dislocation. The black line represents the evolution of the total energy as function of the elastic energy considering a core energy $E(r_c = 2|\mathbf{b_{110}}|) = 0.3$ eV that matches the total energy of a dislocation in the second largest supercell.

We observe a non-linear evolution of the dislocation energy as a function of the elastic energy (i.e.

[1]Available at http://emmanuel.clouet.free.fr/Programs/Babel/.

supercell size). This indicates that in the smallest supercell the dislocations are too close to each other. Their interactions affect their core structure and thus increase the total energy of the dislocation. In the second largest supercell, the dislocation core energy is $E(r_c = 2|\mathbf{b_{110}}|) = 0.3$ eV. The computation of the differential displacement maps in the largest supercell (Figure 5.5a.) shows that the core is not symmetric and spreads in the $(1\bar{1}0)$ plane. This confirms the results of Journaux et al. (2014).

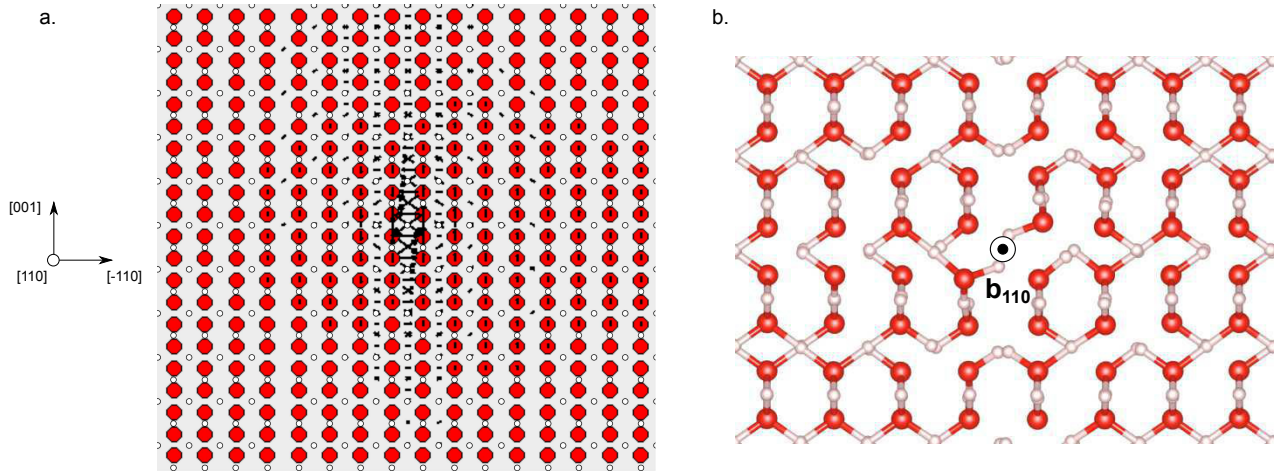

Figure 5.5: a. Differential displacement map of the $a\langle 110\rangle$ screw dislocation core. Red and white dots correspond to the positions of the O and H atoms in the perfect crystal. The black arrows indicate the direction and the magnitude of the displacement induced by the dislocations. b. Relaxed O (red spheres) and H (white spheres) atomic positions in the $\langle 110\rangle$ screw dislocation core.

The atomic positions in the relaxed core (Figure 5.5.b) reveal that the H atoms do not lie at the center of $O-H-O$ triplets as it is the case in perfect ice X. Close to the dislocation line, the $O-H$ bonds are shortened and do not point towards a neighbouring oxygen atom: $O-H\cdots O$ bonds do not exist anymore or are not linear. Thus, in this region the ice X structure is affected by a translational and an orientational disorder of the $O-H$ bonds. Further from the dislocation line, the $O-H$ bonds are also shortened but the hydrogen bonds are preserved; the orientational disorder disappears.

The projected displacement of the atoms in the $(1\bar{1}0)$ plane shows the corresponding dislocation core extension (Figure 5.6). We find a slight discrepancy between the solution of the continuum Peierls-Nabarro model and our data; the maximal disregistry does not reach the theoretical value $|\mathbf{b_{110}}|$ at the center of the core. Such anomaly may result from the possible interactions between the dislocations. The dislocation core width ζ_{110} is defined from the width at half-height of the disregistry and equals 3.4 Å which is smaller than the value of 4.8 Å obtained by Journaux et al. (2014).

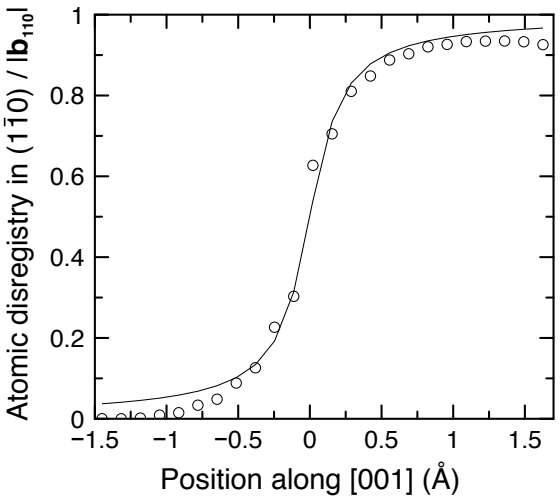

Figure 5.6: Atomic disregistry along [001] in $(1\bar{1}0)$. Circles represent the data obtained from the DFT. The black line is a fit of the solution of the continuum Peierls-Nabarro model. The origin of the x-axis is fixed at the position of the height at half width of the disregistry. It defines the limit of the dislocation core.

5.3.2 Dislocations with Burgers vector $a\langle 111\rangle$

We relax the $\langle 111\rangle$ dislocation quadrupole in three supercells with the following dimensions: $|\mathbf{v_1}| \times 13|\mathbf{v_2}| \times 7|\mathbf{v_3}|$ (3276 atoms), $|\mathbf{v_1}| \times 15|\mathbf{v_2}| \times 9|\mathbf{v_3}|$ (4860 atoms), and $|\mathbf{v_1}| \times 17|\mathbf{v_2}| \times 11|\mathbf{v_3}|$ (6732 atoms). All the quadrupoles containing easy cores are stable during the ionic relaxation. As shown in Figure 5.7 the linear dependence of the total dislocation energy with the elastic energy is respected. Considering a core radius $r_c = 2|\mathbf{b_{111}}|$, we find that the easy core energy is 7.0 eV. The corresponding differential displacement map (Figure 5.7) reveals that in easy cores the sub-lattice of O atoms is perfectly isotrope. As in bcc metals, they present an order 6 symmetry and are very localized. This contrasts with the results of Journaux et al. (2014) who describe a dissociated core for the $\langle 111\rangle$ dislocations with a bimodal distribution of the shear stress on the $\langle 111\rangle\{110\}$ slip system. This disagreement comes from the inherent assumptions of the Peierls-Nabarro model (Peierls, 1940; Nabarro, 1947) that assumes that the dislocations have a planar core related to a given slip-system. Therefore the Peierls stress required to activate the $\langle 111\rangle\{110\}$ slip system calculated in Journaux et al. (2014) is obtained from a misfit energy that does not correspond to a localized core. In the two largest supercells, the metastable hard configurations are preserved during the relaxation due to the mechanical stability imposed by the quadrupole. In a real system only the easy cores exist. In the smallest supercell, the hard cores spontaneously transform into easy cores.

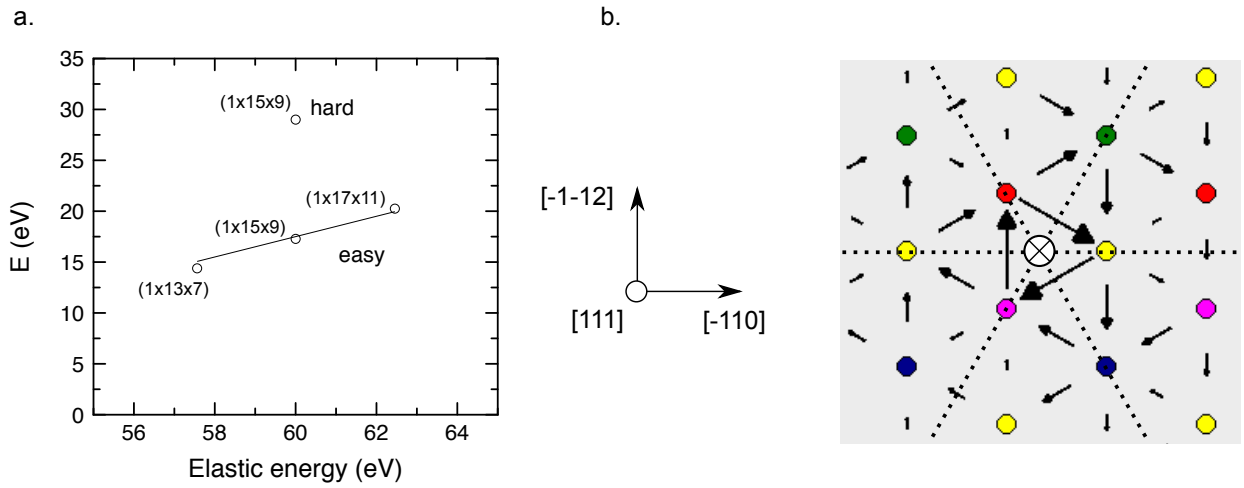

Figure 5.7: a. Evolution of the total energy of the dislocation with Burgers vector $a\langle 111\rangle$ as a function of the elastic energy of the dislocation. The black line represents the evolution of the total energy as function of the elastic energy considering a core energy of $E(r_c = 2|\mathbf{b_{111}}|) = 7.0$ eV that matches the total energy of a dislocation in the second largest supercell. b. Differential displacement map of a $\langle 111\rangle$ screw dislocation easy core. The solid circles correspond to the positions of the O atoms in the perfect crystal and are colored according to their position along $\langle 111\rangle$. The dimensions of the corresponding supercells are given between paranthesis.

Figure 5.8 reveals the perturbation of the H atom sub-lattice close to the $\langle 111\rangle$ dislocation line. In both easy and hard cores, the orientation of the $O-H-O$ triplets is quasi-unchanged in comparison to the perfect ice X. However, the $O-H-O$ symmetry is broken: H atoms form $O-H$ bonds with one O atom and $O\cdots O$ with the other. In the easy core, this results in the formation of water molecules in the second O atom cylinder around the dislocation line. In the hard core, the water molecules are formed in the first O atom cylinder around the dislocation line. In both core configurations the H atoms closest to the dislocation line remain at the center of their respective $O-H-O$ triplets.

The presence of $\langle 111\rangle$ dislocations in the ice X structures should locally enhance the dynamical disorder. Due to the small orientational disorder this effect should be smaller than in presence of $\langle 110\rangle$ dislocations.

From the energy difference between the easy and the hard configurations ($\Delta_{HE}E = E_{\text{hard}} - E_{\text{easy}}$) we determine an upper bound for the stress required to activate the dislocation mobility. $\Delta_{HE}E$ represents the highest Peierls potential barrier that the dislocation has to overcome in order to move from an easy configuration to another. Let us assume that the reaction path is a straight line along $[\bar{1}\bar{1}2]$ between the two easy sites (cf. Figure 5.3), and that the Peierls potential (V_P) has the following

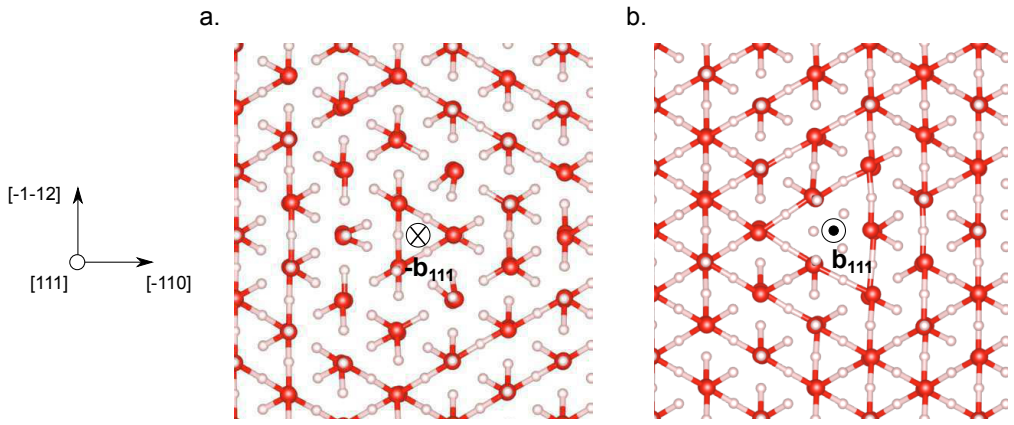

Figure 5.8: Relaxed atomic positions in the ⟨111⟩ dislocation cores. a. Configuration easy. b. Configuration hard. Red and white sphere correspond to the O and H atoms.

sinusoidal form:

$$V_P(u') = \frac{\Delta_{HE}E}{2}\left(1 - \cos\left(\frac{2\pi u'}{a'}\right)\right) \tag{5.2}$$

where u' is the reaction path coordinate and a' is the distance between the two easy sites. The Peierls potential vanishes when the dislocation is in the easy configuration, i.e. $V_P(u' = 0) = V_P(u' = a') = 0$. It is maximal at the mid-distance between the two easy sites, and we consider that $V_P(u' = a'/2) = \Delta_{HE}E$. The motion of a dislocation results from a local force ($\mathbf{F}$) that applies on the dislocation line. Its expression is given by the Peach-Koehler equation:

$$\mathbf{F} = \iota\mathbf{b} \tag{5.3}$$

where $\mathbf{b}$ is the Burgers vector of the dislocation and ι the shear stress in the direction of the dislocation line. The force requiered to overcome the Peierls potential barrier satisfies the following condition:

$$|\mathbf{F}| = \max\left(\frac{\mathrm{d}V_P(u')}{\mathrm{d}u'}\right) \tag{5.4}$$

Substituting $V_P(u')$ and $\mathbf{F}$ by their respective expressions (equations (5.2) and (5.3)) leads to the following conditions for ι:

$$\iota = \frac{\pi\Delta_{HE}E}{a'|\mathbf{b}|} \tag{5.5}$$

In the $|\mathbf{v_1}| \times 15|\mathbf{v_2}| \times 9|\mathbf{v_3}|$ supercell, $\Delta_{HE}E = 11.8$ eV.$|\mathbf{b}|^{-1} = 2.547$ eV.Å^{-1}, $a' = \sqrt{6}a\,[100]/3 =$ 2.184 Å; this gives $\iota = 127$ GPa. Therefore a maximal stress of 127 GPa is required to activate the

$\langle 111 \rangle$ dislocation motion.

5.4 Conclusion

In this chapter, we perform an *ab initio* description of the core structures of the $\langle 110 \rangle$ and $\langle 111 \rangle$ screw dislocations in ice X. The use of periodic quadrupolar arrangements of dislocations allows us to find the most stable positions for the core without any a priori assumption. We confirm that the $\langle 110 \rangle$ screw dislocations present a planar core that spreads in the $\{110\}$ planes. Then, we find that the $\langle 111 \rangle$ screw dislocations share the same core properties as the bcc metals. They present a localized non-planar core with one stable and one metastable configuration (respectively labelled easy and hard) that only depend on the orientation of the Burgers vector. As shown in the previous chapter, the bonding dynamics of the H atoms influences many properties of the bcc water ice but its effect on the plasticity remains unknown. The $O-H$ orientational and translational disorder occuring in the dislocation cores should locally change the dynamics of the $O-H\cdots O$ bonding, and enhance the hydrogen diffusion along the dislocation at high-temperature. This would result in a highly anisotropic diffusion of protons which may locally create a magnetic field. Futher calculations should first investigate the effect of the static orientational disorder in the whole H sub-lattice (ice VII), and in a second step the dislocation dynamics and the effect of the temperature.

Chapter 6

Conclusion and perspectives

In this work, we have extensively investigated the phase diagram and the properties of pure and NaCl-bearing water ices in the thermodynamic conditions relevant for planetary interiors.

Based on *ab initio* molecular dynamics simulations, we have proposed a unified phase diagram for bcc H_2O ices (cf. Figure 3.18) that relates the pressure-induced dissocation of the water molecules with the superionic domain, and that explains the anomalies recently discovered in ice VII and ice VIII around 10-15 GPa. The different phases are distinguished based on the calculations of the diffusion coefficients and on the analysis of the $O-H\cdots O$ triplet structure and dynamics. At ambient temperature, we have retrieved the pressure-induced symmetrization of the hydrogen bonds (ice VII – ice VII′ – ice X transition sequence) that completes around 80 GPa. At 600 K close to the melting line (i.e. between 7 and 15 GPa), we have presented the first *ab initio* evidence for a plastic phase in water. It presents a boundary with the ice VII whose domain closes around 750 K and 15 GPa corresponding to a kink in the melting curve. Above 750 K, the ice VII′ has a common boundary with the fluid, and superionic diffusion occurs as both the rotations of the H_2O molecules and the translation of the H atoms along the $O-H\cdots O$ bonds are activated. Below 1500 K, the proton diffusion is moderately high and the H atoms remain localized in the $O-H\cdots O$ bonds; this is the superionic regime of the ice VII′. At 1500 K, a second kink in the melting curve corresponds to the opening of the superionic ice VII″ domain. Ice VII″ presents the highest diffusion coefficients and is separated from the superionic ice VII′ by a first-order transition. As for the plastic phase, ice VII″ is dominated by the orientational disorder of the H_2O molecules. At higher pressure, we have found that above 1800 K, the complete symmetrization of the hydrogen bonds occurs in the superionic regime. The extrapolation of the boundary between the rotation-driven regimes and the translation-driven regimes to ambient temperature supports a change of bonding dynamics around 10-15 GPa at 300 K.

Next, we have investigated the structural, transport and thermodynamic properties of the NaCl-H_2O binary at 1600 K in the stability domains of bcc water ice. The spontaneous recrystallization of $NaCl\cdot RH_2O$ solutions have confirmed that both Na^+ and Cl^- ions substitute water molecules on bcc

sites. The thermodynamic properties have been computed taking into account the anharmonicity, the NQEs, a linear correction for the GGA and both random and complete sampling of the configurational space. It has revealed that up to 5.88 wt% NaCl can be included in the bcc water ice at 1600 K. The inclusion of NaCl in the ice structure increases the orientational disorder. As a consequence, it extents the superionic domain and shifts the ice VII′ – ice X transition towards high-pressures. Moreover, we have found that the NaCl-bearing ice is denser than the pure water ice. Considering NaCl-bearing ice in the interiors of H_2O-rich exoplanets may prevent the ice X to exist in their lower mantles, and increase the size of the superionic layer. Large ocean planets would present a heavy NaCl-bearing ice layer at the bottom of their ice mantles, and depending on the convection dynamics some amounts of NaCl-bearing ice would take into upwarding currents. This transport of electrolytes from the silicate-ice boundary to the liquid layers is a requirement for the development of life. Therefore, the stability of NaCl in bcc ice needs to be investigated over the range of temperature that correspond to the ice mantles of H_2O-rich exoplanets.

Last, we have performed a rigourous description of the $\langle 110 \rangle$ and $\langle 111 \rangle$ screw dislocations in ice X at 80 GPa based on large *ab initio* relaxations of periodic quadrupolar arrangements of dislocations. We have found that the $\langle 110 \rangle$ screw dislocations present planar cores that spreads in the $\{110\}$ planes, in agreement with preliminary GSF calculations (Journaux et al., 2014). We predict that the $\langle 111 \rangle$ dislocations have the same properties as in bcc metals: the dislocation core is localized and presents a stable and a metastable position depending on the orientation of the Burger vector. These features were not captured from previous GSF calculations that relied on the planar core assumption (Journaux et al., 2014). From the energy difference between the stable and the metastable core structure, we have estimated that a maximum shear stress of 127 GPa is required to activate the $\langle 111 \rangle$ dislocation motion. From these static calculations, we have shown that the dislocation cores create both orientational and translational disorder locally in the hydrogen bond network.

At this point in our work, we suggest that the priority is to continue the efforts to build a rheological law for the bcc water ices. This goes through the investigation of the effect of the different H-disorders on the dislocation core properties at finite temperature. The modeling of the dynamics of the dislocations requires a too large number of atom to be inquired from *ab initio* molecular dynamics; a multi-scale approach involving classical potentials is necessary. Ultimately, the resulting strain-stress relations would allow to model the convection in the ice mantles of large H_2O-rich planets. Then, more realistic H_2O-based compositions have to be considered. Concerning the NaCl-H_2O binary, the

stability of NaCl in the bcc ices and its effects on the ice properties should be explored over the whole stability domain of bcc ices. The onset of orientational disorder caused by the inclusion of the Na^+ and Cl^- ions should extend the plastic ice domain towards high pressures. The determination of the structure and the thermodynamics properties of the hydrates that forms when increasing the concentration of NaCl would allow to compute the effective solubility of NaCl in the ice. Finally, above 6 GPa, the melting of the NaCl-H_2O mixture remains an open question.

Bibliography

Ahart, M., Karandikar, A., Gramsch, S., Boehler, R., and Hemley, R. J. (2014). High P–T Brillouin scattering study of H_2O melting to 26 GPa. *High Pressure Research*, 34(3):327–336. (Cited on pages 9, 10 and 82.)

Ahart, M., Somayazulu, M., Gramsch, S. A., Boehler, R., Mao, H.-k., and Hemley, R. J. (2011). Brillouin scattering of H_2O ice to megabar pressures. *The Journal of chemical physics*, 134(12):124517. (Cited on page 73.)

Allan, N., Barrera, G., Fracchia, R., Lavrentiev, M. Y., Taylor, M., Todorov, I., and Purton, J. (2001). Free energy of solid solutions and phase diagrams via quasiharmonic lattice dynamics. *Physical Review B*, 63(9):094203. (Cited on pages 54 and 55.)

Allen, M. P. and Tildesley, D. J. (1989). *Computer Simulation of Liquids*. Clarendon Press, New York, NY, USA. (Cited on pages 20, 21, 31 and 33.)

Andersen, H. C. (1980). Molecular dynamics simulations at constant pressure and/or temperature. *The Journal of Chemical Physics*, 72(4):2384–2393. (Cited on page 30.)

Aoki, K., Yamawaki, H., Sakashita, M., and Fujihisa, H. (1996). Infrared absorption study of the hydrogen-bond symmetrization in ice to 110 GPa. *Phys. Rev. B*, 54. (Cited on pages 8 and 9.)

Aragones, J. and Vega, C. (2009). Plastic crystal phases of simple water models. *The Journal of chemical physics*, 130(24):244504. (Cited on pages 6, 7, 66 and 81.)

Asahara, Y., Hirose, K., Ohishi, Y., Hirao, N., and Murakami, M. (2010). Thermoelastic properties of ice VII and its high-pressure polymorphs: Implications for dynamics of cold slab subduction in the lower mantle. *Earth and Planetary Science Letters*, 299(3):474–482. (Cited on page 73.)

Ballaran, T. B., Liu, J., Dubrovinsky, L. S., Caracas, R., and Crichton, W. (2009). High-pressure ferroelastic phase transition in aluminosilicate hollandite. *Physical Review B*, 80(21):214104. (Cited on page 71.)

Becke, A. D. and Edgecombe, K. E. (1990). A simple measure of electron localization in atomic and molecular systems. *The Journal of chemical physics*, 92(9):5397–5403. (Cited on page 71.)

Benoit, M., Bernasconi, M., Focher, P., and Parrinello, M. (1996). New high-pressure phase of ice. *Physical Review Letters*, 76(16):2934. (Cited on page 9.)

Benoit, M. and Marx, D. (2005). The shapes of protons in hydrogen bonds depend on the bond length. *ChemPhysChem*, 6(9):1738–1741. (Cited on pages 60 and 63.)

Benoit, M., Marx, D., and Parrinello, M. (1998). Tunnelling and zero-point motion in high-pressure ice. *Nature*, 392(6673):258–261. (Cited on pages 8 and 63.)

Benoit, M., Marx, D., and Parrinello, M. (1999). The role of quantum effects and ionic defects in high-density ice. *Solid State Ionics*, 125. (Cited on pages 8, 63 and 113.)

Benoit, M., Romero, A. H., and Marx, D. (2002). Reassigning Hydrogen-Bond Centering in Dense Ice. *Phys. Rev. Lett.*, 89. (Cited on pages 8 and 63.)

Berens, P. H., Mackay, D. H. J., White, G. M., and Wilson, K. R. (1983). Thermodynamics and quantum corrections from molecular dynamics for liquid water. *The Journal of Chemical Physics*, 79(5):2375–2389. (Cited on page 38.)

Bernal, J. D. and Fowler, R. H. (1933). A Theory of Water and Ionic Solution, with Particular Reference to Hydrogen and Hydroxyl Ions. *The Journal of Chemical Physics*, 1(8). (Cited on page 4.)

Bloch, F. (1928). Quantum mechanics of electrons in crystal lattices. *Z. Phys*, 52:555–600. (Cited on page 26.)

Blöchl, P. E. (1994). Projector augmented-wave method. *Phys. Rev. B*, 50. (Cited on pages 27 and 32.)

Born, M. (1940). On the stability of crystal lattices. I. *Mathematical Proceedings of the Cambridge Philosophical Society*, 36(02):160–172. (Cited on page 53.)

Born, M. and Oppenheimer, R. (1927). Zur Quantentheorie der Molekeln. *Annalen der Physik*, 389(20). (Cited on pages 21 and 22.)

Bove, L. E., Gaal, R., Raza, Z., Ludl, A.-A., Klotz, S., Saitta, A. M., Goncharov, A. F., and Gillet, P. (2015). Effect of salt on the H-bond symmetrization in ice. *Proceedings of the National Academy of Sciences*, 112(27):8216–8220. (Cited on pages 17, 91, 100 and 101.)

Boyce, J. B. and Huberman, B. A. (1979). Superionic conductors: transitions, structures, dynamics. *Physics Reports*, 51(4):189–265. (Cited on pages 12 and 58.)

Bridgman, P. (1937). The phase diagram of water to 45,000 kg/cm^2. *The Journal of Chemical Physics*, 5(12):964–966. (Cited on page 5.)

Bronstein, Y., Depondt, P., Bove, L. E., Gaal, R., Saitta, A. M., and Finocchi, F. (2016). Quantum versus classical protons in pure and salty ice under pressure. *Physical Review B*, 93(2):024104. (Cited on pages 97 and 101.)

Bronstein, Y., Depondt, P., Finocchi, F., and Saitta, A. M. (2014). Quantum-driven phase transition in ice described via an efficient Langevin approach. *Phys. Rev. B*, 89:214101. (Cited on pages 8, 31 and 63.)

Bruneval, F., Donadio, D., and Parrinello, M. (2007). Molecular dynamics study of the solvation of calcium carbonate in water. *The Journal of Physical Chemistry B*, 111(42):12219–12227. (Cited on page 16.)

Brush, S. G. (2013). *Kinetic Theory: The Chapman–Enskog Solution of the Transport Equation for Moderately Dense Gases*, volume 3. Elsevier. (Cited on page 41.)

Car, R. (2006). Chapter 3 Ab initio Molecular Dynamics: Dynamics and Thermodynamic Properties. In Louie, S. G. and Cohen, M. L., editors, *Conceptual Foundations of Materials A Standard Model for Ground- and Excited-State Properties*, volume 2 of *Contemporary Concepts of Condensed Matter Science*. Elsevier. (Cited on page 22.)

Caracas, R. (2008). Dynamical Instabilities of Ice X. *Phys. Rev. Lett.*, 101. (Cited on pages 9, 71, 74 and 75.)

Carnahan, N. F. and Starling, K. E. (1969). Equation of state for nonattracting rigid spheres. *The Journal of Chemical Physics*, 51(2):635–636. (Cited on page 41.)

Carpenter, M. A., Hemley, R. J., and Mao, H.-k. (2000). High-pressure elasticity of stishovite and the $P4_2/mnm$ – Pnnm phase transition. *Journal of Geophysical Research: Solid Earth*, 105(B5):10807–10816. (Cited on page 71.)

Cavazzoni, C., Chiarotti, G. L., Scandolo, S., Tosatti, E., Bernasconi, M., and Parrinello, M. (1999). Superionic and metallic states of water and ammonia giant planet conditions. *Science*, 283. (Cited on pages 7, 12, 13, 15 and 81.)

Chapman, S. and Cowling, T. G. (1939). *The Mathematical Theory of Non-uniform Gases*. Cambridge University Press. (Cited on page 41.)

Chau, R., Mitchell, A., Minich, R., and Nellis, W. (2001). Electrical conductivity of water compressed dynamically to pressures of 70–180 GPa (0.7–1.8 Mbar). *The Journal of Chemical Physics*, 114(3):1361–1365. (Cited on page 11.)

Chevrier, V. F. and Rivera-Valentin, E. G. (2012). Formation of recurring slope lineae by liquid brines on present-day Mars. *Geophysical Research Letters*, 39(21). (Cited on page 16.)

Christensen, U. R. (2006). A deep dynamo generating Mercury's magnetic field. *Nature*, 444(7122):1056–1058. (Cited on page 108.)

Clouet, E. (2011). Dislocation core field. I. Modeling in anisotropic linear elasticity theory. *Physical Review B*, 84(22):224111. (Cited on page 114.)

Connerney, J., Acuña, M. H., and Ness, N. F. (1987). The magnetic field of Uranus. *Journal of Geophysical Research: Space Physics*, 92(A13):15329–15336. (Cited on page 13.)

Connerney, J., Acuña, M. H., and Ness, N. F. (1991). The magnetic field of Neptune. *Journal of Geophysical Research: Space Physics*, 96(S01):19023–19042. (Cited on page 13.)

Daniel, I., Oger, P., and Winter, R. (2006). Origins of life and biochemistry under high-pressure conditions. *Chemical Society Reviews*, 35(10):858–875. (Cited on page 15.)

Datchi, F., Loubeyre, P., and LeToullec, R. (2000). Extended and accurate determination of the melting curves of argon, helium, ice (H_2O), and hydrogen (H_2). *Phys. Rev. B*, 61. (Cited on page 9.)

De Sanctis, M., Raponi, A., Ammannito, E., Ciarniello, M., Toplis, M., McSween, H., Castillo-Rogez, J., Ehlmann, B., Carrozzo, F., Marchi, S., et al. (2016). Bright carbonate deposits as evidence of aqueous alteration on (1) Ceres. *Nature*, 536(7614):54–57. (Cited on page 16.)

Dellago, C., Geissler, P. L., Chandler, D., Hutter, J., and Parrinello, M. (2002). Comment on "Dissociation of water under pressure". *Physical review letters*, 89(19):199601. (Cited on page 11.)

Desjarlais, M. P. (2013). First-principles calculation of entropy for liquid metals. *Phys. Rev. E*, 88:062145. (Cited on pages 38, 41, 42, 43 and 48.)

Dion, M., Rydberg, H., Schröder, E., Langreth, D. C., and Lundqvist, B. I. (2004). Van der Waals Density Functional for General Geometries. *Phys. Rev. Lett.*, 92:246401. (Cited on page 25.)

Dubrovinskaia, N. and Dubrovinsky, L. (2003). Melting curve of water studied in externally heated diamond-anvil cell. *High Pressure Research*, 23(3):307–311. (Cited on page 9.)

Dubrovinsky, L. and Dubrovinskaia, N. (2007). Melting of ice VII and new high-pressure, high-temperature amorphous ice. *Geological Society of America Special Papers*, 421:105–113. (Cited on page 10.)

Enskog, D. (1911). Bemerkungen zu einer Fundamentalgleichung in der kinetischen Gastheorie. *Physik. Zs. Leipzig*, 12:533–539. (Cited on page 41.)

Fanale, F., Li, Y.-H., De Carlo, E., Farley, C., Sharma, S., Horton, K., and Granahan, J. (2001). An experimental estimate of Europa's "ocean" composition independent of Galileo orbital remote sensing. *Journal of Geophysical Research: Planets*, 106(E7):14595–14600. (Cited on page 17.)

Fei, Y., Mao, H.-k., and Hemley, R. J. (1993). Thermal expansivity, bulk modulus, and melting curve of H_2O–ice VII to 20 GPa. *The Journal of chemical physics*, 99(7):5369–5373. (Cited on page 9.)

Feynman, R. P. (1939). Forces in Molecules. *Phys. Rev.*, 56:340–343. (Cited on page 29.)

Flores-Livas, J. A., Sanna, A., Davydov, A., Goedecker, S., and Marques, M. A. L. (2016). Emergence of superconductivity in doped H_2O ice at high pressure. (Cited on page 71.)

Frank, M. R., Aarestad, E., Scott, H. P., and Prakapenka, V. B. (2013). A comparison of ice VII formed in the H_2O, NaCl-H_2O, and CH_3OH-H_2O systems: Implications for H_2O-rich planets. *Physics of the Earth and Planetary Interiors*, 215. (Cited on page 17.)

Frank, M. R., Fei, Y., and Hu, J. (2004). Constraining the equation of state of fluid H_2O to 80 GPa using the melting curve, bulk modulus, and thermal expansivity of Ice VII. *Geochimica et cosmochimica acta*, 68. (Cited on page 9.)

Frank, M. R., Runge, C. E., Scott, H. P., Maglio, S. J., Olson, J., Prakapenka, V. B., and Shen, G. (2006). Experimental study of the NaCl-H_2O system up to 28 GPa: Implications for ice-rich planetary bodies. *Physics of the Earth and Planetary Interiors*, 155. (Cited on pages 17, 18 and 91.)

French, M., Desjarlais, M. P., and Redmer, R. (2016). Ab initio calculation of thermodynamic potentials and entropies for superionic water. *Phys. Rev. E*, 93:022140. (Cited on pages 13, 15, 38, 42, 77, 78, 79 and 80.)

French, M., Hamel, S., and Redmer, R. (2011). Dynamical srceening and ionic conductivity in water from ab initio simulations. *Physical Review Letters*, 107. (Cited on pages 11, 13, 14, 35, 36, 37 and 59.)

French, M., Mattsson, T. R., Nettelmann, N., and Redmer, R. (2009). Equation of state and phase diagram of water at ultrahigh pressures as in planetary interiors. *Physical Review B*, 79(5):054107. (Cited on pages 15, 68 and 69.)

French, M., Mattsson, T. R., and Redmer, R. (2010). Diffusion and electrical conductivity in water at ultrahigh pressures. *Physical Review B*, 82(17):174108. (Cited on pages 11, 13 and 58.)

French, M. and Redmer, R. (2015). Construction of a thermodynamic potential for the water ices VII and X. *Phys. Rev. B*, 91:014308. (Cited on pages 38, 77, 78, 79, 80, 81, 104 and 113.)

Fu, R., O'Connell, R. J., and Sasselov, D. D. (2009). The interior dynamics of water planets. *The Astrophysical Journal*, 708(2):1326. (Cited on page 111.)

Fukui, H., Hiraoka, N., Hirao, N., Aoki, K., and Akahama, Y. (2016). Suppression of X-ray-induced dissociation of H_2O molecules in dense ice under pressure. *Scientific reports*, 6. (Cited on page 83.)

Giauque, W. and Ashley, M. F. (1933). Molecular rotation in ice at 10 K. Free energy of formation and entropy of water. *Physical review*, 43(1):81. (Cited on page 5.)

Goldman, N., Fried, L. E., Kuo, I.-F. W., and Mundy, C. J. (2005). Bonding in superionic phase of water. *Physical Review Letters*, 94. (Cited on pages 11, 13, 15, 58, 62, 68 and 82.)

Goncharov, A. F. and Crowhurst, J. (2007). Proton delocalization under extreme conditions of high pressure and temperature. *Phase Transitions*, 80(10-12):1051–1072. (Cited on pages 6, 9, 13, 15 and 82.)

Goncharov, A. F., Goldman, N., Fried, L. E., Crowhurst, J. C., Kuo, I.-F. W., Mundy, C. J., and Zaug, J. M. (2005). Dynamic ionization of water under extreme conditions. *Physical review letters*, 94(12):125508. (Cited on pages 9, 11, 13, 15, 68 and 82.)

Goncharov, A. F., Sanloup, C., Goldman, N., Crowhurst, J. C., Bastea, S., Howard, W., Fried, L. E., Guignot, N., Mezouar, M., and Meng, Y. (2009). Dissociative melting of ice VII at high pressure. *The Journal of chemical physics*, 130(12):124514. (Cited on pages 9, 11, 13, 68 and 82.)

Goncharov, A. F., Struzhkin, V. V., Mao, H., and Hemley, R. J. (1999). Raman Spectroscopy of Dense H_2O and the Transition to Symmetric Hydrogen Bonds. *Phys. Rev. Lett.*, 83. (Cited on pages 8 and 9.)

Goncharov, A. F., Struzhkin, V. V., Somayazulu, M. S., Hemley, R. J., and Mao, H. K. (1996). Compression of ice to 210 gigapascals: infrared evidence for a symmetric hydrogen-bonded phase. *Science*. (Cited on pages 7, 8 and 9.)

Grau-Crespo, R., Hamad, S., Catlow, C., and De Leeuw, N. (2007). Symmetry-adapted configurational modelling of fractional site occupancy in solids. *Journal of Physics: Condensed Matter*, 19(25):256201. (Cited on page 55.)

Green, M. S. (1954). Markoff random processes and the statistical mechanics of time-dependent phenomena. II. Irreversible processes in fluids. *The Journal of Chemical Physics*, 22(3):398–413. (Cited on page 34.)

Gudipati, M. S. and Castillo-Rogez, J. (2012). *The science of solar system ices*, volume 356. Springer Science & Business Media. (Cited on page 5.)

Guthrie, M., Boehler, R., Tulk, C. A., Molaison, J. J., dos Santos, A. M., Li, K., and Hemley, R. J. (2013). Neutron diffraction observations of interstitial protons in dense ice. *Proceedings of the National Academy of Sciences*, 110(26):10552–10556. (Cited on page 8.)

Head, A. (1964). The [111] dislocation in a cubic crystal. *physica status solidi (b)*, 6(2):461–465. (Cited on page 114.)

Hermann, A., Ashcroft, N. W., and Hoffmann, R. (2013). Isotopic differentiation and sublattice melting in dense dynamic ice. *Physical Review B*, 88(21):214113. (Cited on pages 9 and 15.)

Hernandez, J.-A. and Caracas, R. (2016). Superionic-Superionic Phase Transitions in Body-Centered Cubic H_2O Ice. *Physical Review Letters*, 117(13):135503. (Cited on pages 13, 78 and 80.)

Himoto, K., Matsumoto, M., and Tanaka, H. (2011). Lattice-and network-structure in plastic ice. *Physical Chemistry Chemical Physics*, 13(44):19876–19881. (Cited on page 81.)

Himoto, K., Matsumoto, M., and Tanaka, H. (2014). Yet another criticality of water. *Physical Chemistry Chemical Physics*, 16(11):5081–5087. (Cited on pages 6 and 81.)

Hirel, P. (2015). Atomsk: a tool for manipulating and converting atomic data files. *Computer Physics Communications*, 197:212–219. (Cited on page 114.)

Hohenberg, P. and Kohn, W. (1964). Inhomogeneous Electron Gas. *Phys. Rev.*, 136:B864–B871. (Cited on page 23.)

Holmes, N., Nellis, W., Graham, W., and Walrafen, G. (1985). Spontaneous Raman scattering from shocked water. *Physical review letters*, 55(22):2433. (Cited on page 11.)

Holzapfel, W. (1972). On the symmetry of the hydrogen bonds in ice VII. *The Journal of Chemical Physics*, 56(2):712–715. (Cited on page 7.)

Hoover, W. G. (1985). Canonical dynamics: Equilibrium phase-space distributions. *Phys. Rev. A*, 31. (Cited on page 29.)

Hull, S. (2004). Superionics: crystal structures and conduction processes. *Reports on Progress in Physics*, 67. (Cited on page 12.)

Hultgren, R., Desai, P. D., Hawkins, D. T., Gleiser, M., and Kelley, K. K. (1973). Selected values of the thermodynamic properties of the elements. Technical report, DTIC Document. (Cited on page 48.)

Iess, L., Stevenson, D., Parisi, M., Hemingway, D., Jacobson, R., Lunine, J., Nimmo, F., Armstrong, J., Asmar, S., Ducci, M., et al. (2014). The gravity field and interior structure of Enceladus. *Science*, 344(6179):78–80. (Cited on page 16.)

Iitaka, T., Fukui, H., Li, Z., Hiraoka, N., and Irifune, T. (2015). Pressure-induced dissociation of water molecules in ice VII. *Scientific reports*, 5. (Cited on page 8.)

Ismail-Beigi, S. and Arias, T. (2000). Ab initio study of screw dislocations in Mo and Ta: a new picture of plasticity in bcc transition metals. *Physical Review Letters*, 84(7):1499. (Cited on pages 112 and 114.)

Izawa, M., Nesbitt, H., MacRae, N., and Hoffman, E. (2010). Composition and evolution of the early oceans: evidence from the Tagish Lake meteorite. *Earth and Planetary Science Letters*, 298(3):443–449. (Cited on pages 16 and 17.)

Ji, M., Umemoto, K., Wang, C.-Z., Ho, K.-M., and Wentzcovitch, R. M. (2011). Ultrahigh-pressure phases of H_2O ice predicted using an adaptive genetic algorithm. *Physical Review B*, 84(22):220105. (Cited on page 9.)

Journaux, B., Caracas, R., Carrez, P., Gouriet, K., Cordier, P., and Daniel, I. (2014). Elasticity and dislocations in ice X under pressure. *Physics of the Earth and Planetary Interiors*, 236:10–15. (Cited on pages 71, 73, 111, 112, 114, 116, 117 and 122.)

Journaux, B., Daniel, I., Caracas, R., Montagnac, G., and Cardon, H. (2013). Influence of NaCl on ice {VI} and ice {VII} melting curves up to 6 GPa, implications for large icy moons. *Icarus*, 226. (Cited on pages 9, 17 and 91.)

Kamb, B. and Davis, B. L. (1964). Ice VII, the densest form of ice. *Proceedings of the National Academy of Sciences*, 52(6):1433–1439. (Cited on page 7.)

Katoh, E., Yamawaki, H., Fujihisa, H., Sakashita, M., and Aoki, K. (2002). Protonic diffusion in high-pressure ice VII. *Science*, 295(5558):1264–1266. (Cited on page 15.)

Keen, D. A. (2002). Disordering phenomena in superionic conductors. *Journal of Physics: Condensed Matter*, 14(32):R819. (Cited on page 12.)

Kimura, T., Kuwayama, Y., and Yagi, T. (2014). Melting temperatures of H_2O up to 72 GPa measured in a diamond anvil cell using CO_2 laser heating technique. *The Journal of chemical physics*, 140(7):074501. (Cited on page 9.)

Kimura, T., Ozaki, N., Sano, T., Okuchi, T., Sano, T., Shimizu, K., Miyanishi, K., Terai, T., Kakeshita, T., Sakawa, Y., et al. (2015). P-ρ-T measurements of H_2O up to 260 GPa under laser-driven shock loading. *The Journal of chemical physics*, 142(16):164504. (Cited on page 13.)

Kirkwood, J. G. (1935). Statistical mechanics of fluid mixtures. *The Journal of Chemical Physics*, 3(5):300–313. (Cited on page 62.)

Kirkwood, J. G. and Buff, F. P. (1951). The statistical mechanical theory of solutions. I. *The Journal of chemical physics*, 19(6):774–777. (Cited on page 44.)

Kittel, C. and Kroemer, H. (1998). *Thermal physics*. AAPT. (Cited on page 20.)

Klimeš, J. c. v., Bowler, D. R., and Michaelides, A. (2011). Van der Waals density functionals applied to solids. *Phys. Rev. B*, 83:195131. (Cited on pages 25 and 138.)

Klotz, S., Bove, L. E., Strässle, T., Hansen, T. C., and Saitta, A. M. (2009). The preparation and structure of salty ice VII under pressure. *Nature Materials*, 8. (Cited on pages 17 and 91.)

Klotz, S., Datchi, F., and Ninet, S. (2010). Is there a plastic phase in ice VII at high pressure and high temperature? *ESRF report*. (Cited on pages 9, 10 and 82.)

Klotz, S., Komatsu, K., Pietrucci, F., Kagi, H., Ludl, A.-A., Machida, S., Hattori, T., Sano-Furukawa, A., and Bove, L. (2016). Ice VII from aqueous salt solutions: From a glass to a crystal with broken H-bonds. *Scientific Reports*, 6. (Cited on pages 17 and 91.)

Knudson, M. D., Desjarlais, M. P., Lemke, R., Mattsson, T., French, M., Nettelmann, N., and Redmer, R. (2012). Probing the interiors of the ice giants: Shock compression of water to 700 GPa and 3.8 g/cm^3. *Physical Review Letters*, 108(9):091102. (Cited on page 13.)

Kohn, W. and Sham, L. J. (1965). Self-Consistent Equations Including Exchange and Correlation Effects. *Phys. Rev.*, 140:A1133–A1138. (Cited on page 23.)

Kresse, G. and Furthmüller, J. (1996a). Efficiency of ab-initio total energy calculations for metals and semiconductors using a plane-wave basis set. *Comput. Mat. Sci.*, 6. (Cited on pages 27 and 31.)

Kresse, G. and Furthmüller, J. (1996b). Efficient iterative schemes for ab initio total-energy calculations using a plane-wave basis set. *Phys. Rev. B*, 54. (Cited on page 31.)

Kresse, G. and Joubert, D. (1999). From ultrasoft pseudopotentials to the projector augmented-wave method. *Physical Review B*, 59(3):1758. (Cited on page 32.)

Kubo, R. (1957). Statistical-mechanical theory of irreversible processes. I. General theory and simple applications to magnetic and conduction problems. *Journal of the Physical Society of Japan*, 12(6):570–586. (Cited on page 34.)

Lai, P.-K., Hsieh, C.-M., and Lin, S.-T. (2012). Rapid determination of entropy and free energy of mixtures from molecular dynamics simulations with the two-phase thermodynamic model. *Physical Chemistry Chemical Physics*, 14(43):15206–15213. (Cited on pages 38, 44 and 46.)

Li, J., Wang, C.-Z., Chang, J.-P., Cai, W., Bulatov, V. V., Ho, K.-M., and Yip, S. (2004). Core energy and Peierls stress of a screw dislocation in bcc molybdenum: A periodic-cell tight-binding study. *Physical Review B*, 70(10):104113. (Cited on page 112.)

Lin, J.-F., Militzer, B., Struzhkin, V. V., Gregoryanz, E., Hemley, R. J., and Mao, H.-k. (2004). High pressure-temperature Raman measurements of H_2O melting to 22 GPa and 900 K. *The Journal of chemical physics*, 121(17):8423–8427. (Cited on page 9.)

Lin, S.-T., Blanco, M., and III, W. A. G. (2003). The two-phase model for calculating thermodynamic properties of liquids from molecular dynamics: Validation for the phase diagram of Lennard-Jones fluids. *The Journal of Chemical Physics*, 119(22):11792–11805. (Cited on pages 38, 41 and 46.)

Ludl, A.-A., Bove, L., Corradini, D., Saitta, A., Salanne, M., Bull, C., and Klotz, S. (2017). Probing ice VII crystallization from amorphous NaCl–D_2O solutions at gigapascal pressures. *Physical Chemistry Chemical Physics*. (Cited on pages 17, 91 and 92.)

Lyzenga, G., Ahrens, T. J., Nellis, W., and Mitchell, A. (1982). The temperature of shock-compressed water. *The Journal of Chemical Physics*, 76(12):6282–6286. (Cited on page 11.)

Martin, C. (2017). Water structure and science. (Cited on page 5.)

Martinez, I., Sanchez-Valle, C., Daniel, I., and Reynard, B. (2004). High-pressure and high-temperature Raman spectroscopy of carbonate ions in aqueous solution. *Chemical Geology*, 207(1):47–58. (Cited on page 16.)

Marx, D. and Parrinello, M. (1996). Ab initio path integral molecular dynamics: Basic ideas. *The Journal of chemical physics*, 104(11):4077–4082. (Cited on page 31.)

Mattsson, T. R. and Desjarlais, M. P. (2006). Phase diagram and electrical conductivity of high energy-density water from density functional theory. *Physical review letters*, 97(1):017801. (Cited on pages 11 and 68.)

McCord, T., Hansen, G., Fanale, F., Carlson, R., Matson, D., Johnson, T., Smythe, W., Crowley, J., Martin, P., Ocampo, A., et al. (1998). Salts on Europa's surface detected by Galileo's near infrared mapping spectrometer. *Science*, 280(5367):1242–1245. (Cited on page 16.)

McCord, T. B., Hansen, G. B., and Hibbitts, C. A. (2001). Hydrated salt minerals on Ganymede's surface: Evidence of an ocean below. *Science*, 292(5521):1523–1525. (Cited on page 16.)

McMahon, J. M. (2011). Ground-state structures of ice at high pressures from ab initio random structure searching. *Physical Review B*, 84(22):220104. (Cited on pages 9 and 15.)

Mermin, N. D. (1965). Thermal Properties of the Inhomogeneous Electron Gas. *Phys. Rev.*, 137:A1441–A1443. (Cited on page 25.)

Meyer, E. R., Kress, J. D., Collins, L. A., and Ticknor, C. (2014). Effect of correlation on viscosity and diffusion in molecular-dynamics simulations. *Physical Review E*, 90(4):043101. (Cited on page 43.)

Meyer, E. R., Ticknor, C., Kress, J. D., and Collins, L. A. (2016). Alternative first-principles calculation of entropy for liquids. *Physical Review E*, 93(4):042119. (Cited on pages 38 and 43.)

Militzer, B. and Wilson, H. F. (2010). New Phases of Water Ice Predicted at Megabar Pressures. *Phys. Rev. Lett.*, 105. (Cited on page 9.)

Mishima, O. and Endo, S. (1978). Melting curve of ice VII. *The Journal of Chemical Physics*, 68(10):4417–4418. (Cited on page 9.)

Monkhorst, H. J. and Pack, J. D. (1976). Special points for Brillouin-zone integrations. *Physical review B*, 13(12):5188. (Cited on pages 32 and 113.)

Morrone, J. A., Lin, L., and Car, R. (2009). Tunneling and delocalization effects in hydrogen bonded systems: A study in position and momentum space. *The Journal of chemical physics*, 130(20):204511. (Cited on page 31.)

Mouhat, F. and Coudert, F.-X. (2014). Necessary and sufficient elastic stability conditions in various crystal systems. *Physical Review B*, 90(22):224104. (Cited on page 53.)

Nabarro, F. (1947). Dislocations in a simple cubic lattice. *Proceedings of the Physical Society*, 59(2):256. (Cited on pages 112 and 117.)

Nelmes, R., Loveday, J., Marshall, W., Hamel, G., Besson, J., and Klotz, S. (1998). Multisite disordered structure of ice VII to 20 GPa. *Physical review letters*, 81(13):2719. (Cited on page 83.)

Ninet, S., Datchi, F., and Saitta, A. (2012). Proton disorder and superionicity in hot dense ammonia ice. *Physical review letters*, 108(16):165702. (Cited on page 7.)

Nishiyama, N., Katsura, T., Funakoshi, K.-i., Kubo, A., Kubo, T., Tange, Y., Sueda, Y.-i., and Yokoshi, S. (2003). Determination of the phase boundary between the B1 and B2 phases in NaCl by in situ x-ray diffraction. *Physical Review B*, 68(13):134109. (Cited on pages 102 and 103.)

Noguchi, N. and Okuchi, T. (2016). Self-diffusion of protons in H_2O ice VII at high pressures: Anomaly around 10 GPa. *The Journal of Chemical Physics*, 144(23):234503. (Cited on pages 15 and 83.)

Nose, S. (1984). A unified formulation of the constant temperature molecular dynamics methods. *The Journal of Chemical Physics*, 81. (Cited on page 29.)

Nye, J. F. (1985). *Physical properties of crystals: their representation by tensors and matrices*. Oxford university press. (Cited on page 51.)

Okada, T., Iitaka, T., Yagi, T., and Aoki, K. (2014). Electrical conductivity of ice VII. *Scientific reports*, 4:5778. (Cited on page 83.)

Okhotnikov, K., Charpentier, T., and Cadars, S. (2016). Supercell program: a combinatorial structure-generation approach for the local-level modeling of atomic substitutions and partial occupancies in crystals. *Journal of cheminformatics*, 8(1):17. (Cited on pages 92 and 93.)

Ono, S., Brodholt, J. P., Alfè, D., Alfredsson, M., and Price, G. D. (2008). Ab initio molecular dynamics simulations for thermal equation of state of B2-type NaCl. *Journal of Applied Physics*, 103(2):023510. (Cited on pages 102 and 103.)

Ono, S., Kikegawa, T., and Ohishi, Y. (2006). Structural property of CsCl-type sodium chloride under pressure. *Solid state communications*, 137(10):517–521. (Cited on page 102.)

Parr, R. G. and Yang, W. (1994). *Density-Functional Theory of Atoms and Molecules (International Series of Monographs on Chemistry)*. Oxford University Press, USA. (Cited on pages 22 and 23.)

Parrinello, M. and Rahman, A. (1980). Crystal Structure and Pair Potentials: A Molecular-Dynamics Study. *Phys. Rev. Lett.*, 45:1196–1199. (Cited on pages 30 and 105.)

Parrinello, M. and Rahman, A. (1981). Polymorphic transitions in single crystals: A new molecular dynamics method. *Journal of Applied physics*, 52(12):7182–7190. (Cited on pages 30 and 105.)

Pauling, L. (1935). The Structure and Entropy of Ice and of Other Crystals with Some Randomness of Atomic Arrangement. *Journal of the American Chemical Society*, 57(12):2680–2684. (Cited on page 4.)

Peierls, R. (1940). The size of a dislocation. *Proceedings of the Physical Society*, 52(1):34. (Cited on pages 112 and 117.)

Perdew, J. P., Burke, K., and Ernzerhof, M. (1996). Generalized Gradient Approximation Made Simple. *Phys. Rev. Lett.*, 77:3865–3868. (Cited on pages 25 and 32.)

Petrenko, V. F. and Whitworth, R. W. (1999). *Physics of ice*. OUP Oxford. (Cited on page 5.)

Pickard, C. J., Martinez-Canales, M., and Needs, R. J. (2013). Decomposition and terapascal phases of water ice. *Physical review letters*, 110(24):245701. (Cited on page 9.)

Pistorius, C. W., Pistorius, M. C., Blakey, J., and Admiraal, L. (1963). Melting curve of ice VII to 200 kbar. *The Journal of Chemical Physics*, 38(3):600–602. (Cited on page 9.)

Postberg, F., Schmidt, J., Hillier, J., Kempf, S., and Srama, R. (2011). A salt-water reservoir as the source of a compositionally stratified plume on Enceladus. *Nature*, 474(7353):620–622. (Cited on page 16.)

Pruzan, P., Chervin, J., and Canny, B. (1992). Determination of the D_2O ice VII–VIII transition line by Raman scattering up to 51 GPa. *The Journal of chemical physics*, 97(1):718–721. (Cited on page 6.)

Pruzan, P., Chervin, J. C., and Canny, B. (1993). Stability domain of the ice VIII proton-ordered pahse at very high pressure and low temperature. *Journal of Chemical Physics*, 99. (Cited on pages 6, 7 and 8.)

Pruzan, P., Chervin, J. C., Wolanin, E., Canny, B., Gautier, M., and Hanfland, M. (2003). Phase diagram of ice in the VII-VIII-X domain. Vibrational and structural data for strongly compressed ice VIII. *Journal of Raman Spectroscopy*, 34. (Cited on page 83.)

Redmer, R., Mattsson, T. R., Nettelmann, N., and French, M. (2011). The phase diagram of water and the magnetic fiels of Uranus and Neptune. *Icarus*, 211. (Cited on pages 6, 13, 14 and 81.)

Ryzhkin, I. (1985). Superionic transition in ice. *Solid state communications*, 56(1):57–60. (Cited on page 12.)

Schwager, B. and Boehler, R. (2008). H_2O: another ice phase and its melting curve. *High Pressure Research*, 28(3):431–433. (Cited on pages 9, 10 and 82.)

Schwager, B., Chudinovskikh, L., Gavriliuk, A., and Boehler, R. (2004). Melting curve of H_2O to 90 GPa measured in a laser-heated diamond cell. *Journal of Physics: Condensed Matter*, 16(14):S1177. (Cited on pages 9, 10 and 82.)

Schwegler, E., Galli, G., Gygi, F., and Hood, R. Q. (2001). Dissociation of water under pressure. *Physical Review Letters*, 87(26):265501. (Cited on pages 11 and 68.)

Schwegler, E., Sharma, M., Gygi, F., and Galli, G. (2008). Melting of ice under pressure. *PNAS*, 105. (Cited on pages 10, 13 and 82.)

Schweizer, K. S. and Stillinger, F. H. (1984). High pressure phase transitions and hydrogen-bond symmetry in ice polymorphs. *The Journal of chemical physics*, 80(3):1230–1240. (Cited on page 8.)

Sears, V. (1965). The itinerant oscillator model of liquids. *Proceedings of the Physical Society*, 86(5):953. (Cited on page 42.)

Singwi, K. and Sjölander, A. (1968). Theory of Atomic Motions in Simple Classical Liquids. *Physical Review*, 167(1):152. (Cited on page 42.)

Sohl, F., Spohn, T., Breuer, D., and Nagel, K. (2002). Implications from Galileo observations on the interior structure and chemistry of the Galilean satellites. *Icarus*, 157(1):104–119. (Cited on page 16.)

Somayazulu, M., Shu, J., Zha, C.-s., Goncharov, A. F., Tschauner, O., Mao, H.-k., and Hemley, R. J. (2008). In situ high-pressure x-ray diffraction study of H_2O ice VII. *The Journal of chemical physics*, 128(6):064510. (Cited on page 83.)

Song, M., Yamawaki, H., Fujihisa, H., Sakashita, M., and Aoki, K. (1999). Infrared absorption study of Fermi resonance and hydrogen-bond symmetrization of ice up to 141 GPa. *Physical Review B*, 60(18):12644. (Cited on pages 8, 9, 74 and 75.)

Sotin, C., Grasset, O., and Mocquet, A. (2007). Mass–radius curve for extrasolar Earth-like planets and ocean planets. *Icarus*, 191(1):337–351. (Cited on pages 6, 81, 108 and 109.)

Sugimura, E., Komabayashi, T., Ohta, K., Hirose, K., and Ohishi, Y. (2012). Experimental evidence of superionic conduction in H_2O ice. *Journal of Chemical Physics*, 137. (Cited on pages 13, 15 and 59.)

Sun, J., Clark, B. K., Torquato, S., and Car, R. (2015). The phase diagram of high-pressure superionic ice. *Nature communications*, 6. (Cited on pages 9, 13 and 15.)

Sun, Q. (2012). Raman spectroscopic study of the effects of dissolved NaCl on water structure. *Vibrational Spectroscopy*, 62:110–114. (Cited on page 16.)

Tahir, N., Stöhlker, T., Shutov, A., Lomonosov, I., Fortov, V., French, M., Nettelmann, N., Redmer, R., Piriz, A., Deutsch, C., et al. (2010). Ultrahigh compression of water using intense heavy ion beams: laboratory planetary physics. *New Journal of Physics*, 12(7):073022. (Cited on page 13.)

Takii, Y., Koga, K., and Tanaka, H. (2008). A plastic phase of water from computer simulation. *The Journal of chemical physics*, 128(20):204501. (Cited on pages 6, 66 and 81.)

Todorov, I., Allan, N., Lavrentiev, M. Y., Freeman, C., Mohn, C., and Purton, J. (2004). Simulation of mineral solid solutions at zero and high pressure using lattice statics, lattice dynamics and Monte Carlo methods. *Journal of Physics: Condensed Matter*, 16(27):S2751. (Cited on pages 54 and 55.)

Vargaftik, N., Alekseev, V., Kozhevnikov, V., Ryzhkov, Y. F., and Stepanov, V. (1978). Equation of state of the liquid alkali metals. I. *Journal of Engineering Physics and Thermophysics*, 35(5):1361–1366. (Cited on page 48.)

Verlet, L. (1967). Computer Experiments on Classical Fluids. I. Thermodynamical Properties of Lennard-Jones Molecules. *Phys. Rev.*, 159. (Cited on page 29.)

Vinet, P., Ferrante, J., Smith, J., and Rose, J. (1986). A universal equation of state for solids. *Journal of Physics C: Solid State Physics*, 19(20):L467. (Cited on page 79.)

Vitek, V. (1968). Intrinsic stacking faults in body-centred cubic crystals. *Philosophical Magazine*, 18(154):773–786. (Cited on page 112.)

Vitek, V. (1974). Theory of the core structures of dislocations in BCC metals. *Cryst. Lattice Defects*, 5(1):1–34. (Cited on page 112.)

Vitek, V., Perrin, R., and Bowen, D. (1970). The core structure of 1/2 (111) screw dislocations in bcc crystals. *Philosophical Magazine*, 21(173):1049–1073. (Cited on page 114.)

Walsh, J. M. and Rice, M. H. (1957). Dynamic compression of liquids from measurements on strong shock waves. *The Journal of Chemical Physics*, 26(4):815–823. (Cited on page 11.)

Wang, G., Strachan, A., Cagin, T., and Goddard, W. A. (2001). Molecular dynamics simulations of $1/2a\,\langle 111\rangle$ screw dislocation in Ta. *Materials Science and Engineering: A*, 309:133–137. (Cited on page 112.)

Wang, J. H. (1965). Self-diffusion coefficients of water. *The Journal of Physical Chemistry*, 69(12):4412–4412. (Cited on page 13.)

Wilson, H. F., Wong, M. L., and Militzer, B. (2013). Superionic to superionic phase change in water: consequences for the interiors of Uranus and Neptune. *Physical Review Letters*, 110. (Cited on pages 9, 13 and 15.)

Wolanin, E., Pruzan, P., Chervin, J. C., Canny, B., Gauthier, M., Häusermann, D., and Hanfland, M. (1997). Equation of state of ice VII up to 106 GPa. *Phys. Rev. B*, 56. (Cited on page 8.)

Zolensky, M., Bodnar, R., Schwandt, C., and Yang, S. V. (2000). Halide minerals in the Monahans (1998) and Zag H chondrite regolith breccias. *Lunar Planet. Sci*, 31:1181. (Cited on page 16.)

Zolotov, M. Y. (2012). Aqueous fluid composition in CI chondritic materials: chemical equilibrium assessments in closed systems. *Icarus*, 220(2):713–729. (Cited on page 17.)

Appendix A

Convergence tests for the simulation parameters

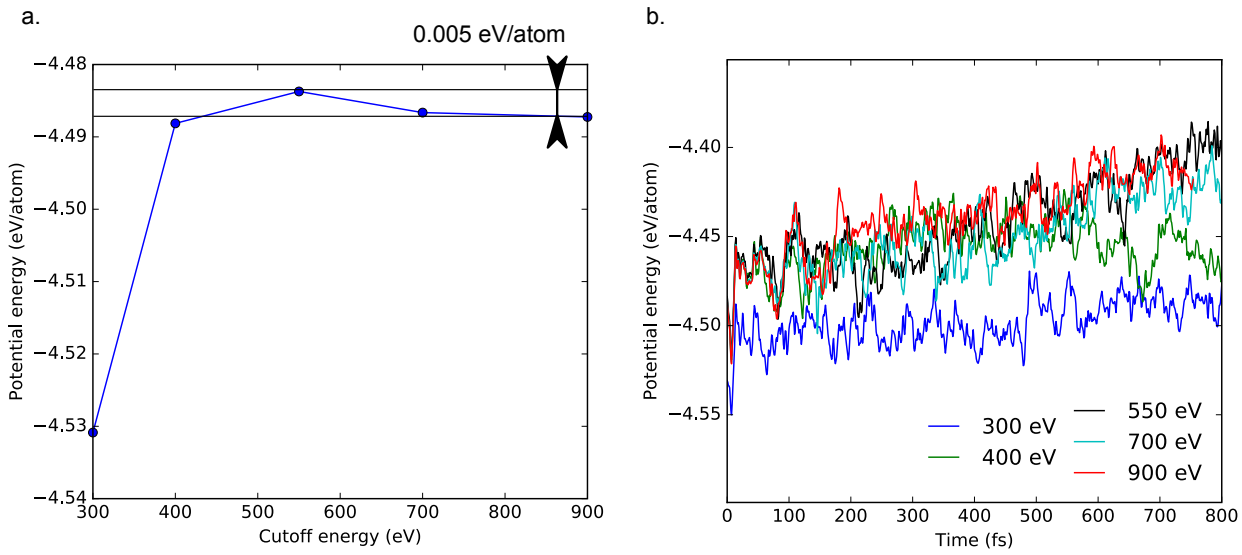

Figure A.1: a. Evolution of the potential energy as function of the cutoff energy for the plane-wave basis set in H_2O at $\rho = 2.453$ g.cm^{-3}. b. Evolution of the potential energy as a function of time for different cutoff energies. These short molecular dynamics simulations are performed in the isokinetic ensemble at 1600 K with a time step of 1 fs and at $\rho = 2.453$ g.cm^{-3} in H_2O; the system is still in the thermalization phase. For the molecular dynamics simulations we choose a cutoff energy equal to 550 eV that leads to an error of 5 meV/atom. We obtain the same accuracy in NaCl-bearing systems. This error is three time smaller than the energy variations that occurs during the molecular dynamics simulations in the production run. We perform the ionic relaxation of the dislocation quadrupoles at 0 K using a cutoff energy of 875 eV. In this case the energy is converged within 1.10^{-5} eV/atom.

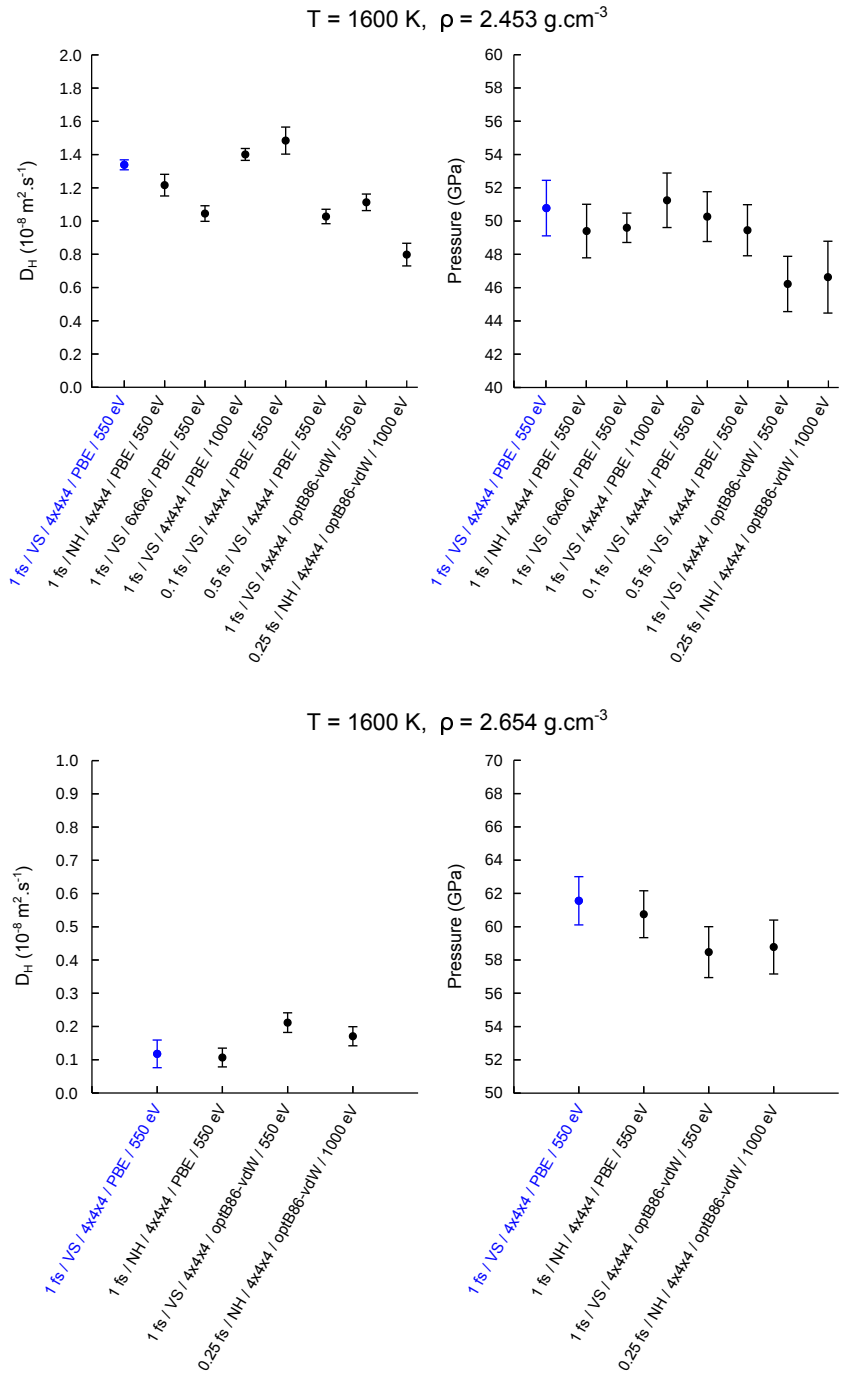

Figure A.2: Influence of different parameters (time step/thermostat/size of the cell/exchange-correlation functional/cutoff) on the H diffusion coefficients and on the pressure at two different densities at 1600 K in H_2O. VS and NH respectively refer to velocity rescaling and to Nose-Hoover thermostat. The set of parameters used to produce the results presented in the article is the first one on the left and appears in blue. Additionally we obtained $D_H = 1.41\ 10^{-8}$ m^2.s^{-1} from an *ab initio* molecular dynamics simulation performed in the NpT ensemble at 50 GPa and 1600 K with a time step of 0.25 fs, an optB86-vdW exchange-correlation functional (Klimeš et al., 2011) and a cutoff energy of 1000 eV.

Appendix B

Additional information for H_2O systems

B.1 Thermodynamic data from *ab initio* molecular dynamics simulations

Table B.1: Temperature, density, OO distance and pressure conditions for all *ab initio* molecular dynamics simulations performed on H_2O.

T (K)	ρ (g.cm^{-3})	p_{MD} (GPa)	Diffusion regime	Phase	
300	4.065	2.122	292.6	Non-diffusive	X
300	3.713	2.187	208.4	Non-diffusive	X
300	3.401	2.252	145.73	Non-diffusive	X
300	3.123	2.317	99.5	Non-diffusive	X
300	2.874	2.382	68.97	Non-diffusive	VII'
300	2.652	2.447	49.89	Non-diffusive	VII'
300	2.451	2.511	36.55	Non-diffusive	VII
300	2.270	2.576	26.52	Non-diffusive	VII
300	2.107	2.641	18.77	Non-diffusive	VII
585	2.270	2.576	28.34	Non-diffusive	VII'
585	2.107	2.641	20.47	Non-diffusive	VII
585	1.959	2.706	14.83	Non-diffusive	Plastic/VII
585	1.770	2.799	9.23	Non-diffusive	Plastic
585	1.675	2.851	7.22	Non-diffusive	Plastic
585	1.626	2.879	7.06	Non-diffusive	Plastic
800	2.451	2.511	38.51	Non-diffusive	VII'
1000	2.451	2.511	39.87	Non-diffusive	VII'
1000	2.270	2.576	30.04	Non-diffusive	VII'
1000	2.214	2.598	27.67	Superionic	VII'
1000	2.160	2.620	25.4	Superionic	VII'
1000	2.107	2.641	23.34	Superionic	VII'
1000	2.056	2.663	21.66	Superionic	VII'
1000	2.007	2.685	20.64	Superionic	VII"
1000	1.959	2.706	21.05	Superionic	VII'?
1000	1.913	2.728	19.59	Superionic	VII"
1000	1.824	2.771	17.77	Fluid	Fluid
1300	4.065	2.122	300.44	Non-diffusive	X
1300	3.713	2.187	217.98	Non-diffusive	X
1300	3.401	2.252	156.27	Non-diffusive	X
1300	3.123	2.317	111.24	Non-diffusive	X
1300	2.874	2.382	79.14	Non-diffusive	VII'

Continued on next page

Table B.1 – continued from previous page

T (K)	ρ (g.cm^{-3})	p_{MD} (GPa)	Diffusion regime	Phase	
1300	2.652	2.447	57.28	Non-diffusive	VII'
1300	2.451	2.511	43.27	Superionic	VII'
1300	2.270	2.576	34.47	Superionic	VII'
1300	2.214	2.598	34.17	Superionic	VII"
1300	2.160	2.620	32.04	Superionic	VII"
1300	2.107	2.641	29.59	Superionic	VII"
1300	1.959	2.706	23.29	Superionic	VII"
1600	4.065	2.122	303.15	Non-diffusive	X
1600	3.713	2.187	221.01	Non-diffusive	X
1600	3.605	2.208	198.49	Non-diffusive	X
1600	3.401	2.252	159.64	Non-diffusive	X
1600	3.123	2.317	114.74	Non-diffusive	X
1600	3.037	2.338	102.85	Non-diffusive	X
1600	2.954	2.360	92.12	Non-diffusive	VII'
1600	2.874	2.382	82.69	Non-diffusive	VII'
1600	2.797	2.403	74.45	Non-diffusive	VII'
1600	2.723	2.425	67.99	Superionic	VII'
1600	2.652	2.447	61.56	Superionic	VII'
1600	2.549	2.479	54.1	Superionic	VII'
1600	2.451	2.511	50.78	Superionic	VII"
1600	2.358	2.544	45.98	Superionic	VII"
1600	2.270	2.576	40.46	Superionic	VII"
1600	2.187	2.609	35.77	Superionic	VII"
1600	2.107	2.641	31.38	Superionic	VII"
1600	1.959	2.706	26.61	Fluid	Fluid
1600	1.824	2.771	20.79	Fluid	Fluid
1800	4.065	2.122	305.57	Non-diffusive	X
1800	3.713	2.187	222.69	Non-diffusive	X
1800	3.401	2.252	161.95	Non-diffusive	X
1800	3.123	2.317	117.43	Superionic	X
1800	2.874	2.382	85.92	Superionic	VII'
1800	2.760	2.414	75.02	Superionic	VII'
1800	2.652	2.447	66.63	Superionic	VII'
1800	2.549	2.479	61.22	Superionic	VII"
1800	2.451	2.511	54	Superionic	VII"
1800	2.270	2.576	41.93	Superionic	VII"
1800	2.107	2.641	35.21	Fluid	Fluid
2000	4.065	2.122	306.06	Non-diffusive	X
2000	3.713	2.187	224.95	Non-diffusive	X
2000	3.401	2.252	164.49	Superionic	X
2000	3.123	2.317	120.4	Superionic	X
2000	2.995	2.349	104.01	Superionic	VII'
2000	2.874	2.382	90.9	Superionic	VII'
2000	2.760	2.414	82.44	Superionic	VII"

Continued on next page

Table B.1 – continued from previous page

T (K)	ρ (g.cm^{-3})	p_{MD} (GPa)	Diffusion regime	Phase	
2000	2.652	2.447	72.28	Superionic	VII"
2000	2.451	2.511	55.55	Superionic	VII"
2000	2.270	2.576	43.7	Superionic	VII"
2000	2.107	2.641	36.14	Fluid	Fluid
2200	3.401	2.187	167.39	Superionic	X
2200	3.123	2.317	126.79	Superionic	VII'
4000	3.496	2.231	203.99	Superionic	?

B.2 Bonding analysis: lifetimes

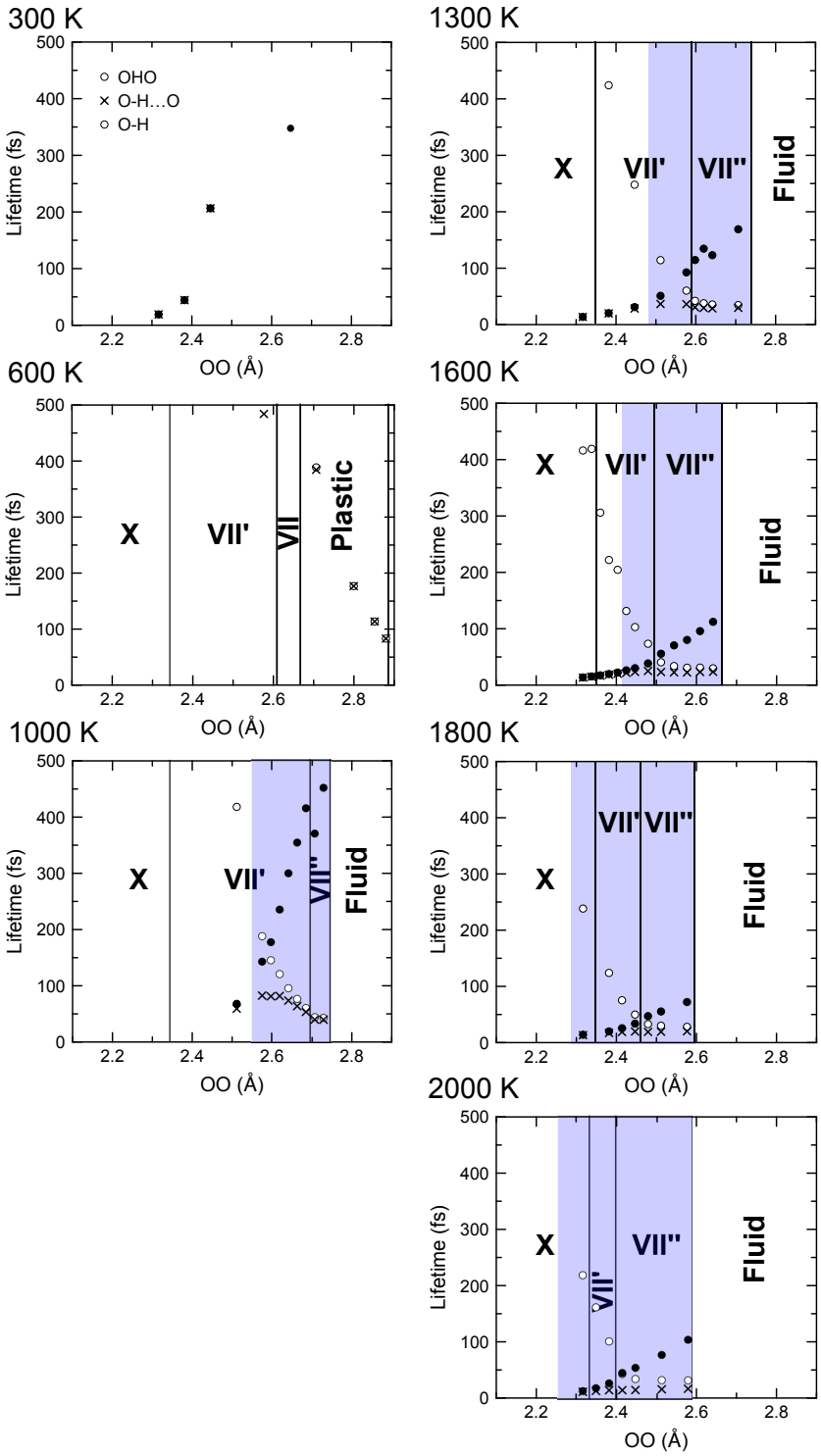

Figure B.1: Evolution of the lifetimes of the $O-H\cdots O$ bonds, $O-H-O$ triplets and $O-H$ bonds as a function of the OO distance as calculated in the bonding analysis described in Chapter 3. Blue areas indicate the regions in which the ice is superionic, i.e. where D_H is statistically positive.

B.3 Fitting parameters for $f(\rho, T)$

Table B.2: We fit the Helmholtz free energy of water ices ($f(\rho, T)$) with a Vinet equation of state: $f(\rho) = f_0 + \frac{2K_0}{\rho_0(K_0'-1)^2}\left\{2 - \left[5 + 3\left(\frac{\rho_0}{\rho}\right)^{1/3}(K_0'-1) - 3K_0'\right]\exp\left(-\frac{3(K_0'-1)}{3}\left[\left(\frac{\rho_0}{\rho}\right)^{1/3} - 1\right]\right)\right\}$ where the fitting parameters are K_0, ρ_0, K_0', f_0. This table gives the parameters obtained for each fit for H_2O.

T (K)	K_0 (GPa)	ρ_0 (g.cm^{-3})	K_0'	f_0 (g.cm^{-3})	Density range of validity (g.cm^{-3})
300	7.978	1.431	8.056	-74.275	$[2.107, 4.065]$
1300	0.333	0.823	10	-78.657	$[2.270, 4.065]$
1600	10.65	1.403	7.147	-77.778	$[2.574, 4.105]$
1800	0.541	0.914	10	-80.850	$[2.652, 4.065]$
2000	0.330	0.814	10	-82.355	$[2.874, 4.065]$

Appendix C

Additional information for $NaCl{\cdot}RH_2O$ systems

C.1 Quantum correction for the internal energy

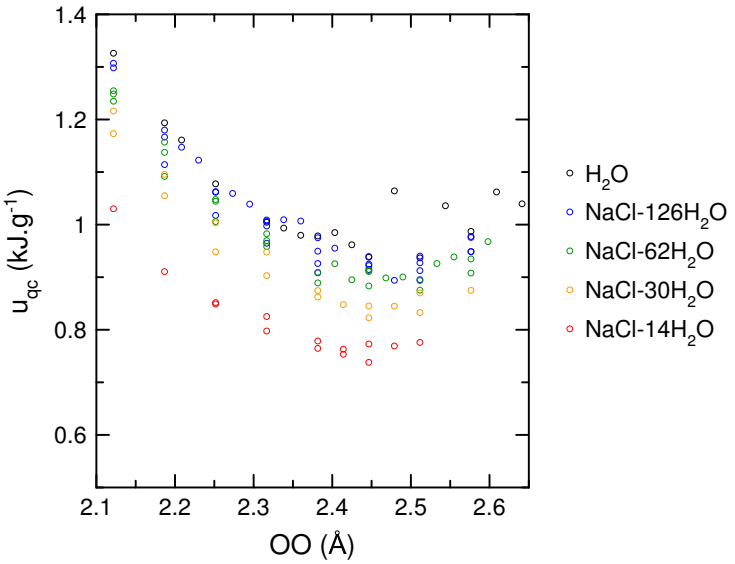

Figure C.1: Quantum correction of the internal energy of $NaCl{\cdot}RH_2O$ under compression.

C.2 Fitting parameters for $f_{sol}(R, \rho, 1600\ \mathrm{K})$

Table C.1: Parameters of the Vinet equations of state used to fit $f_{sol}(R, \rho, 1600\ \mathrm{K})$

R	K_0 (GPa)	ρ_0 (g.cm^{-3})	K_0'	$f_{sol,0}$ (g.cm^{-3})	Density range of validity (g.cm^{-3})
126	10.65	1.403	7.147	-77.778	$[2.574, 4.105]$
62	58.31	1.865	5.273	-74.635	$[2.704, 4.145]$
30	2.842	1.124	8.000	-73.820	$[2.756, 4.226]$
14	11.85	1.444	6.609	-67.456	$[2.750, 4.388]$

Notations

Acronyms

μVT	Grand canonical ensemble
NpH	Isobaric-isoenthalpic ensemble
NpT	Isobaric-isothermal ensemble
NVE	Microcanonical ensemble
NVT	Canonical ensemble
2PT	Two-Phase Thermodynamic (model)
2PT-MF	Two-Phase Thermodynamic Memory Function (model)
CEA	Commissariat à l'Energie Atomique et aux énergies alternatives
CHO	Classical Harmonic Oscillator
CINES	Centre Informatique National de l'Enseignement Supérieur et de la recherche
cpus	Central processing units
DAC	Diamond Anvil Cell
DFT	Density Functional Theory
GGA	Generalized Gradient Approximation
GSF	Generalized Stacking Fault
HS	Hard-Sphere
KBI	Kirkwood-Buff Integral
LDA	Local Density Approximation
LO	Longitudinal Optic
MSD	Mean square displacement
NQEs	Nuclear Quantum Effects
PAW	Projector-Augmented Wave
PBC	Periodic Boundary Conditions
PBE	Perdew-Burke-Ernzerhof
QHO	Quantum Harmonic Oscillator
RDF	Radial Distribution Function

TGCC Très Grand Centre de Calcul

TO Transversal Optic

VASP Vienna Ab initio Simulation Package

VDoS Vibrational density of states

Constants

$\hbar$ Reduced Planck constant

ε_0 Void permitivity

e Electron charge

k_B Boltzmann constant

m_e Electron mass

Variables and operators

$\bar{V}_\alpha$ Partial molar volume

$\Delta\overline{G}_{mix}$ Molar Gibbs free energy of mixing

Δg_{mix} Specific Gibbs free energy of mixing

Δ_α Normalized diffusivity

$\Delta_{HE}E$ Energy difference between the hard and easy configurations of the $\langle 111 \rangle$ dislocations

γ_f Friction coefficient (Langevin thermostat)

$\hat{\cdot}$ Laplace transform of a given quantity

ι Shear stress to apply on the dislocation

κ_v Voigt expression of the bulk modulus

Λ Function that gives the elastic interactions between dislocation pairs

$\langle \cdot \rangle$ Ensemble average

$\langle\ \rangle_{t_0}$ Average over time origins t_0

$\{\mathbf{P}_I\}$ Ensemble of momentum vectors of all nuclei I

$\{\mathbf{R}_I\}$ Ensemble of position vectors of all nuclei I

σ Stress tensor

$\mathbf{b}$ Burgers vector

$\mathbf{F}$ Force that applyies on the dislocation line (Peach-Koehler force)

$\mathbf{f}_f$ Random force associated with γ_f

$\mathbf{G}$ Reciprocal lattice vector

$\mathbf{J}$ Electrical current

$\mathbf{k}$ Wave-vector

$\mathbf{P}_I$ Momentum vector of a nucleus I

$\mathbf{p}_I$ Momentum vector of an electron I

$\mathbf{r}$ Coordinate vector

$\mathbf{R}_I$ Position vector of a nucleus I

$\mathbf{r}_I$ Position vector of an electron I

$\mathbf{v}$ Atom velocity vector

$\mathcal{H}$ Halmitonian

$\mathcal{H}_e$ Electronic halmitonian

$\mathcal{H}_n$ Nuclear halmitonian

$\mathcal{N}_{\alpha\beta}(r)$ Coordination function

$\mathcal{O}$ Microscopic observable

$\mathcal{S}(\nu)$ Vibrational density of states

$\mathcal{S}_\alpha(\nu)$ Vibrational spectrum of atomic species α

$\mathcal{S}^g_\alpha(\nu)$ Gas-like part of the vibrational spectrum of species α

$\mathcal{S}^s_\alpha(\nu)$ Solid-like part of the vibrational spectrum of species α

$\mathcal{T}_0[n(\mathbf{r})]$ Kinetic energy functional of a system of non-interacting electrons of same density

μ Chemical potential

μ_v Voigt expression of the shear modulus

$\nabla_{\mathbf{R}_I}$ Gradient with respect to the positions $\mathbf{R}_I$

ν Frequency

Ω_k Degeneracy of a given configuration k

$\phi_i(\mathbf{r})$ Kohn-Sham orbital i

$\psi^{\mathbf{k}}$ Wavefunction associated to the modulation of wave-vector $\mathbf{k}$

ρ Density

σ^{HS}_α HS diameter

σ_e Electrical conductivity

σ_f Standard deviation of the intensity of $\mathbf{f}_f$

MSD_α Mean square displacement of species α

$\tilde{P}_k$ Weight associated with a given configuration k

ε_i Energy of a Kohn-Sham orbital i

ε_J Components of the strain tensor

ζ Width of a dislocation core

a' Distance that separates two easy sites

A_k Thermodynamic quantity A of the configuration k

C_{IJ} Components of the elastic constant tensor

C_v Total heat capacity

D_α Diffusion coefficient of species α

E Internal energy

E_{cut} Cutoff kinetic energy for the plane-wave basis set

E_d Energy of a dislocation

$E_{e,0}$ Electronic ground state energy

$E_e[n(\mathbf{r})]$ Total electronic energy functional

E_K Kinetic energy

E_P Potential energy

$E_{xc}[n(\mathbf{r})]$ Exchange-correlation energy functional

f Specific Helmholtz free energy

f_α Gas fraction of species α

f^i_{occ} Fermi occupation number

$F_e[n(\mathbf{r})]$ Energy functional accounting for kinetic and potential energies of the electronic system

g Specific Gibbs free energy

$g_{\alpha\beta}(r)$ Radial pair distribution function of an atomic species β around an atomic species α

H Enthalpy

K Number of configurations for the solid solution in a given supercell

K^g_α Memory function kernel for the gas-like vibrational spectrum

K_{red} Number of independent configurations for the solid solution in a given supercell

K_T Isothermal bulk modulus

m_f Mass of the degree of freedom f

M_I Mass of a nuclei I

N Number of particles

$n(\mathbf{r})$ Electronic density

N_α Number of atoms of species α

n_α^{eff} Number of effective particules α

N_e Number of electrons

N_f Number of degrees of freedom

N_n Number of nuclei

N_{sp} Number of atomic species

p Pressure

p_{ext} External pressure

p_{th} Thermal pressure

p_{dis} Probability distribution of all the microstates corresponding to a given macrostate

p_{MD} Pressure obtained from *ab initio* molecular dynamics simulations

P_s Friction coefficient (Nose-Hoover thermostat)

Q Heat bath mass

S Total entropy

S_{conf} Configurational entropy

S_{conf}^{id} Configurational entropy of the ideal solution

S_{el} Electronic entropy

S_{vib} Vibrational entropy

T Temperature

t Time

U Total internal energy

u Specific internal energy

u' Reaction coordinate during the motion of the $\langle 111 \rangle$ dislocations between an easy and a hard site

U_{MD} Internal energy obtained from *ab initio* molecular dynamics simulations

u_{MD} Specific internal energy from the molecular dynamics simulations

u_{qc} Quantum correction for the specific internal energy

V Volume

$V_{\mathrm{eff}}(\mathbf{r})$ Effective potential that acts on the electronic system

$V_e(\mathbf{r})$ External potential that applies on the electronic system

V_P Peierls potential

v_P P-wave velocity

v_S S-wave velocity

$V_{xc}(\mathbf{r})$ Exchange-correlation potential

$W_{A,\alpha}$ Weighting function associated with the thermodynamical variable A and the species α

y_α HS packing fraction

Z Canonical partition function

Z_I Charge of a nucleus I

OH Shortest distance between an oxygen atom and a hydrogen atom

OO Distance between the two oxygen atoms that form the half-diagonal of the bcc unit-cell